

HIGGS SPECTROSCOPY OF SUPERCONDUCTORS IN NONEQUILIBRIUM



im Fachbereich Physik
der Freien Universität Berlin
eingereichte Dissertation
zur Erlangung des akademischen Grades
Dr. rer. nat.

vorgelegt von

Lukas Schwarz

Berlin 2020



Max-Planck Institut
für Festkörperforschung Stuttgart



Freie Universität Berlin

1. Gutachter: Prof. Dr. Dirk Manske
2. Gutachter: Prof. Dr. Piet Brouwer

Tag der Einreichung: 15. April 2020
Tag der Disputation: 5. Oktober 2020

Contents

Abstract	iii
Zusammenfassung	v
1 Introduction	1
2 Theory and Methods	7
2.1 Higgs Physics	7
2.1.1 Spontaneous Symmetry Breaking	7
2.1.2 Higgs and Goldstone Modes	8
2.1.3 Anderson-Higgs Mechanism	10
2.1.4 Superconductors and Meissner Effect	12
2.1.5 Higgs Mode in Other Condensed Matter Physics Systems	14
2.2 BCS Theory	16
2.2.1 Hamiltonian and Energy Gap Equation	16
2.2.2 Nambu-Gorkov Basis	18
2.2.3 Bogoliubov Transformation	18
2.2.4 Equilibrium State	21
2.2.5 Anderson Pseudospin Formalism	22
2.3 Nonequilibrium Dynamic	24
2.3.1 Bloch Equations in Pseudospin Formalism	24
2.3.2 Density Matrix Formalism	25
2.3.3 Iterated Equation of Motion Approach	25
3 Classification and Characterization of Higgs Modes	27
3.1 Excitation of Higgs Oscillations with Interaction Quenches	27
3.1.1 Linear Analysis within Pseudospin Formalism	27
3.1.2 Additional Damping of Oscillations	40
3.1.3 Higher-harmonic Higgs Oscillations	43
3.2 Excitation of Higgs Oscillations with State Quenches	44
3.2.1 Linear Analysis within Pseudospin Formalism	46
3.2.2 Additional Higgs Modes for Nontrivial Gap Symmetries	48
3.2.3 Quench Strength Dependence	51
3.2.4 Time Evolution of the Condensate	54
3.2.5 Temperature Dependence	56
3.2.6 Classification and Characterization of Higgs Oscillations	57
4 Higgs Spectroscopy with Quench-Probe Experiments	61
4.1 Time-resolved Optical Conductivity	61
4.1.1 Coupling to Light and Equations of Motion	61
4.1.2 Induced Gap Oscillations by Quench Pulse	64
4.1.3 Higgs Oscillations in the Optical Conductivity	67
4.1.4 Discussion	70

4.2	Time-resolved ARPES	70
4.2.1	Theory and Iterated Equation of Motion Approach	71
4.2.2	Higgs Oscillations in the Spectral Function	75
4.2.3	Momentum-resolved Condensate Dynamic	78
4.2.4	Analysis of Oscillation Phase	81
4.2.5	Discussion	82
5	Higgs Spectroscopy with Periodic Driving and Third-harmonic Generation	85
5.1	Driven Higgs Oscillations	85
5.2	Observation of Higgs Modes in Third-harmonic Generation Response	92
5.2.1	Temperature Dependence	97
5.2.2	Polarization Dependence	99
5.2.3	Asymmetric Driving	101
5.3	Linear Activation of Higgs Oscillations in Current-carrying States	102
5.3.1	Phenomenological Description	103
5.3.2	Microscopic Description	104
5.3.3	Interpretation via Current-assisted Raman Process	107
5.4	Discussion	108
6	Discussion and Outlook	111
	Appendices	117
A	Numerical Implementation	117
A.1	Implementation of Bloch Equations	117
A.2	Influence of Momentum Grid Resolution	119
A.3	Implementation of Density Matrix Formalism	120
A.4	Implementation of Iterated Equation of Motion Approach	122
A.5	Numerical Evaluation of THG Intensities	122
B	Derivation of Coupling to Light for Pump-Probe	123
C	Derivation of Equations of Motion for Pump-Probe	126
D	Derivation of Probe Pulse Current	132
E	Derivation of Equations of Motion for tr-ARPES	134
F	Effective Interaction Quench due to Periodic Driving	139
	Bibliography	141
	Statement of Authorship	155
	Acknowledgements	157
	Publications	159

Abstract

Superconductors exhibit a collective amplitude mode of the order parameter, which is called Higgs mode. With the upcoming of new THz laser technology in recent years, it was possible to excite Higgs oscillations in nonequilibrium experiments. This thesis studies Higgs oscillations in unconventional superconductors with nontrivial pairing symmetry. In comparison to conventional superconductors, unconventional superconductors show a much richer spectrum of Higgs modes.

The occurring Higgs modes depend on the pairing symmetry and the excitation scheme. These modes are interesting to study as their oscillation frequency encodes multiple ground state properties of the energy gap like number of nodes in the pairing symmetry, sign of the symmetry function, number of gaps or even coupling to other modes. In this thesis, different kinds of excitation schemes are explored, including interaction quenches, state quenches, coupling to ultrashort THz light pulses or periodic driving with light. Excited by these methods, several observables are investigated, including the induced gap oscillation itself, time-resolved optical conductivity, time-resolved ARPES spectra and third-harmonic generation responses. In all of these quantities, Higgs oscillations can be observed, which allows for an experimental observation. This thesis is embedded in a new upcoming field, termed Higgs spectroscopy, which aims for the systematic investigation and identification of Higgs modes in superconductors. As a future perspective, the tool of Higgs oscillations might be used as a novel spectroscopic tool for studies on unconventional superconductors.

Zusammenfassung

In Supraleitern existiert eine kollektive Amplitudenmode des Ordnungsparameters, welche Higgs-Mode genannt wird. Mit Hilfe der in den letzten Jahren aufkommenden THz Laser Technologie war es möglich, Higgs-Oszillationen im Nichtgleichgewicht anzuregen. Diese Arbeit untersucht Higgs-Oszillationen in unkonventionellen Supraleitern mit nichttrivialer Paarungssymmetrie. Im Vergleich zu konventionellen Supraleitern weisen unkonventionelle Supraleiter ein viel komplexeres Spektrum auf.

Die auftretenden Higgs-Moden hängen dabei von der Paarungssymmetrie und der Anregungsart ab. Diese Moden sind interessant zu untersuchen, da ihre Oszillationsfrequenz eine Vielzahl von Grundzustandseigenschaften enthält, wie Anzahl von Knoten der Paarungssymmetrie, das Vorzeichen der Symmetriefunktion, Anzahl an Energielücken oder sogar die Kopplung an andere Moden. In dieser Arbeit werden unterschiedliche Anregungsarten untersucht, wie Wechselwirkungs-Quenches, Zustand-Quenches, Kopplung an ultrakurze THz-Lichtpulse oder periodisches Treiben mit Licht. Nach der Anregung durch diese Methoden werden unterschiedliche Beobachtungsgrößen ausgewertet, darunter die induzierten Energielückenoszillationen, die zeitaufgelöste optische Leitfähigkeit, zeitaufgelöste ARPES-Spektren und die erzeugte dritte-harmonische Antwort. In all diesen Größen können Higgs-Oszillationen beobachtet werden, wodurch eine experimentelle Messung möglich wird. Diese Arbeit ist in einem neuen aufstrebenden Feld, der Higgs-Spektroskopie, eingebettet, welches darauf abzielt, die Higgs-Moden in Supraleitern systematisch zu untersuchen und zu identifizieren. Perspektivisch könnten Higgs-Oszillationen als ein neues spektroskopisches Werkzeug zur Untersuchung von unkonventionellen Supraleitern verwendet werden.

1 Introduction

Condensed matter physics has several conceptual connections to high-energy physics. There are analogies on the fermionic side such as Majorana fermions, where quasiparticles are their antiparticles in topological superconductors [1], or Weyl fermions and massless Dirac particles in semimetals [2]. On the bosonic side, there is one analogy, which is connected to the Higgs mechanism. Actually, this mechanism applied to superconductors was first described by P. W. Anderson in 1963 [3] and was extended to a relativistic description for particle physics by P. Higgs and others one year later [4–6]. In condensed matter physics, it is therefore often called Anderson-Higgs mechanism. While in high-energy physics, the Higgs mechanism gives mass to the W^\pm and Z^0 gauge bosons of the weak interaction, in superconductors, the Higgs mechanism gives mass to the photons. This corresponds to the Meissner effect, i.e. an expulsion, or more accurately, an exponential decay of the magnetic field in the material due to the finite mass of the photon. Just as the Higgs boson is the elementary excitation of the Higgs field, there is also an elementary excitation in superconductors. As the superconducting condensate represents the Higgs field, the Higgs mode is a collective excitation of the superconducting order parameter. On a phenomenological level, there is a basic picture to visualize the Higgs mode. The Ginzburg-Landau free energy of a superconductor has the shape of a Mexican hat (Fig. 1.1), where in the ground state, the order parameter is located at the minimum of the brim. The Higgs mode corresponds to radial excitations in this picture, i.e. fluctuations in the amplitude of the order parameter. In an s -wave superconductor, the energy of the Higgs mode or the frequency of the oscillation is given by the value of the superconducting gap 2Δ .

While the Anderson-Higgs mechanism was already predicted theoretically in the 1960s, there was no experimental evidence for the Higgs mode in superconductors for a long time. This is due to the fact that an excitation of the Higgs mode is rather challenging as its coupling to external probes is weak. The Higgs mode is a scalar mode without electric or magnetic dipole moment. Thus, it cannot couple linearly to light. Its excitation is restricted to nonlinear processes, which makes its detection difficult. The fundamental excitation can be understood as an effective Raman excitation depicted in Fig. 1.2a), which is a two-photon process. However, light cannot couple directly to the Higgs mode as the light-matter coupling occurs in the charge channel, whereas the Higgs mode occurs in the orthogonal amplitude channel [9–11]. Therefore, the vertex shown in Fig. 1.2a) should be understood as an effective vertex including additional components.

Indeed, the first experimental fingerprint was rather indirect. In 1980/1981, it was observed [12, 13] and also theoretically described [14, 15] that in the superconductor NbSe_2 , the Higgs mode can couple to a charge density wave (CDW), which is on a similar energy scale in this specific material. In a Raman experiment, a peak below 2Δ was observed. It was attributed to the renormalized Higgs mode coupling to the CDW and through this, it becomes Raman-active. These experiments were recently repeated for varying temperature comparing NbSe_2 with NbS_2 , where no CDW exists [16, 17]. In addition, pressure dependence has been investigated [18, 19], confirming the results of the early experiments.

A direct excitation of the Higgs mode is believed to be possible only in nonequilibrium experiments. This was predicted for the first time in 1974 [20], where a quench of the superconducting order parameter was considered and the ensuing nonequilibrium dynamic calculated. In the description of the free energy, a quench corresponds to a fast shrinking of the Mexican hat, such that the old equilibrium position is no longer an equilibrium position of the quenched system

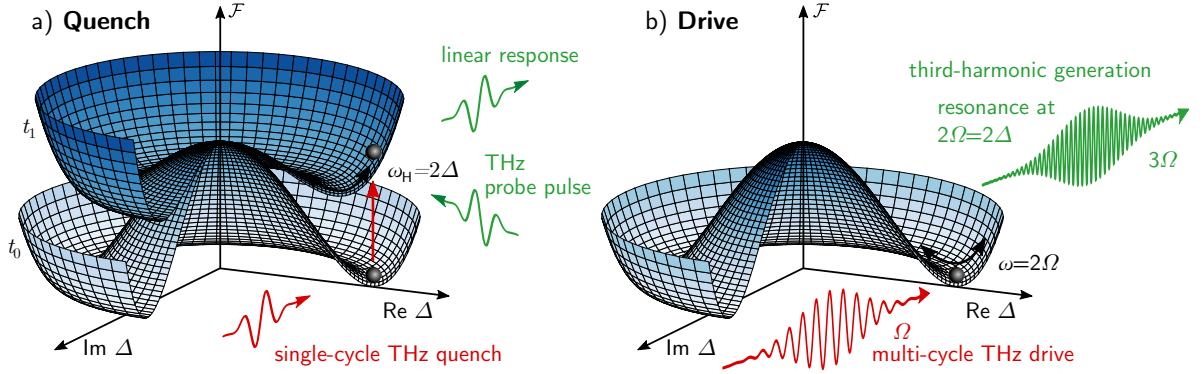


Figure 1.1 a) Free energy \mathcal{F} of a superconductor shaped as a Mexican hat, where the black ball represents the order parameter. After a quench with a THz laser pulse, the equilibrium potential shrinks from $t_0 \rightarrow t_1$. The order parameter ends up in an out of equilibrium position and starts to oscillate around the new minimum with a frequency of $\omega_H = 2\Delta$. This radial oscillation corresponds to the Higgs mode, i.e. a fluctuation in the amplitude of the order parameter. The oscillation can be probed in linear response with a second pulse. b) Driven Higgs oscillations with a multi-cycle THz laser pulse of frequency Ω . Due to the quadratic coupling, the order parameter is enforced to oscillate with 2Ω . A third-harmonic generation (THG) signal is emitted, which shows a resonance when the driving frequency coincides with the energy of the Higgs mode, i.e. at $2\Omega = 2\Delta$. Figure adapted from [7] and [8].

and oscillations around the new minimum occur (Fig. 1.1a). These induced oscillations have a frequency of 2Δ , i.e. the energy of the Higgs mode.

This idea of quenching the superconductor to push it to a nonequilibrium state has led to a large number of theoretical studies including explorations of different quench regimes [21–23], studies about the integrability of the quenched system [24–27], how to quench a superconductor with light pulses [28–31] and studies on 1d [32] or multiband systems [33]. Furthermore, the general theory of Higgs physics in superconductors and other condensed matter systems has been widely explored [9, 34, 35].

However, after these theoretical works, it took a few more years until the first experimental observation of Higgs oscillations in nonequilibrium in the s -wave superconductor $\text{Nb}_{1-x}\text{Ti}_x\text{N}$ in 2013 [36]. In this experiment, Higgs oscillations could be observed in the time-resolved optical conductivity in a pump-probe setup (Fig. 1.1a). Coincidentally, this happened just one year after the detection of the long-sought Higgs boson of the standard model at CERN in 2012 [37, 38], which boosted the research interest on Higgs physics in condensed matter. The nonequilibrium experiment on superconductors requires phase-stable single-cycle ultrafast THz laser pulses in order to quench the superconductor. While THz technology is required to match with the typical energy gap sizes of superconductors in the meV range, single-cycle pulses are crucial to change the system fast in a nonadiabatic way to resemble a quantum quench. Such experiments are a new method compared to traditional pump-probe experiments, where the system is excited by a pump pulse to high energy states and the relaxation is studied by a second weak probe pulse, which is applied after a variable time delay to scan the dynamic. With the ultrafast THz lasers, the pump pulse acts as a quench and excites the system only gently such that its dynamic can be observed with the probe pulse without the whole signal being screened by the response of hot electrons.

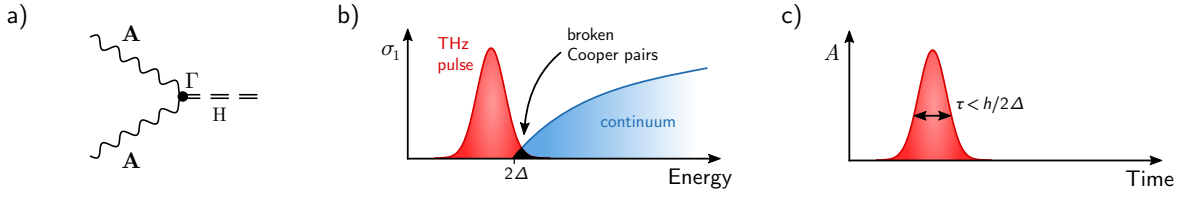


Figure 1.2 a) Feynman diagram describing the excitation of the Higgs mode with light via a nonlinear two-photon effective Raman process. The vertex Γ is an effective vertex describing the coupling of light to the Higgs mode. The wiggly line represents the photon and the double-dashed line the Higgs mode. b) Experimental requirement of the quench pulse energy. The THz pulse should only slightly overlap with the quasiparticle continuum in order to not completely deplete the condensate. c) Experimental requirement of the quench pulse in time. The pulse should be short in time, i.e. $\tau < h/2\Delta$, in order to quench the condensate and induce a nonadiabatic change of the system. Figure adapted from [7].

The actual implementation of the pump or quench pulse contains certain subtleties, which make the quench-probe experiments difficult to conduct. There are two contradictory conditions for the quench pulse, which are depicted in Fig. 1.2b) and c). On the one hand, the pulse should be narrow in energy and positioned inside the gap 2Δ , with only a small overlap over the quasiparticle continuum. With this, the required excitation energy still lies within the bandwidth of the pulse but only with low intensity such that a strong depletion of the condensate is prevented, which would screen the measured signal due to a strong Drude response. On the other hand, the pulse must also be short in time in order to induce a fast change of the system and act as a quench. A pulse which is too wide changes the system only adiabatically, which means, in the picture of the Mexican hat, that the ball would always stay in the ground state during the shrinking of potential and no oscillations occur. These two conditions cannot be fulfilled perfectly simultaneously due to the quantum mechanical energy-time uncertainty. However, single-cycle THz pulses lie exactly in between these two regimes, which makes them the perfect tool for such nonequilibrium excitations.

Only shortly later after the pump-probe experiment, the Higgs mode was measured with an alternative setup in 2014 [39]. Instead of quenching the superconductor, it was periodically driven with a multi-cycle THz pulse (see Fig. 1.1b). Due to the quadratic coupling of light to the condensate, a driving with frequency Ω leads to an effective 2Ω drive. When the energy of the driving field matches with the energy of the Higgs mode, i.e. $2\Omega = 2\Delta$, a resonance occurs, which can be observed in the nonlinear third-harmonic generation (THG) response [40]. This allows to detect the existence of the Higgs mode due to a resonance in the THG spectrum.

With the experimental observability of the Higgs mode proven, a huge number of new theoretical efforts were stimulated. This is demonstrated by the following long enumeration, which gives an overview of pursued research directions. The research includes predictions on the observability of the Higgs mode in time-resolved angle-resolved photo emission spectroscopy (tr-ARPES) [41–44], investigations on additional contributions to the intensity in third-harmonic generation experiments [45–48], further studies on multiband systems [47–51] and pump-probe experiments [52–58], studies on coupling to other modes such as the Bardasis-Schrieffer mode [59–61], Leggett mode [48, 50] or charge density wave and bound-density wave order [62–64], investigations on the effect of impurity scattering in dirty superconductors, which enhances the coupling of light to the Higgs mode [65–70], analysis of dissipation or damping of the Higgs mode [43, 71–73], descriptions

of light-condensate coupling with gauge-invariant theories [69, 74–78], investigations of effects in strongly coupled superconductors [46, 72, 79], studies on linear activation in current-carrying states [80, 81] and further research on more exotic systems such as chiral Higgs modes in nematic superconductors [82], Higgs modes in pair-density wave states [83, 84], triplet superconductors [75, 85, 86], Higgs mode in proximized superconducting systems [87], Higgs mode in transport [88, 89], Rabi-Higgs oscillations in systems where the density of state is driven near the Fermi level [90], quench dynamic in nanorods [91], finite-momentum pairing states [92] or Higgs modes in massless Dirac fermion systems [93] as well as studies on general Higgs physics in superconductors [10, 94–102].

Compared to this large number of theoretical works, there were only a handful of further experimental investigations [103–111], which emphasizes the difficulties in performing these ultrafast THz experiments.

While most of the studies consider only *s*-wave superconductors, only few of them concentrate on unconventional superconductors like *d*-wave systems [29, 42, 53, 78, 94, 112]. These first studies indicate that in superconductors with nontrivial gap symmetry, a much richer spectrum of Higgs oscillations can occur. Thus, one might draw the conclusion that the information from the Higgs oscillation spectrum can be used to learn something about the ground state of the superconductor, despite the fact that the experiments are performed in nonequilibrium. For the simple *s*-wave case, one can already gain information about the value of the gap, to which the frequency of the oscillation corresponds to. Higgs oscillations of multiband systems contain information about all gaps and also the coupling in between them (Leggett mode). Furthermore, if the Higgs mode couples to energetic nearby modes, the energies of these modes can also be found in the frequency spectrum. And finally, if properly excited, nontrivial gap symmetry can lead to additional Higgs modes as well, which encodes information of the symmetry of the order parameter into the oscillation spectrum.

This thesis concentrates mainly on the latter aspect, investigating Higgs oscillations of unconventional superconductors with arbitrary gap symmetry in different kinds of excitation schemes (interaction quenches, state quenches, quenching with light, driving with light) and the resulting observables (gap oscillations, time-resolved optical conductivity, tr-ARPES, THG). It is proposed that the study of Higgs modes in superconductors, termed “Higgs spectroscopy” can serve as a new tool, which might be used in future as an alternative or complementary probe to currently used experiments on superconductors. While the experiments are still challenging to perform today, with future improved THz laser technology, simple table-top setups might be possible.

With the technological obstacles overcome, Higgs spectroscopy has some advantages to the currently used techniques for studying the superconducting ground state properties. To gain detailed information about the gap structure, typically, different kinds of experiments have to be performed. For example, ARPES, spin-lattice relaxation rates $1/T_1$ in NMR experiments, optical conductivity measurements or tunneling experiments can yield information about the amplitude of the gap. NMR Knight shift experiments provide information about the parity, i.e. if the order parameter is singlet or triplet. Kerr effect or muon spin resonance spectroscopy reveal information about whether time reversal symmetry breaking occurs and if the order parameter is complex. Finally, quasiparticle tunneling spectroscopy or Josephson interferometry experiments yield information about the phase of the order parameter. The idea of Higgs spectroscopy is that some of this information such as the amplitude, phase or nodal structure can be, in principle, obtained simultaneously with properly designed experiments and phase-stable THz lasers. Another direction where Higgs spectroscopy may be used in future is to use the observation

of a stable Higgs mode as a signature of superconductivity itself, as the Higgs mode is connected due to the Anderson-Higgs mechanism with the Meissner effect. This will be discussed later in this thesis.

This thesis is organized as follows. In chapter 2, the theory of Higgs physics and related concepts such as spontaneous symmetry breaking are explained in more detail. In addition, the BCS theory in a uniform notation and the Anderson pseudospin formalism are introduced for later chapters. Lastly, the used methods to calculate nonequilibrium dynamic are stated. In chapter 3, the nonequilibrium dynamic of a superconductor is studied, which is induced by a quench of either the pairing interaction or the condensate. The resulting Higgs oscillations are calculated and the occurring Higgs modes for nontrivial gap symmetry are investigated. This chapter concludes with a classification and characterization scheme of Higgs oscillations based on group theory. In chapter 4, quench-probe experiments are simulated, where the superconductor is quenched by a short pump pulse. In such Higgs spectroscopy experiments, oscillations of the gap can be observed either optically in the time-resolved optical conductivity or in the time-resolved ARPES spectrum. In chapter 5, the superconductor is periodically driven to enforce gap oscillations with the external driving frequency. The third-harmonic generation response is calculated, where resonances are observed when the driving frequency coincides with the energy of the Higgs modes. In chapter 6, the findings of the thesis are summarized and discussed and an outlook for future research is given.

2 Theory and Methods

In this chapter, the relevant theories and formalisms for this thesis are introduced with an uniform notation for later calculations. The purpose is to give a compact and selfconsistent overview of topics which are often scattered over various literature with inconsistent notation. References to the corresponding literature will be given for further reading at the respective places.

2.1 Higgs Physics

The theory of Higgs physics can be described most easily on a phenomenological level within an effective field theory description. This allows to introduce the concepts of spontaneous symmetry breaking, collective modes and the Anderson-Higgs mechanism. The following sections give a short introduction into these topics and connect the general concepts to superconductivity.

2.1.1 Spontaneous Symmetry Breaking

Symmetry, i.e. the invariance of a property under a certain operation, plays an important role in theoretical physics. It can either be discrete, such as the reflection or discrete rotation symmetry in the lattice of a solid, which determines the fundamental lattice vibrations, or it is continuous, such as the spatial or temporal translation invariance of macroscopic systems. For each continuous symmetry, the *Noether theorem* ensures a conservation law, e.g. momentum conservation for spatial translation invariance or energy conservation for invariance of time translation.

In contrast to the symmetries themselves, the breaking of symmetries has important consequences as well. Especially for phase transitions, where the phases have different symmetries, *spontaneous symmetry breaking* (SSB) is a crucial concept. Hereby, the ground state of a system has lower symmetry than the system itself, i.e. the ground state breaks the symmetry of the describing Hamiltonian spontaneously [113]. The simplest toy model, which is nevertheless relevant for superconductivity as we will see, is spontaneous $U(1)$ symmetry breaking in a ψ^4 theory. In this theory, one considers a complex field ψ with a potential

$$V(\psi) = \alpha|\psi|^2 + \frac{\beta}{2}|\psi|^4. \quad (2.1)$$

Obviously, due to the absolute square, we can multiply the field with an arbitrary constant phase μ , i.e. $\psi \rightarrow \psi e^{i\mu}$ without changing the potential: The theory is $U(1)$ invariant. The ground state, i.e. the minimum of the potential can easily be derived and reads

$$|\psi_0| = \begin{cases} 0 & \alpha \geq 0 \\ \sqrt{\frac{-\alpha}{\beta}} & \alpha < 0 \end{cases}. \quad (2.2)$$

We have to distinguish the two cases depicted in Fig. 2.1. The $\alpha \geq 0$ case corresponds to the normal phase, where the potential has a bowl shape and the ground state is at the origin having the same $U(1)$ symmetry as the potential, i.e. is invariant under a global phase change. In contrast for $\alpha < 0$, $\psi = 0$ is no longer the ground state. The potential has the shape of a *Mexican hat* and the states with minimum energy lie on the brim. One of these infinite many points is chosen

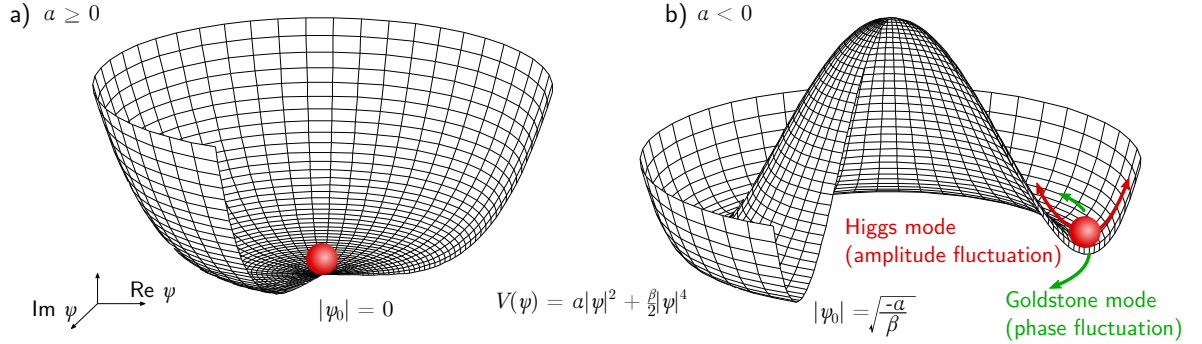


Figure 2.1 Spontaneously broken $U(1)$ symmetry. a) For $\alpha \geq 0$, the system is in the normal state, where the ground state, marked by the red ball, is invariant under a $U(1)$ phase transformation like the potential itself. b) For $\alpha < 0$, the system is in the SSB phase, where the potential takes on the form of a Mexican hat and the ground state no longer lies at the origin and does not possess a $U(1)$ symmetry. In this SSB state, collective modes appear, namely the Goldstone mode azimuthally around the brim of the Mexican hat, i.e. fluctuation of the phase, and the Higgs mode radially, i.e. fluctuations of the amplitude.

spontaneously, which breaks the original $U(1)$ symmetry of the potential: The system is in the spontaneous symmetry broken phase.

A well-known example for SSB in condensed matter is ferromagnetism, where rotational symmetry is spontaneously broken in the ferromagnetic phase due to selection of a particular direction of the magnetization. Another example are crystals, which break the continuous translation and rotation invariance of Euclidean space due to a restriction of the invariance to fixed lattice vectors. Furthermore, in high-energy physics, the electroweak symmetry is spontaneously broken. This creates the massive W^\pm and Z^0 gauge bosons for the weak interaction and the massless photon for the electromagnetic interaction by the (*Anderson*)-*Higgs mechanism*, which is described in more detail in section 2.1.3. In superconductors, the $U(1)$ symmetry of the Hamiltonian is spontaneously broken due to the Cooper pairs (see section 2.1.4), therefore, the following discussion is based on spontaneous $U(1)$ symmetry breaking.

2.1.2 Higgs and Goldstone Modes

Connected with the concept of SSB is the *Goldstone theorem*, which in its simplest formulation states that for every spontaneously broken continuous symmetry, a massless Goldstone boson exists, i.e. an excitation which costs no energy. For spontaneous $U(1)$ symmetry breaking, this can easily be understood. In the SSB phase, the model potential Eq. (2.1) has an infinitely degenerate ground state with $|\psi_0| = \sqrt{\frac{-\alpha}{\beta}}$ and arbitrary phase. Fluctuations in the phase will therefore cost no energy and correspond to the (*Nambu*-)*Goldstone mode* (see Fig. 2.1b)). In addition to these massless or gapless phase fluctuations, there can also be amplitude fluctuations, depicted as the radial oscillations in the Mexican hat potential in Fig. 2.1b). This amplitude oscillation is called *Higgs mode* and has a finite energy, i.e. it is a massive or gapped mode. Both modes are collective modes as they correspond to fluctuations of the order parameter itself.

To describe the dynamic of these modes in more detail, one can make use of a field theoretical approach described by an effective Lagrangian. The dynamical terms can be chosen either

relativistic or nonrelativistic [34, 101], i.e. Lorentz-invariant or non-Lorentz invariant, which will lead to Klein-Gordon- or Gross-Pitaevskii-like equations of motion, respectively. The difference between the relativistic and nonrelativistic description is that in the former case, the equation is in second order in time, whereas in the latter case, it is in first order in time. Thus, the Lagrangian reads

$$\begin{aligned}\mathcal{L}^{\text{KG}} &= (\partial_\mu \psi)^* (\partial^\mu \psi) - V(\psi) \\ &= (\partial_t \psi)^* (\partial_t \psi) - (\nabla \psi)^* (\nabla \psi) - V(\psi) \quad (\text{Lorentz-invariant}),\end{aligned}\quad (2.3a)$$

$$\mathcal{L}^{\text{GP}} = \psi^* (\partial_t \psi) - (\nabla \psi^*) (\nabla \psi) - V(\psi) \quad (\text{non-Lorentz invariant}). \quad (2.3b)$$

Hereby, $V(\psi)$ is the potential of Eq. (2.1) and $\partial^\mu = (\partial_t, -\nabla)$ is the four-vector of time and spatial derivatives using a metric with $(+---)$ signature. Note that $c = 1$. Next, we use an ansatz for fluctuations around the ground state ψ_0

$$\psi(\mathbf{r}, t) = (\psi_0 + H(\mathbf{r}, t)) e^{i\theta(\mathbf{r}, t)} \quad (2.4)$$

with amplitude fluctuations $H(\mathbf{r}, t)$ and phase fluctuations $\theta(\mathbf{r}, t)$. We obtain for the Lagrangian expressed in the fluctuations

$$\mathcal{L}^{\text{KG}} = (\partial_t H)^2 - (\nabla H)^2 + \psi_0^2 \left((\partial_t \theta)^2 - (\nabla \theta)^2 \right) + 2\alpha H^2, \quad (2.5a)$$

$$\mathcal{L}^{\text{GP}} = (\psi_0 + H)(\partial_t H) + i(\psi_0^2 + 2\psi_0 H)(\partial_t \theta) - (\nabla H)^2 - \psi_0^2 (\nabla \theta)^2 + 2\alpha H^2, \quad (2.5b)$$

where constant terms and terms in third order or higher of the fluctuations are neglected. Now, we can minimize the action by evaluating Euler-Lagrange equations for H and θ

$$\frac{d}{dt} \frac{\partial \mathcal{L}}{\partial (\partial_t H)} + \nabla \frac{\partial \mathcal{L}}{\partial (\nabla H)} - \frac{\partial \mathcal{L}}{\partial H} = 0, \quad \frac{d}{dt} \frac{\partial \mathcal{L}}{\partial (\partial_t \theta)} + \nabla \frac{\partial \mathcal{L}}{\partial (\nabla \theta)} - \frac{\partial \mathcal{L}}{\partial \theta} = 0. \quad (2.6)$$

Let us first consider the equations of motion for the fluctuations in the relativistic case

$$(\partial_t^2 - \nabla^2)H = 2\alpha H, \quad (2.7a)$$

$$(\partial_t^2 - \nabla^2)\theta = 0. \quad (2.7b)$$

The equations for amplitude and phase are decoupled and are the Klein-Gordon equations for massive particles in the case of the amplitude fluctuations and massless particles in the case of the phase fluctuations. Using an ansatz of

$$H(\mathbf{r}, t) = H_0 e^{i(\omega t - \mathbf{q}\mathbf{r})}, \quad \theta(\mathbf{r}, t) = \theta_0 e^{i(\omega t - \mathbf{q}\mathbf{r})} \quad (2.8)$$

yields for the dispersion

$$\omega_H^2 = q^2 - 2\alpha, \quad (2.9a)$$

$$\omega_\theta^2 = q^2. \quad (2.9b)$$

In the $q \rightarrow 0$ limit for long wavelengths, this corresponds to the massive Higgs mode $\omega_H^2 = -2\alpha$ and massless Goldstone mode $\omega_\theta = 0$.

In the nonrelativistic case, the equations of motions are coupled

$$-i\psi_0(\partial_t\theta) - (\nabla^2 H) = 2\alpha H, \quad (2.10a)$$

$$i(\partial_t H) - \psi_0(\nabla^2\theta) = 0, \quad (2.10b)$$

such that there are no distinct amplitude and phase modes. The equations can be solved using a single ansatz for the amplitude and phase fluctuations

$$H(\mathbf{r}, t) = \theta(\mathbf{r}, t) = e^{i(\omega t - \mathbf{q}\mathbf{r})}, \quad (2.11)$$

which leads to

$$\omega^2 = 2\alpha q^2 - q^4. \quad (2.12)$$

We can see that in the $q \rightarrow 0$ limit, there are no finite mass modes. A Lorentz-invariant form of the Lagrangian is therefore important for distinct amplitude and phase modes and there is not necessarily a Higgs mode for an arbitrarily given Mexican-hat shaped potential. If the dynamic is described by both relativistic and nonrelativistic terms, there are coupled amplitude and phase fluctuations, where the Higgs-like mode remains massive and is pushed to higher energies [10].

2.1.3 Anderson-Higgs Mechanism

So far, the considered field ψ was uncharged. Having a charged field, a coupling to external gauge fields has to be considered, which will change the spectrum of collective modes in the SSB phase. As for superconductivity the charge is the electric charge, only a coupling to the electromagnetic field, i.e. the photon, will be considered in the following discussion. An example of coupling to other gauge fields can be found in particle physics, where the coupling of the Higgs field to the photon but also to W^\pm and Z gauge bosons of the weak interaction has to be considered. We start with a calculation using the relativistic theory, where the coupling is incorporated by replacing the four-vector of the derivative ∂_μ with the gauge covariant derivative $D_\mu = \partial_\mu + ieA_\mu$ and adding a term describing the dynamic of the gauge field.

$$\begin{aligned} \mathcal{L}^{\text{KG}} &= (D_\mu\psi)^*(D^\mu\psi) - V(\psi) - \frac{1}{4}F_{\mu\nu}F^{\mu\nu} \\ &= ((\partial_\mu - ieA_\mu)\psi^*)((\partial^\mu + ieA^\mu)\psi) - V(\psi) - \frac{1}{4}F_{\mu\nu}F^{\mu\nu}. \end{aligned} \quad (2.13)$$

Hereby, $F_{\mu\nu} = \partial_\mu A_\nu - \partial_\nu A_\mu$ is the electromagnetic field tensor and $A_\mu = (\phi, -\mathbf{A})$ the electromagnetic four-vector with the electric charge e . Now, we can use the same ansatz for the fluctuations of Eq. (2.4) to write down the Lagrangian for the amplitude and phase modes

$$\begin{aligned} \mathcal{L}^{\text{KG}} &= \left(\partial_\mu H - ie \left(A_\mu + \frac{1}{e} \partial_\mu \theta \right) (\psi_0 + H) \right) \left(\partial^\mu H + ie \left(A^\mu + \frac{1}{e} \partial^\mu \theta \right) (\psi_0 + H) \right) \\ &\quad + 2\alpha H^2 - \frac{1}{4}F_{\mu\nu}F^{\mu\nu}. \end{aligned} \quad (2.14)$$

In this expression, we neglected again constant terms and fluctuation terms of higher order than quadratic.

The coupling to the gauge fields adds a gauge freedom to the Lagrangian, i.e. the Lagrangian is invariant under a local phase transformation given by the gauge function $\chi(\mathbf{r}, t)$ if the gauge field is transformed accordingly as well

$$\psi' = \psi e^{i\chi(\mathbf{r}, t)}, \quad A'_\mu = A_\mu - \frac{1}{e} \partial_\mu \chi(\mathbf{r}, t). \quad (2.15)$$

As this transformation does not change the physics, we can exploit this freedom to simplify the expression. By comparing the expression of the gauge transformation with the gauge field and the phase fluctuation in the brackets in Eq. (2.14), we find the same structure as in the transformed gauge field. Thus, a gauge choice of $\chi = -\theta$, i.e.

$$\psi' = \psi e^{-i\theta}, \quad A'_\mu = A_\mu + \frac{1}{e} \partial_\mu \theta \quad (2.16)$$

removes the phase fluctuation completely from the Lagrangian, which are included in the redefined potential A'_μ . This means that in the case of a charged field, the massless phase fluctuations are only an artifact of the original gauge and have no physical meaning. In this context, they are also sometimes called gauge ghosts. Neglecting the primes in the gauge field, the Lagrangian then reads

$$\begin{aligned} \mathcal{L}^{\text{KG}} &= (\partial_\mu H - ieA_\mu(\psi_0 + H)) (\partial^\mu H + ieA^\mu(\psi_0 + H)) + 2\alpha H^2 - \frac{1}{4} F_{\mu\nu} F^{\mu\nu} \\ &= (\partial_\mu H)(\partial^\mu H) + 2\alpha H^2 - \frac{1}{4} F_{\mu\nu} F^{\mu\nu} + e^2 \psi_0^2 A_\mu A^\mu + 2e^2 \psi_0 A_\mu A^\mu H, \end{aligned} \quad (2.17)$$

where for the second equal sign, we neglected again higher-order couplings. In addition to the absence of phase fluctuations, we find a mass term $e^2 \psi_0^2 A_\mu A^\mu$ for the transformed gauge field. In the language of high-energy physics, this is interpreted as “the would-be Goldstone boson is being eaten by the gauge field, which then itself becomes massive”. This is the famous *Anderson-Higgs mechanism*, which describes the mass generation of the W^\pm and Z gauge bosons of the weak interaction and led to the postulation of the Higgs boson in the standard model [4–6] and the final observation at the LHC in CERN in 2012 [37, 38]. To understand the vanishing of the Goldstone mode in more detail, it is helpful to look at the involved degrees of freedom [34]. We started with the massive Higgs mode, the massless Goldstone mode and two massless transversal degrees of freedom from the vector potential corresponding to the two polarization directions of the electromagnetic field. After the gauge transformation, the Goldstone mode vanishes and the gauge field becomes massive, which allows for an additional longitudinal degree of freedom. Hence, the total number of degrees of freedom is conserved, $1 + 1 + 2 = 4$ before the gauge transformation and $1 + 3 = 4$ after the transformation.

For a nonrelativistic theory, the same argumentation is not possible. The Gross-Pitaevskii-like Lagrangian coupled to the gauge field reads

$$\mathcal{L}^{\text{GP}} = (\psi_0 + H)(\partial_t H) + i(\psi_0^2 + 2\psi_0 H)((\partial_t \theta) + e\phi) - (\nabla H)^2 - \psi_0^2 (\nabla \theta)^2 + 2\alpha H^2, \quad (2.18)$$

where the phase fluctuation cannot be gauged away as the Lagrangian does not possess a gauge freedom. Thus, there are still no distinct Higgs and Goldstone modes and there is no Anderson-Higgs mechanism in the nonrelativistic case.

2.1.4 Superconductors and Meissner Effect

Having generally introduced the concepts of Higgs physics for an arbitrary field ψ , let us connect the derived concepts to superconductivity. The spontaneous $U(1)$ symmetry breaking in the microscopic BCS theory will be discussed in the next section. On a phenomenological level, the Ginzburg-Landau theory [114, Chap. 4], [115] is already equivalent to our ψ^4 theory. The free energy of a superconductor close to T_c can be described by the same Mexican hat potential of the previous sections

$$\mathcal{F} = \alpha|\psi|^2 + \frac{\beta}{2}|\psi|^4, \quad (2.19)$$

where ψ is the superconducting order parameter, $\beta = \text{const.}$ and $\alpha = \alpha_0(T - T_c)$ is the temperature-dependent factor describing the transition from $T > T_c$ with $\alpha > 0$ to $T < T_c$ with $\alpha < 0$, i.e. the transition from the normal to the spontaneously symmetry broken superconducting phase. The superconducting order parameter plays the role of the Higgs field and the dynamic has to be described considering the coupling to the electromagnetic field as the superconducting condensate is obviously charged [99, 102]. The microscopic BCS theory is in good approximation particle-hole symmetric, i.e. the quasiparticle dispersion resembles the relativistic Dirac Hamiltonian dispersion near the Fermi momentum k_F such that the Lorentz-invariant theory with the invariance under charge conjugation describes the dynamic of the superconductor relatively well [9, 10, 96].

We can therefore conclude that a massive Higgs mode should exist in a superconductor and the Anderson-Higgs mechanism should prevent massless Goldstone modes and lead to massive photons inside the material. The energy of the Higgs mode $\omega_H = \sqrt{-2\alpha}$, which depends on the phenomenological parameter α , cannot be derived from within the Ginzburg-Landau theory. A comparison with the microscopic description yields $\omega_H = 2\Delta$, i.e. the energy of the Higgs mode corresponds to the value of the energy gap [10].

To see these effects in more detail, let us derive and evaluate the equations of motion for the Higgs mode H and gauge field A_μ from the Lagrangian in Eq. (2.17) [34]. We find for the Higgs field

$$(\partial_t^2 - \nabla^2)H = 2\alpha H + e^2\psi_0(\phi^2 - A^2), \quad (2.20)$$

which is the same as Eq. (2.7a) plus a nonlinear, quadratic coupling term of the electromagnetic field to the Higgs mode. The part of the Lagrangian for the gauge field reads

$$\mathcal{L} = -\frac{1}{2}((\partial_\mu A_\nu)(\partial^\mu A^\nu) - (\partial_\mu A_\nu)(\partial^\nu A^\mu)) + e^2\psi_0^2 A_\mu A^\mu + 2e^2\psi_0 A_\mu A^\mu H. \quad (2.21)$$

Evaluating Euler-Lagrange equations for A_ν yields

$$-(\partial_\mu \partial^\mu A^\nu - \partial_\mu \partial^\nu A^\mu) = 2e^2\psi_0^2 A^\nu + 4e^2\psi_0 A^\nu H \quad (2.22)$$

and explicitly in terms of ϕ and \mathbf{A}

$$-(\partial_t^2 - \nabla^2)\phi + \partial_t^2\phi + \partial_t\nabla\mathbf{A} = 2e^2\psi_0^2\phi + 4e^2\psi_0\phi H, \quad (2.23a)$$

$$-(\partial_t^2 - \nabla^2)\mathbf{A} - \nabla(\nabla\mathbf{A}) - \partial_t\nabla\phi = 2e^2\psi_0^2\mathbf{A} + 4e^2\psi_0\mathbf{A}H. \quad (2.23b)$$

In the static case for small fields with $H = 0$, $\nabla \mathbf{A} = 0$ and $\partial_t \mathbf{A} = \partial_t \phi = 0$, the equation for the vector potential reads

$$\nabla^2 \mathbf{A} = 2e^2 \psi_0^2 \mathbf{A}. \quad (2.24)$$

Applying the curl on both sides leads to

$$\nabla^2 (\nabla \times \mathbf{A}) = 2e^2 \psi_0^2 (\nabla \times \mathbf{A}), \quad (2.25)$$

$$\nabla^2 \mathbf{B} = \frac{1}{\lambda^2} \mathbf{B} \quad (2.26)$$

with the magnetic field \mathbf{B} and the penetration depth $\lambda = \sqrt{\frac{1}{2e^2 \psi_0^2}}$. This equation is the second London equation, describing the *Meissner effect* on a phenomenological level. The solution in one dimension is simply

$$B = B_0 e^{-\frac{1}{\lambda} x}, \quad (2.27)$$

i.e. an exponential decay of the magnetic field; the magnetic field is expelled from the superconductor. We can therefore understand the massive photon generated through the Anderson-Higgs mechanism as the cause of the Meissner effect in superconductors. The new longitudinal mode of the gauge field, which is possible due to the finite mass, plays the role of plasma oscillations in superconductors. Its energy at the plasma edge is large compared to the energy gap. In another way, phase fluctuations of the order parameter can be understood as being associated with fluctuations of the charge density and cost therefore energy due to the long-ranged Coulomb interaction in the charged material. Hence, it is commonly said that “the Goldstone mode in superconductors is shifted to the plasma energy” [10].

From the equation of motion Eq. (2.20) for the Higgs mode, we can observe another important fact: The Higgs mode only couples quadratically to the electromagnetic potential. There is no linear coupling term which restricts the excitation and observation to experiments beyond the linear regime. This is due to the fact that the Higgs mode is a scalar mode with no electric or magnetic dipole moment such that no linear coupling to the vector potential is allowed. Although it may seem that in this description the quadratic coupling is directly to the Higgs mode, the microscopic details are more complicated as we will see later in this thesis.

As a short outlook, the amplitude or Higgs mode is a fluctuation in the τ_1 channel (see Eq. (2.56)), whereas light couples to the charge density in the τ_3 channel (see Eq. (5.4)). As these channels are orthogonal, there is no direct coupling of light to the Higgs mode. While there is a more indirect coupling of light to the Higgs mode due to Raman-active phonons from a coexisting charge density wave (CDW) order in NbSe₂ [10, 14, 15, 17], one can understand the quadratic coupling as an effective Raman vertex interaction to the Higgs mode [11, 45]. This coupling is depicted diagrammatically in Fig. 2.2 and corresponds in the $q \rightarrow 0$ limit to the linearized Anderson pseudospin solution derived in section 5.1 [11, 45].

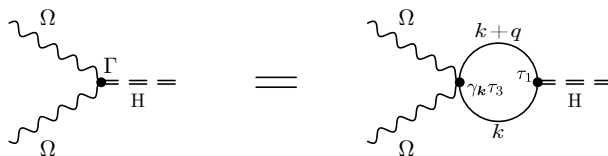


Figure 2.2 Quadratic coupling of light with frequency Ω and momentum \mathbf{q} to the Higgs mode via an effective Raman vertex Γ . Hereby, $\gamma_{\mathbf{k}} \propto \partial_{\mathbf{k}}^2 \epsilon_{\mathbf{k}}$ and τ_i are the Pauli matrices. Wiggly, solid and double-dashed lines represent photon, electron and Higgs propagator, respectively. Figure adapted from [11].

2.1.5 Higgs Mode in Other Condensed Matter Physics Systems

Superconductivity is not the only case in condensed matter physics, where SSB and collective modes play a role. There are other systems where Higgs and Goldstone modes can occur. However, superconductors are the only example of a charged condensate, which is describable by a relativistic theory such that the Anderson-Higgs mechanism occurs leading to a distinct Higgs mode and a vanishing of the Goldstone mode. Strictly speaking, one should call an amplitude mode “Higgs mode” only in the relativistic and charged case, where the name-giving Anderson-Higgs mechanism occurs. In all other cases, it is just an amplitude mode (sometimes also called amplitudon); however, literature is not consistent in this respect and often, any kind of amplitude mode is called “Higgs mode”. In this work, the term amplitude mode and Higgs mode is also used interchangeably. In the following, a few examples of condensed matter physics systems are discussed in which Higgs physics plays a role.

A typical example, in which spontaneous $U(1)$ symmetry breaking occurs, are ultracold Bose gases. If a diluted neutral gas of bosons (e.g. ^{87}Rb , ^{23}Na or ^7Li atoms) is cooled below a critical temperature, Bose-Einstein condensation (BEC) occurs, where all atoms condense into a single coherent quantum state [116]. If an optical lattice is used to trap the condensate, the periodic system is describable by the Bose-Hubbard model, which leads to an inherent particle-hole symmetry and an effective Lorentz-invariant theory as in superconductors [10, 117, 118]. In contrast to superconductors, the condensate is neutral, such that no Anderson-Higgs mechanism occurs and Higgs and Goldstone modes are expected. The advantage of cold atom systems is that their parameters can be controlled and tuned over a large range. As an example, tuning of the lasers for the trap allows to precisely adjust the lattice structure [119] or a variation of an external magnetic field allows to tune the pairing interaction due to Feshbach resonances [120]. Several works have predicted the existence of Higgs modes in ultracold Bose gases, e.g. [117, 118, 121] and indeed, experiments such as [122, 123] have observed an amplitude mode in these systems.

Just as Bose gases can condense at low temperatures, a gas of fermions (e.g. ^{40}K or ^6Li atoms) can condense as well [124–126]. However, the mechanism is completely different as a condensation of fermions is forbidden through the Pauli principle. The process can be understood in analogy to the mechanism of Cooper pairing in superconductors. Two fermions form a pair due to an attractive interaction, which then can condense into a coherent state describable by a single wave function. With the help of the already mentioned Feshbach resonances, the pairing strength can be tuned. For strong interaction, two fermions form a tightly bound pair, which is closer to a boson and the condensation resembles a BEC. For weak interaction, the pair is only loosely

	Klein-Gordon dynamic	Gross-Pitaevskii dynamic
Charged	Higgs mode and Higgs mechanism e.g. superconductors	mixed Higgs and Goldstone modes
Neutral	Higgs and Goldstone modes e.g. BECs in optical lattices, superfluid ^3He , ultracold Fermi gases, excitonic insulators, antiferromagnets, incommensurate CDWs	mixed Higgs and Goldstone modes e.g. superfluid ^4He

Table 2.1 Summary of collective modes in a ψ^4 theory in the spontaneous $U(1)$ symmetry broken phase for neutral and charged fields with relativistic (Klein-Gordon) or nonrelativistic (Gross-Pitaevskii) dynamic with examples from condensed matter physics.

coupled with a large dimension such that many pairs overlap in analogy to BCS Cooper pairs. Changing the interaction strength, BEC to BCS crossover regimes can be explored. In such a system of cold Fermi gases, the emergence and evolution of a Higgs mode has been widely explored on the theoretical side in the BCS or the BEC-BCS cross over regime, e.g. [85, 127–132], and first experimental observations have been reported as well [133].

Helium has two stable isotopes, ^4He , which is a boson, and ^3He , which is a fermion. It can condense at low temperatures as well like the previously discussed Bose or Fermi gases. Superfluid ^3He is a Fermi gas with two known phases, a high-temperature A-phase, which has p -wave symmetry and a low-temperature B phase, which has s -wave symmetry [134]. Several theoretical [135–139] and experimental works [140–144] have investigated the Higgs mode. Due to the p -wave pairing in the A-phase, multiple Higgs modes can be found. In contrast, superfluid ^4He is a Bose gas, which is described by a nonrelativistic theory [9, 10]. Thus, no distinct Higgs and Goldstone modes occur.

In semiconductors or semimetals, there can be a BEC- or BCS-like condensation of excitons into a coherent ground state if the binding energy of the electron-hole pair exceeds either the bandgap or bandwidth, respectively [145]. This phase is called an excitonic insulator. Due to the existence of a spontaneous $U(1)$ symmetry breaking in the semiconductor or semimetal to excitonic insulator phase transition and the emerging of an order parameter, collective amplitude and phase modes are in principle possible. The condensed excitons have no charge, therefore no Anderson-Higgs mechanism occurs, such that Higgs and Goldstone modes are expected. While there are only a few possible material examples, the semiconductor compound Ta_2NiSe_5 is believed to be a good candidate for an excitonic insulator [146]; even though recent theoretical work has proposed that the phase transition is characterized by a discrete symmetry breaking rather than continuous $U(1)$ symmetry breaking [147], which would only allow for gapped collective excitations. Nevertheless, ultrafast pump-probe experiments have revealed oscillations in the reflectivity [148, 149], which are an indicator of collective amplitude oscillations of an excitonic order parameter.

Charge density waves (CDW) are a periodic modulation of the electron density and lattice structure, forming a standing wave pattern, which results from a Peierls transition lowering the

ground state energy due to a shift of adjacent lattice points in opposite direction [150]. This transition into the CDW phase is accompanied by spontaneous symmetry breaking and an incommensurate CDW phase can be described by a complex order parameter, which allows collective amplitude and phase modes. There has been a large number of studies on observing collective amplitude (Higgs) modes in CDW materials with time-resolved pump-probe experiments, e.g. in the quasi-1d system $K_{0.3}MoO_3$ (blue bronze) [151–154], in $TbTe_3$ [155], in the layered compound $LaAgSb_2$ [156] or in underdoped YBCO [157].

Two-dimensional antiferromagnets can be described by a two-dimensional order parameter. The transition into the antiferromagnetic phase breaks the spin rotational symmetry spontaneously and collective phase and amplitude modes can occur. Here, the order parameter is not charged, such that the gapped Higgs mode can decay into the gapless Goldstone modes if not protected by other mechanisms. The Higgs mode in such systems has been explored theoretically e.g. in [158] but also experimentally, e.g. in $TlCuCl_3$ [159, 160], Ca_2RuO_4 [161, 162], $C_9H_{18}N_2CuBr_4$ [163, 164] or $SrMnO_3$ [165].

Besides the discussed systems, there are also efforts on detecting the Higgs mode in crystalline solids [166–168], exciton-polariton condensates in a cavity [169–171], supersolid quantum gases [172, 173], superfluids of neutrons [174] or superfluid Bose-Fermi mixtures [175].

We conclude with a summary of the results of the previous sections in Table 2.1. The table gives an overview of the collective modes for charged and uncharged condensates in a ψ^4 theory with spontaneous $U(1)$ symmetry breaking under a relativistic or nonrelativistic dynamic. The discussed examples from condensed matter physics are assigned to the respective cases.

2.2 BCS Theory

The *BCS theory* is the microscopic theory which describes superconductivity. Originally, it was developed by Bardeen, Cooper and Schrieffer in 1957 [176, 177] to describe conventional superconductors, i.e. superconductors with *s*-wave symmetry and phonon-mediated pairing interaction. However, it can also be extended to describe unconventional superconductors with non-trivial symmetries. Hereby, the symmetry is considered by the symmetry of the pairing interaction, whereas the pairing mechanism is not considered and can be arbitrary. A good introduction to BCS theory is found in the textbooks of Annett [178] and Tinkham [114].

For uniform notation of equilibrium or quenched values and temperature or time dependence of quantities, the following convention is used throughout this thesis: No indices or function values correspond to the equilibrium value, e.g. Δ or $\langle c_{-\mathbf{k}\downarrow}c_{\mathbf{k}\uparrow} \rangle$ correspond to the equilibrium value of the gap or anomalous electron expectation value. If the explicit temperature dependence of the equilibrium value shall be expressed, the index T , e.g. Δ_T or $\langle c_{-\mathbf{k}\downarrow}c_{\mathbf{k}\uparrow} \rangle_T$ is used. A ground state wave function is noted by an index 0, e.g. $|\Psi_0\rangle$. The time-dependence of quantities is written in an explicit functional form such as $\Delta(t)$ or $\langle c_{-\mathbf{k}\downarrow}c_{\mathbf{k}\uparrow} \rangle(t)$. An index q stands for the value directly after a quench, e.g. Δ_q or $\langle c_{-\mathbf{k}\downarrow}c_{\mathbf{k}\uparrow} \rangle_q$. Throughout this thesis, quenches are performed at $t = 0$, such that for these cases, we can identify $\Delta(0) = \Delta_q$ and $\Delta(-\infty) = \Delta$.

2.2.1 Hamiltonian and Energy Gap Equation

The generalized BCS Hamiltonian for singlet superconductors can be derived from the general second quantized Hamiltonian for electrons with two-particle interacting under the assumption that

the single-particle potential is zero and the attractive two-particle interaction is only mediated between electrons with $(\mathbf{k} \uparrow)$ and $(-\mathbf{k} \downarrow)$. It reads

$$H = \sum_{\mathbf{k}\sigma} \epsilon_{\mathbf{k}} c_{\mathbf{k}\sigma}^{\dagger} c_{\mathbf{k}\sigma} - \sum_{\mathbf{k}\mathbf{k}' \in \mathcal{W}} V_{\mathbf{k}\mathbf{k}'} c_{\mathbf{k}\uparrow}^{\dagger} c_{-\mathbf{k}\downarrow}^{\dagger} c_{-\mathbf{k}'\downarrow} c_{\mathbf{k}'\uparrow}, \quad (2.28)$$

where $\epsilon_{\mathbf{k}} = \xi_{\mathbf{k}} - \epsilon_{\text{F}}$ is the electron dispersion $\xi_{\mathbf{k}}$ measured relatively to the Fermi energy ϵ_{F} . The arbitrary pairing interaction is denoted by $V_{\mathbf{k}\mathbf{k}'}$. Note that the second sum runs over all \mathbf{k} such that the energy is smaller than some cutoff energy ϵ_c , i.e. $\mathcal{W} = \{\mathbf{k} \mid |\epsilon_{\mathbf{k}}| < \epsilon_c\}$. For phonon-mediated superconductivity, the cutoff energy is given by the Debye energy. In the following, we will implicitly restrict the \mathbf{k} -range for all \mathbf{k} -sums within this range. Now, one can perform a mean-field approximation

$$c_{\mathbf{k}\uparrow}^{\dagger} c_{-\mathbf{k}\downarrow}^{\dagger} c_{-\mathbf{k}'\downarrow} c_{\mathbf{k}'\uparrow} \approx \langle c_{\mathbf{k}\uparrow}^{\dagger} c_{-\mathbf{k}\downarrow}^{\dagger} \rangle c_{-\mathbf{k}'\downarrow} c_{\mathbf{k}'\uparrow} + \langle c_{-\mathbf{k}'\downarrow} c_{\mathbf{k}'\uparrow} \rangle c_{\mathbf{k}\uparrow}^{\dagger} c_{-\mathbf{k}\downarrow}^{\dagger} + \langle c_{\mathbf{k}\uparrow}^{\dagger} c_{-\mathbf{k}\downarrow}^{\dagger} \rangle \langle c_{-\mathbf{k}'\downarrow} c_{\mathbf{k}'\uparrow} \rangle, \quad (2.29)$$

where the product of two creation and annihilation operators are replaced by their expectation value. Then, we define the superconducting energy gap

$$\Delta_{\mathbf{k}} = \sum_{\mathbf{k}'} V_{\mathbf{k}\mathbf{k}'} \langle c_{-\mathbf{k}'\downarrow} c_{\mathbf{k}'\uparrow} \rangle. \quad (2.30)$$

Neglecting the constant term, one obtains the general mean-field BCS Hamiltonian

$$H = \sum_{\mathbf{k}\sigma} \epsilon_{\mathbf{k}} c_{\mathbf{k}\sigma}^{\dagger} c_{\mathbf{k}\sigma} - \sum_{\mathbf{k}} \Delta_{\mathbf{k}} c_{\mathbf{k}\uparrow}^{\dagger} c_{-\mathbf{k}\downarrow}^{\dagger} - \sum_{\mathbf{k}} \Delta_{\mathbf{k}}^* c_{-\mathbf{k}\downarrow} c_{\mathbf{k}\uparrow}. \quad (2.31)$$

In order to be able to solve the gap equation, we assume a separable pairing interaction of strength V with a symmetry defined by a function $f_{\mathbf{k}}$

$$V_{\mathbf{k}\mathbf{k}'} = V f_{\mathbf{k}} f_{\mathbf{k}'}. \quad (2.32)$$

Due to this separable interaction, we can define a \mathbf{k} -independent gap Δ

$$\Delta_{\mathbf{k}} = \Delta f_{\mathbf{k}} \quad \text{with} \quad \Delta = V \sum_{\mathbf{k}} f_{\mathbf{k}} \langle c_{-\mathbf{k}\downarrow} c_{\mathbf{k}\uparrow} \rangle. \quad (2.33)$$

As the BCS Hamiltonian (2.31) depends explicitly on the energy gap (2.33), which again is determined by the Hamiltonian, the problem has to be solved self-consistently. The symmetry function $f_{\mathbf{k}}$ depends on the considered system. Examples for common symmetry functions are listed in table 2.2.

The transition from the general Hamiltonian Eq. (2.28) to the BCS Hamiltonian Eq. (2.31) via the mean-field approximation creates the spontaneous symmetry breaking, discussed in the previous section, on a microscopic level. The general Hamiltonian is $U(1)$ invariant as a multiplication of creation or annihilation operators with a constant phase μ , i.e. $c_{\mathbf{k}\uparrow} \rightarrow c_{\mathbf{k}\uparrow} e^{i\mu}$ leaves the Hamiltonian invariant due to the pairwise occurrence of creation and annihilation operators. Yet, the BCS Hamiltonian contains only products of two creation or two annihilation operators, such that it is no longer invariant under a $U(1)$ transformation. This can also be seen in the BCS ground state wave function in Eq. (2.51), which also breaks the $U(1)$ symmetry. Moreover, the phenomenological Higgs field ψ from the previous section corresponds to the order parameter Δ on the microscopic level.

Name	Symmetry	Function $f_{\mathbf{k}}$	Polar coordinates $f(\varphi)$
s-wave	1	1	1
nodal s-wave	$(x^2 - y^2)^2$	$(\cos k_x - \cos k_y)^2$	$\cos^2(2\varphi)$
d-wave	$x^2 - y^2$	$-(\cos k_x - \cos k_y)$	$\cos(2\varphi)$
d_{xy} -wave	xy	$\sin k_x \sin k_y$	$\sin(2\varphi)$
g-wave	$xy(x^2 - y^2)$	$-\sin k_x \sin k_y (\cos k_x - \cos k_y)$	$\sin(4\varphi)$

Table 2.2 Common gap symmetry names of singlet superconductors and their representation in momentum space, as well as a function of the polar angle on the Fermi surface.

2.2.2 Nambu-Gorkov Basis

It is often convenient to express the Hamiltonian in the Nambu-Gorkov basis. We start by rewriting the kinetic term in the Hamiltonian (2.31). We assume that the dispersion is parity symmetric, i.e. $\epsilon_{-\mathbf{k}} = \epsilon_{\mathbf{k}}$ and we will neglect all constant terms as they only shift the absolute value of the energy. Using the anti-commutation relation $\{c_{\mathbf{k}\sigma}, c_{\mathbf{k}'\sigma'}^\dagger\} = \delta_{\mathbf{k}\mathbf{k}'}\delta_{\sigma\sigma'}$, we find

$$H_{\text{kin}} = \sum_{\mathbf{k}} \epsilon_{\mathbf{k}} (c_{\mathbf{k}\uparrow}^\dagger c_{\mathbf{k}\uparrow} + c_{\mathbf{k}\downarrow}^\dagger c_{\mathbf{k}\downarrow}) = \sum_{\mathbf{k}} \left(\epsilon_{\mathbf{k}} c_{\mathbf{k}\uparrow}^\dagger c_{\mathbf{k}\uparrow} - \epsilon_{\mathbf{k}} c_{-\mathbf{k}\downarrow} c_{-\mathbf{k}\downarrow}^\dagger \right). \quad (2.34)$$

With this, the full BCS Hamiltonian reads

$$\begin{aligned} H &= \sum_{\mathbf{k}} \left(\epsilon_{\mathbf{k}} c_{\mathbf{k}\uparrow}^\dagger c_{\mathbf{k}\uparrow} - \epsilon_{\mathbf{k}} c_{-\mathbf{k}\downarrow} c_{-\mathbf{k}\downarrow}^\dagger - \Delta_{\mathbf{k}} c_{\mathbf{k}\uparrow}^\dagger c_{-\mathbf{k}\downarrow}^\dagger - \Delta_{\mathbf{k}}^* c_{-\mathbf{k}\downarrow} c_{\mathbf{k}\uparrow} \right) \\ &= \sum_{\mathbf{k}} \begin{pmatrix} c_{\mathbf{k}\uparrow}^\dagger & c_{-\mathbf{k}\downarrow} \end{pmatrix} \begin{pmatrix} \epsilon_{\mathbf{k}} & -\Delta_{\mathbf{k}} \\ -\Delta_{\mathbf{k}}^* & -\epsilon_{\mathbf{k}} \end{pmatrix} \begin{pmatrix} c_{\mathbf{k}\uparrow} \\ c_{-\mathbf{k}\downarrow}^\dagger \end{pmatrix} \\ &= \sum_{\mathbf{k}} \Psi_{\mathbf{k}}^\dagger \begin{pmatrix} \epsilon_{\mathbf{k}} & -\Delta_{\mathbf{k}} \\ -\Delta_{\mathbf{k}}^* & -\epsilon_{\mathbf{k}} \end{pmatrix} \Psi_{\mathbf{k}}, \end{aligned} \quad (2.35)$$

where we define the Nambu-Gorkov spinor

$$\Psi_{\mathbf{k}}^\dagger = \begin{pmatrix} c_{\mathbf{k}\uparrow}^\dagger & c_{-\mathbf{k}\downarrow} \end{pmatrix}. \quad (2.36)$$

2.2.3 Bogoliubov Transformation

The BCS Hamiltonian can be diagonalized by an unitary Bogoliubov transformation. In the Hamiltonian (2.35) for arbitrary gap $\Delta_{\mathbf{k}}(t)$ at time t , which must not necessarily be the equilibrium value, we insert the unitary operator U

$$H(t) = \sum_{\mathbf{k}} \Psi_{\mathbf{k}}^\dagger U U^\dagger \begin{pmatrix} \epsilon_{\mathbf{k}} & -\Delta_{\mathbf{k}}(t) \\ -\Delta_{\mathbf{k}}^*(t) & -\epsilon_{\mathbf{k}} \end{pmatrix} U U^\dagger \Psi_{\mathbf{k}}, \quad (2.37)$$

where we choose the following representation of the unitary matrix

$$U U^\dagger = 1, \quad U = \begin{pmatrix} u_{\mathbf{k}}^* & v_{\mathbf{k}} \\ -v_{\mathbf{k}}^* & u_{\mathbf{k}} \end{pmatrix}, \quad U^\dagger = \begin{pmatrix} u_{\mathbf{k}} & -v_{\mathbf{k}} \\ v_{\mathbf{k}}^* & u_{\mathbf{k}}^* \end{pmatrix}, \quad |u_{\mathbf{k}}|^2 + |v_{\mathbf{k}}|^2 = 1. \quad (2.38)$$

This commonly used choice follows e.g. [114], but other definitions with swapped minus sign and complex conjugation are also found in literature. We define the Bogoliubov quasiparticle operators

$$\begin{pmatrix} \alpha_{\mathbf{k}} \\ \beta_{\mathbf{k}}^\dagger \end{pmatrix} = U^\dagger \Psi_{\mathbf{k}} = \begin{pmatrix} u_{\mathbf{k}} & -v_{\mathbf{k}} \\ v_{\mathbf{k}}^* & u_{\mathbf{k}}^* \end{pmatrix} \begin{pmatrix} c_{\mathbf{k}\uparrow} \\ c_{-\mathbf{k}\downarrow}^\dagger \end{pmatrix} = \begin{pmatrix} u_{\mathbf{k}} c_{\mathbf{k}\uparrow} - v_{\mathbf{k}} c_{-\mathbf{k}\downarrow}^\dagger \\ v_{\mathbf{k}}^* c_{\mathbf{k}\uparrow} + u_{\mathbf{k}}^* c_{-\mathbf{k}\downarrow}^\dagger \end{pmatrix}, \quad (2.39a)$$

$$\begin{pmatrix} c_{\mathbf{k}\uparrow} \\ c_{-\mathbf{k}\downarrow}^\dagger \end{pmatrix} = U \begin{pmatrix} \alpha_{\mathbf{k}} \\ \beta_{\mathbf{k}}^\dagger \end{pmatrix} = \begin{pmatrix} u_{\mathbf{k}}^* & v_{\mathbf{k}} \\ -v_{\mathbf{k}}^* & u_{\mathbf{k}} \end{pmatrix} \begin{pmatrix} \alpha_{\mathbf{k}} \\ \beta_{\mathbf{k}}^\dagger \end{pmatrix} = \begin{pmatrix} u_{\mathbf{k}}^* \alpha_{\mathbf{k}} + v_{\mathbf{k}} \beta_{\mathbf{k}}^\dagger \\ -v_{\mathbf{k}}^* \alpha_{\mathbf{k}} + u_{\mathbf{k}} \beta_{\mathbf{k}}^\dagger \end{pmatrix}, \quad (2.39b)$$

which fulfill the fermionic anticommutation rules

$$\{\alpha_{\mathbf{k}}, \alpha_{\mathbf{k}'}^\dagger\} = \{\beta_{\mathbf{k}}, \beta_{\mathbf{k}'}^\dagger\} = \delta_{\mathbf{k}, \mathbf{k}'}, \quad (2.40a)$$

$$\{\alpha_{\mathbf{k}}, \alpha_{\mathbf{k}'}\} = \{\alpha_{\mathbf{k}}^\dagger, \alpha_{\mathbf{k}'}^\dagger\} = \{\beta_{\mathbf{k}}, \beta_{\mathbf{k}'}\} = \{\beta_{\mathbf{k}}^\dagger, \beta_{\mathbf{k}'}^\dagger\} = 0. \quad (2.40b)$$

Again, we neglect constant terms in the Hamiltonian and find

$$\begin{aligned} H(t) &= \sum_{\mathbf{k}} \begin{pmatrix} \alpha_{\mathbf{k}}^\dagger & \beta_{\mathbf{k}} \end{pmatrix} \begin{pmatrix} R_{\mathbf{k}} & C_{\mathbf{k}} \\ C_{\mathbf{k}}^* & -R_{\mathbf{k}} \end{pmatrix} \begin{pmatrix} \alpha_{\mathbf{k}} \\ \beta_{\mathbf{k}}^\dagger \end{pmatrix} \\ &= \sum_{\mathbf{k}} R_{\mathbf{k}} (\alpha_{\mathbf{k}}^\dagger \alpha_{\mathbf{k}} + \beta_{\mathbf{k}}^\dagger \beta_{\mathbf{k}}) + \sum_{\mathbf{k}} C_{\mathbf{k}} \alpha_{\mathbf{k}}^\dagger \beta_{\mathbf{k}}^\dagger - C_{\mathbf{k}}^* \alpha_{\mathbf{k}} \beta_{\mathbf{k}} \end{aligned} \quad (2.41)$$

with

$$R_{\mathbf{k}}(t) = \epsilon_{\mathbf{k}} \left(|u_{\mathbf{k}}|^2 - |v_{\mathbf{k}}|^2 \right) + \Delta_{\mathbf{k}}(t) u_{\mathbf{k}} v_{\mathbf{k}}^* + \Delta_{\mathbf{k}}^*(t) u_{\mathbf{k}}^* v_{\mathbf{k}}, \quad (2.42a)$$

$$C_{\mathbf{k}}(t) = 2\epsilon_{\mathbf{k}} u_{\mathbf{k}} v_{\mathbf{k}} - \Delta_{\mathbf{k}}(t) u_{\mathbf{k}}^2 + \Delta_{\mathbf{k}}^*(t) v_{\mathbf{k}}^2. \quad (2.42b)$$

We choose the following values for $u_{\mathbf{k}}$ and $v_{\mathbf{k}}$

$$u_{\mathbf{k}} = \sqrt{\frac{1}{2} \left(1 + \frac{\epsilon_{\mathbf{k}}}{E_{\mathbf{k}}} \right)}, \quad v_{\mathbf{k}} = e^{i\kappa} \sqrt{\frac{1}{2} \left(1 - \frac{\epsilon_{\mathbf{k}}}{E_{\mathbf{k}}} \right)} \quad (2.43)$$

with the definition of the quasiparticle energy $E_{\mathbf{k}}$

$$E_{\mathbf{k}} = \sqrt{\epsilon_{\mathbf{k}}^2 + |\Delta_{\mathbf{k}}|^2}, \quad \Delta_{\mathbf{k}} = |\Delta| e^{i\kappa} f_{\mathbf{k}}. \quad (2.44)$$

The value $|\Delta|$ is the absolute value and κ is the phase of the equilibrium energy gap. For finite temperature T , the temperature-dependent value Δ_T has to be used to diagonalize the Hamiltonian in equilibrium. With these values it follows

$$\begin{aligned} R_{\mathbf{k}}(t) &= \epsilon_{\mathbf{k}} \left[\frac{1}{2} \left(1 + \frac{\epsilon_{\mathbf{k}}}{E_{\mathbf{k}}} \right) - \frac{1}{2} \left(1 - \frac{\epsilon_{\mathbf{k}}}{E_{\mathbf{k}}} \right) \right] + \frac{\Delta_{\mathbf{k}}(t)}{2} e^{-i\kappa} \sqrt{1 - \frac{\epsilon_{\mathbf{k}}^2}{E_{\mathbf{k}}^2}} + \frac{\Delta_{\mathbf{k}}^*(t)}{2} e^{i\kappa} \sqrt{1 - \frac{\epsilon_{\mathbf{k}}^2}{E_{\mathbf{k}}^2}} \\ &= \frac{1}{2E_{\mathbf{k}}} \left(2\epsilon_{\mathbf{k}}^2 + \Delta_{\mathbf{k}}(t) \Delta_{\mathbf{k}}^* + \Delta_{\mathbf{k}}^*(t) \Delta_{\mathbf{k}} \right), \end{aligned} \quad (2.45a)$$

$$\begin{aligned} C_{\mathbf{k}}(t) &= 2\epsilon_{\mathbf{k}} \frac{e^{i\kappa}}{2} \sqrt{1 - \frac{\epsilon_{\mathbf{k}}^2}{E_{\mathbf{k}}^2}} - \frac{\Delta_{\mathbf{k}}(t)}{2} \left(1 + \frac{\epsilon_{\mathbf{k}}}{E_{\mathbf{k}}} \right) + \frac{\Delta_{\mathbf{k}}^*(t)}{2} e^{2i\kappa} \left(1 - \frac{\epsilon_{\mathbf{k}}}{E_{\mathbf{k}}} \right) \\ &= \frac{1}{2E_{\mathbf{k}}} \left(2\epsilon_{\mathbf{k}} \Delta_{\mathbf{k}} - \Delta_{\mathbf{k}}(t) (E_{\mathbf{k}} + \epsilon_{\mathbf{k}}) + \Delta_{\mathbf{k}}^*(t) e^{2i\kappa} (E_{\mathbf{k}} - \epsilon_{\mathbf{k}}) \right). \end{aligned} \quad (2.45b)$$

In equilibrium, i.e. $\Delta_{\mathbf{k}}(t) = \Delta_{\mathbf{k}}$, the expressions simplify to

$$R_{\mathbf{k}} = E_{\mathbf{k}}, \quad C_{\mathbf{k}} = 0 \quad (2.46)$$

and the Hamiltonian becomes diagonal

$$H = \sum_{\mathbf{k}} E_{\mathbf{k}} (\alpha_{\mathbf{k}}^{\dagger} \alpha_{\mathbf{k}} + \beta_{\mathbf{k}}^{\dagger} \beta_{\mathbf{k}}). \quad (2.47)$$

For later usage, we express the following four expectation values of the electron operators with the help of the new Bogoliubov operators

$$\begin{aligned} \langle c_{-\mathbf{k}\downarrow} c_{\mathbf{k}'\uparrow} \rangle &= \left\langle \left(-v_{\mathbf{k}} \alpha_{\mathbf{k}}^{\dagger} + u_{\mathbf{k}}^* \beta_{\mathbf{k}} \right) \left(u_{\mathbf{k}'}^* \alpha_{\mathbf{k}'} + v_{\mathbf{k}'} \beta_{\mathbf{k}'}^{\dagger} \right) \right\rangle \\ &= -v_{\mathbf{k}} u_{\mathbf{k}'}^* \langle \alpha_{\mathbf{k}}^{\dagger} \alpha_{\mathbf{k}'} \rangle - u_{\mathbf{k}}^* v_{\mathbf{k}'} \left(\langle \beta_{\mathbf{k}'}^{\dagger} \beta_{\mathbf{k}} \rangle - \delta_{\mathbf{k}\mathbf{k}'} \right) \\ &\quad - u_{\mathbf{k}}^* u_{\mathbf{k}'}^* \langle \alpha_{\mathbf{k}'} \beta_{\mathbf{k}} \rangle - v_{\mathbf{k}} v_{\mathbf{k}'} \langle \alpha_{\mathbf{k}}^{\dagger} \beta_{\mathbf{k}'}^{\dagger} \rangle, \end{aligned} \quad (2.48a)$$

$$\begin{aligned} \langle c_{\mathbf{k}\uparrow}^{\dagger} c_{-\mathbf{k}'\downarrow}^{\dagger} \rangle &= \left\langle \left(u_{\mathbf{k}} \alpha_{\mathbf{k}}^{\dagger} + v_{\mathbf{k}}^* \beta_{\mathbf{k}} \right) \left(-v_{\mathbf{k}'}^* \alpha_{\mathbf{k}'} + u_{\mathbf{k}'} \beta_{\mathbf{k}'}^{\dagger} \right) \right\rangle \\ &= -u_{\mathbf{k}} v_{\mathbf{k}'}^* \langle \alpha_{\mathbf{k}}^{\dagger} \alpha_{\mathbf{k}'} \rangle - v_{\mathbf{k}}^* u_{\mathbf{k}'} \left(\langle \beta_{\mathbf{k}'}^{\dagger} \beta_{\mathbf{k}} \rangle - \delta_{\mathbf{k}\mathbf{k}'} \right) \\ &\quad + v_{\mathbf{k}}^* v_{\mathbf{k}'}^* \langle \alpha_{\mathbf{k}'} \beta_{\mathbf{k}} \rangle + u_{\mathbf{k}} u_{\mathbf{k}'} \langle \alpha_{\mathbf{k}}^{\dagger} \beta_{\mathbf{k}'}^{\dagger} \rangle, \end{aligned} \quad (2.48b)$$

$$\begin{aligned} \langle c_{\mathbf{k}\uparrow}^{\dagger} c_{\mathbf{k}'\uparrow} \rangle &= \left\langle \left(u_{\mathbf{k}} \alpha_{\mathbf{k}}^{\dagger} + v_{\mathbf{k}}^* \beta_{\mathbf{k}} \right) \left(u_{\mathbf{k}'}^* \alpha_{\mathbf{k}'} + v_{\mathbf{k}'} \beta_{\mathbf{k}'}^{\dagger} \right) \right\rangle \\ &= u_{\mathbf{k}} u_{\mathbf{k}'}^* \langle \alpha_{\mathbf{k}}^{\dagger} \alpha_{\mathbf{k}'} \rangle - v_{\mathbf{k}}^* v_{\mathbf{k}'} \left(\langle \beta_{\mathbf{k}'}^{\dagger} \beta_{\mathbf{k}} \rangle - \delta_{\mathbf{k}\mathbf{k}'} \right) \\ &\quad - v_{\mathbf{k}}^* u_{\mathbf{k}'}^* \langle \alpha_{\mathbf{k}'} \beta_{\mathbf{k}} \rangle + u_{\mathbf{k}} v_{\mathbf{k}'} \langle \alpha_{\mathbf{k}}^{\dagger} \beta_{\mathbf{k}'}^{\dagger} \rangle, \end{aligned} \quad (2.48c)$$

$$\begin{aligned} \langle c_{-\mathbf{k}\downarrow} c_{-\mathbf{k}'\downarrow}^{\dagger} \rangle &= \left\langle \left(-v_{\mathbf{k}} \alpha_{\mathbf{k}}^{\dagger} + u_{\mathbf{k}}^* \beta_{\mathbf{k}} \right) \left(-v_{\mathbf{k}'}^* \alpha_{\mathbf{k}'} + u_{\mathbf{k}'} \beta_{\mathbf{k}'}^{\dagger} \right) \right\rangle \\ &= v_{\mathbf{k}} v_{\mathbf{k}'}^* \langle \alpha_{\mathbf{k}}^{\dagger} \alpha_{\mathbf{k}'} \rangle - u_{\mathbf{k}}^* u_{\mathbf{k}'} \left(\langle \beta_{\mathbf{k}'}^{\dagger} \beta_{\mathbf{k}} \rangle - \delta_{\mathbf{k}\mathbf{k}'} \right) \\ &\quad + u_{\mathbf{k}}^* v_{\mathbf{k}'}^* \langle \alpha_{\mathbf{k}'} \beta_{\mathbf{k}} \rangle - v_{\mathbf{k}} u_{\mathbf{k}'} \langle \alpha_{\mathbf{k}}^{\dagger} \beta_{\mathbf{k}'}^{\dagger} \rangle. \end{aligned} \quad (2.48d)$$

The expectation values of the Bogoliubov operators expressed with the electron operators read

$$\begin{aligned} \langle \alpha_{\mathbf{k}} \beta_{\mathbf{k}'} \rangle &= \left\langle \left(u_{\mathbf{k}} c_{\mathbf{k}\uparrow} - v_{\mathbf{k}} c_{-\mathbf{k}\downarrow}^{\dagger} \right) \left(v_{\mathbf{k}'} c_{\mathbf{k}'\uparrow}^{\dagger} + u_{\mathbf{k}'} c_{-\mathbf{k}'\downarrow} \right) \right\rangle \\ &= -u_{\mathbf{k}} v_{\mathbf{k}'} \left(\langle c_{\mathbf{k}'\uparrow}^{\dagger} c_{\mathbf{k}\uparrow} \rangle - \delta_{\mathbf{k}\mathbf{k}'} \right) + v_{\mathbf{k}} u_{\mathbf{k}'} \left(\langle c_{-\mathbf{k}'\downarrow} c_{-\mathbf{k}\downarrow}^{\dagger} \rangle - \delta_{\mathbf{k}\mathbf{k}'} \right) \\ &\quad - u_{\mathbf{k}} u_{\mathbf{k}'} \langle c_{-\mathbf{k}'\downarrow} c_{\mathbf{k}\uparrow} \rangle + v_{\mathbf{k}} v_{\mathbf{k}'} \langle c_{\mathbf{k}'\uparrow}^{\dagger} c_{-\mathbf{k}\downarrow}^{\dagger} \rangle, \end{aligned} \quad (2.49a)$$

$$\begin{aligned} \langle \alpha_{\mathbf{k}}^{\dagger} \beta_{\mathbf{k}'}^{\dagger} \rangle &= \left\langle \left(u_{\mathbf{k}}^* c_{\mathbf{k}\uparrow}^{\dagger} - v_{\mathbf{k}}^* c_{-\mathbf{k}\downarrow} \right) \left(v_{\mathbf{k}'}^* c_{\mathbf{k}'\uparrow} + u_{\mathbf{k}'} c_{-\mathbf{k}'\downarrow}^{\dagger} \right) \right\rangle \\ &= u_{\mathbf{k}}^* v_{\mathbf{k}'} \langle c_{\mathbf{k}\uparrow}^{\dagger} c_{\mathbf{k}'\uparrow} \rangle - v_{\mathbf{k}}^* u_{\mathbf{k}'} \langle c_{-\mathbf{k}\downarrow} c_{-\mathbf{k}'\downarrow}^{\dagger} \rangle - v_{\mathbf{k}}^* v_{\mathbf{k}'} \langle c_{-\mathbf{k}\downarrow} c_{\mathbf{k}'\uparrow} \rangle + u_{\mathbf{k}}^* u_{\mathbf{k}'} \langle c_{\mathbf{k}\uparrow}^{\dagger} c_{-\mathbf{k}'\downarrow}^{\dagger} \rangle, \end{aligned} \quad (2.49b)$$

$$\begin{aligned} \langle \alpha_{\mathbf{k}}^{\dagger} \alpha_{\mathbf{k}'} \rangle &= \left\langle \left(u_{\mathbf{k}}^* c_{\mathbf{k}\uparrow}^{\dagger} - v_{\mathbf{k}}^* c_{-\mathbf{k}\downarrow} \right) \left(u_{\mathbf{k}'} c_{\mathbf{k}'\uparrow} - v_{\mathbf{k}'} c_{-\mathbf{k}'\downarrow}^{\dagger} \right) \right\rangle \\ &= u_{\mathbf{k}}^* u_{\mathbf{k}'} \langle c_{\mathbf{k}\uparrow}^{\dagger} c_{\mathbf{k}'\uparrow} \rangle + v_{\mathbf{k}}^* v_{\mathbf{k}'} \langle c_{-\mathbf{k}\downarrow} c_{-\mathbf{k}'\downarrow}^{\dagger} \rangle - v_{\mathbf{k}}^* u_{\mathbf{k}'} \langle c_{-\mathbf{k}\downarrow} c_{\mathbf{k}'\uparrow} \rangle - u_{\mathbf{k}}^* v_{\mathbf{k}'} \langle c_{\mathbf{k}\uparrow}^{\dagger} c_{-\mathbf{k}'\downarrow}^{\dagger} \rangle, \end{aligned} \quad (2.49c)$$

$$\begin{aligned} \langle \beta_{\mathbf{k}}^{\dagger} \beta_{\mathbf{k}'} \rangle &= \left\langle \left(v_{\mathbf{k}}^* c_{\mathbf{k}\uparrow} + u_{\mathbf{k}} c_{-\mathbf{k}\downarrow}^{\dagger} \right) \left(v_{\mathbf{k}'} c_{\mathbf{k}'\uparrow}^{\dagger} + u_{\mathbf{k}'} c_{-\mathbf{k}'\downarrow} \right) \right\rangle \\ &= -v_{\mathbf{k}}^* v_{\mathbf{k}'} \left(\langle c_{\mathbf{k}'\uparrow}^{\dagger} c_{\mathbf{k}\uparrow} \rangle - \delta_{\mathbf{k}\mathbf{k}'} \right) - u_{\mathbf{k}}^* u_{\mathbf{k}'} \left(\langle c_{-\mathbf{k}'\downarrow} c_{-\mathbf{k}\downarrow}^{\dagger} \rangle - \delta_{\mathbf{k}\mathbf{k}'} \right) \\ &\quad - v_{\mathbf{k}}^* u_{\mathbf{k}'} \langle c_{-\mathbf{k}'\downarrow} c_{\mathbf{k}\uparrow} \rangle - u_{\mathbf{k}}^* v_{\mathbf{k}'} \langle c_{\mathbf{k}'\uparrow}^{\dagger} c_{-\mathbf{k}\downarrow}^{\dagger} \rangle. \end{aligned} \quad (2.49d)$$

Finally, we can express the gap equation in the Bogoliubov quasiparticle basis

$$\begin{aligned}\Delta &= V \sum_{\mathbf{k}} f_{\mathbf{k}} \langle c_{-\mathbf{k}\downarrow} c_{\mathbf{k}\uparrow} \rangle \\ &= V \sum_{\mathbf{k}} f_{\mathbf{k}} \left[u_{\mathbf{k}}^* v_{\mathbf{k}} \left(1 - \langle \alpha_{\mathbf{k}}^\dagger \alpha_{\mathbf{k}} \rangle - \langle \beta_{\mathbf{k}}^\dagger \beta_{\mathbf{k}} \rangle \right) - (u_{\mathbf{k}}^*)^2 \langle \alpha_{\mathbf{k}} \beta_{\mathbf{k}} \rangle - v_{\mathbf{k}}^2 \langle \alpha_{\mathbf{k}}^\dagger \beta_{\mathbf{k}}^\dagger \rangle \right].\end{aligned}\quad (2.50)$$

2.2.4 Equilibrium State

Let us first consider the case for zero temperature $T = 0$. Here, the mean-field ground state can be written with the help of the factor $u_{\mathbf{k}}$ and $v_{\mathbf{k}}$ as

$$|\psi_0\rangle = \prod_{\mathbf{k} < k_F} \left(u_{\mathbf{k}} + v_{\mathbf{k}} c_{\mathbf{k}\uparrow}^\dagger c_{-\mathbf{k}\downarrow}^\dagger \right) |0\rangle. \quad (2.51)$$

Hereby, the factor $u_{\mathbf{k}}$ describes the unoccupation of a pair state ($\mathbf{k} \uparrow, -\mathbf{k} \downarrow$), whereas the factor $v_{\mathbf{k}}$ describes the occupation of a pair state. Their functional form is shown in Fig. 2.3. In the normal state, there is a sharp transition from zero to one at k_F for $v_{\mathbf{k}}^2$ and from one to zero for $u_{\mathbf{k}}^2$. In the BCS state, this transition is smeared out. The equilibrium expectation values for the electron operators can be evaluated and read

$$\begin{aligned}\langle c_{-\mathbf{k}\downarrow} c_{\mathbf{k}\uparrow} \rangle &= \left\langle 0 \left| \left(\prod_{\mathbf{k}'} (u_{\mathbf{k}'}^* + v_{\mathbf{k}'}^* c_{\mathbf{k}'\uparrow}^\dagger c_{-\mathbf{k}'\downarrow}^\dagger) \right) c_{-\mathbf{k}\downarrow} c_{\mathbf{k}\uparrow} \left(\prod_{\mathbf{k}'} (u_{\mathbf{k}'} + v_{\mathbf{k}'} c_{\mathbf{k}'\uparrow}^\dagger c_{-\mathbf{k}'\downarrow}^\dagger) \right) \right| 0 \right\rangle \\ &= u_{\mathbf{k}}^* v_{\mathbf{k}} = \frac{e^{i\kappa}}{2} \sqrt{\frac{|\Delta_{\mathbf{k}}|^2}{E_{\mathbf{k}}^2}} = \frac{\Delta_{\mathbf{k}}}{2E_{\mathbf{k}}},\end{aligned}\quad (2.52a)$$

$$\langle c_{\mathbf{k}\uparrow}^\dagger c_{-\mathbf{k}\downarrow}^\dagger \rangle = u_{\mathbf{k}} v_{\mathbf{k}}^* = \frac{e^{-i\kappa}}{2} \sqrt{\frac{|\Delta_{\mathbf{k}}|^2}{E_{\mathbf{k}}^2}} = \frac{\Delta_{\mathbf{k}}^*}{2E_{\mathbf{k}}}, \quad (2.52b)$$

$$\langle c_{\mathbf{k}\uparrow}^\dagger c_{\mathbf{k}\uparrow} \rangle = |v_{\mathbf{k}}|^2 = \frac{1}{2} - \frac{\epsilon_{\mathbf{k}}}{2E_{\mathbf{k}}}, \quad (2.52c)$$

$$\langle c_{-\mathbf{k}\downarrow} c_{-\mathbf{k}\downarrow}^\dagger \rangle = |u_{\mathbf{k}}|^2 = \frac{1}{2} + \frac{\epsilon_{\mathbf{k}}}{2E_{\mathbf{k}}}. \quad (2.52d)$$

A comparison of Eqs. (2.52a) - (2.52d) with Eqs. (2.48a) - (2.48d) yields for the equilibrium expectation values of the quasiparticles

$$\langle \alpha_{\mathbf{k}} \beta_{\mathbf{k}} \rangle = \langle \alpha_{\mathbf{k}}^\dagger \beta_{\mathbf{k}}^\dagger \rangle = \langle \alpha_{\mathbf{k}}^\dagger \alpha_{\mathbf{k}} \rangle = \langle \beta_{\mathbf{k}}^\dagger \beta_{\mathbf{k}} \rangle = 0. \quad (2.53)$$

This is as expected since the BCS ground state is the vacuum state for the Bogoliubov quasiparticles.

Now, we consider the case of finite temperature T . As the quasiparticles are fermions, they obey the Fermi-Dirac statistic

$$\langle \alpha_{\mathbf{k}}^\dagger \alpha_{\mathbf{k}} \rangle_T = \langle \beta_{\mathbf{k}}^\dagger \beta_{\mathbf{k}} \rangle_T = \frac{1}{1 + \exp\left(\frac{E_{\mathbf{k}}}{k_B T}\right)}, \quad \langle \alpha_{\mathbf{k}} \beta_{\mathbf{k}} \rangle_T = \langle \alpha_{\mathbf{k}}^\dagger \beta_{\mathbf{k}}^\dagger \rangle_T = 0. \quad (2.54)$$

Using Eq. (2.54) and (2.48a) - (2.48d) it follows for the electron expectation values at finite temperature

$$\langle c_{-\mathbf{k}\downarrow} c_{\mathbf{k}\uparrow} \rangle_T = u_{\mathbf{k}}^* v_{\mathbf{k}} \left(1 - \frac{2}{1 + \exp\left(\frac{E_{\mathbf{k}}}{k_B T}\right)} \right) = \frac{\Delta_{\mathbf{k}}}{2E_{\mathbf{k}}} \tanh\left(\frac{E_{\mathbf{k}}}{2k_B T}\right), \quad (2.55a)$$

$$\langle c_{\mathbf{k}\uparrow}^\dagger c_{-\mathbf{k}\downarrow}^\dagger \rangle_T = \frac{\Delta_{\mathbf{k}}^*}{2E_{\mathbf{k}}} \tanh\left(\frac{E_{\mathbf{k}}}{2k_B T}\right), \quad (2.55b)$$

$$\begin{aligned} \langle c_{\mathbf{k}\uparrow}^\dagger c_{\mathbf{k}\uparrow} \rangle_T &= |u_{\mathbf{k}}|^2 \frac{1}{1 + \exp\left(\frac{E_{\mathbf{k}}}{k_B T}\right)} + |v_{\mathbf{k}}|^2 \left(1 - \frac{1}{1 + \exp\left(\frac{E_{\mathbf{k}}}{k_B T}\right)} \right) \\ &= \frac{1}{2} - \frac{\epsilon_{\mathbf{k}}}{2E_{\mathbf{k}}} \tanh\left(\frac{E_{\mathbf{k}}}{2k_B T}\right), \end{aligned} \quad (2.55c)$$

$$\langle c_{-\mathbf{k}\downarrow} c_{-\mathbf{k}\downarrow}^\dagger \rangle_T = \frac{1}{2} + \frac{\epsilon_{\mathbf{k}}}{2E_{\mathbf{k}}} \tanh\left(\frac{E_{\mathbf{k}}}{2k_B T}\right). \quad (2.55d)$$

2.2.5 Anderson Pseudospin Formalism

The *Anderson pseudospin formalism* [179] is a reformulation of the BCS Hamiltonian. It maps the occupation of Cooper pairs ($\mathbf{k} \uparrow, -\mathbf{k} \downarrow$) to (pseudo)spin states such that an up-spin will represent the occupied pair state and a down-spin the unoccupied pair state. This allows for an intuitive pictorial interpretation of the superconducting state and its excitations as we will see in the following.

We start from the BCS Hamiltonian (2.35) expressed in the Nambu-Gorkov basis and split the energy gap in its real and imaginary part $\Delta_{\mathbf{k}} = \Delta'_{\mathbf{k}} + i\Delta''_{\mathbf{k}}$

$$\begin{aligned} H &= \sum_{\mathbf{k}} \Psi_{\mathbf{k}}^\dagger \begin{pmatrix} \epsilon_{\mathbf{k}} & -\Delta_{\mathbf{k}} \\ -\Delta_{\mathbf{k}}^* & -\epsilon_{\mathbf{k}} \end{pmatrix} \Psi_{\mathbf{k}} \\ &= \sum_{\mathbf{k}} \Psi_{\mathbf{k}}^\dagger \left[\epsilon_{\mathbf{k}} \begin{pmatrix} 1 & 0 \\ 0 & -1 \end{pmatrix} - \Delta'_{\mathbf{k}} \begin{pmatrix} 0 & 1 \\ 1 & 0 \end{pmatrix} + \Delta''_{\mathbf{k}} \begin{pmatrix} 0 & -i \\ i & 0 \end{pmatrix} \right] \Psi_{\mathbf{k}} \\ &= \sum_{\mathbf{k}} \Psi_{\mathbf{k}}^\dagger [\epsilon_{\mathbf{k}} \tau_3 - \Delta'_{\mathbf{k}} \tau_1 + \Delta''_{\mathbf{k}} \tau_2] \Psi_{\mathbf{k}} \end{aligned} \quad (2.56)$$

with the Pauli matrices τ_i . Next, we define the Anderson pseudospin

$$\boldsymbol{\sigma}_{\mathbf{k}} = \frac{1}{2} \Psi_{\mathbf{k}}^\dagger \boldsymbol{\tau} \Psi_{\mathbf{k}} = \frac{1}{2} \begin{pmatrix} \Psi_{\mathbf{k}}^\dagger \tau^x \Psi_{\mathbf{k}} \\ \Psi_{\mathbf{k}}^\dagger \tau^y \Psi_{\mathbf{k}} \\ \Psi_{\mathbf{k}}^\dagger \tau^z \Psi_{\mathbf{k}} \end{pmatrix} = \frac{1}{2} \begin{pmatrix} c_{-\mathbf{k}\downarrow} c_{\mathbf{k}\uparrow} + c_{\mathbf{k}\uparrow}^\dagger c_{-\mathbf{k}\downarrow}^\dagger \\ i \left(c_{-\mathbf{k}\downarrow} c_{\mathbf{k}\uparrow} - c_{\mathbf{k}\uparrow}^\dagger c_{-\mathbf{k}\downarrow}^\dagger \right) \\ c_{\mathbf{k}\uparrow}^\dagger c_{\mathbf{k}\uparrow} - c_{-\mathbf{k}\downarrow} c_{-\mathbf{k}\downarrow}^\dagger \end{pmatrix} \quad (2.57)$$

and the pseudomagnetic field

$$\mathbf{b}_{\mathbf{k}}^\top = \left(-2\Delta'_{\mathbf{k}}, \quad 2\Delta''_{\mathbf{k}}, \quad 2\epsilon_{\mathbf{k}} \right). \quad (2.58)$$

With this, the Hamiltonian can be brought into the simple form

$$H = \sum_{\mathbf{k}} \mathbf{b}_{\mathbf{k}} \boldsymbol{\sigma}_{\mathbf{k}}, \quad (2.59)$$

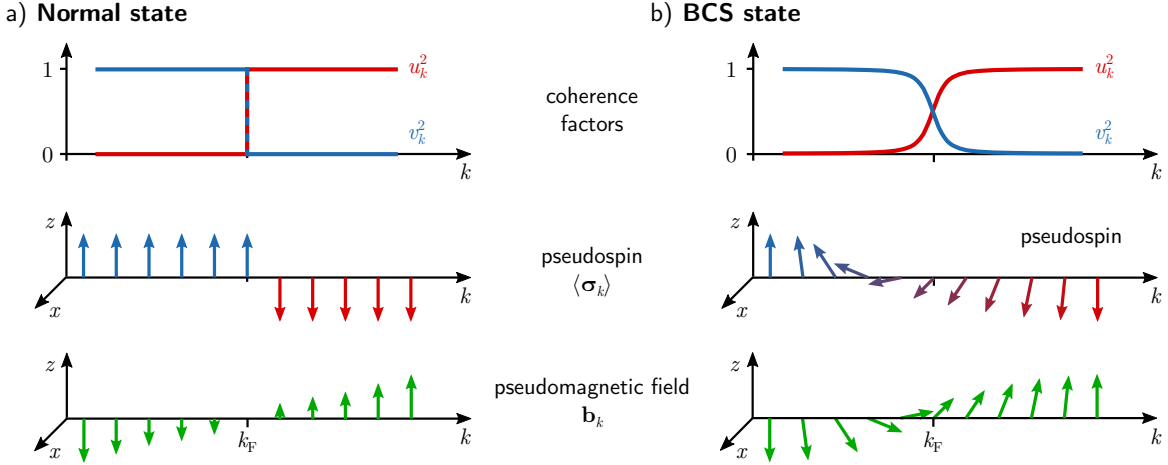


Figure 2.3 Coherence factors u_k and v_k (top), pseudospin $\langle \sigma_k \rangle$ (middle) and pseudomagnetic field \mathbf{b}_k (bottom) in the a) normal or b) BCS state. All quantities are plotted for a 1d momentum k . For the pseudospin and pseudomagnetic field, only the z - and x - component is shown.

which is equivalent to the Hamiltonian of a classic spin $\frac{1}{2}$ exposed to an external magnetic field. The gap equation expressed in this formalism reads

$$\Delta = V \sum_{\mathbf{k}} f_{\mathbf{k}} \langle c_{-\mathbf{k}\downarrow} c_{\mathbf{k}\uparrow} \rangle = V \sum_{\mathbf{k}} f_{\mathbf{k}} (\langle \sigma_{\mathbf{k}}^x \rangle - i \langle \sigma_{\mathbf{k}}^y \rangle). \quad (2.60)$$

Please note that the definition of the pseudomagnetic field is not consistent in literature as the factor of 2 is not always included. Furthermore, in some literature, the gap is defined as the complex conjugate version of the definition used here, i.e. as the sum over the expectation values $\langle c_{\mathbf{k}\uparrow}^\dagger c_{-\mathbf{k}\downarrow}^\dagger \rangle$. This leads to an opposite sign in the y -component of the pseudomagnetic field and the imaginary part in the gap equation.

With the help of equations (2.55a) - (2.55d), the equilibrium expectation values for the pseudospins read

$$\langle \sigma_{\mathbf{k}}^x \rangle_{\text{T}} = \frac{\Delta'_{\mathbf{k}}}{2E_{\mathbf{k}}} \tanh \left(\frac{E_{\mathbf{k}}}{2k_B T} \right), \quad (2.61a)$$

$$\langle \sigma_{\mathbf{k}}^y \rangle_{\text{T}} = -\frac{\Delta''_{\mathbf{k}}}{2E_{\mathbf{k}}} \tanh \left(\frac{E_{\mathbf{k}}}{2k_B T} \right), \quad (2.61b)$$

$$\langle \sigma_{\mathbf{k}}^z \rangle_{\text{T}} = -\frac{\epsilon_{\mathbf{k}}}{2E_{\mathbf{k}}} \tanh \left(\frac{E_{\mathbf{k}}}{2k_B T} \right). \quad (2.61c)$$

By inspecting the definition of the pseudospin in Eq. (2.57) and the equilibrium expectation values in Eq. (2.61), we can see that the z -component of the pseudospin represents the occupation of pair states ($\mathbf{k} \uparrow, -\mathbf{k} \downarrow$), whereas the x - and y -component are a measure of the anomalous expectation values inherent for the BCS state. This can be visualized by plotting the expectation values of the pseudospin as a function of the momentum as shown in Fig. 2.3 for $T = 0$. In the normal state, the anomalous expectation values and therefore the energy gap Δ is zero. All states are occupied up to the Fermi level and unoccupied above. This leads to $\langle \sigma_{\mathbf{k}}^x \rangle = \langle \sigma_{\mathbf{k}}^y \rangle = 0$ and $\langle \sigma_{\mathbf{k}}^z \rangle = -\text{sgn}(\epsilon_{\mathbf{k}})/2$. Thus, occupied states are represented by an up-spin and unoccupied

states are represented by a down-spin with a sharp transition at k_F where $\epsilon_{\mathbf{k}}$ switches its sign. In the BCS state with finite Δ , there is a smooth transition between up- and down-spins across the Fermi level by a rotation through the x - (and y - for complex Δ) plane. This can also be understood from the analogy of the Hamiltonian with a spin $\frac{1}{2}$ in an external field. The spins will align themselves antiparallel to the external field to minimize their energy. By considering the pseudomagnetic field in Eq. (2.58), it is evident that the pseudospins in equilibrium are exactly aligned in the opposite direction.

2.3 Nonequilibrium Dynamic

A superconductor can be brought out of equilibrium by different types of perturbations. Possibilities are, for example, a sudden change of the interaction strength $V \rightarrow V^q$ (interaction quench) or a sudden change of the quasiparticle distribution (state quench) as well as a coupling to external fields, which adds additional time-dependent interaction terms to the Hamiltonian. In nonequilibrium, the expectation value $\langle c_{-\mathbf{k}\downarrow} c_{\mathbf{k}\uparrow} \rangle$ and therefore the energy gap becomes time-dependent

$$\Delta_{\mathbf{k}}(t) = \Delta(t) f_{\mathbf{k}}, \quad \Delta(t) = V \sum_{\mathbf{k}} f_{\mathbf{k}} \langle c_{-\mathbf{k}\downarrow} c_{\mathbf{k}\uparrow} \rangle (t). \quad (2.62)$$

This leads to an implicit time dependence in the Hamiltonian due to the self-consistency relation

$$H \rightarrow H(t) = H(\Delta_{\mathbf{k}}(t)), \quad (2.63)$$

even if the Hamiltonian is not explicitly time-dependent. A Bogoliubov transformation at the fixed equilibrium value $\Delta_{\mathbf{k}}$ will therefore no longer diagonalize the Hamiltonian. To calculate the dynamic, there are different approaches used in this thesis, which are explained in the following.

2.3.1 Bloch Equations in Pseudospin Formalism

The time evolution of the pseudospins can be calculated with the help of Heisenberg's equation of motion

$$\begin{aligned} \partial_t \sigma_{\mathbf{k}} &= \frac{i}{\hbar} [H, \sigma_{\mathbf{k}}] \\ &= \frac{i}{\hbar} \sum_{\mathbf{k}'} \sum_i b_{\mathbf{k}'}^i [\sigma_{\mathbf{k}'}^i, \sigma_{\mathbf{k}}] = \frac{i}{\hbar} \sum_{\mathbf{k}'} \sum_{i,j} b_{\mathbf{k}'}^i \underbrace{[\sigma_{\mathbf{k}'}^i, \sigma_{\mathbf{k}}^j]}_{\sum_l i \epsilon_{ijl} \sigma_{\mathbf{k}}^l \delta_{\mathbf{k}, \mathbf{k}'}} \hat{e}_j \\ &= -\frac{1}{\hbar} \sum_{i,j,l} b_{\mathbf{k}}^i \underbrace{\epsilon_{ijl}}_{=-\epsilon_{ilj}} \sigma_{\mathbf{k}}^l \hat{e}_j = \frac{1}{\hbar} \mathbf{b}_{\mathbf{k}} \times \sigma_{\mathbf{k}}, \end{aligned} \quad (2.64)$$

which takes the form of Bloch equations for spins in a magnetic field [179]. These are three coupled differential equations which have to be solved together with the gap equation for each point \mathbf{k} in momentum space. From the Bloch equations for classical spins, it is known that a perturbation of the spin configuration or magnetic field will lead to a precession dynamic. We can expect the same behavior for the pseudospins. This is depicted schematically in Fig. 2.4. At each point \mathbf{k} in momentum space, a pseudospin precesses around its local pseudomagnetic field. A precession of all the pseudospins will lead to a collective excitation as we will see later.

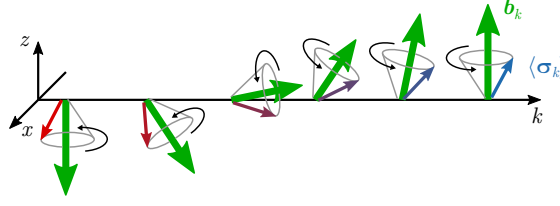


Figure 2.4 Schematic picture of the pseudospin precession triggered by a small perturbation. Each pseudospin precesses around its local pseudomagnetic field. All quantities are plotted for a 1d momentum k and only the z - and x - component of the pseudospin are shown.

2.3.2 Density Matrix Formalism

We can evaluate Heisenberg's equation of motion not only for the pseudospins but in general for any expectation values or density matrices, e.g. the four expectation values of the quasiparticles $\langle \alpha_{\mathbf{k}} \beta_{\mathbf{k}} \rangle$, $\langle \alpha_{\mathbf{k}}^\dagger \beta_{\mathbf{k}}^\dagger \rangle$, $\langle \alpha_{\mathbf{k}}^\dagger \alpha_{\mathbf{k}} \rangle$, $\langle \beta_{\mathbf{k}}^\dagger \beta_{\mathbf{k}} \rangle$ appearing in the gap equation (2.50). For example, for $\langle \alpha_{\mathbf{k}}^\dagger \alpha_{\mathbf{k}} \rangle (t)$, one has to evaluate

$$\partial_t \langle \alpha_{\mathbf{k}}^\dagger \alpha_{\mathbf{k}} \rangle (t) = \frac{i}{\hbar} \langle [H, \alpha_{\mathbf{k}}^\dagger \alpha_{\mathbf{k}}] \rangle (t). \quad (2.65)$$

An evaluation of the commutator on the right-hand side will in general produce additional expectation values for which Heisenberg's equation of motion have to be evaluated as well. If the Hamiltonian is bilinear, we will find a closed set of differential equations. Otherwise, an infinite hierarchy of differential equations appears, which has to be truncated [52, 180–182]. Indeed, in the case of the BCS Hamiltonian, the four expectation values form a closed set of differential equations, which can be solved together with the gap equation for each point \mathbf{k} in momentum space.

2.3.3 Iterated Equation of Motion Approach

If we are not only interested in specific expectation values but in the time evolution of the operators in the Heisenberg picture, we may evaluate Heisenberg's equation of motion for the operators itself, which is called *Iterated Equation of Motion approach* [180]. We are mainly interested in the quasiparticle operators, which read in the Heisenberg picture

$$\alpha_{\mathbf{k}}^\dagger(t) = U^\dagger(t) \alpha_{\mathbf{k}}^\dagger U(t), \quad \beta_{\mathbf{k}}^\dagger(t) = U^\dagger(t) \beta_{\mathbf{k}}^\dagger U(t), \quad (2.66)$$

where $U(t)$ is the unitary time evolution operator. The equation of motion for these read

$$\partial_t \alpha_{\mathbf{k}}^\dagger(t) = \frac{i}{\hbar} [\tilde{H}(t), \alpha_{\mathbf{k}}^\dagger(t)], \quad \partial_t \beta_{\mathbf{k}}^\dagger(t) = \frac{i}{\hbar} [\tilde{H}(t), \beta_{\mathbf{k}}^\dagger(t)] \quad (2.67)$$

with the Hamiltonian $\tilde{H}(t) = U^\dagger(t) H(t) U(t)$ in the Heisenberg picture. From these time-dependent operators, every expectation value can be calculated, e.g.

$$\begin{aligned} \langle \alpha_{\mathbf{k}}^\dagger \alpha_{\mathbf{k}} \rangle (t) &= \langle \psi(t) | \alpha_{\mathbf{k}}^\dagger \alpha_{\mathbf{k}} | \psi(t) \rangle \\ &= \langle \psi_0 | U^\dagger(t) | \alpha_{\mathbf{k}}^\dagger U(t) U^\dagger(t) \alpha_{\mathbf{k}} | U(t) \psi_0 \rangle = \langle \psi_0 | \alpha_{\mathbf{k}}^\dagger(t) \alpha_{\mathbf{k}}(t) | \psi_0 \rangle. \end{aligned} \quad (2.68)$$

Here, we face the same problem that we receive in general an infinite hierarchy of differential equations. The idea of the iterated equation of motion method is to introduce an ansatz for the operators as a superposition of basis functions. This ansatz can then be truncated at a certain expansion level in order to obtain a closed set of equations [180]. For the quasiparticles we choose

$$\alpha_{\mathbf{k}}^{\dagger}(t) = a_{0\mathbf{k}}(t)\alpha_{\mathbf{k}}^{\dagger} + a_{1\mathbf{k}}(t)\beta_{\mathbf{k}}, \quad (2.69a)$$

$$\beta_{\mathbf{k}}^{\dagger}(t) = b_{0\mathbf{k}}(t)\beta_{\mathbf{k}}^{\dagger} + b_{1\mathbf{k}}(t)\alpha_{\mathbf{k}}. \quad (2.69b)$$

With such an ansatz, we exploit again the bilinearity of the Hamiltonian and we obtain again a closed set of differential equations which is exact.

3 Classification and Characterization of Higgs Modes

In this chapter, quantum quenches of the superconducting condensate are studied to gain a basic understanding of the induced dynamic. These quenches simulate the effect of an experimental ultrafast THz pump pulse, which will be considered in the next chapter. There are different possibilities how one can perform such a quench. The simplest possible quench is an interaction quench which is discussed in the first section. As such a quench acts only symmetrically on the condensate, momentum-dependent quenches are introduced in section 3.2 to explore new effects.

3.1 Excitation of Higgs Oscillations with Interaction Quenches

We start by studying interaction quenches. Such a quench is defined by changing the interaction strength abruptly, i.e.

$$V_{\mathbf{k}\mathbf{k}'} = V f_{\mathbf{k}} f_{\mathbf{k}'} \quad \rightarrow \quad V_{\mathbf{k}\mathbf{k}'}^{\text{q}} = V^{\text{q}} f_{\mathbf{k}} f_{\mathbf{k}'}, \quad (3.1)$$

where $V^{\text{q}} = gV$ is the quenched interaction strength changed by a factor g . These kinds of interaction quenches have been studied in multiple papers for s -wave superconductors [20–27, 93, 183] and also for d -wave [53, 183] systems. Furthermore, for strongly interacting fermions in Bose-Einstein condensates (BEC) or in the BCS-BEC crossover regime, the dynamic and different quench regimes have been explored [21–23, 85, 132, 184]. Here, we allow momentum-dependent pairing interaction and generalize the analysis for arbitrary gap symmetry and compare the results with the well-known s -wave case.

3.1.1 Linear Analysis within Pseudospin Formalism

Let us first exploit the simplicity of Anderson pseudospin formalism to obtain an analytic insight into the dynamic triggered by an interaction quench. In this and all following sections, we consider only 2d systems to reduce the computational cost. This choice is also motivated by quasi-2d systems, like the layered cuprates with an unconventional d -wave symmetry.

We assume that the gap only depends on the polar angle φ , therefore we write $f_{\mathbf{k}} = f(\varphi)$. In addition, we assume that the dispersion $\epsilon_{\mathbf{k}} = \epsilon(|\mathbf{k}|)$ depends only on the absolute value of \mathbf{k} near the Fermi surface where all the relevant physics is happening. Then, the momentum sum in the gap equation can easily be replaced with an integral over the energy

$$\begin{aligned} \Delta(t) &= V \sum_{\mathbf{k}} f_{\mathbf{k}} \left(\langle \sigma_{\mathbf{k}}^x \rangle (t) - i \langle \sigma_{\mathbf{k}}^y \rangle (t) \right) \\ &= \lambda \int_{-\epsilon_c}^{\epsilon_c} d\epsilon \int_0^{2\pi} d\varphi f(\varphi) \left(\langle \sigma_{\mathbf{k}}^x \rangle (t) - i \langle \sigma_{\mathbf{k}}^y \rangle (t) \right). \end{aligned} \quad (3.2)$$

Here, we introduce a dimensionless constant $\lambda = VD(\epsilon_{\text{F}})$ with the density of states $D(\epsilon_{\text{F}})$ at the Fermi energy which is assumed to be constant. The constant λ is calculated by considering the equilibrium case for $T = 0$

$$\Delta = \lambda \int_{-\epsilon_c}^{\epsilon_c} d\epsilon \int_0^{2\pi} d\varphi f(\varphi) \frac{\Delta f(\varphi)}{2E_{\mathbf{k}}}, \quad (3.3)$$

which leads to

$$\begin{aligned}\lambda &= \left(\int_0^{2\pi} d\varphi f(\varphi)^2 \int_{-\epsilon_c}^{\epsilon_c} d\epsilon \frac{1}{2\sqrt{\Delta^2 f(\varphi)^2 + \epsilon^2}} \right)^{-1} \\ &= \left(\int_0^{2\pi} d\varphi f(\varphi)^2 \sinh^{-1} \left(\frac{\epsilon_c}{\Delta |f(\varphi)|} \right) \right)^{-1}.\end{aligned}\quad (3.4)$$

For further analysis, we consider a small quench with $g \lesssim 1$. Due to the small quench, it is justified to use the ansatz

$$\langle \sigma_{\mathbf{k}}^x \rangle (t) = \langle \sigma_{\mathbf{k}}^x \rangle + x_{\mathbf{k}}(t), \quad (3.5a)$$

$$\langle \sigma_{\mathbf{k}}^y \rangle (t) = \langle \sigma_{\mathbf{k}}^y \rangle + y_{\mathbf{k}}(t), \quad (3.5b)$$

$$\langle \sigma_{\mathbf{k}}^z \rangle (t) = \langle \sigma_{\mathbf{k}}^z \rangle + z_{\mathbf{k}}(t), \quad (3.5c)$$

where $x_{\mathbf{k}}(t), y_{\mathbf{k}}(t), z_{\mathbf{k}}(t) \ll 1$ are small deviations from the equilibrium state. The same can be assumed for the energy gap

$$\Delta(t) = \Delta_q + \delta\Delta(t) \quad (3.6)$$

with the deviation $\delta\Delta(t)$ and the value $\Delta_q = \Delta(0)$ of the gap directly after the quench. It follows for the gap dynamic after the quench

$$\begin{aligned}\Delta(t) &= \lambda_q \int_{-\epsilon_c}^{\epsilon_c} d\epsilon \int_0^{2\pi} d\varphi f(\varphi) \left(\langle \sigma_{\mathbf{k}}^x \rangle (t) - i \langle \sigma_{\mathbf{k}}^y \rangle (t) \right) \\ &= g\Delta + \lambda_q \int_{-\epsilon_c}^{\epsilon_c} d\epsilon \int_0^{2\pi} d\varphi f(\varphi) \left(x_{\mathbf{k}}(t) - iy_{\mathbf{k}}(t) \right),\end{aligned}\quad (3.7)$$

such that we can identify

$$\Delta_q = \Delta(0) = g\Delta, \quad (3.8a)$$

$$\delta\Delta(t) = \lambda_q \int_{-\epsilon_c}^{\epsilon_c} d\epsilon \int_0^{2\pi} d\varphi f(\varphi) \left(x_{\mathbf{k}}(t) - iy_{\mathbf{k}}(t) \right). \quad (3.8b)$$

The time evolution for the pseudospin is described by the Bloch equations (2.64). Inserting the ansatz (3.5) and (3.6) and using the equilibrium value (2.61) for the pseudospin at $T = 0$, it follows

$$\begin{pmatrix} \dot{x}_{\mathbf{k}}(t) \\ \dot{y}_{\mathbf{k}}(t) \\ \dot{z}_{\mathbf{k}}(t) \end{pmatrix} = \begin{pmatrix} -2f(\varphi)(\Delta'_q + \delta\Delta'(t)) \\ 2f(\varphi)(\Delta''_q + \delta\Delta''(t)) \\ 2\epsilon_{\mathbf{k}} \end{pmatrix} \times \begin{pmatrix} \frac{f(\varphi)\Delta'}{2E_{\mathbf{k}}} + x_{\mathbf{k}}(t) \\ -\frac{f(\varphi)\Delta''}{2E_{\mathbf{k}}} + y_{\mathbf{k}}(t) \\ -\frac{\epsilon_{\mathbf{k}}}{2E_{\mathbf{k}}} + z_{\mathbf{k}}(t) \end{pmatrix} \quad (3.9)$$

and therefore

$$\dot{x}(t) = \frac{\epsilon}{E} f \left(\Delta'' - \Delta''_q - \delta\Delta''(t) \right) + 2f \left(\Delta''_q + \delta\Delta''(t) \right) z(t) - 2\epsilon y(t), \quad (3.10a)$$

$$\dot{y}(t) = \frac{\epsilon}{E} f \left(\Delta' - \Delta'_q - \delta\Delta'(t) \right) + 2f \left(\Delta'_q + \delta\Delta'(t) \right) z(t) + 2\epsilon x(t) \quad (3.10b)$$

$$\begin{aligned}\dot{z}(t) &= \frac{1}{E} f^2 \left(\Delta''(\Delta'_q + \delta\Delta'(t)) - \Delta'(\Delta''_q + \delta\Delta''(t)) \right), \\ &\quad - 2f \left(y(t)(\Delta'_q + \delta\Delta'(t)) + x(t)(\Delta''_q + \delta\Delta''(t)) \right).\end{aligned}\quad (3.10c)$$

Please note that in these equations and the following, the function values \mathbf{k} and φ are omitted for shorter and clearer notation where no ambiguity is possible. In addition, \hbar is set to 1. Up to now, the equations are exact and they will be solved numerically later on. Here, we continue the analytic analysis with a linear approximation by neglecting all terms of higher order in the deviation terms, e.g. terms like $\delta\Delta(t)z(t)$. To solve these coupled differential equations, we perform a Laplace transformation to receive algebraic equations. The Laplace transformation $f(s)$ for a function $f(t)$ is defined as

$$f(s) = \int_0^\infty e^{-st} f(t) dt \quad (3.11)$$

with the complex frequency s . We obtain

$$sx(s) = \frac{1}{s} \frac{\epsilon}{E} f(\Delta'' - \Delta''_q) - \frac{\epsilon}{E} f \delta\Delta''(s) + 2f\Delta''_q z(s) - 2\epsilon y(s), \quad (3.12a)$$

$$sy(s) = \frac{1}{s} \frac{\epsilon}{E} f(\Delta' - \Delta'_q) - \frac{\epsilon}{E} f \delta\Delta'(s) + 2f\Delta'_q z(s) + 2\epsilon x(s), \quad (3.12b)$$

$$sz(s) = \frac{1}{s} \frac{1}{E} f^2 (\Delta''\Delta'_q - \Delta'\Delta''_q) + \frac{1}{E} f^2 (\Delta''\delta\Delta'(s) - \Delta'\delta\Delta''(s)) - 2f (\Delta'_q y(s) + \Delta''_q x(s)) \quad (3.12c)$$

together with the gap equation

$$\delta\Delta(s) = \lambda_q \int_{-\epsilon_c}^{\epsilon_c} d\epsilon \int_0^{2\pi} d\varphi f(x(s) - iy(s)). \quad (3.13)$$

Without loss of generality, we choose the global phase of the equilibrium gap such that $\Delta'' = \Delta''_q = 0$ and therefore neglect the primes on the expressions Δ' and Δ'_q . Solving for $x(s)$ and $y(s)$ yields

$$x(s) = \frac{4\epsilon^2 f \left(\frac{\Delta_q - \Delta}{s} + \delta\Delta'(s) \right)}{2E(4\epsilon^2 + 4\Delta_q^2 f^2 + s^2)} - \frac{2\epsilon f \left(4\Delta_q f^2 \frac{\Delta_q - \Delta}{s} + s \right) \delta\Delta''(s)}{2E(4\epsilon^2 + 4\Delta_q^2 f^2 + s^2)}, \quad (3.14a)$$

$$y(s) = -\frac{4\epsilon^2 f \delta\Delta''(s)}{2E(4\epsilon^2 + 4\Delta_q^2 f^2 + s^2)} - \frac{2\epsilon f ((\Delta_q - \Delta) + s\delta\Delta'(s))}{2E(4\epsilon^2 + 4\Delta_q^2 f^2 + s^2)} - \frac{4f^3 \Delta \Delta_q \delta\Delta''(s)}{2E(4\epsilon^2 + 4\Delta_q^2 f^2 + s^2)}. \quad (3.14b)$$

The solutions for $x(s)$ and $y(s)$ are inserted back into the gap equation. Integral expressions of the form

$$I \propto \int_{-\epsilon_c}^{\epsilon_c} d\epsilon \frac{\epsilon}{2E(4\epsilon^2 + 4\Delta_q^2 f^2 + s^2)} = 0 \quad (3.15)$$

vanish due to the asymmetry of the integrand in ϵ . Thus, real and imaginary parts of the gap are not coupled as the terms mixing both expressions vanish. Furthermore, the equation for $\delta\Delta''(s)$ is underdetermined as $\delta\Delta''(s)$ can be canceled on both sides such that the only valid solution is $\delta\Delta''(s) = 0$. This means that the initial real gap stays real under the dynamic triggered by an interaction quench. The remaining term for $\delta\Delta(s) = \delta\Delta'(s)$ is of the form

$$I \propto \int_{-\epsilon_c}^{\epsilon_c} d\epsilon \int_0^{2\pi} d\varphi \frac{4\epsilon^2 f^2}{2E(4\epsilon^2 + 4\Delta_q^2 f^2 + s^2)}. \quad (3.16)$$

The expression is rewritten by adding a zero in the nominator

$$\begin{aligned}
 I &\propto \int_{-\epsilon_c}^{\epsilon_c} d\epsilon \int_0^{2\pi} d\varphi \frac{f^2(4\epsilon^2 + 4\Delta_q^2 f^2 + s^2 - 4\Delta_q^2 f^2 - s^2)}{2E(4\epsilon^2 + 4\Delta_q^2 f^2 + s^2)} \\
 &= \int_{-\epsilon_c}^{\epsilon_c} d\epsilon \int_0^{2\pi} d\varphi \frac{f^2}{2E} \\
 &\quad - \int_0^{2\pi} d\varphi f^2(4\Delta_q^2 f^2 + s^2) \int_{-\epsilon_c}^{\epsilon_c} d\epsilon \frac{1}{2E(4\epsilon^2 + 4\Delta_q^2 f^2 + s^2)} \\
 &= \frac{1}{\lambda} - F(s).
 \end{aligned} \tag{3.17}$$

In the last step, the equilibrium gap equation (3.3) is identified. The function $F(s)$ reads

$$F(s) = \int_0^{2\pi} d\varphi f^2(4\Delta_q^2 f^2 + s^2) \int_{-\infty}^{\infty} d\epsilon \frac{1}{2E_q(4E_q^2 + s^2)}, \tag{3.18}$$

where the approximation $E \approx E_q = \sqrt{\epsilon^2 + \Delta_q^2 f^2}$ is used for small quenches $g \lesssim 1$. The integral borders are replaced by $\epsilon_c \rightarrow \infty$, which is justified as long as $\epsilon_c \gg \Delta$. With this, the gap equation reads

$$\delta\Delta(s) = \left(\frac{\Delta_q - \Delta}{s} + \delta\Delta(s) \right) \left(\frac{\lambda_q}{\lambda} - \lambda_q F(s) \right) \tag{3.19}$$

and the solution is

$$\delta\Delta(s) = \frac{\Delta - \Delta_q}{s} \frac{\lambda F(s) - 1}{\frac{\lambda}{\lambda_q} - 1 + \lambda F(s)} = \frac{\Delta - \Delta_q}{s} \left(1 - \frac{1}{\lambda F(s)} \right) \tag{3.20}$$

using the approximation $\frac{\lambda}{\lambda_q} - 1 \approx 0$ in the last step. The ϵ integral in $F(s)$ can be evaluated analytically with the help of the formula [185, p. 1091]

$$\int \frac{1}{(ax^2 + b)\sqrt{cx^2 + d}} dx = \frac{\tan^{-1}\left(\frac{x\sqrt{ad-bc}}{\sqrt{b}\sqrt{cx^2+d}}\right)}{\sqrt{b}\sqrt{ad-bc}} \tag{3.21}$$

and the hyperbolic relations

$$\tan^{-1}(ix) = i \tanh^{-1}(x), \quad \tanh^{-1}\left(\frac{x}{\sqrt{x^2 + a^2}}\right) = \sinh^{-1}\left(\frac{x}{|a|}\right). \tag{3.22}$$

We identify

$$a = 4, \quad b = 4\Delta_q^2 f^2 + s^2, \quad c = 4, \quad d = 4\Delta_q^2 f^2, \quad ad - bc = -4s^2 \tag{3.23}$$

and find

$$\begin{aligned}
 F(s) &= \int_0^{2\pi} d\varphi f^2(4\Delta_q^2 f^2 + s^2) \frac{\sinh^{-1}\left(\frac{s}{2\Delta_q|f|}\right)}{s\sqrt{4\Delta_q^2 f^2 + s^2}} \\
 &= \frac{1}{s} \int_0^{2\pi} d\varphi f^2 \sqrt{4\Delta_q^2 f^2 + s^2} \sinh^{-1}\left(\frac{s}{2\Delta_q|f|}\right).
 \end{aligned} \tag{3.24}$$

In order to evaluate the φ integral, we have to consider a specific gap symmetry, which we will do in the following subsections exemplarily for the s -, d - and $d+s$ -wave case.

Solution for s -wave

Let us first consider the simplest case, namely s -wave with $f(\varphi) = 1$. Then, the φ integral is trivial and it follows

$$F(s) = \frac{2\pi}{s} \sqrt{4\Delta_q^2 + s^2} \sinh^{-1} \left(\frac{s}{2\Delta_q} \right) \quad (3.25)$$

and for $\delta\Delta(s)$

$$\delta\Delta(s) = (\Delta - \Delta_q) \left(\frac{1}{s} - \frac{1}{\lambda \sqrt{4\Delta_q^2 + s^2} \sinh^{-1} \left(\frac{s}{2\Delta_q} \right)} \right). \quad (3.26)$$

Hereby, we implicitly define a new $\lambda \rightarrow 2\pi\lambda$ for the s -wave case to absorb the factor 2π . The imaginary axis $s = i\omega$ in Laplace space corresponds to the real frequency axis of a Fourier transform. Therefore, we can already see from this expression that $\delta\Delta(s = i\omega)$ is peaked at $\omega = 2\Delta_q$. This corresponds to $2\Delta_q$ Higgs oscillations of the order parameter. To obtain the solution explicitly in the time-domain, we have to evaluate the Bromwich integral

$$\delta\Delta(t) = \frac{1}{2\pi i} \int_{\gamma-i\infty}^{\gamma+i\infty} ds e^{st} \delta\Delta(s), \quad (3.27)$$

where $\gamma \in \mathbb{R}$ is arbitrary but larger than any of the real parts of the poles of the integrand. The first term $\propto \frac{1}{s}$ in $\delta\Delta(s)$ yields just a constant offset $\Delta - \Delta_q$. For the second term, we extend the integral to the closed loop integral in the complex plane shown in Fig. 3.1 with $R \rightarrow \infty$ and $\epsilon \rightarrow 0$, where we exclude the branch cut $s \in [-2i\Delta_q, 2i\Delta_q]$ and add the contribution from the pole at $s = 0$. The right vertical part c_0 is our sought integral

$$\int_{\gamma-i\infty}^{\gamma+i\infty} = \int_{c_0} = \int_{c_{\text{tot}}} - \sum_{i=1}^8 \int_{c_i}. \quad (3.28)$$

The integral we have to evaluate reads

$$I_0 = \frac{\Delta_q - \Delta}{\lambda} \frac{1}{2\pi i} \int_{\gamma-i\infty}^{\gamma+i\infty} ds \frac{e^{st}}{\sqrt{4\Delta_q^2 + s^2} \sinh^{-1} \left(\frac{s}{2\Delta_q} \right)}. \quad (3.29)$$

According to Cauchy's integral theorem, the closed loop integral is zero as we have excluded all poles. Likewise, the integrals c_1 , c_7 and c_8 are vanishing for $R \rightarrow \infty$. The integrals c_2 and c_6 are canceling each other for $\epsilon \rightarrow 0$. The pole at $s = 0$ contributes with its residue

$$\begin{aligned} I_4 &= \frac{\Delta_q - \Delta}{\lambda} \frac{1}{2\pi i} \int_{c_4} ds \frac{e^{st}}{\sqrt{4\Delta_q^2 + s^2} \sinh^{-1} \left(\frac{s}{2\Delta_q} \right)} \\ &= \frac{\Delta_q - \Delta}{\lambda} \text{Ind}_{c_4}(0) \text{Res}_0 \left(\frac{e^{st}}{\sqrt{4\Delta_q^2 + s^2} \sinh^{-1} \left(\frac{s}{2\Delta_q} \right)} \right) \\ &= -\frac{\Delta_q - \Delta}{\lambda}, \end{aligned} \quad (3.30)$$

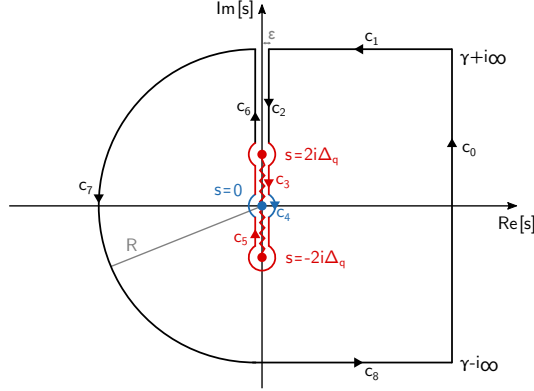


Figure 3.1 Contour to solve the Bromwich integral Eq. (3.29) corresponding to the path c_0 . The red zigzag line from $-2i\Delta_q$ to $2i\Delta_q$ indicates the chosen branch cut for the expression, while the blue dot at $s = 0$ indicates the pole. The total closed loop integral, as well as the contributions c_1 , c_2 , c_6 , c_7 and c_8 are vanishing. There are only contributions from the pole at $s = 0$ and the paths c_3 and c_5 located on the right and left side of the branch cut.

where $\text{Ind}_{c_4}(0) = -1$ is the winding number due to the clockwise circling around the pole. The remaining two paths are parametrized as $s(r) = -ir$ for c_3 and $s(r) = ir$ for c_5 with $r \in [-2\Delta_q, 2\Delta_q]$. The path c_3 is weighted with an additional minus sign due to the opposite side of the branch cut. It follows

$$\begin{aligned} I_3 + I_5 &= \frac{\Delta_q - \Delta}{\lambda} \frac{1}{2\pi i} \int_{-2\Delta_q}^{2\Delta_q} \left(- \frac{e^{-irt} (-i) dr}{\sqrt{4\Delta_q^2 - r^2} \sinh^{-1} \left(\frac{-ir}{2\Delta_q} \right)} + \frac{e^{irt} i dr}{\sqrt{4\Delta_q^2 - r^2} \sinh^{-1} \left(\frac{ir}{2\Delta_q} \right)} \right) \\ &= \frac{\Delta - \Delta_q}{\lambda} \frac{1}{\pi} \int_{-2\Delta_q}^{2\Delta_q} \frac{\sin(rt) dr}{\sqrt{4\Delta_q^2 - r^2} \sin^{-1} \left(\frac{r}{2\Delta_q} \right)}. \end{aligned} \quad (3.31)$$

Next, we substitute the integration variable

$$r = 2\Delta_q \sin(u), \quad u = \arcsin \left(\frac{r}{2\Delta_q} \right), \quad dr = 2\Delta_q \cos(u) du, \quad (3.32)$$

such that it follows

$$I_3 + I_5 = \frac{\Delta - \Delta_q}{\lambda} \frac{1}{\pi} \int_{-\pi/2}^{\pi/2} \frac{\sin(2\Delta_q t \sin(u))}{u} du. \quad (3.33)$$

This expression can be evaluated further in the long-time limit. For large times t , the integrand oscillates fast and cancels out except near the points $u = \pm\pi/2$, where $\sin(\pm\pi/2) = \pm 1$. Thus, we expand the $\sin(u)$ function around $u = \pm\pi/2$

$$\sin(u) = \pm 1 \mp \frac{1}{2} \left(u \mp \frac{\pi}{2} \right)^2 + \mathcal{O}(u^4). \quad (3.34)$$

The integrand is split into the contributions from the two stationary points and expressed again with exponential functions

$$I_3 + I_5 = \frac{\Delta - \Delta_q}{\lambda} \frac{1}{\pi} \int_{-\pi/2}^{\pi/2} \left(\frac{\frac{1}{2i} \left(e^{2i\Delta_q t} e^{-i\Delta_q t(u-\frac{\pi}{2})^2} - e^{-2i\Delta_q t} e^{i\Delta_q t(u-\frac{\pi}{2})^2} \right)}{\pi/2} - \frac{\frac{1}{2i} \left(e^{-2i\Delta_q t} e^{i\Delta_q t(u+\frac{\pi}{2})^2} - e^{2i\Delta_q t} e^{-i\Delta_q t(u+\frac{\pi}{2})^2} \right)}{\pi/2} \right) du. \quad (3.35)$$

We shift the integration variables by $\pm\pi/2$ and summarize the expression

$$I_3 + I_5 = \frac{\Delta - \Delta_q}{\lambda} \frac{2}{\pi^2 i} \left[e^{2i\Delta_q t} \int_0^\pi e^{-i\Delta_q t u^2} du - e^{-2i\Delta_q t} \int_0^\pi e^{i\Delta_q t u^2} du \right]. \quad (3.36)$$

We can replace $\pi \rightarrow \infty$ in the integral border, as the integrand is oscillating fast for large values of u and thus canceling out. One obtains

$$\begin{aligned} I_3 + I_5 &= \frac{\Delta - \Delta_q}{\lambda} \frac{2}{\pi^2 i} \left[e^{2i\Delta_q t} \frac{1}{2} \sqrt{\frac{\pi}{2}} \frac{1-i}{\sqrt{\Delta_q t}} - e^{-2i\Delta_q t} \frac{1}{2} \sqrt{\frac{\pi}{2}} \frac{1+i}{\sqrt{\Delta_q t}} \right] \\ &= -\frac{\Delta - \Delta_q}{\lambda} \frac{2}{\pi^{3/2}} \frac{\cos(2\Delta_q t + \frac{\pi}{4})}{\sqrt{\Delta_q t}}. \end{aligned} \quad (3.37)$$

Collecting all contributions, i.e. $\delta\Delta = \Delta - \Delta_q - I_4 - (I_3 + I_5)$, the total expression for the gap oscillations finally reads

$$\delta\Delta(t) = (\Delta - \Delta_q) \left(1 - \frac{1}{\lambda} + \frac{1}{\lambda} \frac{2}{\pi^{3/2}} \frac{\cos(2\Delta_q t + \frac{\pi}{4})}{\sqrt{\Delta_q t}} \right). \quad (3.38)$$

The order parameter is oscillating with a frequency of $2\Delta_q$, the energy of the Higgs mode.

The square root decay of the oscillations is characteristic for the Higgs mode in s -wave superconductors [20, 23] and describes an intrinsic dephasing independent of any additional damping, which is not included in this calculation but will be present in real experiments, for example due to scattering effects. Additional damping of the oscillations will be discussed on a phenomenological level in section 3.1.2. The origin of the intrinsic dephasing can be understood most easily in the picture of the Anderson pseudospin. The quench causes a change in the pseudomagnetic field and creates an additional time-dependence due to the self-consistent dependence on the gap (see Eq. (3.9)). This causes a precession of the pseudospins around the pseudomagnetic field according to the Bloch equations (see Fig. 2.4). As the pseudomagnetic field is momentum-dependent even for the s -wave case due to the dependence on the dispersion in the z -component, the precession frequency ω_p of each pseudospin in momentum-space differs. The frequency is given by the poles in the expressions Eq. (3.14) corresponding to two times the quasiparticle energy $\omega_p = 2E_k^q = 2\sqrt{\epsilon_k^2 + \Delta_q^2}$. In the gap equation, the precession of all the pseudospins is summed up, where the oscillation at the Fermi-level with $\epsilon_k = 0$ has the largest amplitude and therefore dominates the resulting dynamic with a frequency of $2\Delta_q$. However, the oscillation frequencies different from $2\Delta_q$ cannot be neglected completely. Over time, they start to dephase such that a destructive interference occurs, leading to the observed square root decay. For nontrivial gap symmetry, there will be even more different precession frequencies of the pseudospins as a result

of the strong angular dependence of the gap. As shown in the next section, the decay of the gap oscillations will be stronger.

So far, the analysis of the quench dynamic is performed in the linear regime, where $\Delta_q \approx \Delta$. For stronger quenches, the gap will be substantially reduced and the gap oscillations will be no longer around the equilibrium value but approaching a new value for long times $\Delta_\infty < \Delta_q < \Delta$. In this case, the dynamic of the gap for long times can be described by the general formula

$$\Delta(t) = \Delta_\infty + A \frac{\cos(2\Delta_\infty t + \phi)}{\sqrt{t}}, \quad (3.39)$$

where the parameters Δ_∞ , A and ϕ are determined by the quench strength. This result can be derived analytically for arbitrary quench strength with the help of the Lax reduction method [21–23, 25–27, 54, 112] as the quench dynamic in the s -wave system is integrable.

To determine Δ_∞ for small quenches, we use the expression for $\delta\Delta(s)$ in Laplace space of Eq. (3.20). By using the final value theorem, we can write

$$\begin{aligned} \Delta_\infty &= \lim_{s \rightarrow 0} s\Delta(s) \\ &= \lim_{s \rightarrow 0} s \left(\frac{\Delta_q}{s} + \frac{\Delta_q - \Delta}{s} \left(\frac{\frac{\lambda_q}{\lambda} - \lambda_q F(s)}{1 - \frac{\lambda_q}{\lambda} + \lambda_q F(s)} \right) \right). \end{aligned} \quad (3.40)$$

Using again $\epsilon_c \rightarrow \infty$ for $\epsilon_c \gg \Delta$, the limit for $F(s)$ reads

$$\begin{aligned} F_\infty &= \lim_{s \rightarrow 0} F(s) \\ &= \lim_{s \rightarrow 0} \int_0^{2\pi} d\varphi f^2 (4\Delta_q^2 f^2 + s^2) \int_{-\infty}^{\infty} d\epsilon \frac{1}{2E(4\epsilon^2 + 4\Delta_q^2 f^2 + s^2)} \\ &= \frac{\Delta_q \cos^{-1}\left(\frac{\Delta_q}{\Delta}\right)}{\sqrt{\Delta^2 - \Delta_q^2}} \int_0^{2\pi} d\varphi f^2. \end{aligned} \quad (3.41)$$

With $\Delta_q = g\Delta$ and $\lambda_q = g\lambda$, it follows

$$F_\infty = \frac{g \cos^{-1}(g)}{\sqrt{1 - g^2}} \int_0^{2\pi} d\varphi f^2, \quad (3.42a)$$

$$\Delta_\infty = \Delta \frac{g\lambda F_\infty}{1 + g(\lambda F_\infty - 1)}. \quad (3.42b)$$

In literature, the Lax reduction method has been used to derive an expression for Δ_∞ beyond the linear regime [23]. It is implicitly defined by the equation

$$\Delta_\infty = \Delta \cos \kappa, \quad \log\left(\frac{\Delta_f}{\Delta}\right) = -\kappa \tan \frac{\kappa}{2}. \quad (3.43)$$

Hereby, the parameter Δ_f is the equilibrium value of the gap for the quenched interaction, which is defined by

$$\Delta_f = \lambda_q \int_{-\epsilon_c}^{\epsilon_c} d\epsilon \frac{\Delta_f}{2\sqrt{\Delta_f^2 + \epsilon^2}} = \lambda_q \Delta_f \sinh^{-1}\left(\frac{\epsilon_c}{\Delta_f}\right). \quad (3.44)$$

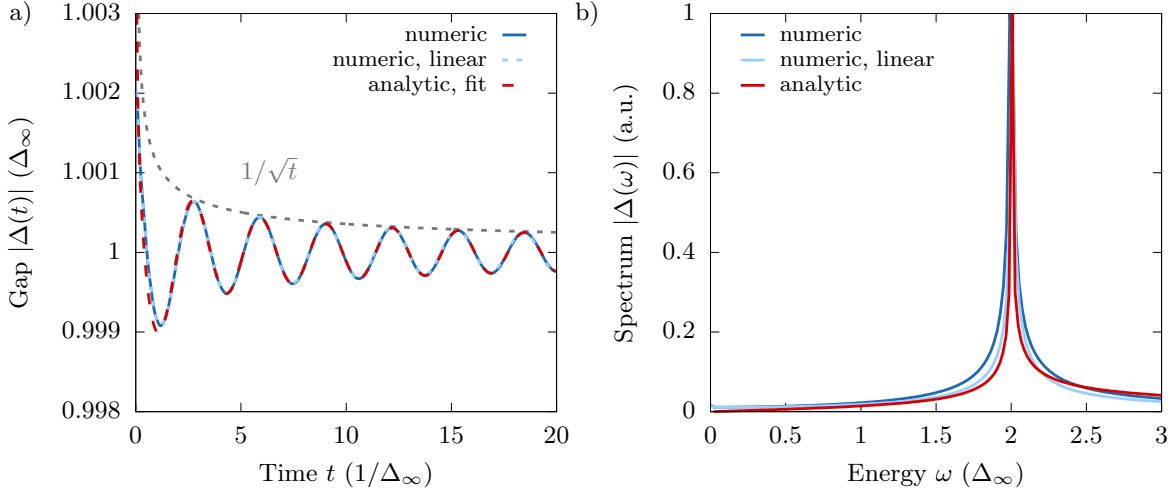


Figure 3.2 Higgs oscillations of s -wave superconductor after interaction quench. a) Comparison of Higgs oscillations calculated numerically without and within linear approximation and a fit with the analytic formula Eq. (3.39) for small quench strength $g = 0.999$. The fit lies exactly on top of the numeric solution. The used parameters and details about the implementation can be found in appendix A. b) Fourier transform of the numeric oscillations compared with the analytic expression of Eq. (3.20). All solutions show a sharp peak at $2\Delta_\infty \approx 2\Delta_q$.

Solving for Δ_f and using $\lambda_q = g\lambda$, it follows

$$\Delta_f = \frac{\epsilon_c}{\sinh\left(\frac{1}{\lambda_q}\right)} = \frac{\epsilon_c}{\sinh\left(\frac{\sinh^{-1}\left(\frac{\epsilon_c}{\Delta}\right)}{g}\right)}. \quad (3.45)$$

In Fig. 3.2, we compare the result from the linear analysis with the full solution and the analytic formula Eq. (3.39) by fitting the function to the numeric result using Δ_∞ , A and ϕ as the fit parameters. The linear and full solution is obtained by evaluating the Bloch equations numerically on a momentum grid. For details about the implementation and the used parameters, see appendix A. All three solutions fit perfectly for the chosen small quench strength $g = 0.999$. A Fourier transform of the oscillations shows a sharp peak at $2\Delta_\infty \approx 2\Delta_q$, which matches the analytic solution of Eq. (3.20) at the imaginary axis $s = i\omega$.

To check whether the result also holds in the nonlinear regime, the interaction quench strength g is varied continuously and the resulting oscillations are fitted again by using the formula (3.39). In addition to the previous fit parameters, we also use the oscillation frequency ω_H as an additional parameter. The result can be found in Fig. 3.3. For each quench strength, a perfect fit is possible as can be seen in Fig. 3.3a). If the quenched interaction drops below $g \approx 0.67$, the gap enters a regime, where it vanishes for long times [21–23, 85, 132, 184]. The resulting fit parameters are shown in Fig. 3.3b),c). There is perfect agreement of $\omega_H = 2\Delta_\infty$ as stated by Eq. (3.39). In addition, we can see that the oscillation amplitude A behaves nonmonotonic. The amplitude increases for increasing quench strength up to a maximum value and then decreases again until it approaches zero. The phase of the oscillations changes monotonically from $\phi = \pi/4$, as found in the linear analysis above and e.g. in [23], to $\phi = 0$ at the quench strength where the gap vanishes. There is a small difference in the phase if one fits the oscillations straight from

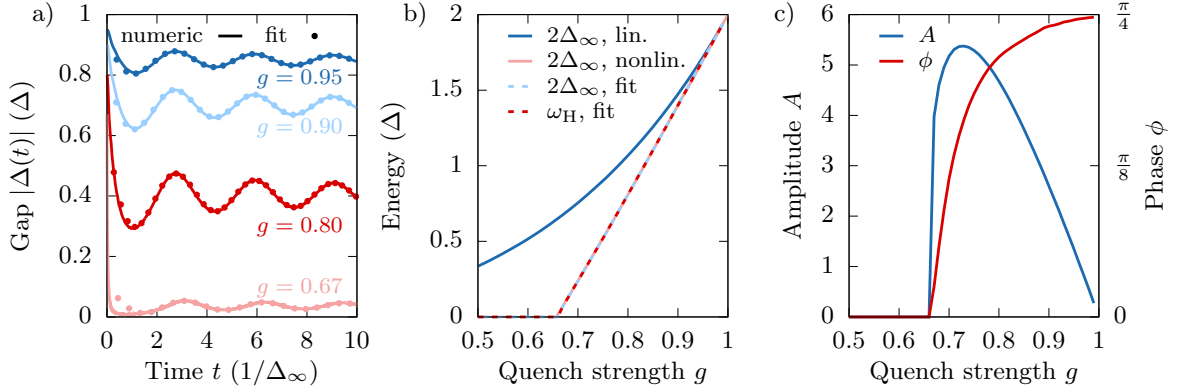


Figure 3.3 Fit parameters for Higgs oscillations of s -wave superconductor after interaction quench. a) Oscillations for different quench strengths g calculated numerically (solid lines) and fitted with the analytic formula (3.39) (points). The formula fits perfectly for all values of g where $\Delta_\infty > 0$. For values $g < 0.67$, the superconductor is quenched into a gapless region with $\Delta(t) = 0$. The time is normalized to the respective Δ_∞ for each g . b) Fit parameters $2\Delta_\infty$, ω_H and the analytic expression Eq. (3.42b) and Eq. (3.43). There is perfect agreement $\omega_H = 2\Delta_\infty$ for all quench strengths. The linear analytic expression is only valid for small quench strengths. c) Fit parameters A and ϕ . The maximum amplitude A is found for $g \approx 0.74$. The phase changes continuously from $\phi = \pi/4$ for small quenches $g \approx 1$ to $\phi = 0$ at the value for g where the gap vanishes. The used parameters and details about the implementation can be found in appendix A.

$t = 0$ or aims for good match in the long-time limit. One obtains the value of $\phi = \pi/4$ for small quenches only in the long-time limit, otherwise the phase is slightly smaller.

In Fig. 3.3b), we also compare the analytic solution of Δ_∞ derived above in the linear regime of Eq. (3.42b) with the solution Eq. (3.43) from literature and the numerical solution. For small quenches $g \approx 1$, there is good agreement; for larger values, the linear formula starts to deviate, whereas Eq. (3.43) holds for all values of g .

Solution for nontrivial gap symmetry

For nontrivial gap symmetry $f = f(\varphi)$, the φ integral in Eq. (3.24) is no longer trivial and we cannot solve it analytically. Nevertheless, it is instructive to study the analytic expression for $\delta\Delta(s)$ derived in the linear regime in frequency space, which reads explicitly

$$\delta\Delta(s) = (\Delta - \Delta_q) \left(\frac{1}{s} - \frac{1}{\lambda \int_0^{2\pi} d\varphi f^2 \sqrt{4\Delta_q^2 f^2 + s^2} \sinh^{-1} \left(\frac{s}{2\Delta_q |f|} \right)} \right). \quad (3.46)$$

Compared with the s -wave case (3.26), there is no longer a sharp peak at $\omega = 2\Delta_q$ for $s = i\omega$ due to the integration and continuous variation of $f(\varphi)$. Yet, any minima in the denominator will lead to peaks in the spectrum and thus determine the frequencies of the Higgs oscillations. The minima in the denominator are approximately given by $\omega = 2\Delta_q f(\varphi_f)$, where φ_f are angles for which $\partial_\varphi f(\varphi_f)^2 = 0$, i.e. flat regions of $f(\varphi)^2$. For these angles, the expression $\sqrt{4\Delta_q^2 f(\varphi)^2 - \omega^2}$ integrated over φ becomes minimal as a larger number of terms for $\varphi \approx \varphi_f$ cancel compared to other values of φ . The exact minima and shape of the resulting peak is determined by the remaining terms in the integrand.

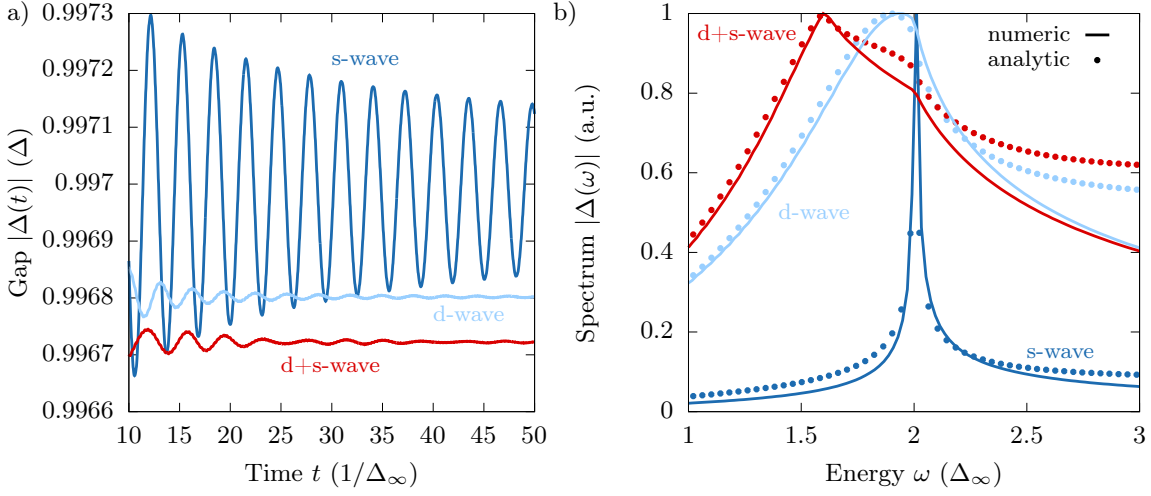


Figure 3.4 Gap oscillation and Fourier spectrum of Higgs oscillations after interaction quench for different gap symmetries. a) Oscillations in time calculated by numerical integration of Bloch equations. b) Fourier transform of the oscillations compared with the analytic expression Eq. (3.46). The time and energy is normalized to Δ_∞ for each symmetry. For details about the calculation, see appendix A.

As an example, we consider d -wave with $f(\varphi) = \cos(2\varphi)$ first. Here, the flat regions are at $\varphi_f = 0, \pi/2, \pi, 3\pi/2$, where $|f(\varphi_f)| = 1$. Thus, we expect again a peak at $\omega \approx 2\Delta_q$, however, with a broader width. As another example, we consider $d+s$ -wave with

$$f(\varphi) = 0.9 \cos(2\varphi) + 0.1, \quad (3.47)$$

i.e. a d -wave order parameter with a small admixture of s -wave as found for example in overdoped YBCO [186–188], or discussed for organic superconductors [189]. Here, the flat regions are again at $\varphi_f = 0, \pi/2, \pi, 3\pi/2$. In contrast to pure d -wave, there are two different values for $f(\varphi_f)$, namely $|f(0)| = |f(\pi)| = 1$ and $|f(\pi/2)| = |f(3\pi/2)| = 0.8$ reflecting two different lobe sizes. Thus, we expect two Higgs modes.

To confirm this analysis, we solve the Bloch equations numerically for these gap symmetries and compare the results with a numerical evaluation of Eq. (3.46). The calculated time dynamic can be found in Fig. 3.4a). Compared to the s -wave case, the oscillations for d -wave and $d+s$ -wave are much stronger damped, which is understandable due to the missing of the exact resonance. As already mentioned in the previous section, this can also be understood as a stronger dephasing effect of the pseudospins compared to the s -wave case as more precession frequencies $\omega_p = 2E_k^q = 2\sqrt{\epsilon_k^2 + \Delta_q^2 f_k^2}$ occur. In a physical picture, this can also be comprehended as a decay of the Higgs mode into gapless quasiparticle excitations which exist in the nodal region. In the $d+s$ -wave case, it can also be observed that the oscillations contain more than one frequency. Please note that the small high-frequency oscillations visible for the d - and $d+s$ -wave case are numerical effects introduced by the energy cutoff. These artifacts are discussed in more detail in appendix A.

In Fig. 3.4b), the Fourier transform of the oscillations compared to the numerical evaluation of Eq. (3.46) is shown. As expected for d -wave, a broad peak slightly below $\omega = 2\Delta_q$ can be observed. In the $d+s$ -wave case, a two-peak or two-kink structure is visible in the spectrum with kinks at $\omega_{H1} \approx 2\Delta_q$ and $\omega_{H2} = 1.6\Delta_q$, corresponding to the values of the two lobes. The

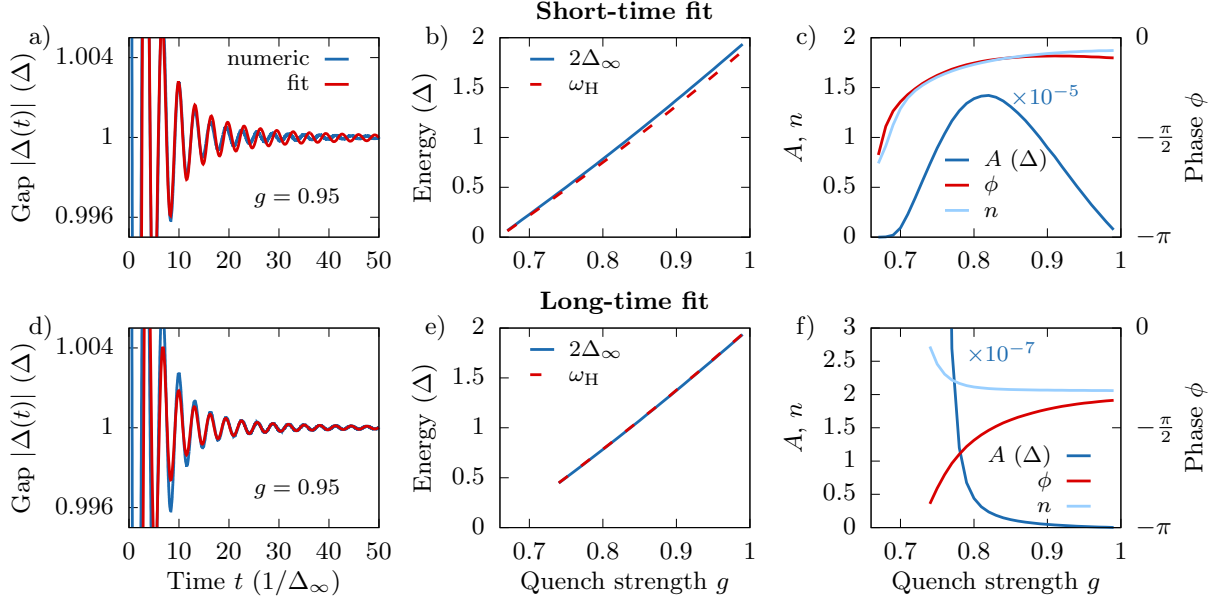


Figure 3.5 Fit of Higgs oscillations for d -wave using Eq. (3.48). For a)-c), the fit tries to match the short-time range $t \lesssim 10$, for d)-f), the fit tries to match the long-time limit $t \gtrsim 30$. a) Numerically calculated gap oscillations exemplary for $g = 0.95$ compared with the fit solution. There is good agreement in the short-time range. b) Fit parameters Δ_∞ and ω_H . There is small deviation from the identity $\omega_H = 2\Delta_\infty$ for small quenches. c) Fit parameters A , ϕ and n . d) Numerically calculated gap oscillations exemplary for $g = 0.95$ compared with the fit solution. There is good agreement in the long-time limit. e) Fit parameters Δ_∞ and ω_H . The identity $\omega_H = 2\Delta_\infty$ fits perfectly. f) Fit parameters A , ϕ and n . In the long-time limit, the data could only be fitted for $g > 0.73$ because for stronger quenches, the Higgs frequency is so low that the required data for the long-time limit could not be obtained. The fit is not useful for $g \lesssim 0.8$ as both the amplitudes and the decay rates change drastically. Details about the calculation and used parameters can be found in appendix A.

evaluation of the analytic formula shows the same qualitative behavior with small deviations due to the approximation used in the derivation.

The numerical solution indicates that the oscillations might be fitted again by a similar formula like in the s -wave case. For the d -wave case, we assume (see also [53])

$$\Delta^d(t) = \Delta_\infty + A \frac{\cos(2\omega_H t + \phi)}{t^n} \quad (3.48)$$

and for the $d+s$ -wave case

$$\Delta^{d+s}(t) = \Delta_\infty + A_1 \frac{\cos(2\omega_{H1} t + \phi_1)}{t^{n_1}} + A_2 \frac{\cos(2\omega_{H2} t + \phi_2)}{t^{n_2}}. \quad (3.49)$$

Compared to the s -wave case, where the decay of the oscillations is fixed with $1/\sqrt{t}$, we introduce an additional parameter n or n_1 and n_2 , which describe a variable decay rate of the oscillations. In Fig. 3.5, we calculate the gap dynamic for d -wave numerically for varying quench strength g and fit the resulting oscillations with the formula (3.48). The simple formula fits the numerical result (locally) well; however, the resulting parameters differ depending on the chosen fit range.

To see the differences, we perform two different fits, one aiming for a good match in the short-time dynamic $t \lesssim 10$, as shown exemplarily for $g = 0.95$ in Fig. 3.5a), and one aiming for

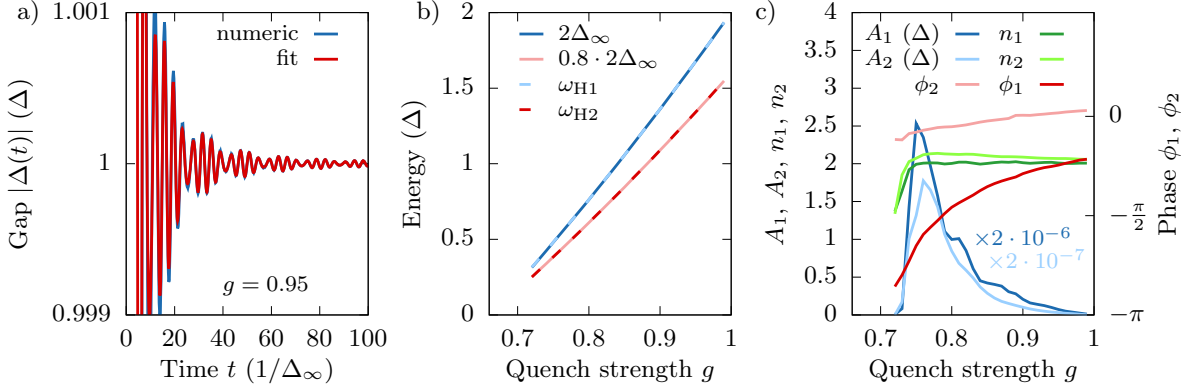


Figure 3.6 Fit of Higgs oscillations for $d+s$ -wave with $f(\varphi) = 0.9 \cos(2\varphi) + 0.1$ using Eq. (3.49). The fit is performed for $t \gtrsim 10$. a) Numerically calculated gap oscillations exemplary for $g = 0.95$ compared with the fit solution. There is good agreement in the chosen time range. b) Fit parameters Δ_∞ , ω_{H1} and ω_{H2} . The identities $\omega_{H1} = 2\Delta_\infty$ and $\omega_{H2} = 0.8 \cdot 2\Delta_\infty$ match perfectly. c) Fit parameters A_1 , A_2 , ϕ_1 , ϕ_2 , n_1 and n_2 . The data could only be fitted for $g > 0.72$. The fit is not useful for $g \lesssim 0.76$ as both the amplitudes and the decay rates change drastically. Details about the calculation and used parameters can be found in appendix A.

a good match in the long-time limit $t \gtrsim 30$, as shown exemplarily for $g = 0.95$ in Fig. 3.5d). Like in the s -wave case, for quench strengths $g < 0.67$, the system is quenched into a gapless regime. The identity $\omega_H = 2\Delta_\infty$ fits again perfectly in the long-time limit (Fig. 3.5e)), in the short-time limit, there is a small deviation from the formula for small quenches (Fig. 3.5b)). In the short-time limit, the amplitude A and phase ϕ behave similar to the s -wave case. There is a value $g \approx 0.8$ for which the amplitude becomes maximal and the phase changes continuously over the whole range. The differences are the values of the parameters. In order to fit the oscillations, the amplitude is 10^5 times larger than in the s -wave case and the phase is shifted to negative values. The decay rate is $n \approx 1.9$ for small quenches and stays approximately constant up to $g \approx 0.8$. From then on, it decreases in size for large quenches, i.e. the oscillations are less damped for strong quenches.

In the long-time limit, the phase is shifted again but shows similar behavior than the short-time dynamic. The decay rate is slightly higher at $n \approx 2$ and stays again constant up to $g \approx 0.8$. For larger quenches, the behavior then deviates drastically from the short-time limit, as the decay rate and the amplitude increases. However, this is due to the fact that the simple formula (3.48) fails to describe the oscillations for large quenches precisely. The fit converges to a solution, where the amplitude increases strongly to compensate for the stronger damping. Formula Eq. (3.48) is just an approximation, the real oscillations contain more components with different frequencies and different decay rates, especially for stronger quenches (see section 3.1.3). Therefore, a simple fit with Eq. (3.48) works only for certain regions, but fails if applied globally. Changing the fit range yields therefore different fit parameters. In addition, the fit formula contains a certain arbitrariness as locally, the same decaying oscillations can be described with either small n and A or large n and A . A strong increase in both parameters has therefore no real meaning. In conclusion, we can state that the d -wave Higgs oscillations are approximately described by Eq. (3.48) with a decay rate of $n \approx 2$ in the long-time limit for small quenches.

Now, we proceed to the $d+s$ -wave case. As already the simple formula for d -wave cannot

describe the dynamic precisely for strong quenches, we do not expect formula Eq. (3.49) to fit the oscillations for the more complex case perfectly. In Fig. 3.6 the result of a fit for a medium-limit time range $t \gtrsim 10$ can be found. Surprisingly, the formula works well for less strong quenches. Moreover, the identities $\omega_{H1} = 2\Delta_\infty$ and $\omega_{H2} = 0.8 \cdot 2\Delta_\infty$ fit perfectly for all quench strengths, i.e. the Higgs modes for $d+s$ -wave are given by the two local gap maxima. The decay rate for both modes is again approximately $n_1 \approx n_2 \approx 2$. At the quench strength $g \approx 0.76$, there seems to be a maximum in the amplitude. However, as already discussed in the d -wave case, at this value, both the decay rate and the amplitude change drastically, such that the fit is no longer useful and the oscillations should be described by a fit formula with more features. Thus, for the $d+s$ -wave case, we can conclude that for small quenches, the oscillations are described by Eq. (3.49) with $n_1 \approx n_2 \approx 2$ in the long-time limit.

3.1.2 Additional Damping of Oscillations

In an actual experiment with real materials, several factors might exist leading to a faster decay of Higgs oscillations compared to the power-law decay predicted by pure BCS theory. This can already be seen in the experimental data of the first direct observation of Higgs oscillations for the s -wave superconductor NbN, where oscillations in the optical conductivity were observed after an excitation with an ultrashort THz laser pulse [36]. The main result of this experiment is shown in Fig. 3.7a). Here, the observed oscillations were fitted with a power-law decay with exponents between 1 and 3 depending on the pump fluence, where BCS theory predicts an exponent of $1/2$ for s -wave superconductors as shown in the previous sections. Possible explanations of such stronger decay are diverse, ranging from scattering on defects, decay into other modes, strong-coupling regimes [190], interaction with the electronic subsystem of quasiparticle and decay into the continuum [71] or crossover into the overdamped phase for strong quenches [22].

On a phenomenological level, we can incorporate damping into BCS theory by introducing relaxation terms in the Bloch equations in analogy to the T_1 and T_2 relaxation times used to describe NMR experiments. A similar approach has been used in a recent study to describe the damping in a THz driving experiment on NbN and Nb₃Sn [71, 191].

The Bloch equations with relaxation terms read

$$\partial_t \langle \sigma_{\mathbf{k}} \rangle (t) = \mathbf{b}_{\mathbf{k}}(t) \times \langle \sigma_{\mathbf{k}} \rangle (t) - \frac{\langle \sigma_{\mathbf{k}} \rangle (t) - \langle \sigma_{\mathbf{k}} \rangle}{\tau}, \quad (3.50)$$

where we use a single relaxation time τ for simplicity. Using again the linear approximation from the previous sections and neglecting the imaginary part of the gap, the Bloch equations in Laplace space read

$$sx(s) = -2\epsilon y(s) - \frac{1}{\tau}x(s), \quad (3.51a)$$

$$sy(s) = \frac{1}{s} \frac{\epsilon}{E} f (\Delta - \Delta_q) - \frac{\epsilon}{E} f \delta\Delta(s) + 2f\Delta_q z(s) + 2\epsilon x(s) - \frac{1}{\tau}y(s), \quad (3.51b)$$

$$sz(s) = -2f\Delta_q y(s) - \frac{1}{\tau}z(s). \quad (3.51c)$$

One finds for the solution for $x(s)$

$$x(s) = \frac{4\epsilon^2 f \left(\frac{\Delta_q - \Delta}{s} + \delta\Delta(s) \right)}{2E \left(4\epsilon^2 + 4\Delta_q^2 f^2 + \left(s + \frac{1}{\tau} \right)^2 \right)}. \quad (3.52)$$

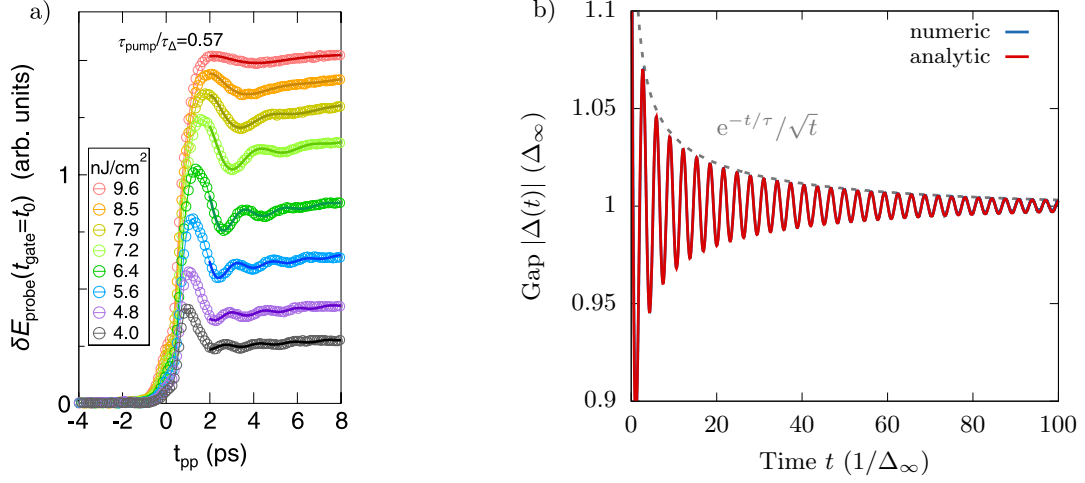


Figure 3.7 Damped Higgs oscillations. a) Experimentally measured Higgs oscillations in a pump-probe experiment for NbN, visible in the change of the transmitted electrical field for different pump fluences. The data has been fitted with an additional power-law decay with exponents between 1 and 3. The figure is taken from [36]. b) Higgs oscillations for s -wave superconductor with additional phenomenological relaxation time $\tau = 0.15 \Delta^{-1}$ calculated numerically using Bloch equations (3.50). For the analytic curve, the solution Eq. (3.39) is fitted to a calculation without damping and then multiplied with $e^{-t/\tau}$ as found by Eq. (3.56). For details about the calculation and used parameters, see appendix A.

Inserting the expression in the gap equation, the gap reads in analogy to section 3.1.1

$$\delta\Delta(s) = \frac{\Delta - \Delta_q}{s} \left(1 - \frac{1}{\lambda F_{\tau}(s)} \right) \quad (3.53)$$

with

$$F_{\tau}(s) = \frac{1}{\left(s + \frac{1}{\tau}\right)} \int_0^{2\pi} d\varphi f^2 \sqrt{4\Delta_q^2 f^2 + \left(s + \frac{1}{\tau}\right)^2} \sinh^{-1} \left(\frac{s + \frac{1}{\tau}}{2\Delta_q |f|} \right). \quad (3.54)$$

In comparison to the expression without additional damping, there is no longer a sharp peak at $\omega = 2\Delta_q$ for $s = i\omega$ even for the s -wave case as the pole is shifted into the complex plane. This leads to a much broader peak, corresponding to a stronger damping. To obtain an explicit solution for the damping factor, we write down the Bromwich integral for the inverse Laplace transform. Concentrating on the last part, the expression reads

$$I = (\Delta_q - \Delta) \frac{1}{2\pi i} \int_{\gamma-i\infty}^{\gamma+i\infty} ds \frac{e^{st}}{\int_0^{2\pi} d\varphi f^2 \sqrt{4\Delta_q^2 f^2 + \left(s + \frac{1}{\tau}\right)^2} \sinh^{-1} \left(\frac{s + \frac{1}{\tau}}{2\Delta_q |f|} \right)}. \quad (3.55)$$

A shift of the integration variable $s \rightarrow s - 1/\tau$ yields

$$I = e^{-t/\tau} (\Delta_q - \Delta) \frac{1}{2\pi i} \int_{\gamma-i\infty}^{\gamma+i\infty} ds \frac{e^{st}}{\int_0^{2\pi} d\varphi f^2 \sqrt{4\Delta_q^2 f^2 + s^2} \sinh^{-1} \left(\frac{s}{2\Delta_q |f|} \right)}, \quad (3.56)$$

i.e. the same expression as in the previous section with an additional exponential decay factor $e^{-t/\tau}$. Thus, the relaxation time τ leads to an exponential decay of the oscillations.

In Fig. 3.7b), the numerically calculated Higgs oscillations for s -wave are shown with a relaxation time $\tau = 0.15 \Delta^{-1}$. To compare the result with the predicted exponential decay from the linear analysis in Eq. (3.56), a calculation with the same parameters without damping is performed. This result is fitted by the solution Eq. (3.39) and then multiplied with an additional exponential decay $e^{-t/\tau}$ using the chosen relaxation time τ . The resulting curve fits the numerical solution perfectly.

Using different relaxation times τ_1 and τ_2 for longitudinal and transversal relaxation adds an additional shift in time. Different relaxation times have also been used in [71] to describe the damping and shift found in the pump-probe experiment on NbN [36]. While there is some analogy of the Bloch equations in NMR experiments with the Bloch equations for the pseudospin, such that in [71], the transverse relaxation time τ_2 was attributed to dephasing of pseudospins like the spin-spin relaxation in NMR and the longitudinal relaxation time τ_1 was attributed to relaxation due to quasiparticle interaction like the spin-lattice relaxation in NMR, there are some differences that make this analogy not complete. The BCS type of Bloch equations contains the self-consistency condition, i.e. the pseudomagnetic field depends on the time-dependent gap itself, such that there is a stronger coupling between all components of the pseudospin. This makes the interpretation of the relaxation times as in NMR experiments more vague.

As stated in the beginning of this section, the microscopic cause of additional damping can be diverse. To conclude this section, we estimate the scattering time for a type-II superconductor in an external magnetic field. As type-II superconductors above the critical field H_{c1} exhibit a finite resistance proportional to the applied magnetic field [192], power might be dissipated leading to damped oscillations. This is caused by movement of vortices due to the Lorentz force on the flux lines [193]

$$\mathbf{F} = \frac{\phi_0}{c} \mathbf{j} \times \hat{e}_{\phi_0}, \quad (3.57)$$

where \mathbf{j} is the external supercurrent density, $\phi_0 = h/(2e)$ the flux quantum and \hat{e}_{ϕ_0} the vector along the flux line. This deflection of the vortices orthogonal to the current is similar to the classic Magnus effect of spinning objects exposed to a flow. As work is done, power is dissipated, which leads to a finite resistance. It was shown that in such a mixed vortex state, collective modes are damped [194, 195]. For the pseudospin precession or Higgs oscillation, such a resistance can be understood as an additional decay channel, which leads to a damping of the oscillation.

There are different mechanisms discussed in literature to describe this dissipation effect in more detail [196–201]. To give a rough estimate of the phenomenological relaxation time τ in our model, we use the result of the Bardeen-Stephen model [197]. This model gives an expression for the flow resistivity ρ_f in dependence of the magnetic field B and the normal resistivity ρ_n if there is no flux pinning

$$\rho_f \approx \rho_n \frac{B}{H_{c2}}. \quad (3.58)$$

We take the Drude model formula, which connects the resistivity with the scattering time τ

$$\rho = \frac{m}{ne^2\tau}. \quad (3.59)$$

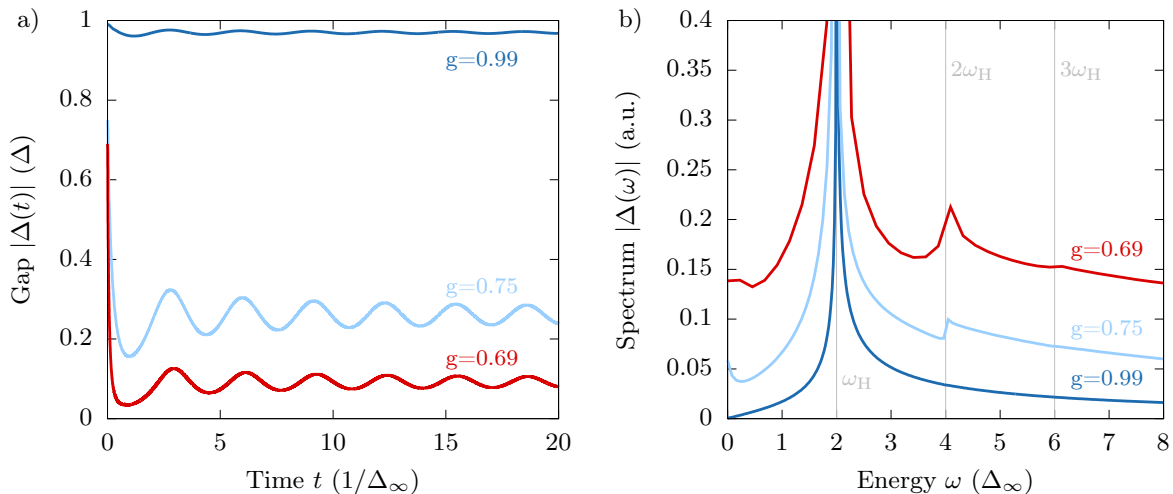


Figure 3.8 Higher-harmonic Higgs oscillations for strong interaction quenches. a) Higgs oscillations for three different quench strengths g . b) Spectrum of oscillations. For increasing quench strength, higher-harmonic Higgs oscillations are visible at ω_H , $2\omega_H$, $3\omega_H$. The time and energy is normalized to the respective Δ_∞ for each quench. The oscillations are calculated numerically. For details about the calculation see Appendix A.

It follows for the scattering time

$$\tau = \frac{m}{ne^2\rho_n} \frac{H_{c2}}{B} \propto \frac{1}{B}. \quad (3.60)$$

We see that the scattering time is inverse proportional to the magnetic field strength; thus, the damping is increased for stronger magnetic fields.

3.1.3 Higher-harmonic Higgs Oscillations

The analysis in section 3.1.1 for Higgs oscillations in s -wave superconductors within the linear approximation (3.38) or the general formula (3.39) suggest that, at least in the long-time limit, the gap oscillates with a single frequency $\omega_H = 2\Delta_\infty$. However, this is not the whole truth as strong quenches can induce nonlinear effects beyond these formulas.

To investigate these effects, we solve again the Bloch equations numerically for increasing quench strength and study the oscillations spectrum in more detail. The result can be found in Fig. 3.8. While looking at higher energies, one observes that for increasing quench strength higher harmonics are visible. For the small quench $g = 0.99$, which is still described by the linear analysis, only one peak in the frequency spectrum in Fig. 3.8b) at $\omega = \omega_H = 2\Delta_\infty$ is visible. For the larger quench strength $g = 0.75$, a second-harmonic peak at $\omega = 2\omega_H$ is visible. For the strongest quench $g = 0.69$, just before the system is quenched into the gapless regime, even a small third-harmonic peak at $\omega = 3\omega_H$ is visible. These effects are not captured by the linear analysis, as higher-order perturbations such as $z_k(t)\delta\Delta(t)$ are explicitly ignored.

Experimentally, these nonlinear effects are probably difficult to measure. The intensity of a quench pulse has to be fine-tuned such that the condensate is quenched maximally just before the system is quenched into the gapless regime. Only for these strong quenches, the effect is visible,

but even then, the second-harmonic is less than 10% of the amplitude of the first-harmonic. In addition, for strong quenches, other difficulties arise, such as heating or screening of the signal by large amount of broken Cooper pairs.

The higher-harmonic Higgs modes should not be confused with the driven higher-harmonic Higgs oscillations found in recent experiments [110, 111]. Driving a superconductor with light of frequency Ω results typically in a driven 2Ω Higgs oscillation. A linear response, i.e. a driven oscillation with Ω , is forbidden due to parity of the Hamiltonian. This will be discussed in more detail in chapter 5. In these experiments, an intense multi-cycle pulse with asymmetric shape drives the superconductor and induces higher-harmonic oscillations at 4Ω in addition to 2Ω oscillations. Furthermore, due to the asymmetric shape of the pulse, an effective dc component is induced, which leads to a dynamical symmetry breaking. As a result, the usual forbidden odd order driven oscillations are allowed, and Higgs oscillations at Ω and 3Ω are observed as well. Driving with light in the presence of a dc current is discussed in more detail in section 5.3. In contrast, the oscillations discussed here are the intrinsic Higgs modes at fixed frequencies ω_H , $2\omega_H$, etc. independent of the frequency of a quench pulse.

3.2 Excitation of Higgs Oscillations with State Quenches

As we have seen in the previous section, interaction quenches can be used to push a superconductor out of equilibrium and excite Higgs oscillations. However, they are difficult to realize experimentally for superconductors in contrast to cold atom systems, where the interaction can be tuned more easily with Feshbach resonances [120]. Moreover, a change only in the pairing strength excites the system in a symmetric fashion regarding the ground state gap symmetry, i.e. the quench is \mathbf{k} -independent. As a result, the condensate oscillates always within its ground state symmetry channel. For nontrivial gap symmetry, we expect richer features if we were able to apply a \mathbf{k} -dependent quench. Parts of the following calculation and analysis have already been published in [7].

To implement a quench with these properties, we will go beyond the usually used interaction quench scheme and quench the condensate directly, which allows to modify the symmetry of the condensate. We name such a quench a *state quench* as it alters the state of the system, i.e. the condensate or quasiparticle distribution, compared to the interaction quench, which changes the Hamiltonian. Moreover, a change in the quasiparticle distribution reflects more closely the effect of pump pulses used in experiments to push the system out of equilibrium as the light pulse breaks some of the Cooper pairs and therefore excites quasiparticles. In the context of the Anderson pseudospin picture, the effect of a pump pulse has also been described in literature as “scrambling of the orientations of Anderson pseudospins” [54].

According to section 2.2.4, the equilibrium expectation values at temperature T read

$$\langle c_{-\mathbf{k}\downarrow} c_{\mathbf{k}\uparrow} \rangle = \frac{\Delta_{\mathbf{k}}}{2E_{\mathbf{k}}} \tanh\left(\frac{E_{\mathbf{k}}}{2k_{\text{B}}T}\right), \quad (3.61a)$$

$$\langle c_{\mathbf{k}\uparrow}^{\dagger} c_{-\mathbf{k}\downarrow}^{\dagger} \rangle = \frac{\Delta_{\mathbf{k}}^*}{2E_{\mathbf{k}}} \tanh\left(\frac{E_{\mathbf{k}}}{2k_{\text{B}}T}\right), \quad (3.61b)$$

$$\langle c_{\mathbf{k}\uparrow}^{\dagger} c_{\mathbf{k}\uparrow} \rangle = \frac{1}{2} - \frac{\epsilon_{\mathbf{k}}}{2E_{\mathbf{k}}} \tanh\left(\frac{E_{\mathbf{k}}}{2k_{\text{B}}T}\right), \quad (3.61c)$$

$$\langle c_{-\mathbf{k}\downarrow} c_{-\mathbf{k}\downarrow}^{\dagger} \rangle = \frac{1}{2} + \frac{\epsilon_{\mathbf{k}}}{2E_{\mathbf{k}}} \tanh\left(\frac{E_{\mathbf{k}}}{2k_{\text{B}}T}\right). \quad (3.61d)$$

One can see that these expectation values follow the same symmetry as the energy gap. In particular, if we consider $\langle c_{-k\downarrow}c_{k\uparrow} \rangle$ at \mathbf{k} values far from the Fermi level, where $\epsilon_{\mathbf{k}} \gg \Delta$, we can approximate for $T = 0$

$$\langle c_{-k\downarrow}c_{k\uparrow} \rangle \approx \frac{\Delta}{2\epsilon_{\mathbf{k}}} f_{\mathbf{k}} \propto f_{\mathbf{k}}. \quad (3.62)$$

Thus, $\langle c_{-k\downarrow}c_{k\uparrow} \rangle$ at values far from k_F is a good representation of the gap symmetry and even the exact functional form.

To push the system out of equilibrium in an asymmetric way, we perform a quench by changing the symmetry of these expectation values. In order to have a controlled excitation, we assume that the system starts at an equilibrium position of a different symmetry $f_{\mathbf{k}}^{\text{mod}}$ and let it then evolve in the system with the original symmetry $f_{\mathbf{k}}$. We define the quenched expectation values

$$\langle c_{-k\downarrow}c_{k\uparrow} \rangle^{\text{q}} = \frac{\Delta f_{\mathbf{k}}^{\text{mod}}}{2E_{\mathbf{k}}^{\text{mod}}} \tanh\left(\frac{E_{\mathbf{k}}^{\text{mod}}}{2k_{\text{B}}T}\right), \quad (3.63\text{a})$$

$$\langle c_{k\uparrow}^{\dagger}c_{-k\downarrow}^{\dagger} \rangle^{\text{q}} = \frac{(\Delta f_{\mathbf{k}}^{\text{mod}})^*}{2E_{\mathbf{k}}^{\text{mod}}} \tanh\left(\frac{E_{\mathbf{k}}^{\text{mod}}}{2k_{\text{B}}T}\right), \quad (3.63\text{b})$$

$$\langle c_{k\uparrow}^{\dagger}c_{k\uparrow} \rangle^{\text{q}} = \frac{1}{2} - \frac{\epsilon_{\mathbf{k}}}{2E_{\mathbf{k}}^{\text{mod}}} \tanh\left(\frac{E_{\mathbf{k}}^{\text{mod}}}{2k_{\text{B}}T}\right), \quad (3.63\text{c})$$

$$\langle c_{-k\downarrow}c_{-k\downarrow}^{\dagger} \rangle^{\text{q}} = \frac{1}{2} + \frac{\epsilon_{\mathbf{k}}}{2E_{\mathbf{k}}^{\text{mod}}} \tanh\left(\frac{E_{\mathbf{k}}^{\text{mod}}}{2k_{\text{B}}T}\right), \quad (3.63\text{d})$$

where $E_{\mathbf{k}}^{\text{mod}} = \sqrt{\epsilon_{\mathbf{k}}^2 + |\Delta f_{\mathbf{k}}^{\text{mod}}|^2}$. For the modified symmetry function $f_{\mathbf{k}}^{\text{mod}}$, we assume that it is a deviation from the original symmetry of strength g in another symmetry channel $f'_{\mathbf{k}}$, i.e.

$$f_{\mathbf{k}}^{\text{mod}} = f_{\mathbf{k}} + g f'_{\mathbf{k}}. \quad (3.64)$$

Please note that in contrast to the interaction quench, where a value of $g \approx 0$ corresponds to a strong quench, here, a value of $g \approx 0$ corresponds to a small quench. In analogy, we define the quenched expectation values for the pseudospins

$$\langle \sigma_{\mathbf{k}}^x \rangle^{\text{q}} = \frac{\Delta' f_{\mathbf{k}}^{\text{mod}'}}{2E_{\mathbf{k}}^{\text{mod}'}} \tanh\left(\frac{E_{\mathbf{k}}^{\text{mod}'}}{2k_{\text{B}}T}\right), \quad (3.65\text{a})$$

$$\langle \sigma_{\mathbf{k}}^y \rangle^{\text{q}} = -\frac{\Delta'' f_{\mathbf{k}}^{\text{mod}''}}{2E_{\mathbf{k}}^{\text{mod}''}} \tanh\left(\frac{E_{\mathbf{k}}^{\text{q}}}{2k_{\text{B}}T}\right), \quad (3.65\text{b})$$

$$\langle \sigma_{\mathbf{k}}^z \rangle^{\text{q}} = -\frac{\epsilon_{\mathbf{k}}}{2E_{\mathbf{k}}^{\text{mod}}} \tanh\left(\frac{E_{\mathbf{k}}^{\text{mod}}}{2k_{\text{B}}T}\right) \quad (3.65\text{c})$$

and the quenched expectation values for the Bogoliubov quasiparticles

$$\langle \alpha_{\mathbf{k}} \beta_{\mathbf{k}} \rangle^{\text{q}} = \frac{\epsilon_{\mathbf{k}} (\Delta_{\mathbf{k}} - \Delta f_{\mathbf{k}}^{\text{mod}})}{2E_{\mathbf{k}} E_{\mathbf{k}}^{\text{mod}}} \tanh \left(\frac{E_{\mathbf{k}}^{\text{mod}}}{2k_{\text{B}} T} \right), \quad (3.66a)$$

$$\langle \alpha_{\mathbf{k}}^{\dagger} \beta_{\mathbf{k}}^{\dagger} \rangle^{\text{q}} = -\frac{\epsilon_{\mathbf{k}} (\Delta_{\mathbf{k}}^* - (\Delta f_{\mathbf{k}}^{\text{mod}})^*)}{2E_{\mathbf{k}} E_{\mathbf{k}}^{\text{mod}}} \tanh \left(\frac{E_{\mathbf{k}}^{\text{mod}}}{2k_{\text{B}} T} \right), \quad (3.66b)$$

$$\langle \alpha_{\mathbf{k}}^{\dagger} \alpha_{\mathbf{k}} \rangle^{\text{q}} = \frac{1}{2} \left(1 - \frac{\epsilon_{\mathbf{k}}^2 + |\Delta|^2 f_{\mathbf{k}} f_{\mathbf{k}}^{\text{mod}}}{E_{\mathbf{k}} E_{\mathbf{k}}^{\text{mod}}} \tanh \left(\frac{E_{\mathbf{k}}^{\text{mod}}}{2k_{\text{B}} T} \right) \right), \quad (3.66c)$$

$$\langle \beta_{\mathbf{k}}^{\dagger} \beta_{\mathbf{k}} \rangle^{\text{q}} = \langle \alpha_{\mathbf{k}}^{\dagger} \alpha_{\mathbf{k}} \rangle^{\text{q}}. \quad (3.66d)$$

After applying such a quench, we let the system evolve freely in time again and study the time dynamic.

3.2.1 Linear Analysis within Pseudospin Formalism

To gain a basic understanding, we again make use of the simplicity of the BCS Hamiltonian in the linearized pseudospin representation for $T = 0$. We use a similar ansatz for the pseudospins and the gap as in the calculation for the interaction quench

$$\langle \sigma_{\mathbf{k}}^x \rangle (t) = \langle \sigma_{\mathbf{k}}^x \rangle^{\text{q}} + x_{\mathbf{k}}(t), \quad (3.67a)$$

$$\langle \sigma_{\mathbf{k}}^y \rangle (t) = \langle \sigma_{\mathbf{k}}^y \rangle^{\text{q}} + y_{\mathbf{k}}(t), \quad (3.67b)$$

$$\langle \sigma_{\mathbf{k}}^z \rangle (t) = \langle \sigma_{\mathbf{k}}^z \rangle^{\text{q}} + z_{\mathbf{k}}(t), \quad (3.67c)$$

$$\Delta(t) = \Delta_{\text{q}} + \delta\Delta(t) \quad (3.67d)$$

with

$$\begin{aligned} \Delta_{\text{q}} &= \lambda \int_{-\epsilon_c}^{\epsilon_c} d\epsilon \int_0^{2\pi} d\varphi f(\varphi) (\langle \sigma_{\mathbf{k}}^x \rangle^{\text{q}} - i \langle \sigma_{\mathbf{k}}^y \rangle^{\text{q}}) \\ &= \Delta \lambda \int_0^{2\pi} d\varphi f(\varphi) f^{\text{mod}}(\varphi) \sinh^{-1} \left(\frac{\epsilon_c}{\Delta |f^{\text{mod}}(\varphi)|} \right), \end{aligned} \quad (3.68a)$$

$$\delta\Delta(t) = \lambda \int_{-\epsilon_c}^{\epsilon_c} d\epsilon \int_0^{2\pi} d\varphi f(\varphi) (x_{\mathbf{k}}(t) - i y_{\mathbf{k}}(t)). \quad (3.68b)$$

The linearized equations of motion (2.64) in Laplace space for real equilibrium gap Δ read

$$sx(s) = -\frac{\epsilon}{E_{\text{mod}}} f \delta\Delta''(s) - 2\epsilon y(s), \quad (3.69a)$$

$$sy(s) = \frac{1}{s} \frac{\epsilon}{E_{\text{mod}}} (\Delta f^{\text{mod}} - \Delta_{\text{q}} f) - \frac{\epsilon}{E_{\text{mod}}} f \delta\Delta'(s) + 2f \Delta_{\text{q}} z(s) + 2\epsilon x(s), \quad (3.69b)$$

$$sz(s) = -\frac{1}{E_{\text{mod}}} f f^{\text{mod}} \Delta \delta\Delta''(s) - 2f \Delta_{\text{q}} y(s). \quad (3.69c)$$

Solving for $x(s)$, $y(s)$ and $z(s)$ yields

$$x(s) = \frac{4\epsilon^2 \left(\frac{\Delta_q f - \Delta f^{\text{mod}}}{s} + f \delta \Delta'(s) \right)}{2E^{\text{mod}}(4\epsilon^2 + 4\Delta_q^2 f^2 + s^2)} - \frac{2\epsilon f \left(4\Delta_q f \frac{\Delta_q f - \Delta f^{\text{mod}}}{s} + s \right) \delta \Delta''(s)}{2E^{\text{mod}}(4\epsilon^2 + 4\Delta_q^2 f^2 + s^2)}, \quad (3.70a)$$

$$y(s) = -\frac{4\epsilon^2 f \delta \Delta''(s)}{2E^{\text{mod}}(4\epsilon^2 + 4\Delta_q^2 f^2 + s^2)} - \frac{2\epsilon((\Delta_q f - \Delta f^{\text{mod}}) + s f \delta \Delta'(s))}{2E^{\text{mod}}(4\epsilon^2 + 4\Delta_q^2 f^2 + s^2)} - \frac{4f^2 f^{\text{mod}} \Delta \Delta_q \delta \Delta''(s)}{2E^{\text{mod}}(4\epsilon^2 + 4\Delta_q^2 f^2 + s^2)}, \quad (3.70b)$$

$$z(s) = \frac{4\epsilon f^2 \Delta_q \delta \Delta'(s)}{2E^{\text{mod}}(4\epsilon^2 + 4\Delta_q^2 f^2 + s^2)} + \frac{2f(4\epsilon^2 \frac{\Delta_q f - \Delta f^{\text{mod}}}{s} - s \Delta f^{\text{mod}}) \delta \Delta''(s)}{2E^{\text{mod}}(4\epsilon^2 + 4\Delta_q^2 f^2 + s^2)} + \frac{4f\epsilon \Delta_q \frac{\Delta_q f - \Delta f^{\text{mod}}}{s}}{2E^{\text{mod}}(4\epsilon^2 + 4\Delta_q^2 f^2 + s^2)}. \quad (3.70c)$$

The solution is inserted into the gap equation (3.68b). Like in the interaction quench case, the real and imaginary part are not coupled and again, the imaginary part is zero. For $\delta \Delta(s)$, it follows

$$\delta \Delta(s) = \frac{\Delta_q I_1(s) - \Delta I_2(s)}{s} + \delta \Delta(s) I_1(s) \quad (3.71)$$

with

$$I_1(s) = \lambda \int_{-\epsilon_c}^{\epsilon_c} d\epsilon \int_0^{2\pi} d\varphi \frac{4\epsilon^2 f^2}{2E^{\text{mod}}(4E_q^2 + s^2)} = C_f - \lambda H(s), \quad (3.72a)$$

$$I_2(s) = \lambda \int_{-\epsilon_c}^{\epsilon_c} d\epsilon \int_0^{2\pi} d\varphi \frac{4\epsilon^2 f f^{\text{mod}}}{2E^{\text{mod}}(4E_q^2 + s^2)} = \frac{\Delta_q}{\Delta} - \lambda G(s), \quad (3.72b)$$

where

$$C_f = \lambda \int_{-\epsilon_c}^{\epsilon_c} d\epsilon \int_0^{2\pi} d\varphi \frac{f^2}{2E^{\text{mod}}} = \lambda \int_0^{2\pi} d\varphi f^2 \sinh^{-1} \left(\frac{\epsilon_c}{\Delta |f^{\text{mod}}|} \right), \quad (3.73a)$$

$$G(s) = \int_0^{2\pi} d\varphi f f^{\text{mod}} (4\Delta_q^2 f^2 + s^2) \int_{-\epsilon_c}^{\epsilon_c} d\epsilon \frac{1}{2E^{\text{mod}}(E_q^2 + s^2)}, \quad (3.73b)$$

$$H(s) = \int_0^{2\pi} d\varphi f^2 (4\Delta_q^2 f^2 + s^2) \int_{-\epsilon_c}^{\epsilon_c} d\epsilon \frac{1}{2E^{\text{mod}}(E_q^2 + s^2)}. \quad (3.73c)$$

Thus, it follows finally

$$\delta \Delta(s) = \frac{1}{s} \left(\Delta \frac{\lambda G(s)}{1 - C_f + \lambda H(s)} - \Delta_q \right). \quad (3.74)$$

The ϵ integral in $G(s)$ and $H(s)$ can be evaluated and the result reads

$$G(s) = \int_0^{2\pi} d\varphi f f^{\text{mod}} \sqrt{4\Delta_q^2 f^2 + s^2} \frac{\tanh^{-1} \left(\frac{\sqrt{4\Delta_q^2 f^2 - 4\Delta^2 (f^{\text{mod}})^2 + s^2}}{\sqrt{4\Delta_q^2 f^2 + s^2}} \right)}{\sqrt{4\Delta_q^2 f^2 - 4\Delta^2 (f^{\text{mod}})^2 + s^2}}, \quad (3.75a)$$

$$H(s) = \int_0^{2\pi} d\varphi f^2 \sqrt{4\Delta_q^2 f^2 + s^2} \frac{\tanh^{-1} \left(\frac{\sqrt{4\Delta_q^2 f^2 - 4\Delta^2 (f^{\text{mod}})^2 + s^2}}{\sqrt{4\Delta_q^2 f^2 + s^2}} \right)}{\sqrt{4\Delta_q^2 f^2 - 4\Delta^2 (f^{\text{mod}})^2 + s^2}}. \quad (3.75b)$$

We stop here with a further analytic evaluation. The gap $\delta\Delta(s)$ has no exact poles; however, any peaks in the spectrum are determined by the expressions $G(s)$ and $H(s)$ and more specifically by the terms $\sqrt{4\Delta_q^2 f^2 - 4\Delta^2 (f^{\text{mod}})^2 + s^2}$ and $\sqrt{4\Delta_q^2 f^2 + s^2}$ in a nontrivial way. What we can see is that the difference between the gap symmetry f and the changed symmetry f^{mod} plays a crucial role. In the next section, we will calculate the gap dynamic numerically for certain gap and quench symmetries and compare the result with the here analytically derived formula.

3.2.2 Additional Higgs Modes for Nontrivial Gap Symmetries

In principle, we can choose any modified symmetry function $f_{\mathbf{k}}^{\text{mod}}$ to quench the system and push it out of equilibrium. To perform a systematic study, we restrict the deviations from the original symmetry to the fundamental symmetry channels, which are important with respect to the point group of the system. As an example, cuprate superconductors with d -wave symmetry have a square lattice described by the D_{4h} point group. The irreducible representations for this group are A_{1g} , A_{2g} , B_{1g} and B_{2g} [202], where the d -wave symmetry is represented by the B_{1g} channel. Hereby, A (B) means symmetric (antisymmetric) under rotation by $\pi/2$ around the z -axis and the subscript 1 (2) means symmetric (antisymmetric) under reflection at the x - or y -axis. The symmetry functions are given in Table 3.1. Exemplary, a quench of a d -wave symmetry in the A_{1g} channel of strength g would look like

$$f_{\mathbf{k}}^{\text{mod}} = f_{\mathbf{k}} + g f'_{\mathbf{k}} = \cos(2\varphi) + g. \quad (3.76)$$

Hereby, $f_{\mathbf{k}} = \cos(2\varphi)$ is the gap symmetry and $f'_{\mathbf{k}} = 1$ the quench symmetry.

One can visualize the effect of these quenches by plotting $f_{\mathbf{k}}^{\text{mod}}$. This is done for all combinations of the irreducible representations as gap and quench symmetry in Fig. 3.9. A condensate quenched away from its original symmetry will then start to oscillate around its ground state symmetry. We name this oscillation according to its symmetry. As an example, an s -wave superconductor quenched in the A_{1g} channel (first column, first row in Fig. 3.9) stays in its original symmetry channel and performs therefore a symmetric A_s^{1g} oscillation, where the index s indicates the original symmetry. The same would be true for a B_{1g} -quench for d -wave (third column, third row), which is named $A_{x^2-y^2}^{1g}$. A different combination of gap and quench symmetry will induce asymmetric oscillations. For d -wave, the motion is sketched in Fig. 3.10, where the arrows indicate the movement of the lobes. Whether these asymmetric oscillations lead to additional Higgs modes is not clear from the beginning as the spectrum is determined in a nontrivial way by the integrals in Eq. (3.75). The time dynamic has to be calculated explicitly by numerical integration.

We start with d -wave symmetry, which we quench in all four different symmetry channels. The result can be found in Fig. 3.11, exemplary for a quench strength of $g = 0.2$. A Fourier transform

Irreducible representation	Basis function	Basis function in polar coordinates
A_{1g}	1	1
A_{2g}	$xy(x^2 - y^2)$	$\sin(4\varphi)$
B_{1g}	$x^2 - y^2$	$\cos(2\varphi)$
B_{2g}	xy	$\sin(2\varphi)$

Table 3.1 Even parity basis functions for D_{4h} point group in Cartesian coordinates and as a function of the azimuthal angle φ in polar coordinates [202].

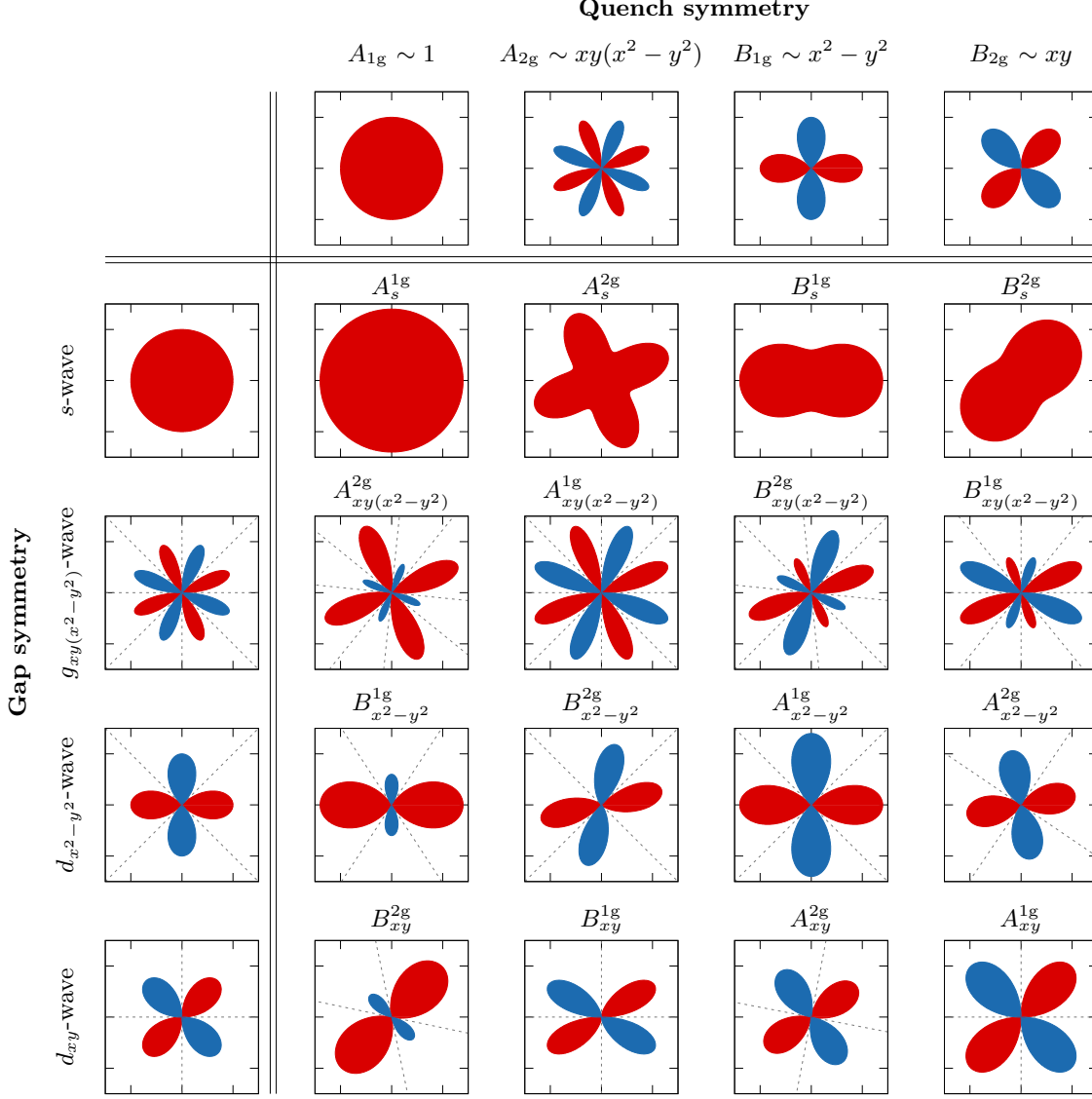


Figure 3.9 Effect of quenches on a symmetry function for all combinations of irreducible representations as gap and quench symmetry of the D_{4h} point group. The left column represents the gap symmetry $f_{\mathbf{k}}$, the top row the quench symmetry $f'_{\mathbf{k}}$ and the cells the resulting modified function $f_{\mathbf{k}}^{\text{mod}}$ according to Eq. (3.64) exemplary for a quench strength of $g = 0.4$. The grey dotted lines are the nodal lines. The cell labels describe the induced oscillations, which are named according to their symmetry property with an additional subscript indicating the ground state symmetry. Figure adapted from [7].

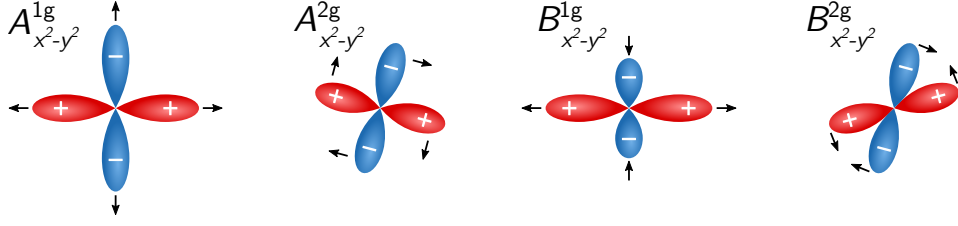


Figure 3.10 Fundamental oscillations for d -wave symmetry. The $A_{x^2-y^2}^{1g}$ oscillation represents a breathing mode, the $A_{x^2-y^2}^{2g}$ oscillation represents a rotating mode, the $B_{x^2-y^2}^{1g}$ oscillation represents an oscillating mode, the $B_{x^2-y^2}^{2g}$ oscillation represents a clapping mode. Figure adapted from [7].

of the oscillations in Fig. 3.11a) is shown in Fig. 3.11b). The spectra for the quenches differ. For the B_{1g} and A_{2g} quench, the spectrum resembles the interaction quench case with a broad peak at $\omega \approx 2\Delta_\infty$. For the A_{1g} and B_{2g} quench, a pronounced kink at $\omega \approx 0.4\Delta_\infty$ is visible in addition to the $\omega \approx 2\Delta_\infty$ peak. By restricting the Fourier transform to the long-time limit (Fig. 3.11c)), the kink transforms into a clear peak. These two quenches induce therefore a second Higgs mode at lower energies.

Now, two questions arise. First, what is the difference between the quenches or induced oscillations such that in one case, one observes two Higgs modes and in the other case, only one Higgs mode, despite the fact that in both cases (except for the A_{1g} quench) asymmetric oscillations are induced? And second, what determines the energy of the new Higgs mode? It will turn out that both questions are coupled.

To find an answer, it is instructive to look at the analytic expression for $\delta\Delta(s)$ in Eq. (3.74) and the expressions for $G(s)$ and $H(s)$ in Eq. (3.75) again. As already mentioned, in these expressions, the difference between the gap symmetry f and the modified symmetry f^{mod} plays an important role. As in the interaction quench, minima in the denominator determine the frequency spectrum. Here, the minima cannot easily be seen as the expressions are more complex. We expect new modes if there are significant changes to the gap symmetry. In particular it turns out, new modes arise if the quench shifts the nodal lines between positive and negative lobes compared to the ground state symmetry. This is visualized with the grey dotted lines in Fig. 3.9, representing the nodal directions. In the d -wave case, one observes that the A_{1g} and B_{2g} quenches shift the nodal lines, whereas the A_{2g} and B_{1g} quenches do not. This corresponds with the arising of two or one Higgs modes for these quenches, respectively. In section 3.2.6, we summarize the observed modes for all gap and quench symmetries. In the next section, we will answer the questions what determines the energy of the Higgs modes and how it can be tuned.

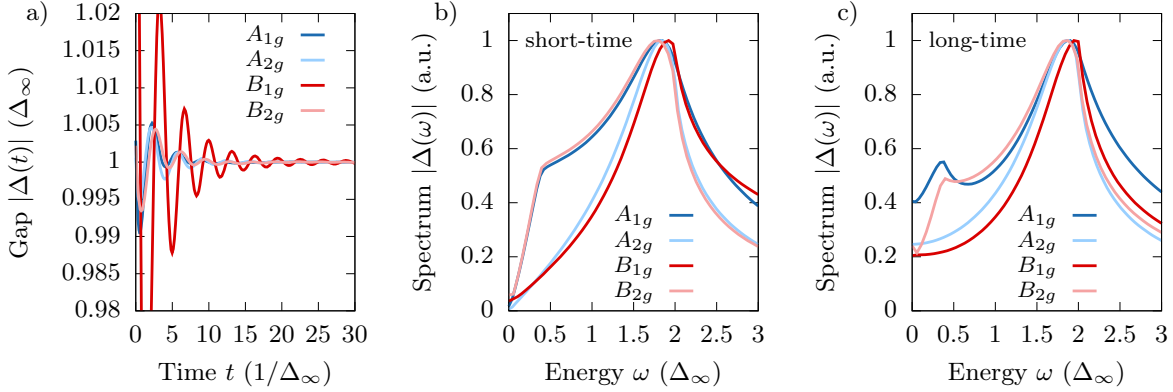


Figure 3.11 State quench of d -wave superconductor in the four different symmetry channels A_{1g} , A_{2g} , B_{1g} and B_{2g} with a strength of $g = 0.2$. a) Gap oscillations b) Spectrum of oscillations over the whole time range. For the A_{1g} and B_{2g} quench, a pronounced kink at $\omega \approx 0.4\Delta_\infty$ is visible in addition to the peak at $\omega \approx 2\Delta_\infty$. c) Spectrum of oscillations in the long-time limit $t \gtrsim 15$. The low-lying kink becomes a visible peak. All times and energies are normalized to the respective Δ_∞ for each quench. Details about the numerics and the used parameters can be found in appendix A.

3.2.3 Quench Strength Dependence

From the interaction quench strength analysis, we already know that the “usual” Higgs mode has an energy of $\omega_H = 2\Delta_\infty$, where $2\Delta_\infty$ is the asymptotic long-time value of the gap. The energy of the Higgs mode therefore decreases for increasing quench strength as more energy is pumped into the system, which reduces the gap. The same is true in the state quench case, which one can see in the expression Eq. (3.75) in the linear analysis where $\Delta_\infty \approx \Delta_q$. As in the interaction quench case, an expression $\sqrt{4\Delta_q^2 f^2 + s^2}$ occurs, which creates the $2\Delta_\infty$ peak in the spectrum. A possible second peak is controlled by the expression $\sqrt{4\Delta_q^2 f^2 - 4\Delta^2 (f^{\text{mod}})^2 + s^2}$. For $g = 0$, the expression $4\Delta_q^2 f^2 - 4\Delta^2 (f^{\text{mod}})^2$ vanishes and scales with g for increasing quench strength. Therefore, one can expect a second mode appearing at zero energy, which increases in energy for increasing quench strength.

As a rough estimate, we fit a two frequency oscillation like Eq. (3.49) to the oscillations of a d -wave order parameter quenched in the A_{1g} channel, whose spectrum shows a two-peak structure (Fig. 3.11). The result for varying quench strength g can be found in Fig. 3.12. Using the simple two frequency fit formula yields accurate results for Δ_∞ and ω_{H1} and ω_{H2} . Hereby, the identity $2\Delta_\infty = \omega_{H1}$ is fulfilled, where Δ_∞ decreases for increasing quench strength g . As expected, the frequency of ω_{H2} increases for increasing quench strength as the difference between the gap and modified symmetry increases. For large enough quench strength, the second mode approaches the $2\Delta_\infty$ Higgs mode and merges; however, a clear answer about the behavior cannot be given from the fit data as for higher quenches, a fit is no longer reliable. In Fig. 3.12b), all other fit parameters are shown. The result is unusable. While the frequencies can be captured rather well by the simple formula, amplitudes, decay rates and phase cannot, i.e. one would have to use a multiple frequency fit to model the dynamic more accurately. Nevertheless, one can draw the conclusion that the decay rates are typically higher at about $n \approx 3$ compared to the interaction quench case with $n \approx 2$. This can also be seen directly in the oscillations in Fig. 3.11a).

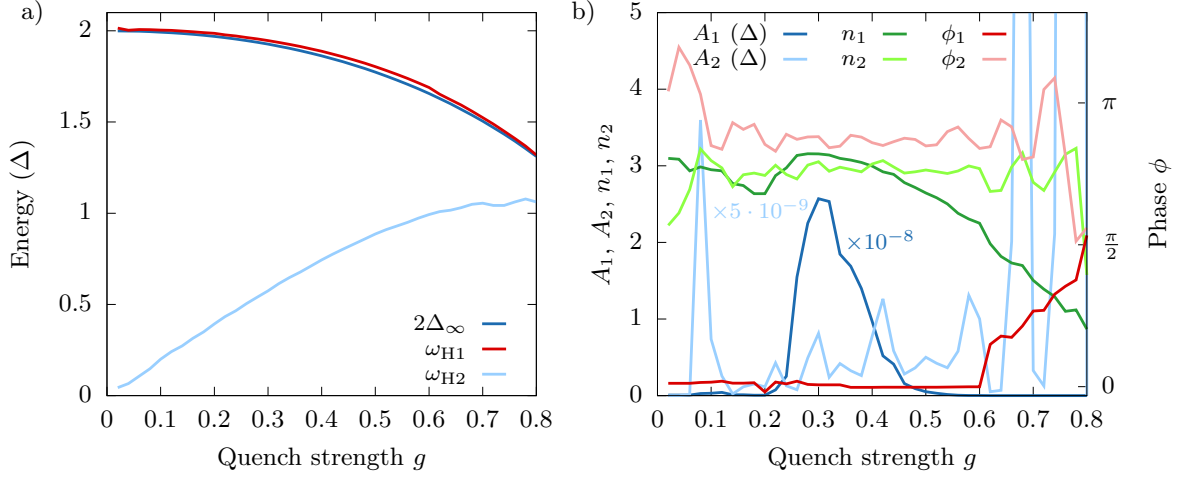


Figure 3.12 Fit of gap oscillations of d -wave order parameter quenched in the A_{1g} channel for varying quench strength g using a two frequency formula Eq. (3.49) in a range $t \gtrsim 15$. a) Fit parameters Δ_∞ , ω_{H1} and ω_{H2} . The identity $2\Delta_\infty = \omega_{H1}$ holds rather accurately. b) Fit parameters A_1 , A_2 , ϕ_1 , ϕ_2 , n_1 , n_2 . The two frequency fit formula is too simple to capture the dynamic, which leads to erratic fit results. Details about the numerics and the used parameters can be found in appendix A.

To study the energy of the Higgs modes in more detail, we plot the Fourier transform of the oscillations for all quench channels as a function of the quench strength g in Fig. 3.13. Hereby, we concentrate on the longtime limit, where the peaks are more pronounced. The behavior of the analysis with the simple two-frequency fit can clearly be seen. In the A_{1g} and B_{2g} cases, a low-lying Higgs mode starting at $\omega = 0$ for $g = 0$ is visible, whose energy increases for increasing quench strength. At the same time, the energy of the $2\Delta_\infty$ Higgs mode decreases until it merges with the second Higgs mode. For the A_{2g} and B_{1g} quenches, there is always only one peak visible.

To see whether the analytic formula Eq. (3.74) captures the discussed behavior, we evaluate the formula exemplarily for d -wave symmetry with an A_{1g} quench in Fig. 3.14. The formula fits nearly perfectly for high frequencies, even for the chosen quench strengths beyond the linear approximation. At low frequencies, the formula also captures the low-lying Higgs mode and its shift to higher frequencies for increasing quench strength. There are deviations in the low frequencies regime, which are a result of errors from the numerical evaluation of the integrals in Eq. (3.75). The integrands are not well-behaved and problematic to evaluate and one has to take special care of poles in the integration range.

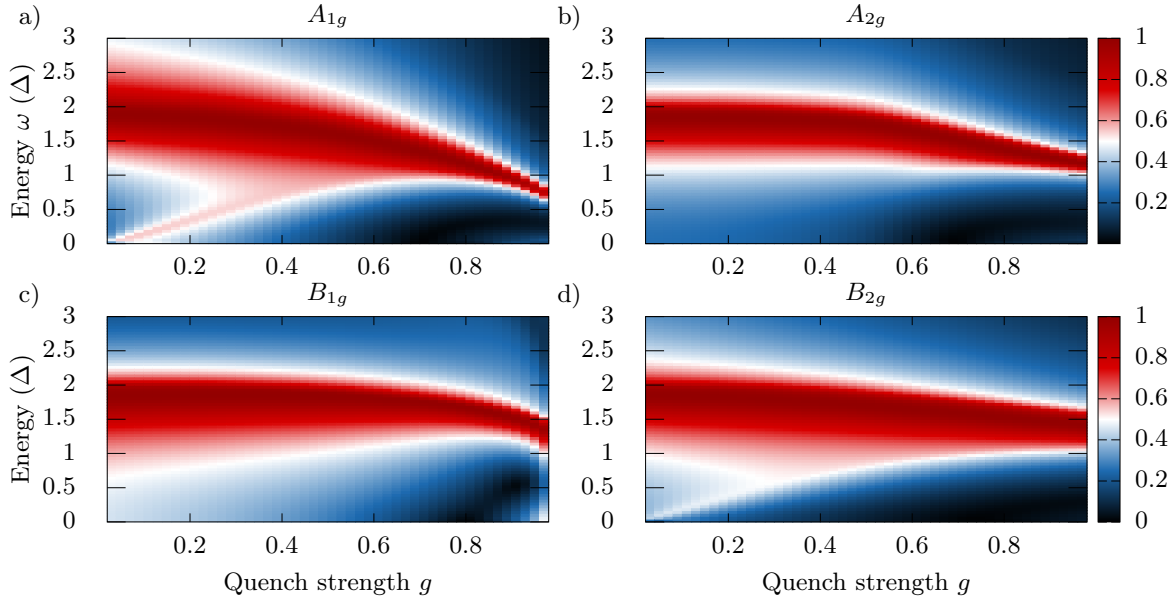


Figure 3.13 Spectrum of Higgs oscillations of d -wave superconductor after state quench in a) A_{1g} , b) A_{2g} , c) B_{1g} and d) B_{2g} channel for varying quench strength g . The Fourier transform is performed in the longtime limit for $t \gtrsim 15$. In the A_{1g} and B_{2g} case, a second low-lying Higgs mode is visible, whose energy increases for increasing quench strength and merges with the $2\Delta_\infty$ Higgs mode. Details about the numerics and the used parameters can be found in appendix A.

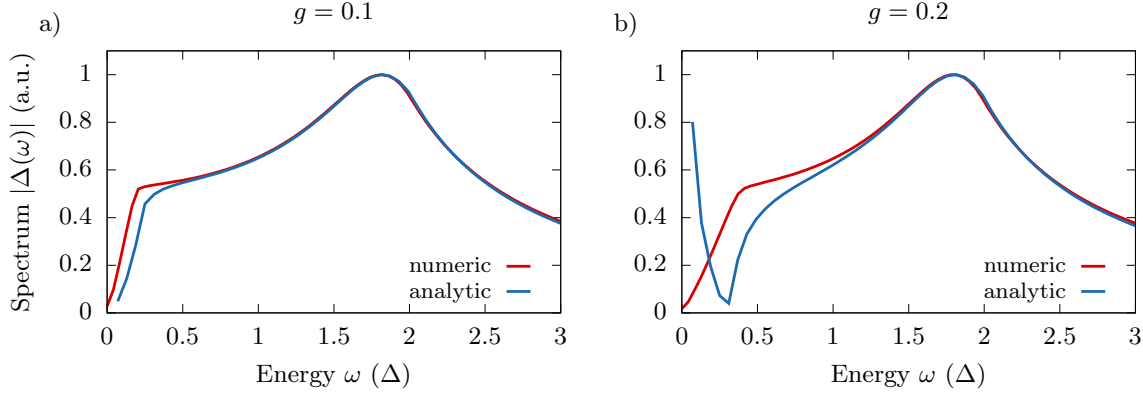


Figure 3.14 Comparison of the analytic formula for the state quench Eq. (3.74) with the numerical result, exemplarily evaluated for d -wave gap symmetry with an A_{1g} quench for two different quench strengths. The formula fits the numeric result well for high frequencies and also captures the low-lying Higgs mode and its shift to higher energies for increasing quench strength even for the strong quench strengths beyond the linear analysis. The observed deviations in the low frequency regime result from the approximation of the analytic formula as well as numerical instabilities while evaluating the integrals in Eq. (3.75). Details about the numerics and the used parameters can be found in appendix A.

3.2.4 Time Evolution of the Condensate

To gain a deeper understanding of the dynamic induced by the state quenches, we will have a closer look at the condensate itself, i.e. we will study the time evolution of $\langle c_{-\mathbf{k}\downarrow} c_{\mathbf{k}\uparrow} \rangle (t)$. As noted in Eq. (3.62), this expectation value far from k_F gives a rough estimate of the shape of the symmetry function $f_{\mathbf{k}}$. Values close to k_F have the same symmetry (nodal structure and sign) but a different shape. As an example, in equilibrium $\langle c_{-k_F\downarrow} c_{k_F\uparrow} \rangle = \frac{1}{2} \text{sgn}(f(\varphi))$, i.e. the expectation values have the same signs and nodal lines as a function of φ but no longer the shape of $f(\varphi)$. In the previous sections, it was stated that the condensate will oscillate around its equilibrium value, where we already introduced a naming scheme for the oscillations. Now, we will confirm this ad hoc definition.

To this end, we quench a d -wave order parameter exemplarily and extract the expectation value $\langle c_{-\mathbf{k}\downarrow} c_{\mathbf{k}\uparrow} \rangle (t)$. The result at different time steps can be seen in Fig. 3.15. We plot this expectation value as a function of the polar angle φ in a polar plot for two fixed values of $k = |\mathbf{k}|$, one far away from the Fermi level, i.e. $k \ll k_F$, and one close to the Fermi level, i.e. $k \approx k_F$. From the pseudospin analysis, we know that each point in momentum space oscillates with a frequency of $\omega_p = 2\sqrt{\epsilon_{\mathbf{k}}^2 + \Delta_{\infty}^2 f_{\mathbf{k}}^2}$. Thus, it follows that for $k \approx k_F$, the oscillation frequency is $\omega_p \approx 2\Delta_{\infty} |f_{\mathbf{k}}|$, whereas for $k \ll k_F$ the oscillation frequency is $\omega_p \approx 2|\epsilon_{\mathbf{k}}|$.

First, let us concentrate on an A_{1g} quench (Fig. 3.15a) and b)). Here, we can clearly see that the quench increases the positive lobe (red part) and decreases the negative lobe (blue part) compared to the equilibrium shape (grey curve). After half of the oscillation period $T = 2\pi/\omega_p$, the situation is exactly reversed. Now, the negative lobe has increased while the positive lobe has decreased for $k \ll k_F$. This continues for progressing time, corresponding exactly to the oscillating $B_{x^2-y^2}^{1g}$ oscillations, shown schematically in Fig. 3.10. For $k \approx k_F$, the shape approaches $\frac{1}{2} \text{sgn}(f(\varphi))$ as shown before; however, an increase of the positive lobe can also be seen directly after the quench. For progressing time, an oscillation is hardly visible, which is due to the fact that the oscillation amplitude at k_F approaches zero. This can be seen, for example, in the solution for $x_{\mathbf{k}}(s)$ in the linear analysis in Eq. (3.70). The term scales with ϵ^2 , which results in a vanishing for $k \rightarrow k_F$.

For the B_{1g} quench (Fig. 3.15c) and d)), the situation is analogous. The quench rotates all lobes in one direction and the following oscillation consists of a rotating $A_{x^2-y^2}^{2g}$ mode.

The distortions seen for longer times in Fig. 3.15b) and d) have two causes. On the one hand, there are high-frequency oscillation artifacts introduced by the finite energy cutoff in the numerical simulation (see Appendix A for more details). On the other hand, a distortion is also intrinsic. As the frequency is $\omega_p = 2\sqrt{\epsilon_{\mathbf{k}}^2 + \Delta_{\infty}^2 f_{\mathbf{k}}^2}$, there is of course also an angular dependence of the frequency, which leads to an oscillation with different frequency at different angles. The calculation is performed for a dispersion $\epsilon_{\mathbf{k}} = \epsilon(|k|)$, where the only angular dependence stems from $f(\varphi)$. Thus, as shown above, for $k \ll k_F$, the angular influence is smaller, whereas for $k \approx k_F$, a stronger distortion due to multiple frequency oscillation occurs.

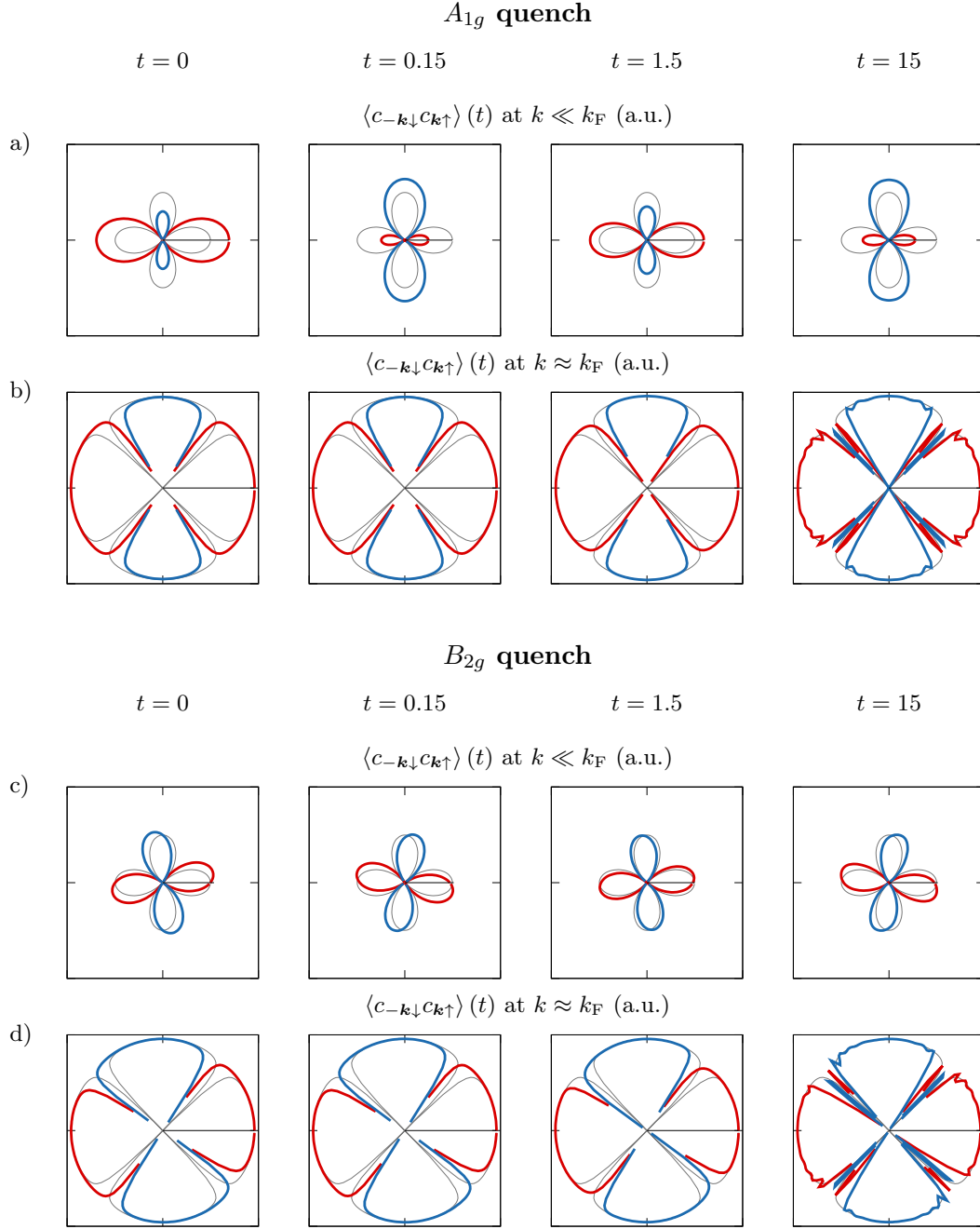


Figure 3.15 Snapshots of time evolution of the condensate $\langle c_{-\mathbf{k}\downarrow} c_{\mathbf{k}\uparrow} \rangle$ at $k \ll k_F$ for a),c) and $k \approx k_F$ for b),d) for d -wave superconductor after A_{1g} and B_{2g} quenches with $g = 0.4$. The expectation value is plotted as polar plot, where positive parts are colored red and negative parts are colored blue. The equilibrium shape is shown as a thin grey line. For $k \ll k_F$, the oscillation period is $T = \frac{2\pi}{\omega_p} = \frac{2\pi}{2\sqrt{\epsilon_k^2 + \Delta_\infty^2} f_k^2} \approx 0.15$, whereas for $k \approx k_F$, the oscillation period is $T \approx 3$. For $k \approx k_F$, the oscillation is hardly visible as the amplitude of the oscillation is much smaller than for $k \ll k_F$. The oscillating $B_{x^2-y^2}^{1g}$ oscillation can clearly be seen for the A_{1g} quench and the rotating $A_{x^2-y^2}^{2g}$ oscillation for the B_{2g} quench. All times are given in units of $1/\Delta_\infty$. Details about the numerics and the used parameters can be found in appendix A.

3.2.5 Temperature Dependence

So far, all calculations have been performed for zero temperature. In this section, the effect of finite temperature will be investigated. According to the BCS gap equation, the temperature dependence of the gap reads

$$\Delta_T = V \sum_{\mathbf{k}} f_{\mathbf{k}} \frac{\Delta_T f}{2E_{\mathbf{k}}} \tanh\left(\frac{E_{\mathbf{k}}}{2k_{\text{B}}T}\right). \quad (3.77)$$

This equation cannot be solved analytically, but has to be evaluated iteratively. For $T \approx 0$ or near the critical temperature $T \approx T_c$, approximate formulas can be derived [114, 178]. For the whole temperature range, there exists an interpolation formula

$$\Delta_T = \Delta \tanh\left(\kappa \sqrt{\frac{T_c}{T}} - 1\right), \quad (3.78)$$

where κ is a parameter depending on the gap symmetry. As the gap decreases with increasing temperature, we obviously expect the energy of the usual Higgs mode $\omega_{\text{H}} = 2\Delta_{\infty}$ to follow the same temperature dependence.

For the low-lying Higgs modes resulting from the asymmetric oscillations, the temperature dependence is not obvious. Keeping the temperature dependence and performing the same analysis as in section 3.2.1, we end up with a similar result except that in Eq. (3.73), the temperature dependence factor $\tanh\left(E_{\mathbf{k}}^{\text{mod}}/(2k_{\text{B}}T)\right)$ occurs in the integrand. This prevents an analytic evaluation of the ϵ integral.

In Fig. 3.16, a numerical evaluation of the temperature dependence of the oscillations spectrum is shown exemplarily for d -wave symmetry with an A_{1g} quench for two different quench strengths. As expected, the $2\Delta_{\infty}$ Higgs mode follows the temperature dependence of the gap, shown as a solid black line, exactly. For the low-lying Higgs mode, the behavior is exactly the opposite. For increasing temperature, the energy increases until it merges with the $2\Delta_{\infty}$ Higgs mode. The behavior looks similar as for increasing quench strength in Fig. 3.13 and is also qualitatively the same for different gap and quench symmetries. Thus, we can conclude that finite temperature increases the energy of the asymmetric Higgs modes until they merge with the upper Higgs mode. Low temperatures are therefore advantageous for the visibility of a distinct low-lying Higgs mode.

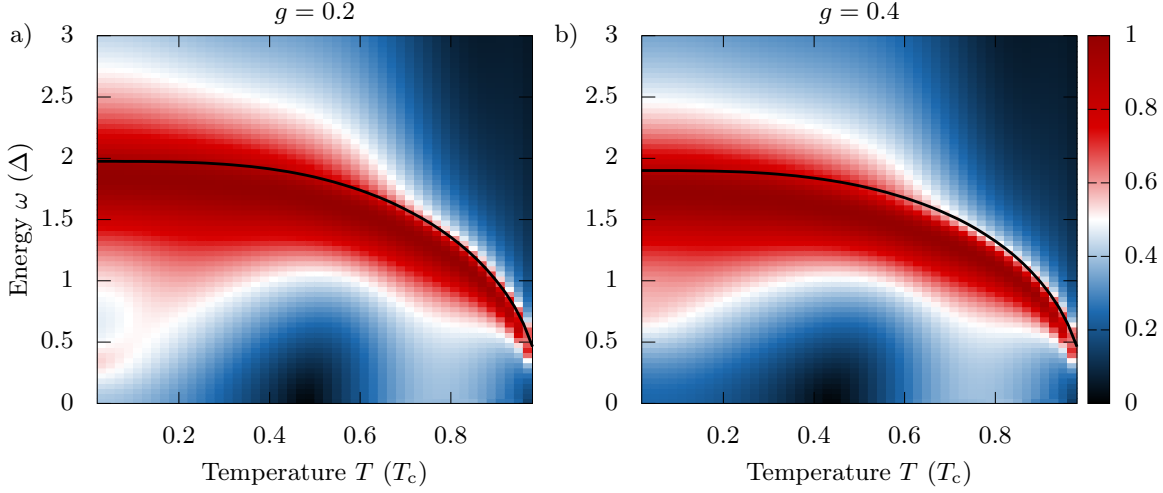


Figure 3.16 Spectrum of Higgs oscillations of d -wave superconductor after A_{1g} state quench for a) $g = 0.2$ and b) $g = 0.4$ as a function of temperature T . As a comparison, the black curve is the numerically calculated $\Delta(0) = \Delta_q$ for finite T . It can be rather accurately described by Eq. (3.78), using $\kappa = 1.68$ and replacing the equilibrium Δ with the quenched value Δ_q for $T = 0$. The Fourier transform is performed in the longtime limit for $t \gtrsim 15$. For finite T , the order parameter is reduced, leading to a decrease of the 2Δ Higgs mode. In contrast, the energy of the low-lying Higgs mode is increased for finite temperature. Details about the numerics and the used parameters can be found in appendix A.

3.2.6 Classification and Characterization of Higgs Oscillations

As we have seen in the previous sections, quenches, which change the symmetry of the superconducting condensate with respect to the ground state, induce asymmetric oscillations, which can be classified according to the irreducible representation of the lattice point group of the system. Whether these asymmetric oscillations show up as additional Higgs modes depends on the specific change of the symmetry, e.g. whether nodal lines between positive and negative lobes are shifted due to the quench. There is no general rule and different systems have to be studied case by case.

To study this systematically, we quench an s -wave, $g_{xy(x^2-y^2)}$ -wave, $d_{x^2-y^2}$ -wave, d_{xy} -wave, $s_{(x^2-y^2)^2}$ -wave and $d+s$ -wave superconductor in all symmetry channels of the D_{4h} point group. The result can be seen in Fig. 3.17. It confirms the previous analysis. The $2\Delta_\infty$ mode is always present, i.e. A_{1g} oscillations are always excited independent of the quench. In the cases, where the quench symmetry deviates from the gap symmetry significantly, a low-lying mode can be observed. This can lead up to three modes for $d+s$ -wave as two modes are always present as seen before. The nodal $s_{(x^2-y^2)^2}$ -wave is a special case. It belongs to the A_{1g} representation, but has the same nodal structure as a d -wave. Here, the resulting Higgs modes depend on the exact shape of the symmetry function. For the chosen function $f(\varphi) = \cos(2\varphi)^2$, every quench different from the A_{1g} symmetry shows a second peak as the modified symmetry function $f_{\mathbf{k}}^{\text{mod}}$ has induced negative parts with shifted or new nodal lines. On the contrary, a function $f(\varphi) = |\cos(2\varphi)|$, which is also in the A_{1g} channel with the same nodal structure, shows only a second Higgs mode for the B_{2g} quench. Only in this case, a negative part is induced with shifted nodal lines, whereas for the other quenches, only the positive lobes are shifted, which does not lead to a second Higgs mode.

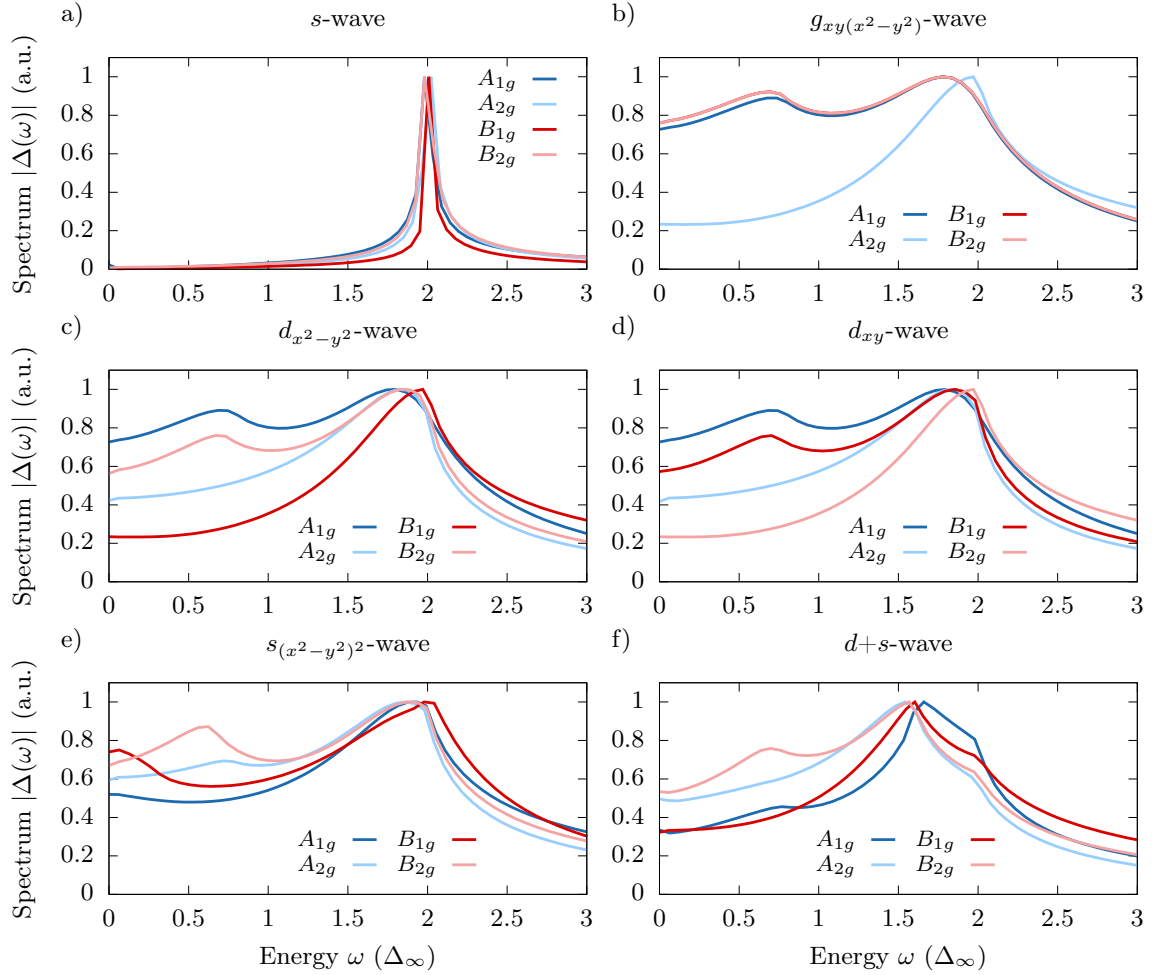


Figure 3.17 Spectrum of Higgs oscillations of a) s -wave, b) $g_{xy}(x^2-y^2)$ -wave, c) $d_{x^2-y^2}$ -wave, d) d_{xy} -wave, e) $s_{(x^2-y^2)^2}$ -wave, f) $d+s$ -wave superconductors after quenching in different symmetry channels. The symmetry functions are defined in Table 2.2. The quench strength is $g = 0.4$ and the Fourier transform is performed in the long-time limit. Details about the numerics and the used parameters can be found in appendix A.

The result is summarized in Table 3.2, where all the investigated gap symmetries are listed with all combinations of quench symmetries and the resulting condensate oscillations. In the last column, the expected number of observable Higgs modes is shown. A measurement of the time-resolved optical conductivity or the resonances in the third-harmonic generation signal can reveal the number of Higgs mode as it will be shown in chapters 4 and 5. Such a table can then be used to determine the underlying gap symmetry based on the number of observed modes. However, as the spectra are degenerate, a combination of multiple selected excitations is required to obtain an unique result. Whether and how these specific excitation can be realized experimentally will be discussed in later chapters, yet, this is still an open question for future research.

The derived fundamental oscillations in this chapter are general, even though the analysis has been performed by quenching the condensate explicitly in certain symmetry channels. With this procedure, it is possible to selectively excite the fundamental oscillations. Yet, any other excitation mechanism works as well, e.g. the experimental excitation with ultrashort THz laser pulses or driving a symmetry channel periodically. With such excitation schemes, the excitation is less selective and may result in a superposition of fundamental oscillation modes, which requires a more careful analysis.

In an optical experiment, the resulting condensate oscillations $\langle c_{-\mathbf{k}\downarrow} c_{\mathbf{k}\uparrow} \rangle(t)$ cannot be resolved directly as the response is determined by the momentum-summed quantity $\Delta(t)$. Therefore, these kinds of experiments can access only the information about the number and energy of Higgs modes. In contrast, angle-resolved photoemission experiments allow to gain information about the momentum resolution and with this, a direct observation of $\langle c_{-\mathbf{k}\downarrow} c_{\mathbf{k}\uparrow} \rangle(t)$ if performed time-resolved. This will be explored in more detail in section 4.2, where the actual condensate oscillation is observable in the spectral function.

One can perform such an analysis for any gap symmetry and quench symmetry and also extend it for multiband or triplet superconductors. In these cases, a multitude of new gap symmetries can be considered, such as s^{++} , s^{\pm} , $s + is$, $s + id$, $d + id$ as well as p or chiral $p_x + ip_y$ and much more. For these, multiple Higgs modes are expected independent of the quench [48–51, 112], namely one for each superconducting gap as well as a relative phase mode between coupled gaps (Leggett mode). However, quenched in a symmetry channel different from the ground state, one can expect an even richer spectrum in these cases. What exactly the spectrum looks like in these cases is an open question for further investigations.

3 Classification and Characterization of Higgs Modes


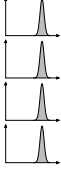

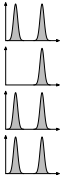

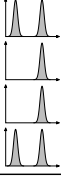

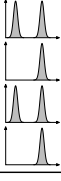

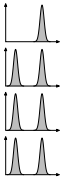

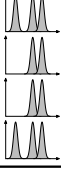
Gap symmetry $f_{\mathbf{k}}$	Quench symmetry $f'_{\mathbf{k}}$	Condensate oscillations $\langle c_{-\mathbf{k}\downarrow} c_{\mathbf{k}\uparrow} \rangle (t)$	Higgs modes
s 	1 $xy(x^2 - y^2)$ $x^2 - y^2$ xy	A_s^{1g} $A_s^{2g} + A_s^{1g}$ $B_s^{1g} + A_s^{1g}$ $B_s^{2g} + A_s^{1g}$	
$g_{xy(x^2-y^2)}$ 	1 $xy(x^2 - y^2)$ $x^2 - y^2$ xy	$A_{xy(x^2-y^2)}^{2g} + A_{xy(x^2-y^2)}^{1g}$ $A_{xy(x^2-y^2)}^{1g}$ $B_{xy(x^2-y^2)}^{2g} + A_{xy(x^2-y^2)}^{1g}$ $B_{xy(x^2-y^2)}^{1g} + A_{xy(x^2-y^2)}^{1g}$	
$d_{x^2-y^2}$ 	1 $xy(x^2 - y^2)$ $x^2 - y^2$ xy	$B_{x^2-y^2}^{1g} + A_{x^2-y^2}^{1g}$ $B_{x^2-y^2}^{2g} + A_{x^2-y^2}^{1g}$ $A_{x^2-y^2}^{1g}$ $A_{x^2-y^2}^{2g} + A_{x^2-y^2}^{1g}$	
d_{xy} 	1 $xy(x^2 - y^2)$ $x^2 - y^2$ xy	$B_{xy}^{2g} + A_{xy}^{1g}$ $B_{xy}^{1g} + A_{xy}^{1g}$ $A_{xy}^{2g} + A_{xy}^{1g}$ A_{xy}^{1g}	
$s_{(x^2-y^2)^2}$ 	1 $xy(x^2 - y^2)$ $x^2 - y^2$ xy	$A_{(x^2-y^2)^2}^{1g}$ $A_{(x^2-y^2)^2}^{2g} + A_{(x^2-y^2)^2}^{1g}$ $B_{(x^2-y^2)^2}^{1g} + A_{(x^2-y^2)^2}^{1g}$ $B_{(x^2-y^2)^2}^{2g} + A_{(x^2-y^2)^2}^{1g}$	
$d+s$ 	1 $xy(x^2 - y^2)$ $x^2 - y^2$ xy	$B_{d+s}^{1g} + A_{d+s}^{1g}$ $B_{d+s}^{2g} + A_{d+s}^{1g}$ A_{d+s}^{1g} $A_{d+s}^{2g} + A_{d+s}^{1g}$	

Table 3.2 Summary of condensate oscillations and expected Higgs modes for various gap symmetries. The first column depicts a certain gap symmetry. The second column lists all fundamental symmetries of the even parity basis functions of the D_{4h} point group used as quench symmetry. The third column lists the induced condensate oscillations. The fourth column shows a schematic picture of the number of expected Higgs modes. Table adapted from [7].

4 Higgs Spectroscopy with Quench-Probe Experiments

In the previous chapter, the superconductor has been quenched directly by changing either the interaction strength or the condensate abruptly. Interaction quenches are only possible in cold atom experiments, where the pairing interaction can be tuned by Feshbach resonances [120]. But this is not possible in superconductors in which no such tuning knob exists. However, in superconductors, the system can be excited by light pulses, which disturb the quasiparticle distribution. Hence, such experiments are an implementation of the proposed state quenches. The excitation with light pulses will be explored in the first part of this chapter. Furthermore, the time-resolved optical conductivity, which is measurable in a pump-probe experiment, is calculated to investigate whether the Higgs signal is observable in this quantity. In the second part of this chapter, the time-resolved ARPES signal is explored as another possible pump-probe setup. While THz pump-probe experiments on *s*-wave superconductors have already been performed to study Higgs oscillations in the optical response there are neither such experiments for unconventional systems nor THz tr-ARPES experiments even only for *s*-wave superconductors.

4.1 Time-resolved Optical Conductivity

We start by studying the coupling of light pulses to the condensate to simulate THz pump-probe experiments. We will see that for short enough pump pulses, the effect of the pulse resembles the effect of a state quench. Thus, we also name the pump pulse *quench pulse*. In addition to the induced gap oscillations, the time-resolved optical conductivity as a physically measurable quantity is also calculated, where the Higgs oscillations can be observed as well. Some parts of the calculation and discussion in this chapter have already been published in [7]. The used density matrix formalism applied to the BCS theory coupled to light is similar to the methods used e.g. in [28, 50, 52].

4.1.1 Coupling to Light and Equations of Motion

The light pulse is described by a vector potential $\mathbf{A}(\mathbf{r}, t)$, which relates to the electric field $\mathbf{E}(\mathbf{r}, t)$ via $\mathbf{E}(\mathbf{r}, t) = -\partial_t \mathbf{A}(\mathbf{r}, t)$. Here, we work in a gauge, in which the scalar potential $\phi(\mathbf{r}, t)$ is set to zero. The vector potential enters the Hamiltonian via minimal coupling $\mathbf{p} \rightarrow \mathbf{p} + e\mathbf{A}(\mathbf{r}, t)$ with the electron charge e . Assuming a quadratic dispersion $\epsilon(\mathbf{p}) = \frac{\mathbf{p}^2}{2m}$, the BCS Hamiltonian in second quantization coupled to the vector potential reads

$$H = H_{\text{BCS}} + H_{\text{em}}^{(1)} + H_{\text{em}}^{(2)}, \quad (4.1a)$$

$$H_{\text{em}}^{(1)} = \frac{e\hbar}{2m} \sum_{\mathbf{k}, \mathbf{q}, \sigma} (2\mathbf{k} + \mathbf{q}) \mathbf{A}_{\mathbf{q}}(t) c_{\mathbf{k}+\mathbf{q}, \sigma}^\dagger c_{\mathbf{k}, \sigma}, \quad (4.1b)$$

$$H_{\text{em}}^{(2)} = \frac{e^2}{2m} \sum_{\mathbf{k}, \mathbf{q}, \sigma} \left[\sum_{\mathbf{q}'} \mathbf{A}_{\mathbf{q}-\mathbf{q}'}(t) \cdot \mathbf{A}_{\mathbf{q}'}(t) \right] c_{\mathbf{k}+\mathbf{q}, \sigma}^\dagger c_{\mathbf{k}, \sigma}. \quad (4.1c)$$

Hereby, H_{BCS} is the BCS Hamiltonian in Eq. (2.31). A derivation of the expressions can be found in appendix B. For finite light momentum \mathbf{q} , the interaction terms couple off-diagonal

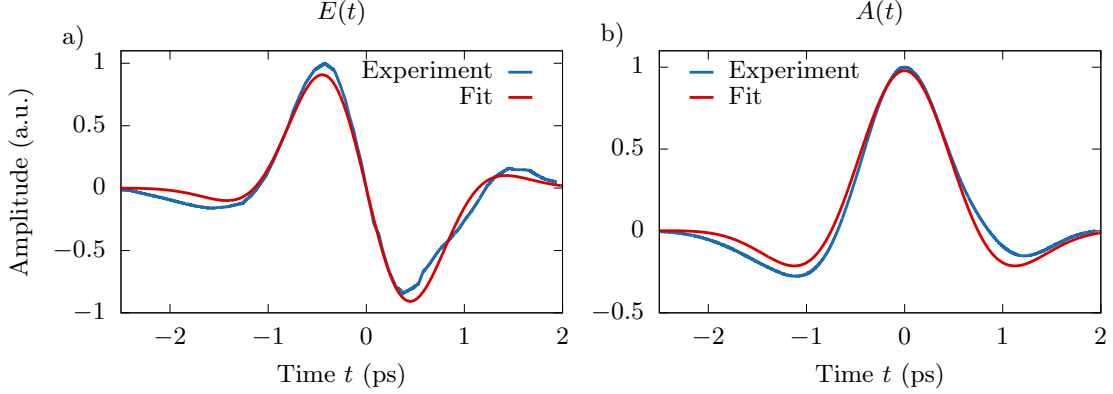


Figure 4.1 Fit of experimentally obtained single-cycle THz pulse with the Gaussian-shaped envelope pulse in Eq. (4.4). a) Electric field. b) Vector potential. The fit parameters are $\Omega = 1.38$ meV (0.33 THz) and $\tau = 1.72$ ps. Experimental data has been provided by Stefan Kaiser (MPI Stuttgart). Figure adapted from [7].

elements $(\mathbf{k}, \mathbf{k} + \mathbf{q})$, such that a description with only diagonal elements (\mathbf{k}, \mathbf{k}) in the Anderson pseudospin picture is not possible. In order to calculate the time dynamic, we use the density matrix formalism described in section 2.3.2. For this, it is advantageous to perform the Bogoliubov transformation Eq. (2.39) to calculate the dynamic of the Bogoliubov quasiparticle expectation values. After the transformation, the interaction part of the Hamiltonian reads

$$H_{\text{em}}^{(1)} = \frac{e\hbar}{2m} \sum_{\mathbf{k}, \mathbf{q}} (2\mathbf{k} + \mathbf{q}) \mathbf{A}_{\mathbf{q}}(t) \left(L_{\mathbf{k}, \mathbf{q}}^{(+)} \alpha_{\mathbf{k}+\mathbf{q}}^{\dagger} \alpha_{\mathbf{k}} - L_{\mathbf{k}, \mathbf{q}}^{(+)*} \beta_{\mathbf{k}}^{\dagger} \beta_{\mathbf{k}+\mathbf{q}} + M_{\mathbf{k}, \mathbf{q}}^{(-)*} \alpha_{\mathbf{k}+\mathbf{q}}^{\dagger} \beta_{\mathbf{k}}^{\dagger} + M_{\mathbf{k}, \mathbf{q}}^{(-)} \alpha_{\mathbf{k}} \beta_{\mathbf{k}+\mathbf{q}} \right), \quad (4.2a)$$

$$H_{\text{em}}^{(2)} = \frac{e^2}{2m} \sum_{\mathbf{k}, \mathbf{q}} \left[\sum_{\mathbf{q}'} \mathbf{A}_{\mathbf{q}-\mathbf{q}'}(t) \cdot \mathbf{A}_{\mathbf{q}'}(t) \right] \left(L_{\mathbf{k}, \mathbf{q}}^{(-)} \alpha_{\mathbf{k}+\mathbf{q}}^{\dagger} \alpha_{\mathbf{k}} + L_{\mathbf{k}, \mathbf{q}}^{(-)*} \beta_{\mathbf{k}}^{\dagger} \beta_{\mathbf{k}+\mathbf{q}} + M_{\mathbf{k}, \mathbf{q}}^{(+)*} \alpha_{\mathbf{k}+\mathbf{q}}^{\dagger} \beta_{\mathbf{k}}^{\dagger} - M_{\mathbf{k}, \mathbf{q}}^{(+)} \alpha_{\mathbf{k}} \beta_{\mathbf{k}+\mathbf{q}} \right) \quad (4.2b)$$

with the following abbreviations

$$L_{\mathbf{k}, \mathbf{q}}^{(\pm)} = u_{\mathbf{k}+\mathbf{q}} u_{\mathbf{k}}^* \pm v_{\mathbf{k}+\mathbf{q}} v_{\mathbf{k}}^*, \quad M_{\mathbf{k}, \mathbf{q}}^{(\pm)} = u_{\mathbf{k}+\mathbf{q}}^* v_{\mathbf{k}}^* \pm v_{\mathbf{k}+\mathbf{q}}^* u_{\mathbf{k}}^*. \quad (4.3)$$

For the calculation, one has to specify a certain functional form of the vector potential. To simulate ultrafast THz pump-probe experiments, a single-cycle pulse is required. We assume that the laser pulse has a Gaussian-shaped envelope in time. Therefore, we write

$$\mathbf{A}(\mathbf{r}, t) = \mathbf{A}_0 e^{-4 \ln(2) \left(\frac{t}{\tau}\right)^2} \cos(\Omega t - \mathbf{q}_0 \mathbf{r}). \quad (4.4)$$

with the central frequency Ω , wave momentum $|\mathbf{q}_0| = q_0 = \frac{\Omega}{c}$ and full width at half maximum τ of the Gaussian envelope. To confirm that the chosen form is reasonable, it is compared to the shape of an experimental pulse obtained from a THz laser pulse in Fig. 4.1. There is good agreement between the Gaussian shaped pulse and the experimental pulse shape. For the calculation, we

need the spatial Fourier representation of the vector potential

$$\begin{aligned}\mathbf{A}_q(t) &= \frac{1}{V} \int d^3\mathbf{r} \mathbf{A}(\mathbf{r}, t) e^{-i\mathbf{q}\mathbf{r}} \\ &= \mathbf{A}_0 e^{-4\ln(2)\left(\frac{t}{\tau}\right)^2} \left(\delta_{\mathbf{q},\mathbf{q}_0} e^{i\Omega t} + \delta_{\mathbf{q},-\mathbf{q}_0} e^{-i\Omega t} \right).\end{aligned}\quad (4.5)$$

The wave vector \mathbf{q}_0 and amplitude \mathbf{A}_0 are parameterized by spherical coordinates

$$\mathbf{q}_0 = -q_0 \hat{e}_r, \quad \mathbf{A}_0 = A_0 (\cos \chi \hat{e}_\vartheta + \sin \chi \hat{e}_\varphi) \quad (4.6)$$

with

$$\hat{e}_r = \begin{pmatrix} \sin \vartheta \cos \varphi \\ \sin \vartheta \sin \varphi \\ \cos \vartheta \end{pmatrix}, \quad \hat{e}_\varphi = \begin{pmatrix} -\sin \varphi \\ \cos \varphi \\ 0 \end{pmatrix}, \quad \hat{e}_\vartheta = \begin{pmatrix} \cos \vartheta \cos \varphi \\ \cos \vartheta \sin \varphi \\ -\sin \vartheta \end{pmatrix} \quad (4.7)$$

and the polarization angle χ . For the following calculations in two dimensions, we assume an in-plane wave vector, i.e. $\vartheta = \pi/2$, and fix the polarization to also be in-plane, i.e. $\chi = \pi/2$. This simplifies the expressions to

$$\mathbf{q}_0^\top = (\cos \varphi, \sin \varphi, 0), \quad \mathbf{A}_0^\top = E_0 (-\sin \varphi, \cos \varphi, 0) \quad (4.8)$$

with the single angular parameter φ determining the incident direction of the pulse. The integrated fluence of this pulse is given by $f_A = A_0^2 \tau$.

Using the density matrix formalism, we write down equations of motion for the four expectation values $\langle \alpha_{\mathbf{k}}^\dagger \beta_{\mathbf{k}'}^\dagger \rangle$, $\langle \alpha_{\mathbf{k}} \beta_{\mathbf{k}'} \rangle$, $\langle \alpha_{\mathbf{k}}^\dagger \alpha_{\mathbf{k}'} \rangle$ and $\langle \beta_{\mathbf{k}}^\dagger \beta_{\mathbf{k}'} \rangle$ occurring in the gap equation (2.50). Due to the bilinearity of the BCS Hamiltonian, they form a closed set of differential equations together with the gap equation. The equations of motion are derived by evaluating the commutator in Heisenberg's equation of motion, i.e.

$$\begin{aligned}\partial_t \langle \alpha_{\mathbf{k}}^\dagger \beta_{\mathbf{k}'}^\dagger \rangle(t) &= \frac{i}{\hbar} \langle [H, \alpha_{\mathbf{k}}^\dagger \beta_{\mathbf{k}'}^\dagger] \rangle(t), & \partial_t \langle \alpha_{\mathbf{k}} \beta_{\mathbf{k}'} \rangle(t) &= \frac{i}{\hbar} \langle [H, \alpha_{\mathbf{k}} \beta_{\mathbf{k}'}] \rangle(t), \\ \partial_t \langle \alpha_{\mathbf{k}}^\dagger \alpha_{\mathbf{k}'} \rangle(t) &= \frac{i}{\hbar} \langle [H, \alpha_{\mathbf{k}}^\dagger \alpha_{\mathbf{k}'}] \rangle(t), & \partial_t \langle \beta_{\mathbf{k}}^\dagger \beta_{\mathbf{k}'} \rangle(t) &= \frac{i}{\hbar} \langle [H, \beta_{\mathbf{k}}^\dagger \beta_{\mathbf{k}'}] \rangle(t).\end{aligned}\quad (4.9)$$

The resulting expressions are rather lengthy and the derivation can be found in appendix C. As an example, using the explicit expression for the vector potential in Eq. (4.5), the equation for $\langle \alpha_{\mathbf{k}}^\dagger \beta_{\mathbf{k}'}^\dagger \rangle$ reads

$$\begin{aligned}\partial_t \langle \alpha_{\mathbf{k}}^\dagger \beta_{\mathbf{k}'}^\dagger \rangle(t) &= \frac{i}{\hbar} \left\{ (R_{\mathbf{k}} + R_{\mathbf{k}'}) \langle \alpha_{\mathbf{k}}^\dagger \beta_{\mathbf{k}'}^\dagger \rangle - C_{\mathbf{k}}^* (\langle \beta_{\mathbf{k}'}^\dagger \beta_{\mathbf{k}} \rangle - \delta_{\mathbf{k},\mathbf{k}'}) - C_{\mathbf{k}'}^* \langle \alpha_{\mathbf{k}}^\dagger \alpha_{\mathbf{k}'} \rangle \right. \\ &+ \frac{e\hbar}{2m} \sum_{\mathbf{q}=\pm\mathbf{q}_0} 2\mathbf{k} \mathbf{A}_q(t) \left(L_{\mathbf{k},\mathbf{q}}^{(+)} \langle \alpha_{\mathbf{k}+\mathbf{q}}^\dagger \beta_{\mathbf{k}'}^\dagger \rangle + M_{\mathbf{k},\mathbf{q}}^{(-)} (\langle \beta_{\mathbf{k}'}^\dagger \beta_{\mathbf{k}+\mathbf{q}} \rangle - \delta_{\mathbf{k}+\mathbf{q},\mathbf{k}'}) \right. \\ &\quad \left. \left. - L_{\mathbf{k}',-\mathbf{q}}^{(+)} \langle \alpha_{\mathbf{k}}^\dagger \beta_{\mathbf{k}'-\mathbf{q}}^\dagger \rangle - M_{\mathbf{k}',-\mathbf{q}}^{(-)} \langle \alpha_{\mathbf{k}}^\dagger \alpha_{\mathbf{k}'-\mathbf{q}} \rangle \right) \right. \\ &+ \frac{e^2}{2m} \sum_{\mathbf{q}=0,\pm 2\mathbf{q}_0} \left[\sum_{\mathbf{q}'=\pm\mathbf{q}_0} \mathbf{A}_{\mathbf{q}-\mathbf{q}'}(t) \cdot \mathbf{A}_{\mathbf{q}'}(t) \right] \left(L_{\mathbf{k},\mathbf{q}}^{(-)} \langle \alpha_{\mathbf{k}+\mathbf{q}}^\dagger \beta_{\mathbf{k}'}^\dagger \rangle \right. \\ &\quad \left. + L_{\mathbf{k}',-\mathbf{q}}^{(-)} \langle \alpha_{\mathbf{k}}^\dagger \beta_{\mathbf{k}'-\mathbf{q}}^\dagger \rangle - M_{\mathbf{k},\mathbf{q}}^{(+)} (\langle \beta_{\mathbf{k}'}^\dagger \beta_{\mathbf{k}+\mathbf{q}} \rangle - \delta_{\mathbf{k}+\mathbf{q},\mathbf{k}'}) \right. \\ &\quad \left. \left. - M_{\mathbf{k}',-\mathbf{q}}^{(+)} \langle \alpha_{\mathbf{k}}^\dagger \alpha_{\mathbf{k}'-\mathbf{q}} \rangle \right) \right\}.\end{aligned}\quad (4.10)$$

For $\mathbf{q}_0 = 0$, one has $L_{\mathbf{k},0}^{(+)} = 1$ and $M_{\mathbf{k},0}^{(-)} = 0$, such that the linear coupling to \mathbf{A} vanishes. With $\mathbf{q}_0 \neq 0$, particle-hole symmetry is broken and a linear coupling due to the $\propto \mathbf{p}\mathbf{A}$ term is possible, which enhances the coupling of light to the condensate. Since \mathbf{q}_0 is small for a THz laser pulse (on the order of $\sim 10^{-5}k_F$), the effect is small but not completely negligible. In addition, the momentum couples elements $(\mathbf{k}, \mathbf{k} + \mathbf{q}_0)$, i.e. it populates off-diagonal elements of the density matrices. This can lead to asymmetric state quenches as we will see.

The equations of motion are implemented on a grid in momentum space. Details about the calculation and used parameters can be found in appendix A.3.

4.1.2 Induced Gap Oscillations by Quench Pulse

In this section, the dynamic induced by a single pump pulse will be explored. This pulse acts as a quench and the resulting gap oscillations will be calculated.

Quench vs. Adiabatic Excitation

The quenches of the previous chapter act instantaneously per definition. The system is altered suddenly. In contrast, an excitation with a pump pulse can never be instantaneous as any realistic pulse lasts for a certain time. In order to quench the system, the pulse must be shorter than the intrinsic timescale of the dynamic which shall be triggered. Otherwise, the change is adiabatic, during which the system always stays approximately in equilibrium describable by an effective temperature. The dynamic we want to observe is, of course, the oscillation of the gap. As a consequence, the pulse width τ should be smaller than the Higgs oscillation period, i.e. $\tau < T_H = h/(2\Delta)$ [28, 31, 33, 52, 181]. In the following, we will apply pulses of different widths to verify the quench and adiabatic excitation regimes.

In Fig. 4.2, the gap dynamic $\Delta(t)$ of an s - and d -wave superconductor is shown under the influence of pump pulses with different widths τ . For the widths of the pulses, we choose $\tau = 0.25T_H$, $\tau = T_H$, $\tau = 1.5T_H$, such that we are below, at and above the intrinsic time scale. Following literature [28, 31, 33, 52], we keep the fluence $f_A = A_0^2\tau$ constant (left column). We can clearly see that for the short pump pulse, Higgs oscillations are induced, whereas the long pulse only leads to an adiabatic change without inducing oscillations. This observation has already been made in previous theoretical studies and is well-known [28, 31, 33, 52, 181]. Here, we can see that it also holds for the d -wave case. Yet, this transition from the nonadiabatic to the adiabatic regime by increasing the pulse width is only valid for keeping the fluence constant. If we increase the pump fluence, e.g. by keeping the amplitude constant while increasing the pulse width, the picture changes. This can be seen in the right column of Fig. 4.2. In this case, also pulses with $\tau > T_H$ induce oscillations due to the increased pump energy. This can be contributed to the nonlinear effects by the quadratic coupling, which become more important for strong pulses [181]. Hence, the criterion $\tau < T_H = h/(2\Delta)$ is not a strict rule but rather a rule of thumb valid for lower fluence.

Additional Higgs Modes

We want to examine, whether a pump pulse can induce an additional Higgs mode below 2Δ as discussed in the previous chapter. We have seen that in order to excite one of these additional Higgs modes, a quench in a different symmetry channel is required. One possibility to control an asymmetric excitation is to vary the incident direction of the pump pulse with respect to

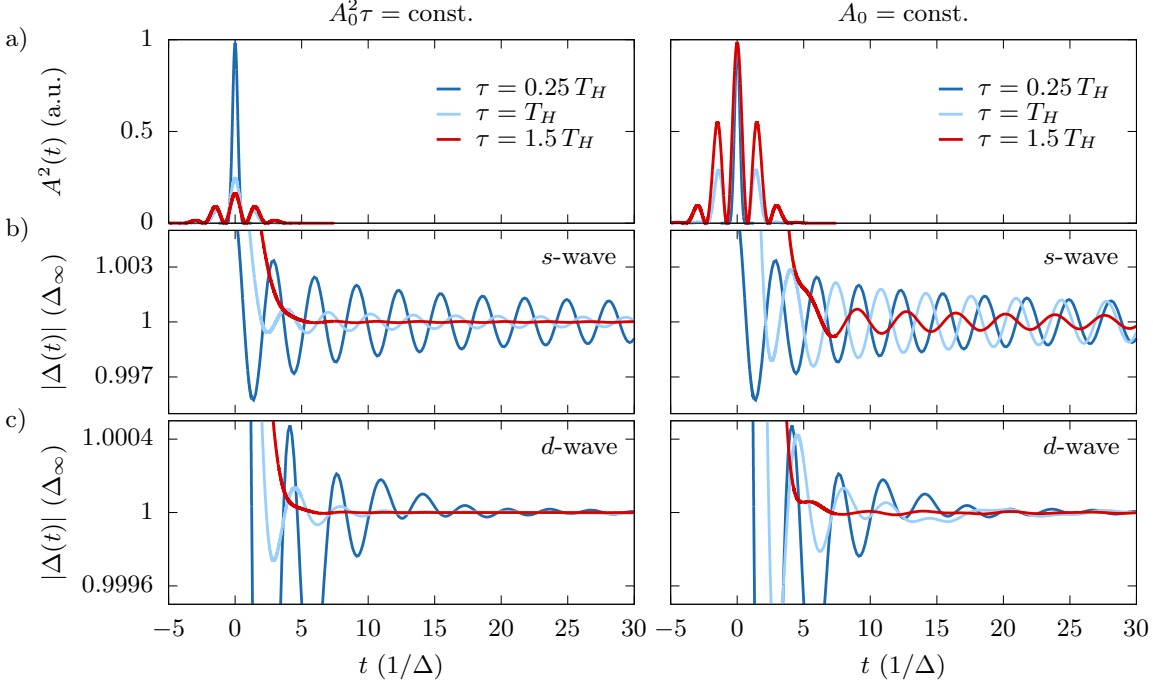


Figure 4.2 Gap dynamic induced by pump pulses of different widths. In the first column, the pump fluence $A_0^2\tau$ is kept constant, while in the second column, the amplitude A_0 of the vector potential is kept constant. a) Vector potential $A(t)^2$ given by Eq. (4.4). b) Gap dynamic of s -wave superconductor. c) Gap dynamic of d -wave superconductor. The energies are normalized individually to Δ_∞ for each calculation. Details about the parameters can be found in appendix A.3.

the gap symmetry. In the coupling term of the Hamiltonian in Eq. (4.1), one can see that the light momentum \mathbf{q}_0 introduces a preferred direction as points in momentum space \mathbf{k} are coupled with $\mathbf{k} + \mathbf{q}_0$. Thus, a change in symmetry can be expected, which is controllable by changing the incident angle φ . In Fig. 4.3, the gap oscillations induced by a pulse with varying angles φ are shown for s -, d - and $d+s$ -wave. For s -wave (Fig. 4.3a)), all directions are equivalent; there is no φ dependence and the gap oscillates with a single frequency of $2\Delta_\infty$. For d -wave (Fig. 4.3b)), a second peak below 2Δ is observable for $\varphi = 0$. Rotating the incident angle to $\varphi = \pi/4$, the second peak vanishes. In the case of $d+s$ -wave (Fig. 4.3c)), a three-peak structure is visible for $\varphi = 0$, which turns into a two-peak structure for $\varphi = \pi/4$. These findings fit the previous results perfectly. In the case of $\varphi = 0$, the pulse quenches the positive lobes differently compared to the negative lobes as the lobe axes are parallel or perpendicular to the pulse directions. This changes the original ground state symmetry and induces asymmetric oscillations of the condensate, which lead to a second Higgs mode in the spectrum. For $\varphi = \pi/4$, the effect of the pump pulse is the same for both lobes as the incident direction is exactly in between both lobes along the nodal lines. Hence, the condensate oscillates symmetrically and no second Higgs mode is visible. For other angles, the change in symmetry is less than for $\varphi = 0$, which shifts the second Higgs mode to lower energies. For $d+s$ -wave, the same effect occurs leading to a low-lying Higgs mode for $\varphi = 0$, in addition to the always present two-peak structure due to the lobes of different sizes as discussed in the previous chapter.

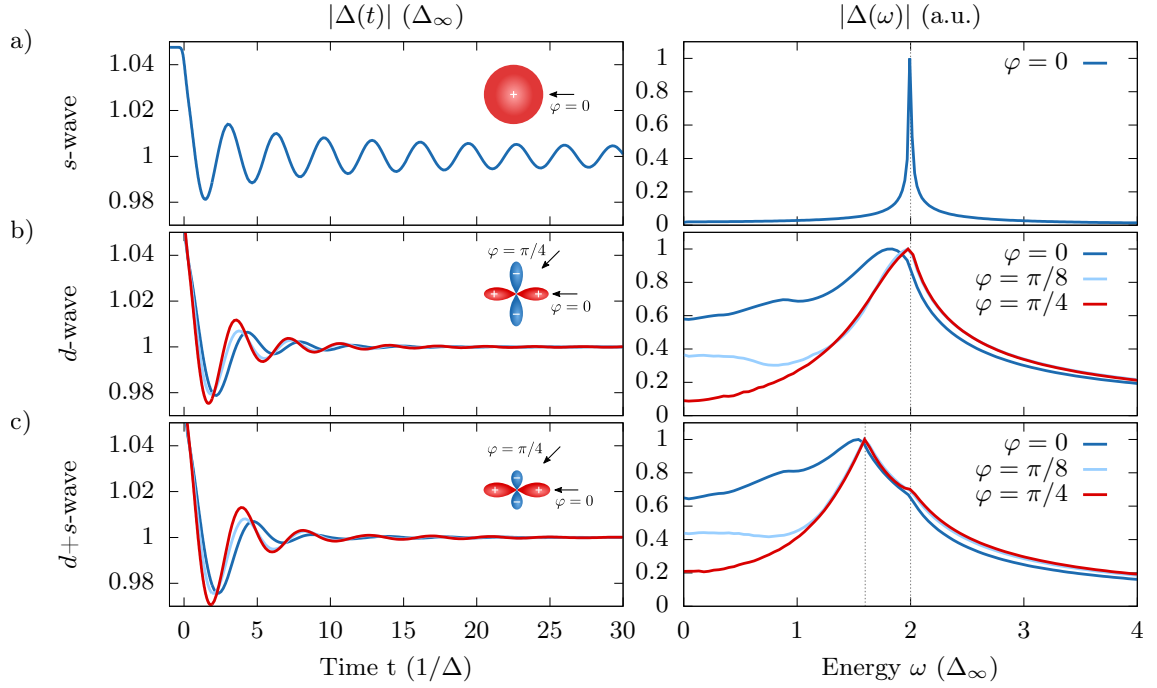


Figure 4.3 Gap oscillations of a) *s*-wave, b) *d*-wave, c) *d+s*-wave superconductor excited by a pump pulse with different incident direction φ . For *s*-wave, only the 2Δ Higgs mode is excited independently of φ . For *d*-wave, a second low-lying Higgs mode is visible for $\varphi = 0$. For *d+s*-wave, there are always two Higgs modes as a result of the lobes with different sizes. For $\varphi = 0$, a low-lying Higgs mode is visible. Details about the parameters can be found in appendix A.3.

Fluence Dependence

In analogy to section 3.2.3, where the quench strength dependence on the Higgs modes has been investigated, we will investigate the fluence dependence on the Higgs modes. To this end, the amplitude A_0 of the pump pulse is varied at constant pulse width and the resulting oscillations for an *s*-, *d*- and *d+s*-wave superconductor are calculated. The spectrum of the oscillations can be found in Fig. 4.4. The resulting energy dependence curves resemble the result of the quench analysis in Fig. 3.13 closely. For increasing fluence, the gap is suppressed, leading consequently to a reduction of the energy of the 2Δ Higgs mode. As in the quench case, the energy of the low-lying Higgs mode, resulting from the asymmetric oscillation of the condensate, increases in energy for increasing pump fluence. This confirms again that the effect of the pump pulse is captured closely by the state quench.

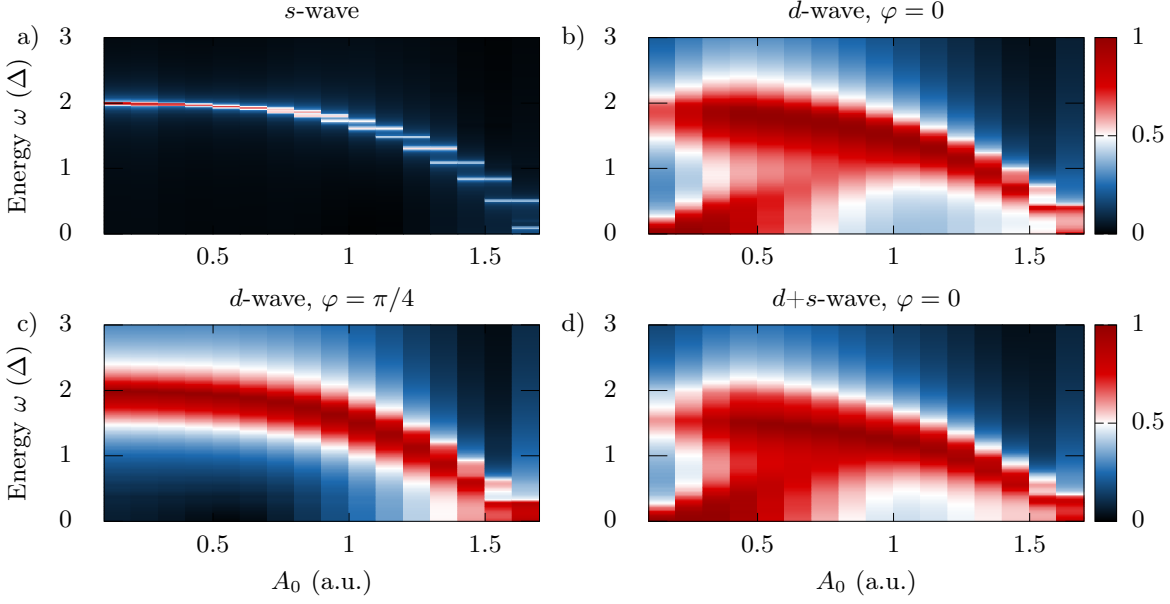


Figure 4.4 Fluence dependence of Higgs modes for a) *s*-wave, b) *d*-wave pumped in $\varphi = 0$ direction, c) *d*-wave pumped in $\varphi = \pi/4$ direction, d) *d+s*-wave pumped in $\varphi = 0$ direction. Please note that, as can be seen in Fig. 4.3c), the peak at $2\Delta_\infty$ is rather a kink, which makes the always present two-peak structure difficult to see in the *d+s*-wave case. Details about the parameters can be found in appendix A.3.

4.1.3 Higgs Oscillations in the Optical Conductivity

To measure the induced gap oscillations, a pump-probe experiment can be performed. Hereby, a second probe pulse is applied after the pump pulse. The intensity of the probe pulse should be weak, such that it does not disturb the system and induce an additional nonlinear dynamic. Its purpose is to capture the instantaneous state of the system measurable as the linear optical response. By repeating the experiment with varying time delay t_{pp} between pump and probe pulse, the dynamic of the system can be scanned. This is depicted schematically in Fig. 4.5.

In linear response, the optical conductivity $\sigma(\omega)$ is defined by

$$\mathbf{j}_q(\omega, t_{pp}) = \sigma_q(\omega, t_{pp}) \mathbf{E}_q(\omega, t_{pp}) = -i\omega \sigma_q(\omega, t_{pp}) \mathbf{A}_q(\omega, t_{pp}), \quad (4.11)$$

where we use $\mathbf{E}_q(t) = -\frac{\partial \mathbf{A}_q(t)}{\partial t}$ or $\mathbf{E}_q(\omega) = -i\omega \mathbf{A}_q(\omega)$. With $\mathbf{A}_q(\omega) = A_q(\omega) \hat{e}_A$ and $|\hat{e}_A| = 1$, we obtain for the optical conductivity

$$\sigma_q(\omega, t_{pp}) = \frac{\mathbf{j}_q(\omega, t_{pp}) \hat{e}_A}{-i\omega A_q(\omega, t_{pp})}. \quad (4.12)$$

In this expression, the pump-probe delay t_{pp} is a variable parameter, for which the calculation is repeated. This time delay is chosen such that pump and probe pulse do not overlap.

The current $\mathbf{j}_q(t) = \mathbf{j}_q^{(1)}(t) + \mathbf{j}_q^{(2)}(t)$ consists of two terms, where the second term $\mathbf{j}_q^{(2)}(t) \propto A(t)$ can be neglected as it only leads to an offset in the imaginary part of the conductivity [28]. The

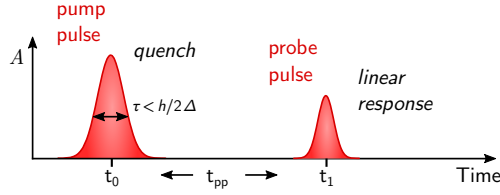


Figure 4.5 Schematic picture of a pump-probe experiment. The pump pulse is applied at time t_0 and acts as a quench to trigger the nonequilibrium dynamic. After a variable time delay t_{pp} , a second weak probe pulse is applied at time t_1 to measure the instantaneous state of the system.

first term expressed in the Bogoliubov quasiparticles reads (see appendix D for a derivation)

$$\begin{aligned} \mathbf{j}_q^{(1)} = & -\frac{e\hbar}{2mV} \sum_{\mathbf{k}} (2\mathbf{k} + \mathbf{q}) \left(L^{(+)*} \alpha_{\mathbf{k}}^\dagger \alpha_{\mathbf{k}+\mathbf{q}} - L^{(+)} \beta_{\mathbf{k}+\mathbf{q}}^\dagger \beta_{\mathbf{k}} \right. \\ & \left. - M^{(-)*} \alpha_{\mathbf{k}}^\dagger \beta_{\mathbf{k}+\mathbf{q}}^\dagger - M^{(-)} \alpha_{\mathbf{k}+\mathbf{q}} \beta_{\mathbf{k}} \right). \end{aligned} \quad (4.13)$$

In Fig. 4.6, the time-resolved optical conductivity is shown for s -, d - and $d+s$ -wave superconductors for different pumping angles φ . Details of the numerical calculation can be found in appendix A.3. For s -wave, the conductivity is independent of the angle φ . The real part of the optical conductivity σ_1 is peaked at the energy $2\Delta_\infty$ (Fig. 4.6a)). As a function of the time delay t_{pp} , one can clearly see an oscillation in the amplitude, both at the peak maximum (black curve) and next to it (dark and bright red curve). The Fourier spectrum along the shown three cuts at fixed energy ω are shown in the lower part in comparison to the spectrum of the gap oscillation (blue curve). One can observe that the oscillation frequency of the optical conductivity coincides with the Higgs oscillation frequency at $2\Delta_\infty$. Yet, as the time evolution of the optical conductivity is restricted due to high computational costs, the resolution of the spectrum is lower compared to the spectrum of the gap oscillation.

As shown before, the dynamic in the d -wave case depends on the pumping angle φ . Examples for $\varphi = \pi/4$ and $\varphi = 0$ are shown in Fig. 4.6b) and c). For $\varphi = \pi/4$, the real part of the optical conductivity is peaked at $2\Delta_\infty$; however, the peak is slightly broader. There are oscillations visible as a function of the time delay and a Fourier transform along cuts at fixed energy reveals again a single Higgs oscillation frequency as expected for d -wave pumped at $\varphi = \pi/4$. For $\varphi = 0$, the real part of the optical conductivity has spectral weight at $\omega = 2\Delta_\infty$ again but, in addition, also weight below delta at $\omega \approx 0.9\Delta$, which corresponds roughly to the second observed Higgs mode for the chosen pump fluence. We can understand this in such a way that the superconductor not only absorbs light at the usual 2Δ Higgs mode but also at a lower energy corresponding to the second Higgs mode. The optical conductivity also exhibits oscillations in the time delay t_{pp} . The spectrum shown in Fig. 4.6c) clearly shows a two-peak structure, which coincides with the two-peak structure of the gap oscillation spectrum. The same behavior is observable for the $d+s$ -wave case (Fig. 4.6d)). Here, a three-peak structure is visible, both in the real part of the optical conductivity and in the spectrum of the time-resolved optical conductivity.

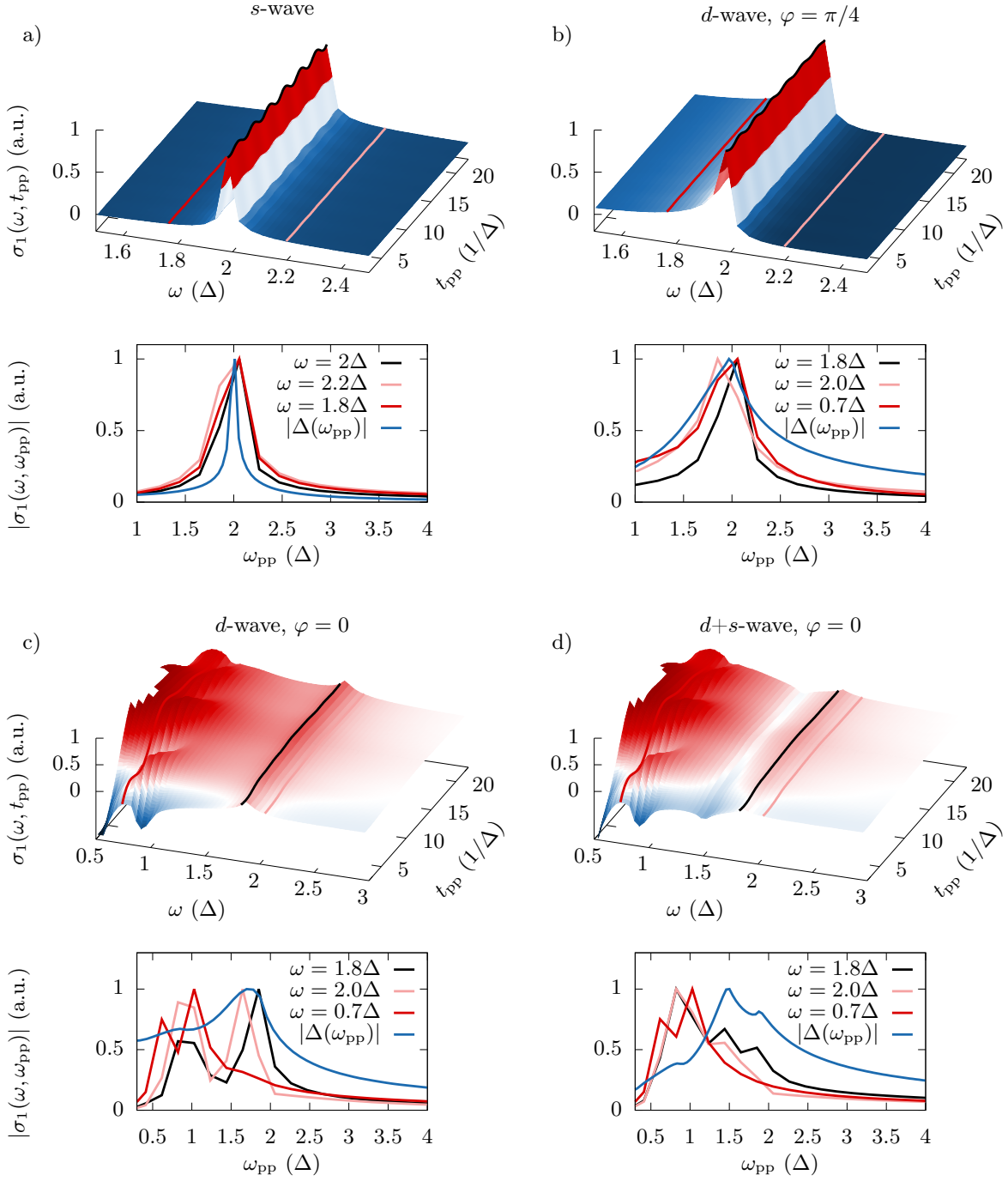


Figure 4.6 Time-resolved optical conductivity (real part) for a) *s*-wave, b) *d*-wave at $\varphi = \pi/4$, c) *d*-wave at $\varphi = 0$ and d) *d*+*s*-wave at $\varphi = 0$. The upper figure in each case shows the real part of the optical conductivity σ_1 as a function of energy ω and pump-probe time delay t_{pp} . The lower figure always shows the Fourier transform along three different cuts at fixed energies ω along the time axis t_{pp} , in comparison to the Fourier transform of the gap oscillations $\Delta(\omega_{pp})$. Details about the numerics and the used parameters can be found in appendix A.3.

4.1.4 Discussion

A calculation of the gap dynamic induced by a pump pulse shows that the effect is captured relatively well by the state quench analysis of the previous chapter. For short enough pump pulses, the condensate is quenched and Higgs oscillations occur. Here, an asymmetry of the quench can be controlled by the incident direction of the pulse with respect to the ground state symmetry. With the proposed coupling of light to the condensate, only certain quench symmetries can be realized. With the pump pulse along the antinodal direction of a d -wave order parameter, one lobe is quenched stronger than the other, which resembles an A_{1g} -quench and induces $B_{x^2-y^2}^{1g}$ oscillation of the condensate. A possible excitation with two pulses along the x - and y -directions with a short time delay in between could implement such a quench even more closely.

The simulation of a pump-probe experiment with variable time delay and calculation of the time-resolved optical conductivity shows that the Higgs oscillations can be found in the optical response as amplitude oscillations of the conductivity. Another study has shown that oscillations of the conductivity in energy should also be visible [56]. For this, a slightly modified pump-probe scheme is considered, in which the Fourier transform is not performed along the pump-probe time delay axis. In this scheme, the total time is kept fixed and the probe pulse is swept backwards in time. Then, along this new time axis, the Fourier transform is performed. This has the advantage that the system is always in the same state after the pump pulse. As an alternative, it is proposed that if the decay of the induced current is considered, which is not included in our model, the probe pulse should also resolve oscillations in energy with the method used in this thesis. The reason, why the energy oscillations cannot be resolved with the method used here, is based on the fact that due to the long oscillating current, the oscillations in energy are averaged effectively and the peak position in the optical conductivity is fixed at the mean value Δ_∞ . Nevertheless, the simulations show that Higgs oscillations excited by a pump pulse can be measured effectively as amplitude or, possibly, energy oscillations of the optical conductivity.

4.2 Time-resolved ARPES

Photoemission spectroscopy is a spectroscopic technique which makes use of the photoelectric effect, namely the emission of electrons due to absorption of light. If one analyzes the angular dependence on the emitted electrons, one calls the method angle-resolved photoemission spectroscopy (ARPES) [203–206]. This allows for a direct measurement of the density of single electron excitations and thus, a measurement of the electron band structure. In addition, if the system is brought into an excited state prior to the photoemission, a time-resolved ARPES (tr-ARPES) experiment can be used to study the dynamic of the nonequilibrium system.

In this section, the tr-ARPES signal of a superconductor excited by a quantum quench will be investigated. A tr-ARPES experiment has the advantage that one has access to the momentum-resolved dynamic of the system. In comparison, an optical pump-probe experiment, as considered in the previous section, measures only a momentum-averaged quantity. This enables us to study and observe not only the collective Higgs oscillations but also the underlying condensate dynamic. So far, there have been little theoretical research efforts studying nonequilibrium Higgs oscillations with tr-ARPES [41–44]. In addition, these studies only considered oscillations of the maximum of the energy distribution curve, which reflects the collective Higgs oscillations. While this indeed allows to observe the gap oscillations in tr-ARPES, it does not make full use of the additional momentum-resolved information contained in the ARPES spectrum. In this section,

the amplitude oscillation of the spectral function will be studied, which is a direct measure of the momentum-resolved condensate dynamic and thus, contains more information. This section is based on the publication [207] from which figures, text and calculations are partly taken.

4.2.1 Theory and Iterated Equation of Motion Approach

One possibility to describe the photoemission process is called *one-step model*, where photon absorption, electron excitation, emission and detection are treated in a single coherent process. This is the most correct description, yet a difficult task. The many-body excited state, electron-electron interactions and mixture of the final free electron and remaining bulk state have to be considered. Therefore, one often makes use of the *three-step model*. Hereby, the excitation process is split into three independent parts:

1. Excitation of an electron from initial to final bulk Bloch state
2. Travel of the excited electron to the surface
3. Transmission of the photoelectron from the bulk into vacuum

This has the advantage that each process can be treated separately in a much simpler way. The two processes are depicted in Fig. 4.7 schematically. In addition, one often uses the *independent-particle picture*, in which many-body interactions are neglected and the *sudden approximation*, in which the photoemission process is assumed to be sudden. With this assumption, there is no interaction between the excited photoelectron and the system left behind. The removal of the electron is much faster than the relaxation time of the excited system. The description of time-resolved ARPES contains further difficulties as the nonequilibrium state induced by the pump pulse has to be considered. Nevertheless, following the usual approach in literature and neglecting transition matrix element effects, the time-resolved ARPES intensity $A(\mathbf{k}, \omega, t)$ is proportional to the electron removal spectral function, which is defined in terms of the lesser Green's function [41, 44, 208–211]

$$A(\mathbf{k}, \omega, t) \propto \text{Im} \int dt_2 \int dt_1 G^<(\mathbf{k}, t_1, t_2) p(t_1 - t) p(t_2 - t) e^{i\omega(t_1 - t_2)}, \quad (4.14)$$

where the lesser Green's function in the time-domain is given by

$$G^<(\mathbf{k}, t_1, t_2) = i \langle c_{\mathbf{k}\uparrow}^\dagger(t_2) c_{\mathbf{k}\uparrow}(t_1) \rangle. \quad (4.15)$$

Hereby, the finite width of the probe pulse is incorporated by a Gaussian function

$$p(t) = \sqrt{\frac{4 \log 2}{\pi \tau_p^2}} \exp\left(-4 \log 2 \left(\frac{t}{\tau_p}\right)^2\right) \quad (4.16)$$

with full width at half maximum τ_p , which broadens the spectral function. Details about the numerical evaluation of the integral can be found in appendix E.

In order to obtain the two-time lesser Green's function, we can no longer use the density matrix formalism as in the previous chapter. The reason is that now, we need expectation values of the product of two operators at different times, whereas the density matrix formalism only provides expectation values for equal times. To calculate the required quantities, we switch to

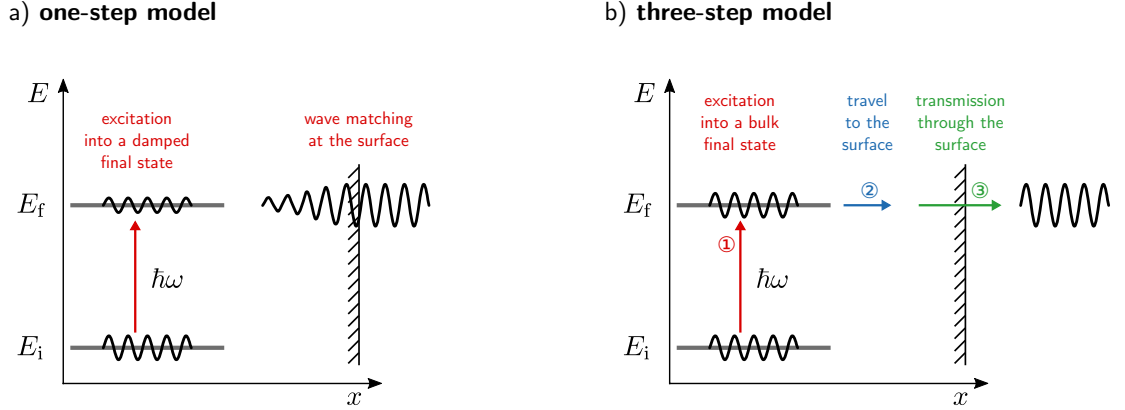


Figure 4.7 Description of the photoemission process in the a) one-step model and b) three-step model. Figure adapted from [206].

the Heisenberg picture and calculate the time evolution of the required operators individually, such that we can construct the expectation values of two operators for arbitrary times. We make use of the iterated equation of motion approach introduced in section 2.3.3 to write down an ansatz for the time-dependent operators and to evaluate the equations of motion. As the BCS Hamiltonian is bilinear, there will be no infinite hierarchy of coupled equations and the simple ansatz of Eq. (2.69), i.e.

$$\alpha_{\mathbf{k}}^{\dagger}(t) = a_{0\mathbf{k}}(t)\alpha_{\mathbf{k}}^{\dagger} + a_{1\mathbf{k}}(t)\beta_{\mathbf{k}}, \quad \beta_{\mathbf{k}}^{\dagger}(t) = b_{0\mathbf{k}}(t)\beta_{\mathbf{k}}^{\dagger} + b_{1\mathbf{k}}(t)\alpha_{\mathbf{k}} \quad (4.17)$$

will be sufficient to express the time-dependent operators without approximation and create a closed set of differential equations. For these operators, Heisenberg's equation of motion

$$\partial_t \alpha_{\mathbf{k}}^{\dagger}(t) = \frac{i}{\hbar} [\tilde{H}(t), \alpha_{\mathbf{k}}^{\dagger}(t)], \quad \partial_t \beta_{\mathbf{k}}^{\dagger}(t) = \frac{i}{\hbar} [\tilde{H}(t), \beta_{\mathbf{k}}^{\dagger}(t)] \quad (4.18)$$

can be evaluated. The derivation of the equations can be found in appendix E. The resulting differential equations for the prefactors read

$$\begin{aligned} \partial_t a_{0\mathbf{k}}(t) = & \frac{i}{\hbar} \left[R_{\mathbf{k}}(t) \left[a_{0\mathbf{k}}(t) \left(|a_{0\mathbf{k}}(t)|^2 + |a_{1\mathbf{k}}(t)|^2 - |b_{1\mathbf{k}}(t)|^2 \right) - a_{1\mathbf{k}}(t) b_{0\mathbf{k}}(t) b_{1\mathbf{k}}^*(t) \right] \right. \\ & + C_{\mathbf{k}}(t) \left[a_{0\mathbf{k}}(t) \left(a_{0\mathbf{k}}(t) b_{1\mathbf{k}}(t) + a_{1\mathbf{k}}(t) b_{0\mathbf{k}}(t) \right) \right] \\ & \left. + C_{\mathbf{k}}^*(t) \left[b_{1\mathbf{k}}^*(t) \left(|a_{0\mathbf{k}}(t)|^2 + |a_{1\mathbf{k}}(t)|^2 \right) \right] \right], \end{aligned} \quad (4.19a)$$

$$\begin{aligned} \partial_t a_{1\mathbf{k}}(t) = & \frac{i}{\hbar} \left[-R_{\mathbf{k}} \left[a_{1\mathbf{k}}(t) \left(|b_{0\mathbf{k}}(t)|^2 - |a_{1\mathbf{k}}(t)|^2 - |a_{0\mathbf{k}}(t)|^2 \right) + a_{0\mathbf{k}}(t) b_{0\mathbf{k}}^*(t) b_{1\mathbf{k}}(t) \right] \right. \\ & + C_{\mathbf{k}}(t) \left[a_{0\mathbf{k}}(t) a_{1\mathbf{k}}(t) b_{1\mathbf{k}}(t) + a_{1\mathbf{k}}(t)^2 b_{0\mathbf{k}}(t) \right] \\ & \left. + C_{\mathbf{k}}^*(t) \left[b_{0\mathbf{k}}^*(t) \left(|a_{0\mathbf{k}}(t)|^2 + |a_{1\mathbf{k}}(t)|^2 \right) \right] \right], \end{aligned} \quad (4.19b)$$

$$\begin{aligned}
 \partial_t b_{0\mathbf{k}}(t) &= \frac{i}{\hbar} \left[R_{\mathbf{k}}(t) \left[b_{0\mathbf{k}}(t) \left(|b_{0\mathbf{k}}(t)|^2 + |b_{1\mathbf{k}}(t)|^2 - |a_{1\mathbf{k}}(t)|^2 \right) - a_{0\mathbf{k}}(t) a_{1\mathbf{k}}^*(t) b_{1\mathbf{k}}(t) \right] \right. \\
 &\quad - C_{\mathbf{k}} \left[a_{1\mathbf{k}}(t) b_{0\mathbf{k}}(t)^2 + a_{0\mathbf{k}}(t) b_{0\mathbf{k}}(t) b_{1\mathbf{k}}(t) \right] \\
 &\quad \left. - C_{\mathbf{k}}^* \left[a_{1\mathbf{k}}^*(t) \left(|b_{0\mathbf{k}}(t)|^2 + |b_{1\mathbf{k}}(t)|^2 \right) \right] \right], \tag{4.19c}
 \end{aligned}$$

$$\begin{aligned}
 \partial_t b_{1\mathbf{k}}(t) &= \frac{i}{\hbar} \left[-R_{\mathbf{k}}(t) \left[b_{1\mathbf{k}}(t) \left(|a_{0\mathbf{k}}(t)|^2 - |b_{0\mathbf{k}}(t)|^2 - |b_{1\mathbf{k}}(t)|^2 \right) + a_{0\mathbf{k}}^*(t) a_{1\mathbf{k}}(t) b_{0\mathbf{k}}(t) \right] \right. \\
 &\quad - C_{\mathbf{k}} \left[a_{1\mathbf{k}}(t) b_{0\mathbf{k}}(t) b_{1\mathbf{k}}(t) + a_{0\mathbf{k}}(t) b_{1\mathbf{k}}(t)^2 \right] \\
 &\quad \left. - C_{\mathbf{k}}^*(t) \left[a_{0\mathbf{k}}^*(t) \left(|b_{0\mathbf{k}}(t)|^2 + |b_{1\mathbf{k}}(t)|^2 \right) \right] \right]. \tag{4.19d}
 \end{aligned}$$

To solve these equations, initial values of the prefactors have to be provided

$$\begin{aligned}
 a_{0\mathbf{k}}(0) &= \sqrt{1 - \langle \alpha_{\mathbf{k}}^\dagger \alpha_{\mathbf{k}} \rangle (0)}, & b_{0\mathbf{k}}(0) &= \sqrt{1 - \langle \beta_{\mathbf{k}}^\dagger \beta_{\mathbf{k}} \rangle (0)}, \\
 a_{1\mathbf{k}}(0) &= \frac{\langle \alpha_{\mathbf{k}}^\dagger \beta_{\mathbf{k}}^\dagger \rangle (0)}{\sqrt{1 - \langle \beta_{\mathbf{k}}^\dagger \beta_{\mathbf{k}} \rangle (0)}}, & b_{1\mathbf{k}}(0) &= \frac{\langle \alpha_{\mathbf{k}} \beta_{\mathbf{k}} \rangle^* (0)}{\sqrt{1 - \langle \alpha_{\mathbf{k}}^\dagger \alpha_{\mathbf{k}} \rangle (0)}}. \tag{4.20}
 \end{aligned}$$

These are derived in appendix E. Depending on the desired calculation, the initial expectation values $\langle \alpha_{\mathbf{k}}^\dagger \alpha_{\mathbf{k}} \rangle (0)$ etc. are chosen either to be the temperature-dependent equilibrium distribution Eq. (2.54) or according to Eq. (3.66) in the quenched case. Finally, the two-time electron expectation value, required to express the Green's function (4.15), is expressed with the time-dependent Bogoliubov quasiparticle operators

$$\begin{aligned}
 \langle c_{\mathbf{k}\uparrow}^\dagger(t_2) c_{\mathbf{k}\uparrow}(t_1) \rangle &= |u_{\mathbf{k}}|^2 \langle \alpha_{\mathbf{k}}^\dagger(t_2) \alpha_{\mathbf{k}}(t_1) \rangle \\
 &\quad + |v_{\mathbf{k}}|^2 \left(b_{0\mathbf{k}}^*(t_2) b_{0\mathbf{k}}(t_1) + b_{1\mathbf{k}}^*(t_2) b_{1\mathbf{k}}(t_1) - \langle \beta_{\mathbf{k}}^\dagger(t_1) \beta_{\mathbf{k}}(t_2) \rangle \right) \\
 &\quad + u_{\mathbf{k}}^* v_{\mathbf{k}} \left(a_{0\mathbf{k}}^*(t_1) b_{1\mathbf{k}}^*(t_2) + a_{1\mathbf{k}}^*(t_1) b_{0\mathbf{k}}^*(t_2) \right. \\
 &\quad \left. - \langle \alpha_{\mathbf{k}}(t_1) \beta_{\mathbf{k}}(t_2) \rangle \right) + u_{\mathbf{k}} v_{\mathbf{k}} \langle \alpha_{\mathbf{k}}^\dagger(t_2) \beta_{\mathbf{k}}^\dagger(t_1) \rangle. \tag{4.21}
 \end{aligned}$$

To obtain a basic understanding of the spectral function, let us consider the equilibrium case for $T = 0$. Here, an analytic calculation can be performed. The Hamiltonian is diagonal and time-independent

$$H = \sum_{\mathbf{k}} E_{\mathbf{k}} (\alpha_{\mathbf{k}}^\dagger \alpha_{\mathbf{k}} + \beta_{\mathbf{k}}^\dagger \beta_{\mathbf{k}}), \tag{4.22}$$

i.e. $R_{\mathbf{k}}(t) = E_{\mathbf{k}}$ and $C_{\mathbf{k}}(t) = 0$. According to Eq. (4.20), the initial conditions read

$$a_{0\mathbf{k}}(0) = b_{0\mathbf{k}}(0) = 1, \quad a_{1\mathbf{k}}(0) = b_{1\mathbf{k}}(0) = 0, \tag{4.23}$$

i.e. $\alpha_{\mathbf{k}}^\dagger(0) = \alpha_{\mathbf{k}}^\dagger$ and $\beta_{\mathbf{k}}^\dagger(0) = \beta_{\mathbf{k}}^\dagger$. Thus, from (4.19) it follows

$$a_{1\mathbf{k}}(t) = b_{1\mathbf{k}}(t) = 0 \tag{4.24}$$

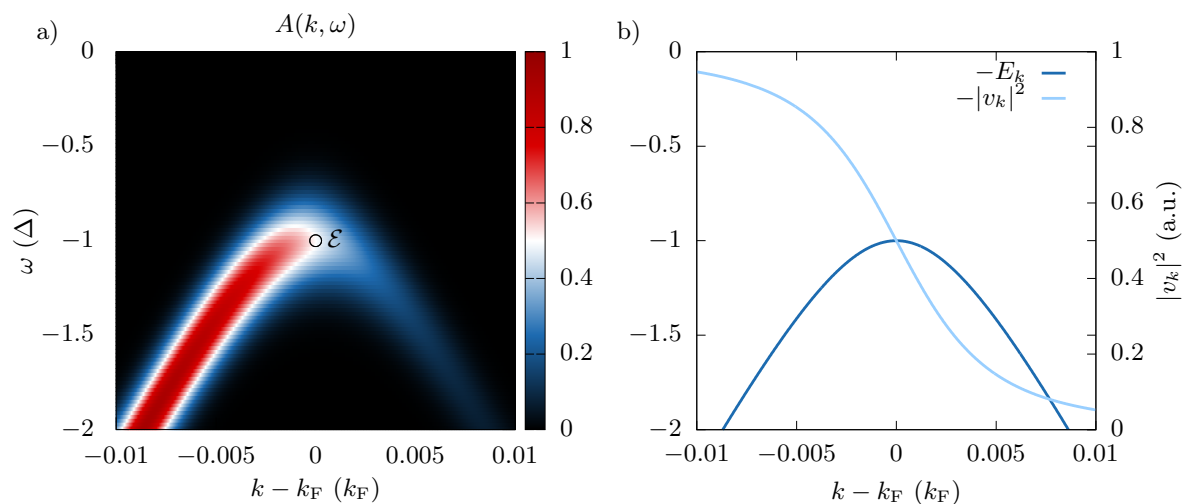


Figure 4.8 Equilibrium spectral function of an s -wave superconductor. a) Spectral function $A(k, \omega)$ according to Eq. (4.28). The energy distribution curve maximum is marked by \mathcal{E} . b) Quasiparticle energy E_k and coherence factor $|v_k|^2$. The spectral function traces the quasiparticle energy weighted by the coherence factor. The used parameters are given in Eq. (A.9) and $\tau_p = 10$.

and

$$\partial_t a_{0\mathbf{k}}(t) = i \frac{E_{\mathbf{k}}}{\hbar} a_{0\mathbf{k}}(t) |a_{0\mathbf{k}}(t)|^2, \quad \partial_t b_{0\mathbf{k}}(t) = i \frac{E_{\mathbf{k}}}{\hbar} b_{0\mathbf{k}}(t) |b_{0\mathbf{k}}(t)|^2. \quad (4.25)$$

The solution is

$$a_{0\mathbf{k}}(t) = e^{i \frac{E_{\mathbf{k}}}{\hbar} t}, \quad b_{0\mathbf{k}}(t) = e^{i \frac{E_{\mathbf{k}}}{\hbar} t}, \quad (4.26)$$

which leads to the following Green's function

$$G^<(\mathbf{k}, t_1, t_2) = i |v_{\mathbf{k}}|^2 b_{0\mathbf{k}}^*(t_2) b_{0\mathbf{k}}(t_1) = i |v_{\mathbf{k}}|^2 e^{i \frac{E_{\mathbf{k}}}{\hbar} (t_1 - t_2)}, \quad (4.27)$$

which depends only on the time difference $t_1 - t_2$. The spectral function in frequency domain using Eq. (4.14) reads

$$A(\mathbf{k}, \omega) \propto |v_{\mathbf{k}}|^2 e^{\frac{\tau_p^2}{8 \log(2)} \left(\omega + \frac{E_{\mathbf{k}}}{\hbar} \right)^2}. \quad (4.28)$$

A plot of the spectral function for an s -wave superconductor is shown in Fig. 4.8 in comparison to the quasiparticle energy. We can see that the spectral function traces the quasiparticle energy $E_{\mathbf{k}}$ weighted by the coherence factor $|v_{\mathbf{k}}|^2$, i.e. the occupation of pair states. The value of the gap can be read off from the position \mathcal{E} . It is the maximum of the energy distribution curve (EDC), i.e. the vertical cut of the spectral function at $k = k_F$. This quantity will be defined in the next section, in which we will study its time-dependence and also the time-dependence of the amplitude of the spectral function \mathcal{A} .

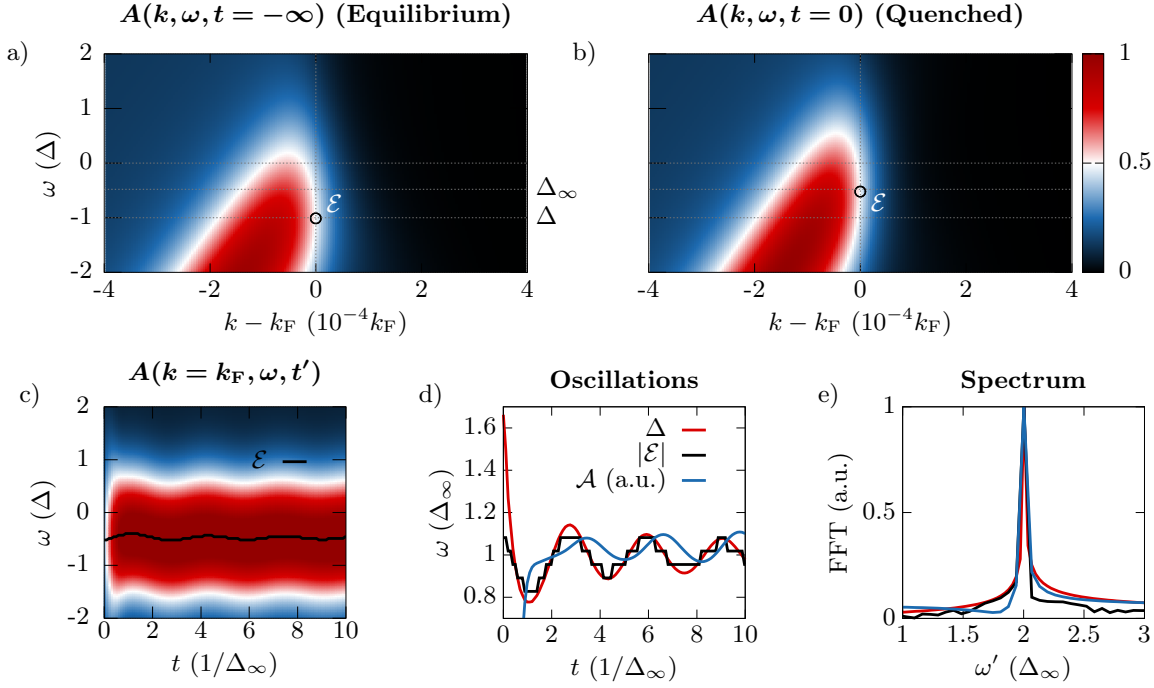


Figure 4.9 Spectral function of an s -wave superconductor after performing an interaction quench. a) Equilibrium spectral function $A(k, \omega, t = -\infty)$; the maximum of the energy distribution curve (EDC) at $k = k_F$ is marked by a circle and labeled \mathcal{E} . b) Spectral function $A(k, \omega, t = 0)$ after the interaction quench, spectral weight is shifted towards the Fermi level. c) Time evolution of the EDC at $k = k_F$. d) Gap oscillations $\Delta(t)$, oscillations of the EDC maximum $|\mathcal{E}(t)|$ and amplitude oscillation $\mathcal{A}(t, k = k_F)$ of the spectral function. The edges in $\mathcal{E}(t)$ are an artifact due to the finite frequency resolution and the decreased amplitude of the spectral function in the beginning results from decreased weight due to the cutoff of the probe pulse envelope at $t = 0$. e) Fourier transform of oscillations; all quantities oscillate with the Higgs frequency $\omega = 2\Delta_\infty$. The probe pulse width is $\tau_p = 1$. The used parameters are given in appendix A.4. Figure adapted from [207].

4.2.2 Higgs Oscillations in the Spectral Function

In the following, we will investigate the dynamics of two quantities. On the one hand, we will consider the position of the maximum of the *energy distribution curve* (EDC) at $k = k_F$, i.e.

$$\mathcal{E}(t, \varphi) = \operatorname{argmax}_\omega A(k = k_F, \varphi, \omega, t). \quad (4.29)$$

This quantity, i.e. the position of the maximum with respect to the Fermi level reflects the energy gap. On the other hand, we will follow the dynamic of the amplitude of the spectral function at $\omega = -\Delta_\infty$, where the strongest dynamic can be expected, i.e.

$$\mathcal{A}(t, k, \varphi) = A(k, \varphi, \omega = -\Delta_\infty, t). \quad (4.30)$$

In these expressions, the momentum is expressed in polar coordinates with absolute value k and polar angle φ . While the first quantity is typically used to trace the time evolution of the system [41, 42], it will appear that an investigation of the second quantity yields even more information.

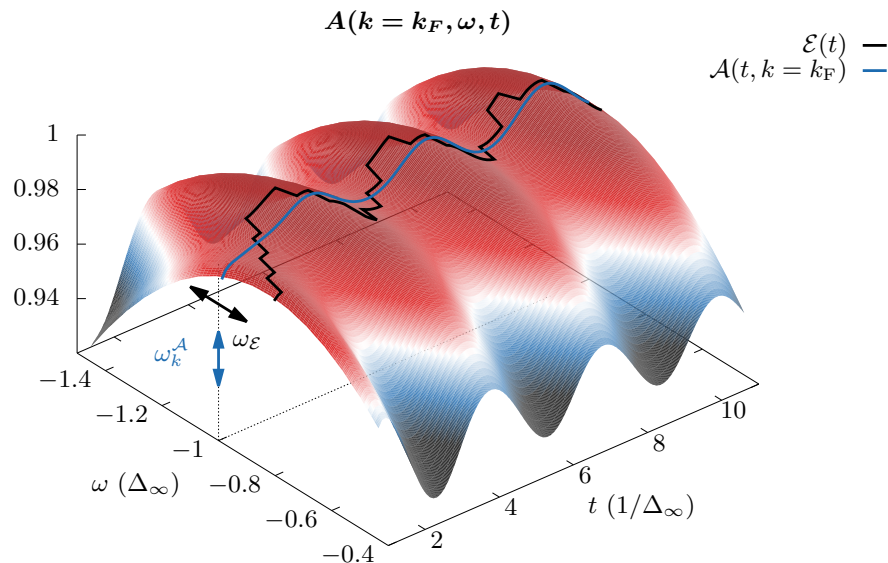


Figure 4.10 Time evolution of the EDC at $k = k_F$. It corresponds to Fig. 4.9c) plotted as a 3d plot for better visualization. There are two different kinds of dynamics: Oscillations in energy of the maximum of the EDC curve (black line) as defined in Eq. (4.29) with the momentum-independent frequency $\omega_E = 2\Delta_\infty$ and oscillations in the amplitude of the spectral function (blue line) as defined in Eq. (4.30) with the momentum-dependent frequency $\omega_k^A = 2\sqrt{\epsilon_k^2 + (\Delta_\infty f_k)^2}$. At $k = k_F$ and $f_k = 1$, $\omega_k^A = \omega_E = 2\Delta_\infty$. Figure adapted from [207].

Before studying superconductors with nontrivial gap symmetry, we first consider the s -wave case with $f_k = 1$, where we perform a simple interaction quench to trigger the time dynamic. In Fig. 4.9, the time evolution of the spectral function can be found. One observes that after the quench (Fig. 4.9b)), spectral weight is shifted towards and above the Fermi level compared to the equilibrium case (Fig. 4.9a)). This can especially be seen by determining \mathcal{E} as defined in (4.29). This position of the maximum, indicated by a circle in Fig. 4.9a) and Fig. 4.9b) is shifted from its initial value $|\mathcal{E}(t = -\infty)| = \Delta$ to a smaller value $|\mathcal{E}(t = 0)| < \Delta$, which indicates a suppression of the energy gap after the quench. To trace the induced dynamic, we look at the time evolution of the EDC at $k = k_F$ shown in Fig. 4.9c) and Fig. 4.10, where we extract the two quantities $\mathcal{E}(t)$ and $\mathcal{A}(t, k = k_F)$. The oscillation dynamic in energy or amplitude is indicated with a black arrow labeled ω_E and with a blue arrow labeled ω_k^A , respectively.

For a sufficient short probe pulse (small τ_p), the time resolution is high enough to directly observe the induced Higgs oscillations of the order parameter as oscillations of $\mathcal{E}(t)$, i.e. an oscillation of the spectral function in energy. The extracted curve $\mathcal{E}(t)$ is shown in Fig. 4.9d) in comparison to the calculated dynamic of the order parameter $\Delta(t)$, where a close accordance can be observed.

In addition to the oscillation of $\mathcal{E}(t)$, we also look at the dynamic of the amplitude of the spectral function $\mathcal{A}(t, k = k_F)$ as defined in Eq. (4.30), shown as well in Fig. 4.9d) and Fig. 4.10 for comparison. We find oscillations with the same frequency as the order parameter. This is confirmed in Fig. 4.9e), where the Fourier transform of the order parameter $\Delta(t)$, the maximum of the EDC $\mathcal{E}(t)$ and the spectral function $\mathcal{A}(t, k = k_F)$ are compared. All three quantities show the

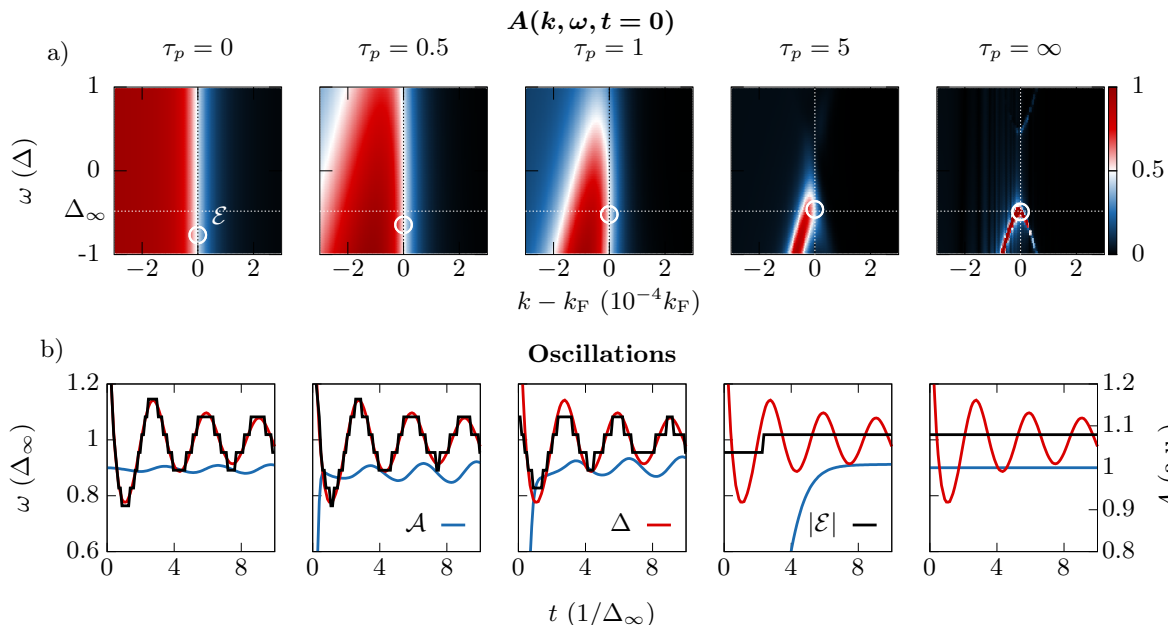


Figure 4.11 Influence of probe pulse width on ARPES spectrum and its time evolution for an s -wave superconductor after an interaction quench. For decreasing probe pulse width (right to left), the energy resolution of the spectral function decreases while the time resolution of oscillation in $\mathcal{E}(t)$ and $\mathcal{A}(t)$ increases. The edges in \mathcal{E} are an artifact due to the finite frequency resolution. The decreased amplitude of the spectral function in the beginning results from decreased weight due to the cutoff of the probe pulse envelope at $t = 0$. The used parameters are given in appendix A.4. Figure adapted from [207].

same oscillation with a frequency of $\omega = 2\Delta_\infty$, the energy of the Higgs mode. Thus, the spectral function provides a direct measure of Higgs oscillations for superconductors in nonequilibrium, both in energy and amplitude.

The pulse width plays a crucial role for the resolution of the gap dynamic in \mathcal{E} and \mathcal{A} [211]. If the probe pulse is too wide, it cannot resolve the oscillations of the system. Hereby, the pulse width has to be compared with the timescale of the intrinsic oscillations of the system, i.e. the energy of the Higgs mode. As a result of too wide pulses, \mathcal{E} will be constant in time at the mean value Δ_∞ , the value of the order parameter after a long time and \mathcal{A} will be constant as well. However, if the probe pulse is short in time, i.e. shorter than the intrinsic oscillation period of the system, it can scan the oscillations, which leads to oscillations of the spectral function in energy and amplitude.

In Fig. 4.11, the spectral function of an s -wave superconductor after an interaction quench is shown for different probe pulse widths. An infinite long probe pulse with $\tau_p = \infty$ leads to a sharp spectral function in energy (Fig. 4.11a) right). However, no oscillations in the spectral function can be observed in this case (black and blue curve in Fig. 4.11b) right), despite the oscillations in the gap (red curve). For decreasing probe pulse width (right to left), the energy resolution of the spectral function decreases and the spectral function peak becomes broader. Simultaneously, the time resolution increases and oscillations of the EDC maximum $\mathcal{E}(t)$ and the spectral function's amplitude $\mathcal{A}(t)$ can be observed.

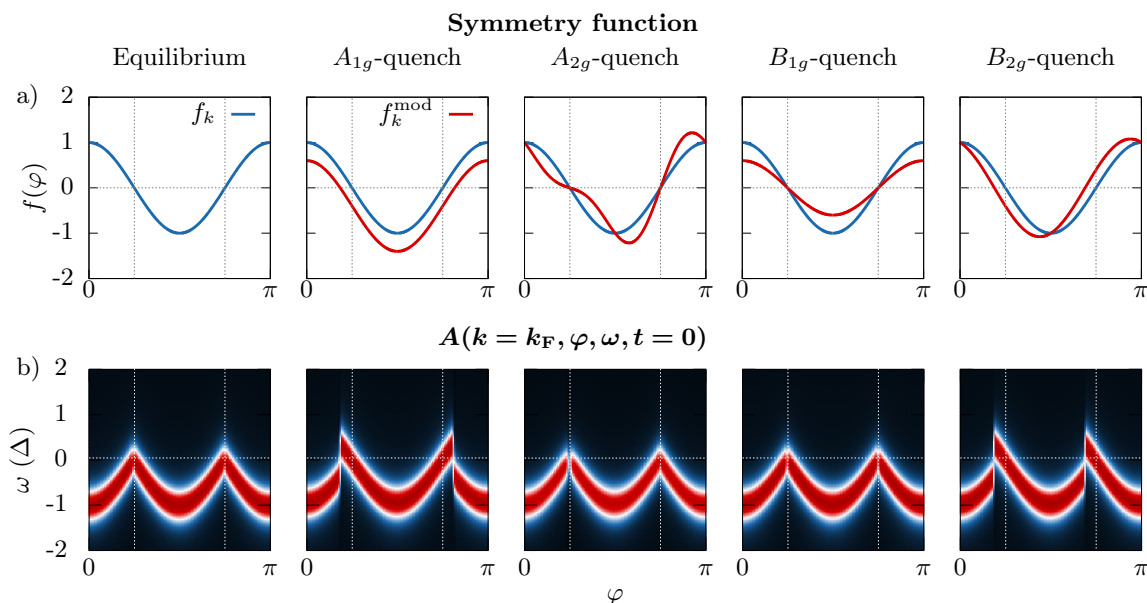


Figure 4.12 Spectral function of a d -wave superconductor after a state quench. a) Symmetry function $f_{\mathbf{k}}$ (blue) and quenched symmetry function $f_{\mathbf{k}}^{\text{mod}}$ (red) for different channels. b) Corresponding spectral function. A shift of nodal lines is reflected by a shift of spectral weight in the nodal region. The probe pulse width is $\tau_p = 10$. The used parameters are given in appendix A.4. Figure adapted from [207].

4.2.3 Momentum-resolved Condensate Dynamic

After having considered the s -wave case with an isotropic interaction quench, we will proceed to a d -wave superconductor, which we will quench in different symmetry channels with the help of a state quench as defined in section 3.2. We will consider all four fundamental quenches for the D_{4h} point group as discussed in section 3.2.2. The symmetry function and the quenched symmetry function, as well as the spectral function after the quench, can be found in Fig. 4.12. First of all, in the equilibrium case, the spectral function resembles the angular dependence of the absolute value of the symmetry function closely. In the antinodal directions at $\varphi = [0, \pi/2, \pi, 3\pi/2]$, a full open gap can be observed with $|\mathcal{E}| = \Delta$. Moving φ towards the nodal directions $\varphi = [\pi/4, 3\pi/4, 5\pi/4, 7\pi/4]$, the maximum \mathcal{E} approaches zero.

The influence of the different quenches is also reflected in the change in the spectral function. The A_{1g} - and B_{2g} -quenches shift the position of the nodes. In the case of the A_{1g} -quench, the shift is in opposite directions relative to the lobe maxima, which creates lobes with different sizes. The B_{2g} -quench shifts all nodes in the same direction, which results in a rotation of all lobes. This can be seen by a transfer of spectral weight above the Fermi level at exactly these points in the spectral function. The B_{1g} -quench does not change the symmetry at all and the A_{2g} -quench only shifts weight inside the lobes, such that for these two quenches, no obvious change in the symmetry of the spectral function is observable. As it was discussed earlier in section 3.2.2, this fact is crucial for the induced Higgs oscillations of the gap, as for the A_{1g} - and B_{2g} -quenches, the shift of the nodal lines creates a second low-lying Higgs mode, whereas for the other two quenches, it will not.

Now, we will analyze the amplitude oscillations of the spectral function $\mathcal{A}(t)$ in more detail to gain a deeper understanding of the dynamic creation of the low-lying Higgs mode. According

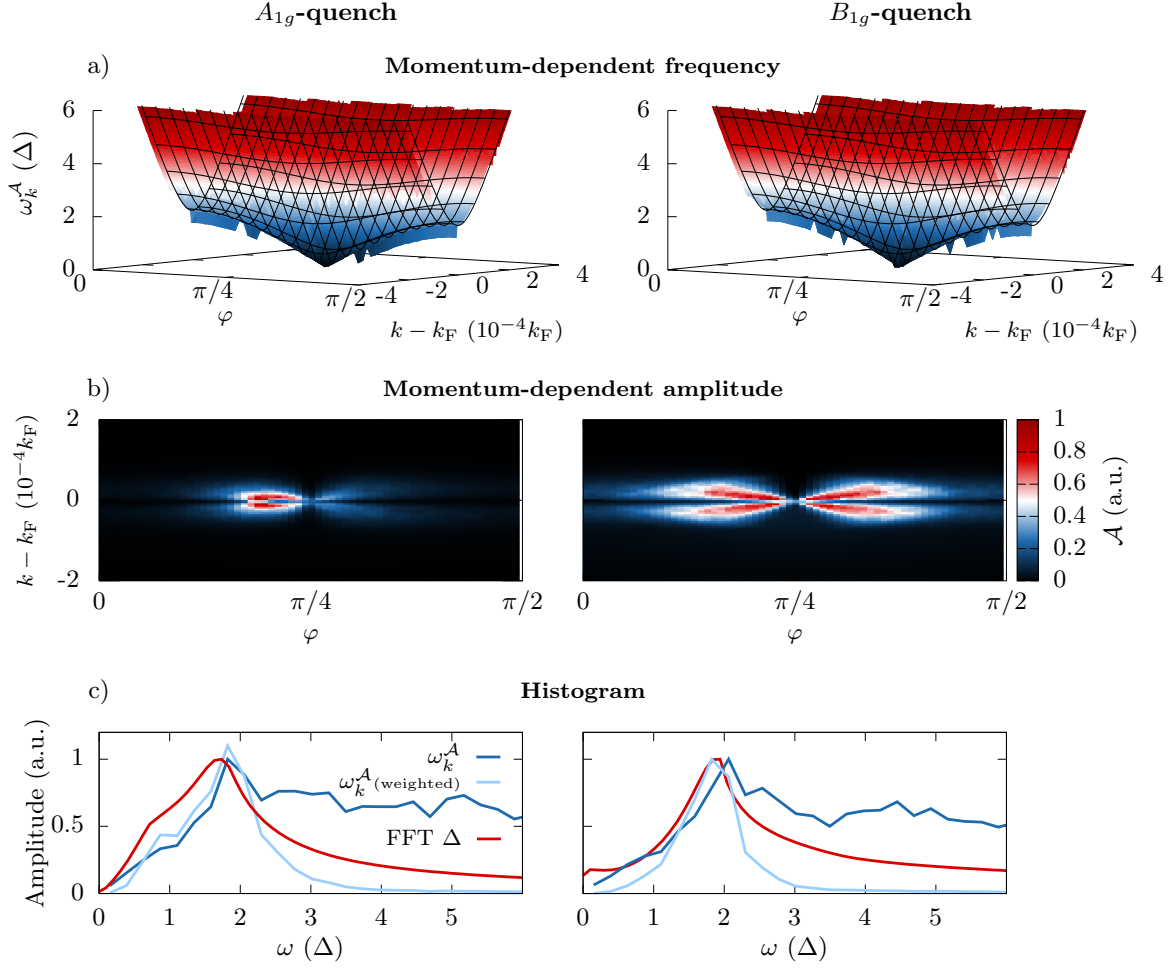


Figure 4.13 Frequency distribution of spectral function oscillation for A_{1g} -quench (left) and B_{1g} -quench (right). a) Momentum-dependent frequency ω_k^A of $\mathcal{A}(t, k, \varphi)$ (colored) compared with the theoretical formula of Eq. (4.31) (lines). There is perfect agreement. The frequency distribution is independent of the quench and thus, the same for A_{1g} - and B_{1g} -quench. b) Momentum-dependent amplitudes of the oscillations. The A_{1g} -quench creates an asymmetry in the amplitudes with respect to the positive and negatives lobe, whereas for the B_{1g} -quench, the amplitudes are symmetric. c) Histogram of occurring frequencies compared with Fourier transform of gap oscillations. The probe pulse width is $\tau_p = 1$. The used parameters are given in appendix A.4. Figure adapted from [207].

to the gap equation (2.62), the value of $\Delta(t)$ is obtained by a summation over the condensate $\langle c_{-k\downarrow}c_{k\uparrow} \rangle(t)$. Both, the anomalous Green's function $\langle c_{-k\downarrow}c_{k\uparrow} \rangle(t)$ and the normal Green's function $\langle c_{k\uparrow}^\dagger c_{k\uparrow} \rangle(t)$ share a similar dynamic as their equations of motion are coupled. This can be seen in the Bloch equations (3.10), where the differential equations for the x - and z -components, which correspond to the anomalous or normal Green's function, respectively, are coupled. Therefore, a momentum-resolved analysis of the spectral function, i.e. $\mathcal{A}(t, k, \varphi)$, which is proportional to the normal Green's function, can reveal important information about the dynamic processes. In comparison, an angle-resolved evaluation of the maximum of the EDC curve, i.e. $\mathcal{E}(t, \varphi)$, as considered in [42], does not give further insight as it only traces the momentum-averaged quantity $\Delta(t)$ and does not depend on φ .

To this end, we extract $\mathcal{A}(t, k, \varphi)$ and its frequency $\omega_{\mathbf{k}}^A$ not only at $k = k_F$ but for all points in momentum space and plot its distribution in Fig. 4.13a) for a d -wave superconductor quenched in the A_{1g} - and B_{1g} -channels. The resulting frequencies are momentum-dependent, yet, do not depend on the quench. They are exactly the same for the A_{1g} - and B_{1g} -quenches. The momentum-dependent frequencies are given by the pseudospin precession frequencies. For the state quench, we can read off the precession frequency as the poles in Eq. (3.70). The frequency at each momentum point \mathbf{k} is given by

$$\omega_{\mathbf{k}}^A = 2\sqrt{\epsilon_{\mathbf{k}}^2 + (\Delta_{\infty} f_{\mathbf{k}})^2}. \quad (4.31)$$

Hereby, we generalize the solution of the linear analysis in the pseudospin calculation and replace $\Delta_q \rightarrow \Delta_{\infty}$. The same result for s -wave symmetry and an interaction quench was also found in [23]. A comparison of the extracted frequencies and the analytic formula shows perfect agreement as shown in Fig. 4.13a).

In the summation process of the gap equation, the frequency with the largest weight will dominate the oscillations. In the case of s -wave with $f_{\mathbf{k}} = 1$, this turns out to be at $k = k_F$, where $\epsilon_{\mathbf{k}} = 0$, which results in a single main frequency $\omega = 2\Delta_{\infty}$. However, as the other frequencies still contribute, the superposition of all different frequencies drives the oscillations out of phase in the long-time limit, which results in the $1/\sqrt{t}$ decay as seen in the previous chapters. In the case of d -wave, there is a much larger variety of frequencies due to the angular dependence of the gap $\Delta_{\mathbf{k}}$. As shown in section 3.1.1, the summation process creates a much stronger decay.

The second low-lying frequency for certain quenches can be explained in the same picture. In Fig. 4.13b), we show the extracted amplitudes for $\omega_{\mathbf{k}}^A$ at each momentum point, which correspond to the actual weight for each frequency. While there is no difference in the frequency distribution between different quenches in Fig. 4.13a), we can clearly see a difference in the amplitudes between the A_{1g} -quench, which shows a second peak in the Higgs oscillations, and the B_{1g} -quench, which shows no second peak. The change in symmetry due to the quench creates a strong asymmetry in the weights regarding the positive and negative lobe directions in the case of the A_{1g} -quench, while the amplitudes for the B_{1g} -quench are symmetric. This can result in the summation process in an additional enhancement of frequencies other than $\omega = 2\Delta_{\infty}$. In Fig. 4.13c), we show the histogram of the frequencies of all momentum points. The raw histogram (dark blue curve) looks exactly the same for both quenches, with a peak at $\omega = 2\Delta_{\infty}$ already without additional weighting. Now, if we weight the histogram with the amplitude of the oscillation, the picture changes (light blue curve). In the case of the A_{1g} -quench, a two-peak or two-kink structure becomes visible, similar to the Fourier transform of the gap oscillation (red curve), whereas the symmetric weighting in the case of the B_{1g} -quench only shows a one-peak structure. Hence,

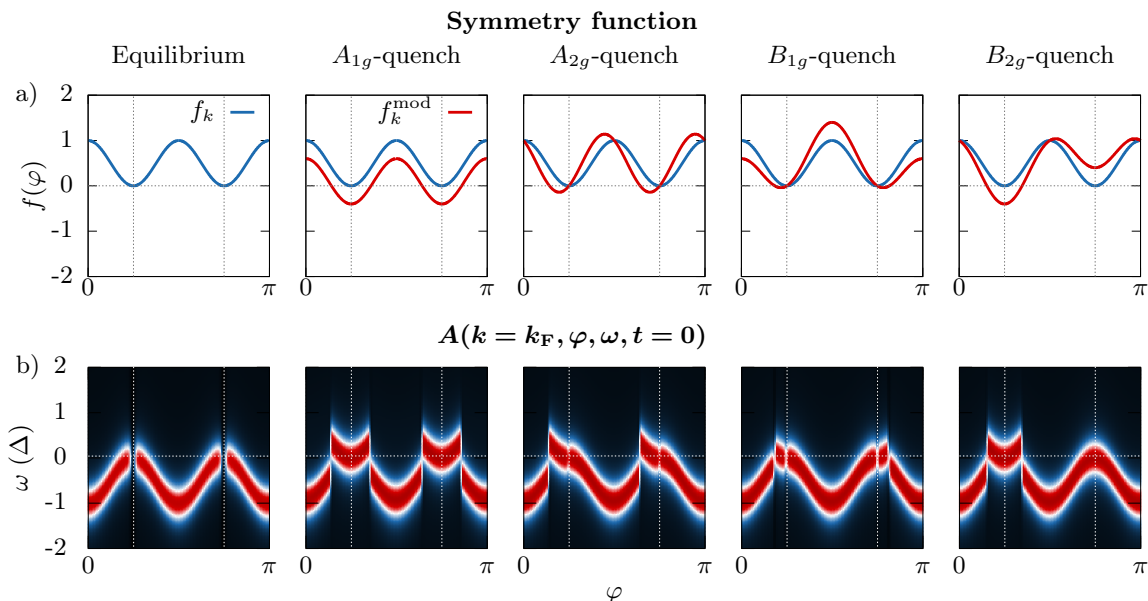


Figure 4.14 Spectral function of a nodal s -wave superconductor after a state quench. Top: Symmetry function $f_{\mathbf{k}}$ (blue) and quenched symmetry function $f_{\mathbf{k}}^{\text{mode}}$ (red) for different channels. Bottom: Corresponding spectral function; shift of nodal lines is reflected by a shift of spectral weight in the nodal region. The probe pulse width is $\tau_p = 10$. The used parameters are given in appendix A.4. Figure adapted from [207].

a careful analysis of the momentum-resolved frequencies in the ARPES spectrum reveals the dynamic of the condensate and explains the underlying processes leading to the collective Higgs oscillations.

In analogy to Fig. 4.12, we quench a nodal s -wave superconductor in all symmetry channels of the D_{4h} lattice point group. The result can be found in Fig. 4.14. In the areas, in which the quench shifts nodal lines, we can observe a corresponding shift in spectral weight. For the chosen quench strength $g = -0.4$, all quenches shift nodal lines resulting in a two-peak or two-kink structure for all quenches. In comparison, the quench with opposite sign $g = +0.4$ in Fig. 3.17 does not shift nodes in the A_{1g} case, where no second peak can be observed. In the case of the B_{1g} -quench, this shift is smaller compared to the other quenches, which results in a lower frequency of the second Higgs mode (see 3.17).

4.2.4 Analysis of Oscillation Phase

In the previous section we have seen how the oscillation of the spectral function can provide a deep insight into the creation process of the collective Higgs oscillation of the order parameter. Now, we will analyze the phase of these oscillations at different points in momentum space to resolve the collective condensate dynamic. We have seen that an A_{1g} -quench for d -wave changes the sizes of the positive and negative lobes, i.e. the lobes of one sign increase in size while the others decrease. The resulting movement of the condensate will therefore be an oscillation, in which the smaller lobe increases while the larger lobe decreases. Thus, the movement of the lobes is out of phase (see Fig. 4.15a) and Fig. 3.10).

The same quench applied to a nodal s -wave superconductor with $f_{\mathbf{k}} = \cos^2(2\varphi)$, which has

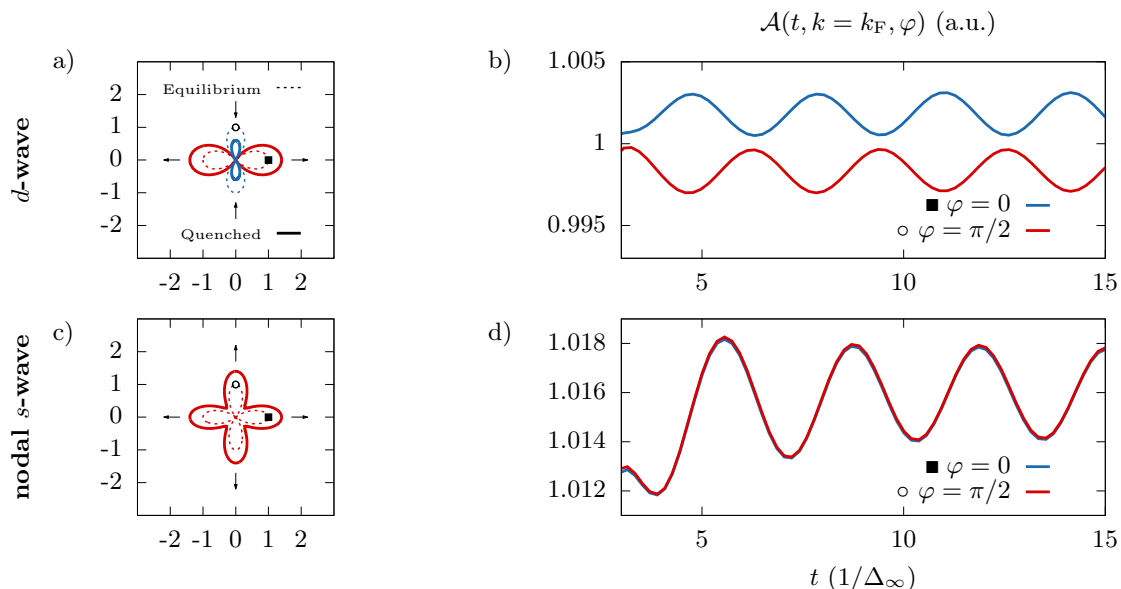


Figure 4.15 Oscillation of spectral function after A_{1g} -quench for d -wave (top) and nodal s -wave (bottom) superconductor. Points in momentum space rotated by $\pi/2$ oscillate with opposite phase in the case of d -wave and in phase in the case of nodal s -wave. For a B_{1g} -quench, the situation would be reversed. The decreased amplitude of the spectral function in the beginning results from decreased weight due to the cutoff of the probe pulse envelope at $t = 0$. The probe pulse width is $\tau_p = 1$. The used parameters are given in appendix A.4. Figure adapted from [207].

the same nodal structure, will change its lobes all equally due to the same sign of the gap. The resulting oscillations are therefore in phase (see Fig. 4.15c)). Even though the oscillation of the lobes is in phase for this quench, the gap oscillation shows a two-peak structure due to a shift of nodal lines as discussed in the previous section. Thus, a comparison of the Higgs oscillation spectrum does not allow to distinguish between d -wave and nodal s -wave in this case.

To see whether we can observe the different condensate dynamics for these two gap symmetries in the spectral function, we extract the amplitude oscillations $\mathcal{A}(t, k = k_F, \varphi)$ at $\varphi = 0$ and $\varphi = \pi/2$, i.e. at points in momentum space rotated by $\varphi = \pi/2$, which should oscillate with opposite phase in the case of d -wave and with the same phase for the nodal s -wave. The result can be found in Fig. 4.15b) and d) and confirms the expected oscillatory behavior. For a B_{1g} -quench, the situation would be reversed. Oscillations of the spectral function's amplitude provide therefore not only information about the amplitude of the gap but also relative phase information at different points in momentum space can be extracted. This shows that the information obtainable from the time-dependent amplitude of the spectral function allows to clearly trace the collectively induced condensate movement.

4.2.5 Discussion

The analysis of the spectral function measurable in tr-ARPES experiments shows how the collective Higgs oscillations of the superconducting order parameter can be traced back and observed as oscillations of the spectral function. There are two kinds of dynamics, namely momentum-independent oscillations of the EDC maximum $\mathcal{E}(t)$, which directly correspond to

oscillations of the energy gap $\Delta(t)$, and momentum-dependent oscillations of the amplitude of the spectral function $\mathcal{A}(t, k, \varphi)$. While the \mathcal{E} dynamic only reveals information about the momentum-averaged quantity $\Delta(t)$, the amplitude oscillation of the spectral function \mathcal{A} allows to perform a momentum-resolved analysis of the condensate dynamic. Experimental conditions might dictate which quantity can be observed more easily. Both quantities require short enough probe pulses to resolve the Higgs oscillations. The EDC maximum oscillations are restricted in their amplitude by the oscillation amplitude of the gap, which can be in the sub-percentage range depending on quench strength and gap symmetry. In contrast, the amplitude oscillations of the spectral function can be up to several percentages in size and thus, much larger for certain conditions. However, they might be more difficult to resolve in general than oscillations in energy.

A tracking of the amplitude oscillation frequencies ω_k^A of the spectral function $\mathcal{A}(t, k, \varphi)$ at different momenta leads to a deeper understanding of the microscopic creation process of collective Higgs oscillations $\Delta(t)$. While the frequencies can be described with a single formula independent of gap and quench symmetry, the relative weight of each frequency contributing to the collective amplitude oscillation of the order parameter is determined by the gap and quench symmetry in a nontrivial way. If there are asymmetries in the weights, additional Higgs modes can appear, which are dynamically created due to quenching the condensate in a symmetry channel different from its equilibrium value.

Furthermore, quenching the condensate in defined symmetry channels and observing the oscillation phase of the spectral function allows to resolve the exact condensate movement. This condensate dynamic depends on the gap and quench symmetry. Here, the quench symmetry for a certain gap was given such that the resulting condensate movement, like an in-phase or out-of-phase oscillation of lobes of a d -wave or nodal s -wave superconductor, is clearly defined. This explicit construction of a quench symmetry allows to distinguish between the two different gaps with the same nodal structure but different phase. Experimentally, it is not yet clear how to quench the condensate in a defined symmetry channel. This is an open question for further research. Nevertheless, this analysis shows that tr-ARPES experiments are in principle able to retrieve phase information of the superconducting gap if the oscillation phase of the spectral function is evaluated.

5 Higgs Spectroscopy with Periodic Driving and Third-harmonic Generation

This chapter changes the perspective compared to the previous ones. While before, quenches of superconductors were studied, which excite the intrinsic Higgs oscillations, here, driven or enforced Higgs oscillations will be explored. For s -wave superconductors, it was shown that driven Higgs oscillations resonate with the energy of the Higgs mode, which can be observed in the third-harmonic response [40]. In a nutshell, one can understand this effect as follows. The quadratic coupling to the condensate of a multi-cycle light pulse $A(t)$ with frequency Ω induces oscillations of the energy gap $\delta\Delta(t)$ with twice the driving frequency 2Ω . This nonlinear coupling also induces a higher-order current j , where a third-harmonic generation (THG) component $j^{(3)}(t)$ arises. It results from the driven gap oscillations, i.e. $j^{(3)}(t) \propto A(t)\delta\Delta(t)$. If the effective 2Ω driving frequency is tuned to the energy of the Higgs mode 2Δ , a resonance occurs in the gap oscillation and consequently, also in the THG intensity, which indicates the existence of the Higgs mode. This process is depicted schematically in the introduction in Fig. 1.1b). The analysis of the known s -wave case will be extended for unconventional superconductors to investigate the resonance behavior for these cases.

There are two important points which have to be kept in mind in the following. The first one is a conceptual one resulting from experimental conditions. With current technology, there is no tunable THz laser available in the required energy range. Therefore, one cannot sweep the driving frequency to hit the resonance with the Higgs mode. Instead, experiments are performed with fixed driving frequency. To find the resonance, the energy of the Higgs mode $2\Delta_T$ is tuned by varying the temperature T . It is therefore important to study the temperature dependence of the THG signal, which will be done in section 5.2.1.

The second point concerns the uniqueness of the resonance in the signal. Recent studies have pointed out that *charge density fluctuations* (CDF) can contribute to the THG resonance as well [45–48]. Actually, in clean superconductors, this contribution is much larger than the Higgs contribution. Yet, impurity scattering in dirty superconductors can enhance the Higgs signal significantly due to a paramagnetic coupling of light to the condensate [65–70]. The analysis in this chapter is within the clean limit with no impurity scattering. Thus, the calculated CDF contribution will dominate the total THG signal. Nevertheless, one can extract important information about the polarization dependence of the different contributions, which should also be valid in the dirty case. A full analysis revealing the strength of each contribution for real materials depends on many parameters and will not be considered. Here, the CDF contribution is calculated, but the main attention is to study the influence of nontrivial pairing symmetry on the THG response resulting from Higgs oscillations. This chapter is based on the publication [8], from which figures, text and calculations are partly taken.

5.1 Driven Higgs Oscillations

To study the periodic driving, we neglect the light momentum \mathbf{q}_0 , which allows us to use a description within the Anderson pseudospin formalism. Using minimal substitution, the BCS

Hamiltonian reads

$$H = \sum_{\mathbf{k}\sigma} \epsilon_{\mathbf{k}-e\mathbf{A}(t)} c_{\mathbf{k}\sigma}^\dagger c_{\mathbf{k}\sigma} - \sum_{\mathbf{k}} \Delta_{\mathbf{k}} c_{\mathbf{k}\uparrow}^\dagger c_{-\mathbf{k}\downarrow}^\dagger - \sum_{\mathbf{k}} \Delta_{\mathbf{k}}^* c_{-\mathbf{k}\downarrow} c_{\mathbf{k}\uparrow}, \quad (5.1)$$

where we use

$$\mathbf{A}(t) = \begin{pmatrix} A_x(t) \\ A_y(t) \end{pmatrix} = \mathbf{A}_0 A(t) = A_0(t) \hat{e}_A = A_0 \sin(\Omega t) \begin{pmatrix} \cos(\chi) \\ \sin(\chi) \end{pmatrix} \quad (5.2)$$

with the driving amplitude A_0 , polarization vector \hat{e}_A and the explicit time-dependence

$$A(t) = \sin(\Omega t) \quad (5.3)$$

with driving frequency Ω and polarization angle χ . Compared with the parametrization of the vector potential in chapter 4, this corresponds to the choice $\vartheta = 0$ and $\varphi = 0$, i.e. the in-plane component of the light momentum \mathbf{q}_0 is zero as the light direction is perpendicular to the xy -plane and the polarization is in-plane. For simplicity, in order to perform an analytic analysis, the time-dependence of the light is chosen purely sinusoidally; however, in a numerical calculation the sine function can be, in principle, convolved with an arbitrary envelope to resemble experimental multi-cycle pulses.

Transforming the Hamiltonian to the Anderson pseudospin formalism is possible in an analogous way to section 2.2.5 with a redefined pseudomagnetic field

$$\mathbf{b}_{\mathbf{k}}^\top = \left(-2\Delta'_{\mathbf{k}}, \quad 2\Delta''_{\mathbf{k}}, \quad \epsilon_{\mathbf{k}-e\mathbf{A}(t)} + \epsilon_{\mathbf{k}+e\mathbf{A}(t)} \right). \quad (5.4)$$

One observes that the coupling of light to the system happens in the z -component of the pseudomagnetic field, i.e. in the τ_3 channel, whereas the Higgs oscillations live in the x -component, i.e. the τ_1 channel. Thus, light-condensate coupling is not direct but through the τ_3 charge channel.

For the further analysis, we expand the z -component of the pseudomagnetic field into powers of A_0

$$\epsilon_{\mathbf{k}-e\mathbf{A}(t)} + \epsilon_{\mathbf{k}+e\mathbf{A}(t)} = 2\epsilon_{\mathbf{k}} + \gamma_{\mathbf{k}}^{A^2}(t) + \mathcal{O}(A_0^4) \quad (5.5)$$

with

$$\gamma_{\mathbf{k}}^{A^2}(t) = e^2 \sum_{ij} \partial_{ij}^2 \epsilon_{\mathbf{k}} A_i(t) A_j(t) = e^2 A_0^2 \sin^2(\Omega t) D_{\epsilon_{\mathbf{k}}}(\chi) \quad (5.6)$$

and the definition of

$$D_{\epsilon_{\mathbf{k}}}(\chi) = \cos^2(\chi) \partial_{xx}^2 \epsilon_{\mathbf{k}} + \sin^2(\chi) \partial_{yy}^2 \epsilon_{\mathbf{k}} + 2 \sin(\chi) \cos(\chi) \partial_{xy}^2 \epsilon_{\mathbf{k}}, \quad (5.7)$$

where the abbreviation $\partial_{ij}^2 \epsilon_{\mathbf{k}} = \frac{\partial^2 \epsilon_{\mathbf{k}}}{\partial k_i \partial k_j}$ is used. Due to particle-hole symmetry, i.e. $\epsilon_{\mathbf{k}} = \epsilon_{-\mathbf{k}}$, the term linear in A_0 , or in general all odd orders, vanish and light only couples in even powers of A_0 to the condensate. The term $D_{\epsilon_{\mathbf{k}}}(\chi)$ contains the polarization dependence and the second derivatives of the dispersion. For a parabolic dispersion, it becomes k -independent, which leads to a vanishing of the coupling as shown later. Thus, the coupling of light to the condensate is relatively small, as it is only possible in second order and depends on the deviations from a

parabolic dispersion. An enhancement is possible due to finite in-plane light momentum \mathbf{q}_0 , as shown in chapter 4, or in the dirty-limit [67, 68, 70]. In both cases, a paramagnetic coupling via the $\mathbf{p}\mathbf{A}$ term is possible and the quadratic coupling does not vanish for parabolic dispersion.

For small driving amplitude, an analytic evaluation is possible in analogy to chapter 3. With the ansatz for the pseudospins of Eq. (3.5) and

$$\Delta(t) = \Delta + \delta\Delta(t), \quad (5.8)$$

the linearized Bloch equations in Laplace space read

$$sx_{\mathbf{k}}(s) = -2\epsilon_{\mathbf{k}}y_{\mathbf{k}}(s) - \frac{f_{\mathbf{k}}}{E_{\mathbf{k}}}\epsilon_{\mathbf{k}}\delta\Delta''(s), \quad (5.9a)$$

$$sy_{\mathbf{k}}(s) = 2\epsilon_{\mathbf{k}}x_{\mathbf{k}}(s) + 2f_{\mathbf{k}}\Delta z_{\mathbf{k}}(s) + \frac{f_{\mathbf{k}}}{E_{\mathbf{k}}}\left(\frac{1}{2}\gamma_{\mathbf{k}}^{A^2}(s)\Delta - \epsilon_{\mathbf{k}}\delta\Delta'(s)\right), \quad (5.9b)$$

$$sz_{\mathbf{k}}(s) = -2f_{\mathbf{k}}\Delta y_{\mathbf{k}}(s) - \frac{\Delta f_{\mathbf{k}}^2}{E_{\mathbf{k}}}\delta\Delta''(s). \quad (5.9c)$$

For the solution, it follows

$$x_{\mathbf{k}}(s) = \frac{\epsilon_{\mathbf{k}}f_{\mathbf{k}}\left(2\epsilon_{\mathbf{k}}\delta\Delta'(s) - \Delta\gamma_{\mathbf{k}}^{A^2}(s) - s\delta\Delta''(s)\right)}{E_{\mathbf{k}}(4E_{\mathbf{k}}^2 + s^2)}, \quad (5.10a)$$

$$y_{\mathbf{k}}(s) = \frac{-f_{\mathbf{k}}\left(2s\epsilon_{\mathbf{k}}\delta\Delta'(s) - s\Delta\gamma_{\mathbf{k}}^{A^2}(s) + 4E_{\mathbf{k}}^2\delta\Delta''(s)\right)}{2E_{\mathbf{k}}(4E_{\mathbf{k}}^2 + s^2)}, \quad (5.10b)$$

$$z_{\mathbf{k}}(s) = \frac{\Delta f_{\mathbf{k}}^2\left(2\epsilon_{\mathbf{k}}\delta\Delta'(s) - \Delta\gamma_{\mathbf{k}}^{A^2}(s) - s\delta\Delta''(s)\right)}{E_{\mathbf{k}}(4E_{\mathbf{k}}^2 + s^2)} \quad (5.10c)$$

with the Laplace transform of the coupling term

$$\gamma_{\mathbf{k}}^{A^2}(s) = e^2 A_0^2 \frac{2\Omega^2}{s(s^2 + 4\Omega^2)} D_{\epsilon_{\mathbf{k}}}(\chi). \quad (5.11)$$

To proceed, we use several assumptions and approximations. The x - and y -directions shall be equivalent for $f_{\mathbf{k}}^2$ and $\epsilon_{\mathbf{k}}$, i.e. $f(k_x, k_y)^2 = f(k_y, k_x)^2$ and $\epsilon(k_x, k_y) = \epsilon(k_y, k_x)$. This assumption is true for energies like $\epsilon_{\mathbf{k}} = \epsilon(|\mathbf{k}|)$ or tight-binding dispersions $\epsilon_{\mathbf{k}} \propto \cos(k_x) + \cos(k_y)$ and s -wave $f_{\mathbf{k}} = 1$ or d -wave $f_{\mathbf{k}} \propto \cos(k_x) - \cos(k_y)$ symmetry functions. With this, it follows for any function $a_{\mathbf{k}}$ whose \mathbf{k} -dependence only stems from $f_{\mathbf{k}}^2$ or $\epsilon_{\mathbf{k}}$ that

$$\sum_{\mathbf{k}}(\partial_{xx}^2 \epsilon_{\mathbf{k}})a_{\mathbf{k}} = \sum_{\mathbf{k}}(\partial_{yy}^2 \epsilon_{\mathbf{k}})a_{\mathbf{k}} = \frac{1}{2} \sum_{\mathbf{k}}(\nabla^2 \epsilon_{\mathbf{k}})a_{\mathbf{k}}. \quad (5.12)$$

As we are mostly interested in values close to the Fermi energy ϵ_{F} , i.e. values of $\epsilon_{\mathbf{k}} \approx 0$, we expand the Laplacian of the dispersion to first order in the dispersion

$$\frac{1}{2}\nabla^2 \epsilon_{\mathbf{k}} = \alpha_0 + \alpha_1 \epsilon_{\mathbf{k}} + \mathcal{O}(\epsilon_{\mathbf{k}}^2). \quad (5.13)$$

Hereby, α_i are expansion coefficients. In fact, for the single-band tight-binding dispersion on the square lattice with nearest neighbor hopping t

$$\epsilon_{\mathbf{k}} = -2t(\cos(k_x) + \cos(k_y)) - \epsilon_{\text{F}}, \quad (5.14)$$

the expansion is exact with $\alpha_0 = -\epsilon_F/2$ and $\alpha_1 = -1/2$. Further, we assume that for typical dispersions, the mixed derivatives vanish, i.e. $\partial_{xy}^2 \epsilon_{\mathbf{k}} = 0$. Using these assumptions, the interaction term $\gamma_{\mathbf{k}}^{A^2}(t)$ can be simplified if summed over in momentum space

$$\sum_{\mathbf{k}} \gamma_{\mathbf{k}}^{A^2}(t) a_{\mathbf{k}} = e^2 A_0^2 \sin^2(\Omega t) \sum_{\mathbf{k}} (\alpha_0 + \alpha_1 \epsilon_{\mathbf{k}}) a_{\mathbf{k}}. \quad (5.15)$$

In this expression, the polarization dependence has vanished. With this knowledge, the gap equation can be evaluated, i.e.

$$\delta\Delta'(s) = \lambda \int_{-\epsilon_c}^{\epsilon_c} d\epsilon \int_0^{2\pi} d\varphi f(\varphi) x_{\mathbf{k}}(s), \quad (5.16a)$$

$$\delta\Delta''(s) = -\lambda \int_{-\epsilon_c}^{\epsilon_c} d\epsilon \int_0^{2\pi} d\varphi f(\varphi) y_{\mathbf{k}}(s). \quad (5.16b)$$

First, we start by evaluating the real part of the gap. For parabolic band dispersion, i.e. k -independent $D_{\epsilon_{\mathbf{k}}}$, the integral over the terms $\propto \gamma_{\mathbf{k}}^{A^2}(s)$ vanishes according to Eq. (3.15), such that the real part of the gap is unaffected by the driving. The terms $\propto \delta\Delta''(s)$ and $\propto \alpha_0$ always vanish and the remaining part can be evaluated in analogy to section 3.1.1. It follows

$$\delta\Delta'(s) = \frac{1}{2} \alpha_1 \Delta e^2 A_0^2 \frac{2\Omega^2}{s(s^2 + 4\Omega^2)} \left(1 - \frac{1}{\lambda F(s)} \right) \quad (5.17)$$

with $F(s)$ given by Eq. (3.24) and the replacement $\Delta_{\mathbf{q}} = \Delta$. The solution in time-domain is obtained by the inverse Laplace transform, i.e. the Bromwich integral Eq. (3.27). The first summand $\propto 1$ in the bracket of Eq. (5.17) is trivial and yields

$$\delta\Delta_D(t) = \alpha_1 \Delta e^2 A_0^2 \frac{1 - \cos(2\Omega t)}{4}, \quad (5.18)$$

which is just a forced oscillation with 2Ω due to the quadratic coupling. Hereby, the index D stands for driven. For the second part, the Bromwich integral reads explicitly

$$I(t) = \alpha_1 \Delta e^2 A_0^2 \frac{1}{2\pi i} \int_{\gamma-i\infty}^{\gamma+i\infty} e^{st} \frac{\Omega^2}{s^2 + 4\Omega^2} \frac{1}{\lambda \int_0^{2\pi} d\varphi f^2 \sqrt{4\Delta^2 f^2 + s^2} \sinh^{-1} \left(\frac{s}{2\Delta|f|} \right)}. \quad (5.19)$$

It can be evaluated similarly to section 3.1.1 by extending the integration into a closed loop integral in the complex plane excluding the poles and the branch cut as shown in Fig. 5.1

$$\int_{\gamma-i\infty}^{\gamma+i\infty} = \int_{c_0} = \int_{c_{\text{tot}}} - \sum_{i=1}^{12} \int_{c_i}. \quad (5.20)$$

The difference to section 3.1.1 is that there are two new poles located at $s = \pm 2i\Omega$, which can merge with the branch points when $2\Omega = 2\Delta$. This indicates the existence of a resonance at these points. The contributions from the paths c_{tot} , c_1 , c_3 , c_6 , c_8 , c_{10} , c_{11} and c_{12} are zero. The paths around the poles can be evaluated with the help of the residue theorem

$$\sum_{i=2,5,7} \frac{1}{2\pi i} \int_{c_i} I_{\text{int}} ds = \sum_{i=2,5,7} \text{Ind}_{c_i}(s_i) \text{Res}_{s_i}(I_{\text{int}}), \quad (5.21)$$

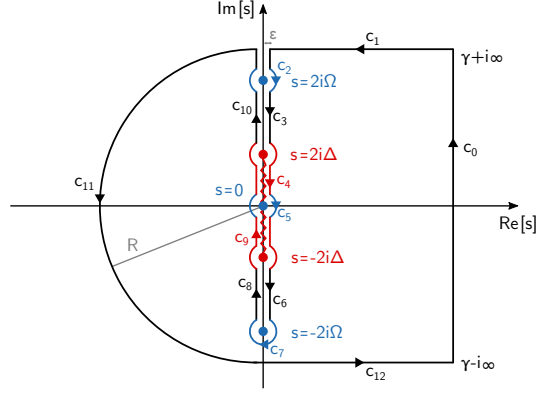


Figure 5.1 Contour to solve the Bromwich integral Eq. (5.19) corresponding to the path c_0 . The red zigzag line from $-2i\Delta$ to $2i\Delta$ indicates the chosen branch cut for the expression, while the blue dots at $s = 0, \pm 2i\Omega$ indicate the poles. The total closed loop integral as well as the contributions $c_1, c_3, c_6, c_8, c_{10}, c_{11}$ and c_{12} are vanishing. There are only contributions from the poles at $s = 0, \pm 2i\Omega$ and the paths c_4 and c_9 located on the right and left side of the branch cut.

where s_i are the poles enclosed by the path c_i and I_{int} stands for the integrand in Eq. (5.19) and $\text{Ind}_{c_i}(s_i) = -1$ is the winding number due to the clockwise circling around the pole. It follows

$$\text{Ind}_{c_5}(0) \text{Res}_0(I_{\text{int}}) = -\frac{1}{4\lambda \int_0^{2\pi} f^2 d\varphi}, \quad (5.22a)$$

$$\text{Ind}_{c_{2,7}}(\pm 2i\Omega) \text{Res}_{\pm 2i\Omega}(I_{\text{int}}) = \frac{\Omega e^{\pm 2i\Omega t}}{8\lambda \int_0^{2\pi} d\varphi f^2 \sqrt{\Delta^2 f^2 - \Omega^2} \sin^{-1}\left(\frac{\Omega}{\Delta|f|}\right)}. \quad (5.22b)$$

The solution for the poles $\pm 2i\Omega$ represents a driven oscillation with a resonant amplitude due to the $\sqrt{\Delta^2 f^2 - \Omega^2}$ term in the denominator. The paths c_4 and c_9 are parametrized as $s(r) = -ir$ for c_4 and $s(r) = ir$ for c_9 with $r \in [-2\Delta, 2\Delta]$. It follows in analogy to Eq. (3.31)

$$\begin{aligned} & \frac{1}{2\pi i} \left(\int_{c_4} I_{\text{int}} ds + \int_{c_9} I_{\text{int}} ds \right) \\ &= -\frac{1}{\pi} \int_{-2\Delta}^{2\Delta} \frac{\Omega^2}{4\Omega^2 - r^2} \frac{\sin(rt) dr}{\lambda \int d\varphi f^2 \sqrt{4\Delta^2 f^2 - r^2} \sin^{-1}\left(\frac{r}{2\Delta|f|}\right)}. \end{aligned} \quad (5.23)$$

Combining all the expressions, we obtain

$$\delta\Delta'(t) = \alpha_1 \Delta e^2 A_0^2 (\delta\Delta_D(t) + \delta\Delta_H(t) + \delta\Delta_R(t)), \quad (5.24)$$

where

$$\delta\Delta_D(t) = \frac{1 - \cos(2\Omega t)}{4}, \quad (5.25a)$$

$$\delta\Delta_H(t) = -\frac{1}{\pi} \int_{-2\Delta}^{2\Delta} \frac{\Omega^2}{4\Omega^2 - r^2} \frac{\sin(rt) dr}{\lambda \int d\varphi f^2 \sqrt{4\Delta^2 f^2 - r^2} \sin^{-1}\left(\frac{r}{2\Delta|f|}\right)} - \frac{1}{4\lambda \int f^2 d\varphi}, \quad (5.25b)$$

$$\delta\Delta_R(t) = \frac{\Omega \cos(2\Omega t)}{4\lambda \int d\varphi f^2 \sqrt{\Delta^2 f^2 - \Omega^2} \sin^{-1}\left(\frac{\Omega}{\Delta|f|}\right)}. \quad (5.25c)$$

The term $\delta\Delta_D(t)$ is a driven oscillation with frequency 2Ω . The term $\delta\Delta_H(t)$ is the intrinsic Higgs oscillation with a frequency of $\sim 2\Delta$ induced by an effective interaction quench due to the periodic driving (see appendix F for details). The amplitude of the Higgs oscillation depends on the driving frequency Ω . Without solving the integral explicitly, one observes that there will be a resonant behavior when $2\Omega = 2\Delta$ induced by the prefactor $(4\Omega^2 - r^2)^{-1}$. We can understand this as a matching of the two oscillations 2Ω and 2Δ , when Ω is tuned to Δ . In the s -wave case, the expression can be evaluated in analogy to section 3.1.1 (see also [40]). It follows

$$\delta\Delta_H^{s\text{-wave}}(t) = \frac{1}{4\lambda} \left(\frac{2}{\pi^{3/2}} \frac{\Omega^2}{\Omega^2 - \Delta^2} \frac{\cos(2\Delta t + \frac{\pi}{4})}{\sqrt{\Delta t}} - 1 \right). \quad (5.26)$$

This resonance can also be found in the third term, which is again a forced oscillation of 2Ω , yet having a frequency-dependent amplitude. In the longtime limit, the 2Ω oscillation survives, as the intrinsic 2Δ oscillation is damped as shown in the previous chapters. We rewrite the resonance term as

$$\delta\Delta_R(t) = \frac{1}{4\lambda} A(\Omega) e^{-i\zeta(\Omega)} \cos(2\Omega t), \quad (5.27)$$

where $A(\Omega)$ represents the oscillation amplitude and $\zeta(\Omega)$ the phase relative to the driving. For s -wave, these terms were already evaluated in [40]. There are two isolated branch points at $s = \pm 2i\Delta$, which lead to an exact resonance in the amplitude if $2\Omega = 2\Delta$. With $f(\varphi) = 1$ and $\lambda \rightarrow 2\pi\lambda$, it follows

$$A^{s\text{-wave}}(\Omega) = \begin{cases} \frac{\Omega}{\sqrt{\Delta^2 - \Omega^2}} \frac{1}{\sin^{-1}\left(\frac{\Omega}{\Delta}\right)} & \Omega < \Delta \\ \frac{\Omega}{\sqrt{\Omega^2 - \Delta^2}} \frac{1}{\sqrt{\cosh^{-1}\left(\frac{\Omega}{\Delta}\right)^2 + \left(\frac{\pi}{2}\right)^2}} & \Omega > \Delta \end{cases}, \quad (5.28a)$$

$$\zeta^{s\text{-wave}}(\Omega) = \begin{cases} 0 & \Omega < \Delta \\ -\tan^{-1}\left(\frac{\pi/2}{\cosh^{-1}\left(\frac{\Omega}{\Delta}\right)}\right) & \Omega > \Delta \end{cases}. \quad (5.28b)$$

This amplitude and phase are plotted in Fig. 5.2. One observes a sharp resonance in $A(\Omega)$ and a sharp $\pi/2$ phase jump at the resonance condition.

Next, let us consider the d -wave case where $f(\varphi) = \cos(2\varphi)$. Here, we do no longer have an exact resonance condition, but there is still a maximum of the amplitude given by the minimum of the integral in the denominator of Eq. (5.25c). This leads to a broad peak in the amplitude accompanied by a smooth phase change of $\zeta(0) - \zeta(\Delta) < \pi/2$. The peak in the amplitude is at an energy slightly below $2\Omega = 2\Delta$, whereas a sharp kink in the phase at $2\Omega = 2\Delta$ is found.

For nontrivial gap symmetry, the gap oscillation spectrum does not have to be peaked at exactly 2Δ . We have already observed this behavior in section 3.1 about the interaction quench. For d -wave, the spectrum was peaked slightly below 2Δ . In particular, here, the position of the peak is determined by the interplay between the terms f^2 and $\sqrt{\Delta^2 f^2 - \Omega^2}$ under the integral over φ in (5.25c). For values $2\Omega \approx 2\Delta$, the terms with the highest weights, i.e. $f \approx 1$, vanish, which decreases the value of the integral and creates its minimum. Therefore, in the case of d -wave, the maximum of the amplitude can still be found roughly at $2\Omega \approx 2\Delta$. Depending on the exact shape of f , it can be shifted to lower energies. For values $2\Omega > 2\Delta$, the square root is always imaginary for each value of φ , which leads to the sharp edge in the phase at $2\Omega = 2\Delta$.

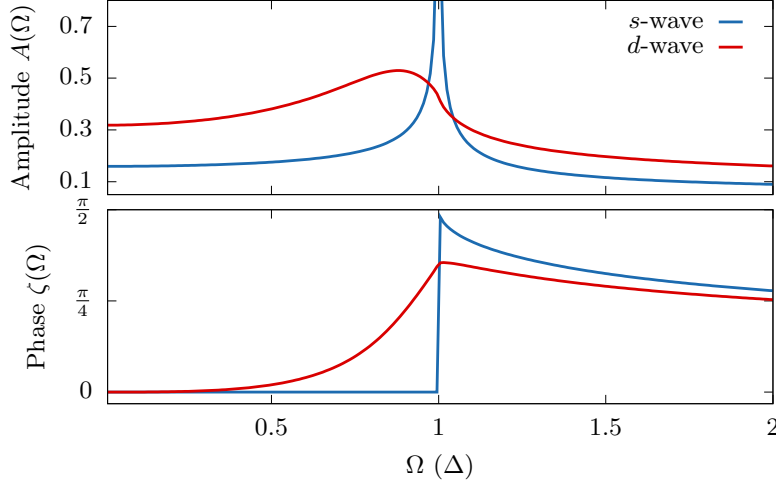


Figure 5.2 Amplitude A and phase ζ of the driven gap oscillation in Eq. (5.27). In the case of *s*-wave, a sharp resonance at $2\Omega = 2\Delta$ occurs, whereas for *d*-wave, a broad peak slightly below 2Δ is apparent. In addition, the phase of *s*-wave shows a sharp jump from 0 for $2\Omega < 2\Delta$ to $\pi/2$ at $2\Omega = 2\Delta$ and a drifting for $2\Omega > 2\Delta$. For *d*-wave, there is a broad phase change from 0 for $\Omega = 0$ up to a value slightly below $\pi/2$ for $2\Omega = 2\Delta$. At this point, there is a sharp kink and a drifting for $2\Omega > 2\Delta$ similar to the *s*-wave case. Figure adapted from [8].

After studying the real part, finally, we will also calculate the imaginary part of the gap with Eq. (5.16b). Similar to the real part, the terms $\propto \delta\Delta'(s)$ and $\propto \alpha_1$ vanish and we are left with

$$\begin{aligned} \delta\Delta''(s) &= -\alpha_0\Delta e^2 A_0^2 s \frac{2\Omega^2}{s(s^2 + 4\Omega^2)} \lambda \int d\varphi \frac{f^2}{2E^2(4E^2 + s^2)} \\ &\quad + \delta\Delta''(s) - \delta\Delta''(s)s^2 \lambda \int d\varphi \frac{f^2}{2E^2(4E^2 + s^2)}. \end{aligned} \quad (5.29)$$

Solving for $\delta\Delta''(s)$ yields

$$\delta\Delta''(s) = -\alpha_0\Delta e^2 A_0^2 \frac{2\Omega}{s^2(s^2 + 4\Omega^2)} \quad (5.30)$$

and the solution in time-domain is given by

$$\delta\Delta''(t) = -\alpha_0\Delta e^2 A_0^2 \left(\frac{t}{2} - \frac{\sin(2\Omega t)}{4\Omega} \right) = -\alpha_0\Delta e^2 \int_0^t A_0(t')^2 dt'. \quad (5.31)$$

We can see that the imaginary part is independent of the gap symmetry and it follows the oscillation of the driving frequency with a frequency-independent amplitude. In addition, it contains a drift linear in time. As in the *s*-wave case, for small driving amplitudes, the imaginary part only contributes to the phase φ_Δ of the gap $\Delta(t) = |\Delta(t)|e^{i\varphi_\Delta(t)}$

$$\varphi_\Delta(t) = \arctan \left(\frac{\delta\Delta''(t)}{\Delta + \delta\Delta'(t)} \right) \approx \frac{\delta\Delta''(t)}{\Delta}. \quad (5.32)$$

The absolute value of the gap is independent of the imaginary part and is solely determined by the real part

$$|\Delta(t)| = \sqrt{(\Delta + \delta\Delta'(t))^2 + \delta\Delta''(t)^2} \approx \Delta + \delta\Delta'(t). \quad (5.33)$$

5.2 Observation of Higgs Modes in Third-harmonic Generation Response

The resonance of the forced gap oscillation with the Higgs mode can be found experimentally in the transmitted light field. The nonlinear coupling of the vector potential to the condensate leads to higher-harmonic generation where the lowest non-vanishing order is third-harmonic generation. Its intensity I^{THG} , which is proportional to the amplitude squared of the induced third-order current $j^{(3)}(3\Omega)$

$$I^{\text{THG}} \propto \left| j^{(3)}(3\Omega) \right|^2, \quad (5.34)$$

shows the same resonance as the gap oscillation and will be calculated in the following. However, as mentioned in the introduction of this chapter, not only the driven gap oscillations contribute to THG but also charge density fluctuations, i.e. single particle excitations resonating at the pair-breaking energy 2Δ . Therefore, this contribution is considered and calculated in this section as well and compared to the contribution of the Higgs oscillation.

Driving the superconductor periodically will induce an electric current [40]

$$\mathbf{j}(t) = e \sum_{\mathbf{k}} \mathbf{v}_{\mathbf{k}-e\mathbf{A}(t)} \langle n_{\mathbf{k}} \rangle (t) \quad (5.35)$$

with the group velocity $\mathbf{v}_{\mathbf{k}} = \nabla \epsilon_{\mathbf{k}}$ and the charge density

$$\langle n_{\mathbf{k}} \rangle (t) = \langle c_{\mathbf{k}\uparrow}^\dagger c_{\mathbf{k}\uparrow} + c_{\mathbf{k}\downarrow}^\dagger c_{\mathbf{k}\downarrow} \rangle (t). \quad (5.36)$$

To calculate the lowest order response, we expand the velocity in A_0

$$\mathbf{v}_{\mathbf{k}-e\mathbf{A}(t)} = \mathbf{v}_{\mathbf{k}} - e \sum_j A_j(t) \partial_j \mathbf{v}_{\mathbf{k}} + \mathcal{O}(A_0^2). \quad (5.37)$$

The charge density can be expressed with the z -component of the pseudospin and we obtain for the current

$$\mathbf{j}(t) = \mathbf{j}^{(0)}(t) + \mathbf{j}^{(1)}(t) + \mathbf{j}^{(3)}(t), \quad (5.38)$$

where

$$\mathbf{j}^{(0)}(t) = e \sum_{\mathbf{k}} \mathbf{v}_{\mathbf{k}} \langle n_{\mathbf{k}} \rangle (t), \quad (5.39a)$$

$$\mathbf{j}^{(1)}(t) = -2e^2 \sum_{\mathbf{k}} \sum_j A_j(t) \partial_j \mathbf{v}_{\mathbf{k}} \left(\langle \sigma_{\mathbf{k}}^z \rangle (0) + \frac{1}{2} \right), \quad (5.39b)$$

$$\mathbf{j}^{(3)}(t) = -2e^2 \sum_{\mathbf{k}} \sum_j A_j(t) \partial_j \mathbf{v}_{\mathbf{k}} z_{\mathbf{k}}(t). \quad (5.39c)$$

The first term $\mathbf{j}^{(0)}(t)$ vanishes due to parity, the second term $\mathbf{j}^{(1)}(t)$ represents the induced current oscillating with the driving frequency Ω . The third term $\mathbf{j}^{(3)}(t)$ is the lowest order of higher-order generation, which oscillates with 3Ω because of the proportionality $\propto A_j(t) z_{\mathbf{k}}(t)$. This is due to the fact that $z_{\mathbf{k}}(t)$ oscillates with 2Ω as we have seen in the previous section. The

induced current for an arbitrary angle relative to the polarization of the vector potential can be decomposed into a parallel and perpendicular component, which we will calculate separately. We insert the expression for the vector potential and expand the summation of the components

$$j_{\parallel\perp}^{(3)}(t) = \mathbf{j}^{(3)}(t) \cdot \hat{e}_A^{\parallel\perp} = -2e^2 A_0(t) \sum_{\mathbf{k}} D_{\epsilon_{\mathbf{k}}}^{\parallel\perp}(\chi) z_{\mathbf{k}}(t) \quad (5.40)$$

with the directions parallel $\hat{e}_A^{\parallel} = (\cos(\chi), \sin(\chi))^{\top}$ and perpendicular $\hat{e}_A^{\perp} = (\sin(\chi), -\cos(\chi))^{\top}$ to the light polarization. For the terms containing the derivatives, we use $D_{\epsilon_{\mathbf{k}}}^{\parallel}(\chi) = D_{\epsilon_{\mathbf{k}}}(\chi)$ of Eq. (5.7) and define additionally

$$D_{\epsilon_{\mathbf{k}}}^{\perp}(\chi) = \sin(\chi) \cos(\chi) (\partial_{xx}^2 \epsilon_{\mathbf{k}} - \partial_{yy}^2 \epsilon_{\mathbf{k}}) + \partial_{xy}^2 \epsilon_{\mathbf{k}} (\sin^2(\chi) - \cos^2(\chi)). \quad (5.41)$$

To obtain an expression for the spectrum, we perform a Fourier transform to frequency ω

$$j_{\parallel\perp}^{(3)}(\omega) = -2e^2 \sum_{\mathbf{k}} D_{\epsilon_{\mathbf{k}}}^{\parallel\perp}(\chi) \frac{1}{\sqrt{2\pi}} \int A_0(\omega') z_{\mathbf{k}}(\omega - \omega') d\omega'. \quad (5.42)$$

Using the expression for the vector potential (5.3), the convolution can be evaluated and the current at $\omega = 3\Omega$ reads

$$j_{\parallel\perp}^{(3)}(3\Omega) = ie^2 A_0 \sum_{\mathbf{k}} D_{\epsilon_{\mathbf{k}}}^{\parallel\perp}(\chi) z_{\mathbf{k}}(2\Omega), \quad (5.43)$$

where the additionally occurring higher-order oscillation term $z_{\mathbf{k}}(4\Omega)$ is neglected for small driving amplitude. We can see that the THG response 3Ω is determined by the 2Ω response of the system. For further analysis, we make use of the solution $z_{\mathbf{k}}(\omega) = z_{\mathbf{k}}(s = i\omega)$ of the linearized Bloch equations (5.10c) and also include the temperature dependence. The term $z_{\mathbf{k}}(s)$ has three contributions, namely, one term proportional to the real part of the gap $\propto \delta\Delta'(s)$, one term proportional to the imaginary part of the gap $\propto \delta\Delta''(s)$ and one term proportional to driving $\gamma_{\mathbf{k}}^{A^2}(s)$. Therefore, we write

$$j_{\parallel\perp}^{(3)}(3\Omega) = j_{\parallel\perp}^{(3)\text{H}}(3\Omega) + j_{\parallel\perp}^{(3)\text{P}}(3\Omega) + j_{\parallel\perp}^{(3)\text{C}}(3\Omega), \quad (5.44)$$

where the indices H, P, C stand for Higgs, phase and charge, respectively. We insert the solution $z_{\mathbf{k}}(s)$ in Eq. (5.10c) into the expression (5.43) for the current. To write the resulting expressions in a compact form, we define several quantities

$$x_0(s) = V \sum_{\mathbf{k}} \frac{f_{\mathbf{k}}^2}{E_{\mathbf{k}}(4E_{\mathbf{k}}^2 + s^2)} \tanh\left(\frac{E_{\mathbf{k}}}{2k_B T}\right), \quad (5.45a)$$

$$x_1(s) = V \sum_{\mathbf{k}} \frac{f_{\mathbf{k}}^4}{E_{\mathbf{k}}(4E_{\mathbf{k}}^2 + s^2)} \tanh\left(\frac{E_{\mathbf{k}}}{2k_B T}\right), \quad (5.45b)$$

$$x_2(s) = V \sum_{\mathbf{k}} \frac{\epsilon_{\mathbf{k}} f_{\mathbf{k}}^2}{E_{\mathbf{k}}(4E_{\mathbf{k}}^2 + s^2)} \tanh\left(\frac{E_{\mathbf{k}}}{2k_B T}\right), \quad (5.45c)$$

$$x_3(s) = V \sum_{\mathbf{k}} \frac{\epsilon_{\mathbf{k}}^2 f_{\mathbf{k}}^2}{E_{\mathbf{k}}(4E_{\mathbf{k}}^2 + s^2)} \tanh\left(\frac{E_{\mathbf{k}}}{2k_B T}\right), \quad (5.45d)$$

$$x_4^{\parallel\perp}(s) = V \sum_{\mathbf{k}} \frac{D_{\epsilon_{\mathbf{k}}}^{\parallel\perp} f_{\mathbf{k}}^2}{E_{\mathbf{k}}(4E_{\mathbf{k}}^2 + s^2)} \tanh\left(\frac{E_{\mathbf{k}}}{2k_B T}\right), \quad (5.45e)$$

$$x_5^{\parallel\perp}(s) = V \sum_{\mathbf{k}} \frac{\epsilon_{\mathbf{k}} D_{\epsilon_{\mathbf{k}}}^{\parallel\perp} f_{\mathbf{k}}^2}{E_{\mathbf{k}}(4E_{\mathbf{k}}^2 + s^2)} \tanh\left(\frac{E_{\mathbf{k}}}{2k_B T}\right), \quad (5.45f)$$

$$x_6^{\parallel\perp}(s) = V \sum_{\mathbf{k}} \frac{D_{\epsilon_{\mathbf{k}}}^{\parallel} D_{\epsilon_{\mathbf{k}}}^{\perp} f_{\mathbf{k}}^2}{E_{\mathbf{k}}(4E_{\mathbf{k}}^2 + s^2)} \tanh\left(\frac{E_{\mathbf{k}}}{2k_B T}\right). \quad (5.45g)$$

It follows for the three contributions

$$j_{\parallel\perp}^{(3)H}(3\Omega) = ie^2 A_0 \frac{1}{V} 2\Delta x_5^{\parallel\perp}(2i\Omega) \delta\Delta'(2i\Omega), \quad (5.46a)$$

$$j_{\parallel\perp}^{(3)P}(3\Omega) = -ie^2 A_0 \frac{1}{V} s\Delta x_4^{\parallel\perp}(2i\Omega) \delta\Delta''(2i\Omega), \quad (5.46b)$$

$$j_{\parallel\perp}^{(3)C}(3\Omega) = -ie^4 A_0^3 A^2(2i\Omega) \frac{1}{V} \Delta^2 x_6^{\parallel\perp}(2i\Omega). \quad (5.46c)$$

The real and imaginary part of the gap expressed within the same formalism reads

$$\delta\Delta'(s) = \Delta e^2 A_0^2(s) \frac{s^2 x_2(s) x_4^{\parallel}(s) + 2x_5^{\parallel}(s) (2\Delta^2 x_1(s) + 2x_3(s) - 1)}{2s^2 x_2(s)^2 + 2(2x_3(s) - 1)(2\Delta^2 x_1(s) + 2x_3(s) - 1)}, \quad (5.47a)$$

$$\delta\Delta''(s) = s\Delta e^2 A_0^2(s) \frac{2x_3(s) x_4^{\parallel}(s) - x_4^{\parallel}(s) - 2x_2(s) x_5^{\parallel}(s)}{2s^2 x_2(s)^2 + 2(2x_3(s) - 1)(2\Delta^2 x_1(s) + 2x_3(s) - 1)}. \quad (5.47b)$$

Up to now, the expressions are exact within the linear regime. For a better understanding, we make use of the same assumptions about the isotropy of dispersion and symmetry functions as in the previous sections and we set $T = 0$. This simplifies the terms and we obtain

$$x_2(s) = x_4^{\perp}(s) = x_5^{\perp}(s) = 0, \quad (5.48a)$$

$$x_4^{\parallel}(s) = V \sum_{\mathbf{k}} \frac{\partial_{xx}^2 \epsilon_{\mathbf{k}} f_{\mathbf{k}}^2}{E_{\mathbf{k}}(4E_{\mathbf{k}}^2 + s^2)} = \alpha_0 x_0(s), \quad (5.48b)$$

$$x_5^{\parallel}(s) = V \sum_{\mathbf{k}} \frac{\epsilon_{\mathbf{k}} \partial_{xx}^2 \epsilon_{\mathbf{k}} f_{\mathbf{k}}^2}{E_{\mathbf{k}}(4E_{\mathbf{k}}^2 + s^2)} = \alpha_1 x_3(s), \quad (5.48c)$$

$$\begin{aligned} x_6^{\perp}(s) &= \frac{1}{4} \sin(4\chi) V \sum_{\mathbf{k}} f_{\mathbf{k}}^2 \frac{(\partial_{xx}^2 \epsilon_{\mathbf{k}})^2 - (\partial_{xx}^2 \epsilon_{\mathbf{k}})(\partial_{yy}^2 \epsilon_{\mathbf{k}})}{E_{\mathbf{k}}(4E_{\mathbf{k}}^2 + s^2)} \\ &\approx \frac{1}{4} \sin(4\chi) (2\alpha_0^2 x_0(s) + 2\alpha_1^2 x_3(s)), \end{aligned} \quad (5.48d)$$

$$\begin{aligned} x_6^{\parallel}(s) &= \left(1 - \frac{1}{2} \sin^2(2\chi)\right) V \sum_{\mathbf{k}} \frac{(\partial_{xx}^2 \epsilon_{\mathbf{k}})^2 f_{\mathbf{k}}^2}{E_{\mathbf{k}}(4E_{\mathbf{k}}^2 + s^2)} \\ &\quad + \frac{1}{2} \sin^2(2\chi) V \sum_{\mathbf{k}} \frac{(\partial_{xx}^2 \epsilon_{\mathbf{k}})(\partial_{yy}^2 \epsilon_{\mathbf{k}}) f_{\mathbf{k}}^2}{E_{\mathbf{k}}(4E_{\mathbf{k}}^2 + s^2)} \\ &\approx \left(1 - \frac{1}{2} \sin^2(2\chi)\right) (2\alpha_0^2 x_0(s) + 2\alpha_1^2 x_3(s)). \end{aligned} \quad (5.48e)$$

In these expression, we used the identities

$$\sin^4(\chi) + \cos^4(\chi) = 1 - \frac{1}{2} \sin^2(2\chi), \quad (5.49a)$$

$$2 \sin^2(\chi) \cos^2(\chi) = \frac{1}{2} \sin^2(2\chi), \quad (5.49b)$$

$$\sin(\chi) \cos(\chi) (\cos^2(\chi) - \sin^2(\chi)) = \frac{1}{4} \sin(4\chi) \quad (5.49c)$$

and neglected sums with terms $\propto (\partial_{xx}^2 \epsilon_{\mathbf{k}})(\partial_{yy}^2 \epsilon_{\mathbf{k}})$. Using these simplified expressions, the real part of the gap reduces to

$$\delta\Delta'(s) = \frac{1}{2} \alpha_1 \Delta e^2 A_0^2(s) \left(1 + \frac{1}{2x_3(s) - 1} \right). \quad (5.50)$$

With the general identity

$$2x_3(s) = 1 - 2\Delta^2 x_1(s) - \frac{1}{2} s^2 x_0(s) = 1 - \lambda F(s) \quad (5.51)$$

the expression is equivalent to the result Eq. (5.17) from the previous section. In analogy, the imaginary part reduces to Eq. (5.30)

$$\delta\Delta''(s) = -\alpha_0 \Delta e^2 \frac{A_0^2(s)}{s}. \quad (5.52)$$

Within this approximation, the resulting THG currents read

$$j_{\perp}^{(3)H}(3\Omega) = j_{\perp}^{(3)P}(3\Omega) = 0, \quad (5.53a)$$

$$j_{\parallel}^{(3)H}(3\Omega) = ie^4 A_0^3 A^2(2i\Omega) \frac{1}{V} \Delta^2 \alpha_1^2 x_3(2i\Omega) \left(1 + \frac{1}{2x_3(2i\Omega) - 1} \right), \quad (5.53b)$$

$$j_{\parallel}^{(3)P}(3\Omega) = ie^4 A_0^3 A^2(2i\Omega) \frac{1}{V} \Delta^2 \alpha_0^2 x_0(2i\Omega), \quad (5.53c)$$

$$j_{\parallel}^{(3)C}(3\Omega) = -ie^4 A_0^3 A^2(2i\Omega) \frac{1}{V} \Delta^2 \left(1 - \frac{1}{2} \sin^2(2\chi) \right) \left(2\alpha_0^2 x_0(s) + 2\alpha_1^2 x_3(s) \right), \quad (5.53d)$$

$$j_{\perp}^{(3)C}(3\Omega) = -ie^4 A_0^3 A^2(2i\Omega) \frac{1}{V} \Delta^2 \frac{1}{4} \sin(4\chi) \left(2\alpha_0^2 x_0(s) + 2\alpha_1^2 x_3(s) \right). \quad (5.53e)$$

Now, we write the sums as integrals using the identity Eq. (5.51) and writing $x_0(s) = 2\lambda K(s)$ with

$$K(s) = \int_0^{2\pi} d\varphi f^2 \int_{-\infty}^{\infty} d\epsilon \frac{1}{2E(4E^2 + s^2)} = \int_0^{2\pi} d\varphi f^2 \frac{\sinh^{-1}\left(\frac{s}{2\Delta|f|}\right)}{s\sqrt{4\Delta^2 f^2 + s^2}}. \quad (5.54)$$

This leads to

$$j_{\parallel}^{(3)H}(3\Omega) \propto \alpha_1^2 \Delta^2 A_0^3 \left(1 - \frac{\lambda F(2i\Omega)}{2} - \frac{1}{2\lambda F(2i\Omega)} \right), \quad (5.55a)$$

$$j_{\parallel}^{(3)P}(3\Omega) \propto \alpha_0^2 \Delta^2 A_0^3 2\lambda K(2i\Omega), \quad (5.55b)$$

$$j_{\parallel}^{(3)C}(3\Omega) \propto -\Delta^2 A_0^3 \left(1 - \frac{1}{2} \sin^2(2\chi) \right) \left(4\alpha_0^2 \lambda K(2i\Omega) + \alpha_1^2 (1 - \lambda F(2i\Omega)) \right), \quad (5.55c)$$

$$j_{\perp}^{(3)C}(3\Omega) \propto -\Delta^2 A_0^3 \frac{1}{4} \sin(4\chi) \left(4\alpha_0^2 \lambda K(2i\Omega) + \alpha_1^2 (1 - \lambda F(2i\Omega)) \right). \quad (5.55d)$$

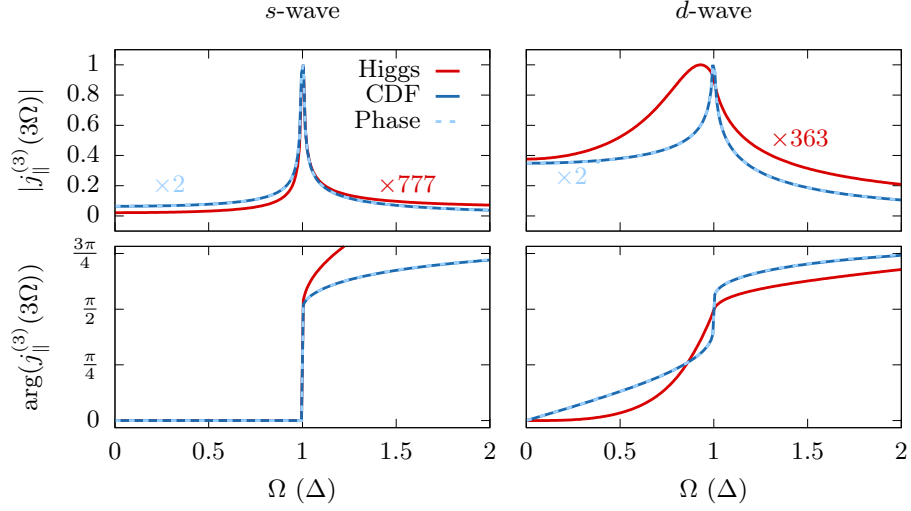


Figure 5.3 Individual contributions of the current $j_{\parallel}^{(3)}(3\Omega)$ for s - and d -wave originating from Higgs, CDF and phase oscillations using Eqs. (5.55a), (5.55b) and (5.55c). The phase and CDF contribution lie approximately on top of each other. The parameters are $\Delta = 20$ meV, $\chi = 0$, $\lambda = 0.1$ and $\alpha_0 = -\epsilon_F/2$, $\alpha_1 = -0.5$ with $\epsilon_F = -400$ meV assuming the tight-binding dispersion (5.14). Figure adapted from [8].

These are the final expressions for the THG currents derived in this chapter.

The first term $j^{(3)H}(3\Omega)$ is the Higgs contribution following from the amplitude oscillation of the order parameter. The second term $j^{(3)P}(3\Omega)$ follows from the oscillation of the imaginary part of the gap, i.e. oscillations of the phase. The third term $j^{(3)C}(3\Omega)$ describes charge density fluctuations as the expression has the form of a density-density correlation function [45]. Each of the three terms for the current contribute to the THG intensity

$$I_{\parallel\perp}^{\text{THG}} \propto \left| j_{\parallel\perp}^{(3)}(3\Omega) \right|^2. \quad (5.56)$$

Within the chosen assumptions we obtain an important result, namely that the Higgs and phase contributions are polarization-independent and their contributions perpendicular to the polarization vector vanish. In case of the CDF, both parallel and perpendicular contributions exist and are polarization-dependent with a characteristic functional form independent of the gap symmetry and dispersion. Both expressions $K(2i\Omega)$ occurring in the phase and CDF terms as well as $1/F(2i\Omega)$ in the Higgs term diverge for $2\Omega = 2\Delta$ in the s -wave case or show a maximum in the d -wave case. Hence, the resonance of the amplitude oscillation with the Higgs mode is not the only cause of the peak found in the THG. In particular, the individual strengths are determined by the parameters λ and α_0 .

For $\alpha_0 = 0$, e.g. the half-filling case in the tight-binding model, the resonance due to the K term vanishes, which removes the phase contribution completely and suppresses the CDF term strongly. For a polarization value of $\chi = \pi/4$, the perpendicular CDF contribution vanishes and the diverging part due to K in the parallel contribution cancels exactly the phase contribution. The polarization dependence will be discussed in more detail in section 5.2.2. For large λ , i.e. large interaction strength, the CDF contribution is enhanced over the Higgs contribution. It can be understood in such a way that the resonance term for the Higgs contribution scales with $\frac{1}{\lambda}$ due to the $\frac{1}{F}$ term, whereas the resonance term for the CDF contribution scales with λ due to

the K term. Therefore, one can roughly estimate that $j_{\parallel}^{(3)H}(3\Omega) \propto 1/\lambda^2 j_{\parallel}^{(3)C}(3\Omega)$.

In Fig 5.3, a comparison of the individual contributions for the s - and d -wave case are shown by evaluating the expressions (5.55a), (5.55b) and (5.55c) for typical parameters. We can see that the CDF term exceeds the Higgs term by more than two orders of magnitude. Within the chosen approximations and parameters, the phase term is roughly 1/2 of the CDF term. Both terms, CDF and phase, show a sharp peak at $2\Omega = 2\Delta$ for the s - and d -wave case. This results from the resonance in $K(2i\Omega)$, which is sharply peaked at 2Δ independent of the pairing symmetry. The shape of the Higgs term, originating from the resonance in the amplitude oscillation $1/F(2i\Omega)$, follows the shape shown in Fig. 5.2, i.e. a sharp peak for s -wave and a broad peak for d -wave. Again for d -wave, there is a lot of weight in the range $2\Omega < 2\Delta$ as for any Ω , there is always a $\Delta_{\mathbf{k}}$ for which $2\Omega = 2\Delta_{\mathbf{k}}$ leading to an enhancement of the amplitude. The phase change in the s -wave case is sharp for all contributions, while for the d -wave case, there are small differences. The phase change in the Higgs term is similar to the phase change of the amplitude oscillation, while the phase change of the CDF and phase term is smooth in the beginning but contains a steep step around $2\Omega = 2\Delta$.

Despite the fact that the CDF contribution exceeds the Higgs contribution in our simple analysis, it is still useful for the understanding of the physical mechanisms. The actual weighting of the terms in an experiment depends strongly on the material by further effects not considered in our analysis, like retardation effects in materials with phonon-mediated interaction [46] or the paramagnetic coupling for superconductors in the dirty-limit [65–68, 70, 74].

After having gained a first understanding of the terms contributing to the THG intensity under the chosen assumptions for $\epsilon_{\mathbf{k}}$ and $f_{\mathbf{k}}$, we will drop these in the following sections and solve the summations numerically without approximation and also include the temperature dependence. This allows for arbitrary dispersion and gap symmetries to be considered, which can introduce new features like additional resonances and polarization dependencies.

5.2.1 Temperature Dependence

In all current experiments so far, the driving frequency cannot be tuned continuously as done in the theoretical analysis of the previous section. In order to find the resonance, the driving frequency is fixed and the temperature is varied until $2\Omega = 2\Delta_T$ is fulfilled [39]. In the following, we will solve the sums (5.45a)-(5.45g) numerically without further approximations. For details about the implementation and used parameters, see appendix A.5.

In Fig. 5.4, the temperature dependence of the THG intensity and the phase shift for d -wave in comparison with s -wave are shown for different driving frequencies. For driving frequencies $\Omega > \Delta$, no resonance occurs and the THG intensity follows the temperature dependence of the energy gap to the power of four, i.e. $\sim \Delta_T^4$ roughly, which can be seen in Eq. (5.55). As soon as $\Omega < \Delta$, there is a temperature where $\Omega = \Delta_T$ and a resonance occurs. There are two main differences in the intensities of s - and d -wave for the Higgs contribution (dotted lines). First, for the same driving frequency, the resonance peaks are broader for d -wave as there is no single resonance point as in the s -wave case. Second, due to the continuous variation of the gap from 0 to Δ for d -wave, there is always some resonant gap for temperatures $T < T_R$, where T_R is the temperature for which $\Omega = \Delta_{T_R}$. This leads to a larger THG intensity background in that temperature range. One can also see that for the chosen parameters, the CDF contribution dominates as there is still a sharp resonance peak in the total d -wave intensity.

Even though the calculation for a pure s -wave order parameter compared to a pure d -wave order

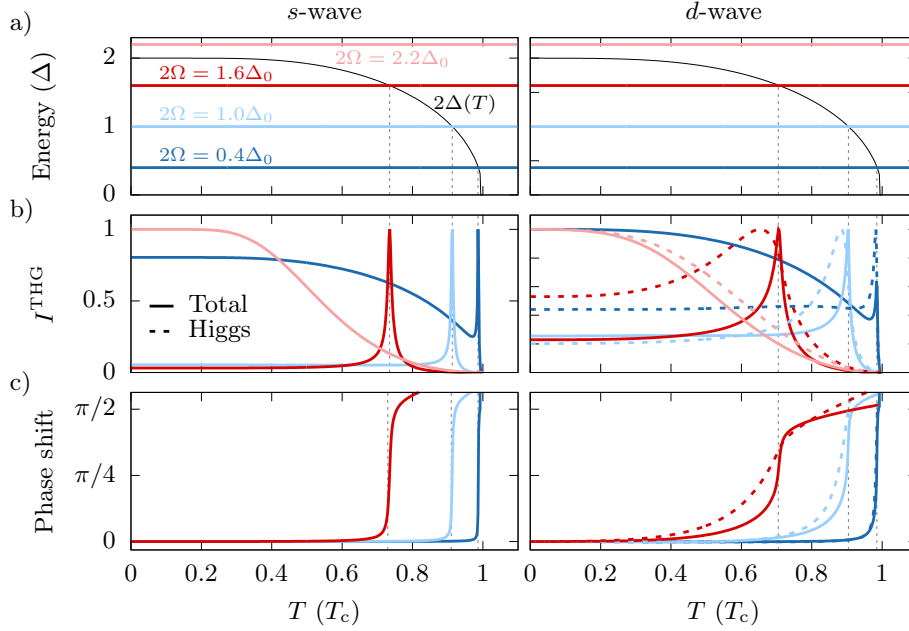


Figure 5.4 Temperature dependence of THG intensity for s -wave (left) and d -wave (right) for four different driving frequencies. a) Driving frequencies in relation to the energy gap. b) THG intensity c) Phase shift of THG signal. The polarization is $\chi = 0$. The solid lines are the full THG intensity, the dotted lines only the Higgs contribution. All intensities are normalized to their individual maximum. For details about the parameters, see appendix A.5. Figure adapted from [8].

parameter shows a clear difference in the peak-to-background ratio for the Higgs contribution, a comparison of intensities in an experiment is difficult. On the one hand, there is nothing to compare to for a given material. On the other hand, peak intensities can vary due to additional damping effects, which makes a clear distinguishing unreliable.

The phase analysis confirms the analytic result in Fig. 5.3. For s -wave, a sharp phase jump of $\pi/2$ occurs at the resonance, whereas for d -wave, the phase jump is much broader.

After having studied the d -wave case, we want to explore whether a multigap structure can also be seen in the THG response. To this end, we will investigate the $d+s$ -wave case, as already introduced in section 3.1.1 in Eq. (3.47). In the quench analysis, we have seen that the gap structure results in two Higgs modes peaked at the local maxima. The temperature dependence of the THG intensity is shown in Fig. 5.5. In the upper row, we show the temperature dependence of the two local gap maxima, i.e. $\Delta_1^{\max} = \Delta$ and $\Delta_2^{\max} = 0.8\Delta$. We can see that if $\Omega < \Delta_2^{\max}$, two resonances occur when the driving frequency matches these two maxima. This can be seen both in the THG intensity as two peaks and in the phase where a broad phase transition occurs in the range of the two resonance temperatures with sharp kinks at the resonance points.

It is interesting to note that the two-peak structure is an effect originating alone from the Higgs contribution despite its smaller value. While the CDF contribution only shows a single peak, it is the Higgs contribution which shows the two-peak structure. We can understand this as two Higgs modes at energies Δ_1^{\max} and Δ_2^{\max} for each local gap maxima, which resonate with the driving frequency. This shows that even if the CDF contribution dominates, the Higgs

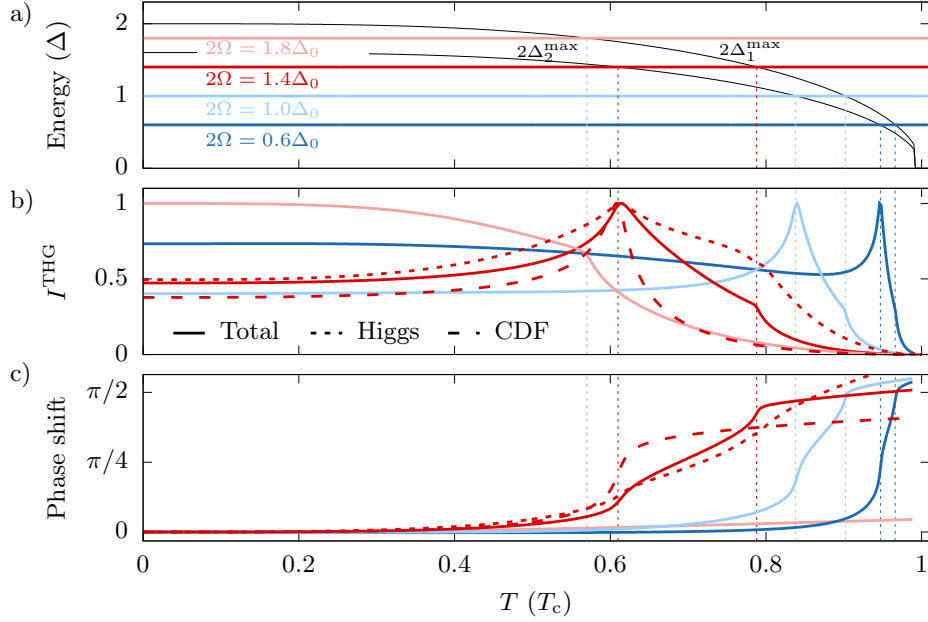


Figure 5.5 Temperature dependence of THG intensity for $d+s$ -symmetry. a) Driving frequency in relation to the temperature-dependent maxima of the energy gap. b) THG intensity. Total THG intensity is shown with solid lines and exemplary for one driving frequency, the respective CDF (dashed) and Higgs (dotted) contribution. The intensity values are normalized individually to their maximum. c) Phase shift of THG signal. For details about the parameters, see appendix A.5. Figure adapted from [8].

contribution may still contribute to specific features visible in the spectrum. If the polarization is tuned to $\chi = \pi/4$, the CDF contribution contains a two-peak structure as well. This results from the fact that the previously dominant K term in Eq. (5.55c) is suppressed due to the equivalent term with opposite sign in Eq. (5.55b). The single-peak structure of the K term vanishes and the smaller F term with the two-peak structure becomes visible. We can conclude this section by stating that additional Higgs modes present due to nontrivial pairing symmetries can be observed in the THG spectrum as additional resonances.

5.2.2 Polarization Dependence

As stated above, one possibility to gain more insight about the relative weight of Higgs and CDF contributions in an experiment is the polarization dependence. As one can see in Eq. (5.55c), the CDF contribution has a characteristic polarization dependence, whereas the Higgs and phase terms do not depend on the polarization, independent of the gap symmetry. If there is no polarization dependence in an experiment, it can be a hint that the Higgs contribution is stronger than the CDF part. This was observed in [105], where it was concluded that in NbN, the Higgs contribution dominates the THG intensity. If we look at the expressions (5.55c) and (5.55b) for the CDF and phase contribution of the current, we can see that for $\chi = \pi/4$, the $K(2i\Omega)$ term in the CDF expression cancels exactly the $K(2i\Omega)$ term in the phase expression. This means that for this particular polarization angle, only the Higgs contribution remains.

However, the derived formulas for the current are only valid under the chosen special assump-

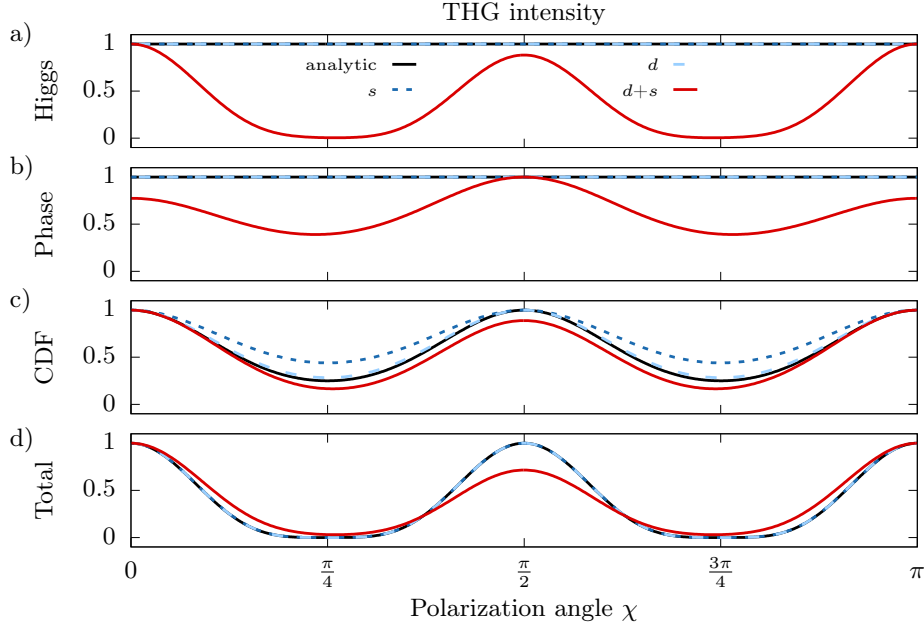


Figure 5.6 Polarization dependence of the a) Higgs contribution, b) phase contribution, c) CDF contribution and d) total THG intensity. The analytic formulas of Eqs. (5.55a)-(5.55c), derived using the assumption of equivalence of x - and y -direction in $f_{\mathbf{k}}^2$ and $\epsilon_{\mathbf{k}}$, are compared with the numerically calculated results for s - and d -wave using dispersion Eq. (5.14) and $d+s$ -wave using dispersion Eq. (5.57) without approximation. The analytic solution matches exactly the numerical solution for s - and d -wave. All expressions are normalized to their maximum value. For details about the parameters, see appendix A.5. Figure adapted from [8].

tions that $f_{\mathbf{k}}^2$ and $\epsilon_{\mathbf{k}}$ are symmetric under the exchange of $k_x \leftrightarrow k_y$, as it is the case for s - or d -wave symmetry and a single band tight-binding dispersion. For the $d+s$ -wave case this is no longer valid. In Fig. 5.6, the polarization dependence for s -, d - and $d+s$ -symmetry calculated numerically is shown in comparison with the analytic result. To show the influence of the dispersion, we use a slightly distorted square lattice dispersion in the $d+s$ -wave case

$$\epsilon_{\mathbf{k}} = -2t((1 + \delta_0) \cos k_x + (1 - \delta_0) \cos k_y) - 4t' \cos k_x \cos k_y - \epsilon_F \quad (5.57)$$

with $\delta_0 = -0.03$, $t = 200$ meV, $t' = -80$ meV and $\epsilon_F = -240$ meV [186]. One can see that for s - and d -wave, the numerical result follows the approximation closely, i.e. the Higgs contribution is polarization-independent and the CDF contribution has a $\propto 1 - \frac{1}{2} \sin^2(2\chi)$ dependence with a small offset resulting from the chosen approximations in the analytic calculation. This changes for $d+s$, where the Higgs and phase terms also become polarization-dependent and the polarization dependence of the total THG intensity deviates from the analytic formula. Choosing a different dispersion can lead to another polarization dependence. We can see that the polarization dependence alone is not enough to unambiguously distinguish between Higgs and CDF contributions if the band dispersion is not exactly known. This was also concluded in [47], where it was shown that under certain circumstances, the Higgs contribution can become polarization-dependent as well, while the polarization dependence of the CDF contribution can be suppressed.

5.2.3 Asymmetric Driving

In an experiment, the coupling of light to the superconducting condensate may contain more subtleties and consists not only of a symmetric diamagnetic A^2 term. For example, small in-plane components of the wavevector, as discussed in chapter 4, may induce an asymmetry while driving.

Here, a phenomenological asymmetric driving scheme is explored to describe generally such effects in an experiment. Due to a momentum-dependent driving, the gap symmetry is altered by an additional symmetry component f'_k . We add such a term to the pseudomagnetic field altering the gap symmetry with the same time dependence as the usual driving term

$$\mathbf{b}_k = \begin{pmatrix} -2\Delta'(f_k + g \sin^2(\Omega t) f'_k) \\ 2\Delta''(f_k + g \sin^2(\Omega t) f'_k) \\ 2\epsilon_k + \gamma_k^{A^2}(t) \end{pmatrix}, \quad (5.58)$$

where g determines the strength of the asymmetric driving. In comparison to the static quench of the condensate in chapter 3.2, here, we drive the gap directly. There is some similarity to [94], where, however static and ab initio, a composite pairing interaction leads to multiple Higgs modes in the different pairing channels.

This approach is purely phenomenological and neglects additional polarization dependencies, which are likely to occur due to the asymmetric driving. As the polarization dependence is difficult to predict without a detailed understanding of the actual microscopic coupling, we neglect it in this approach.

Using the modified pseudomagnetic field and performing a linearization in the same way as in the previous sections, one would neglect important contributions of the products between the asymmetric driving term and the deviations, e.g. $g \sin^2(\Omega t) f'_k x_k(t)$, etc. Therefore, in this section, the Bloch equations are solved numerically without any approximation by integrating the differential equations in time. As we have not added an additional polarization dependence, we can suppress the CDF contribution by choosing $\chi = \pi/4$ to obtain the contribution of the Higgs channel.

In Fig. 5.7, we show the temperature dependence of the THG intensity for a d -wave gap with an asymmetric driving $f'_k = 1$, i.e. a distortion in the s -wave channel. This corresponds to driving the B_{1g} mode of the d -wave gap. It does not correspond to any experimental excitation scheme directly but acts as a proof of principle to study the induced effects. Any possible experimental realizations are likely a superposition of fundamental symmetries. For low driving frequencies, one can observe a second resonance peak in the THG signal below the 2Δ peak, which is also accompanied by a phase change of $\pi/2$. Higher driving frequencies do not show such a resonance. This can be understood better by calculating the frequency dependence of THG for different temperatures from which one can extract the temperature dependence of the modes. For the chosen set of parameters, the resulting curve of the second mode follows approximately $\omega_{B_{1g}} = 0.44\Delta_T$, which is also shown in Fig. 5.7a). As one can see, the chosen higher driving frequency of $2\Omega = \Delta$ always stays above the second mode, which explains that there is no second resonance peak. For the lower driving frequency of $2\Omega = 0.4\Delta$, the second resonance peak appears at the point where $2\Omega = \omega_{B_{1g}}$.

This short analysis acts as a proof of principle to show that an asymmetrically driven superconductor can show additional resonances in the THG spectrum. The chosen approach is purely phenomenological and does not directly correspond to an experimental excitation scheme. Yet, it demonstrates possible new effects resulting from special driving geometries.

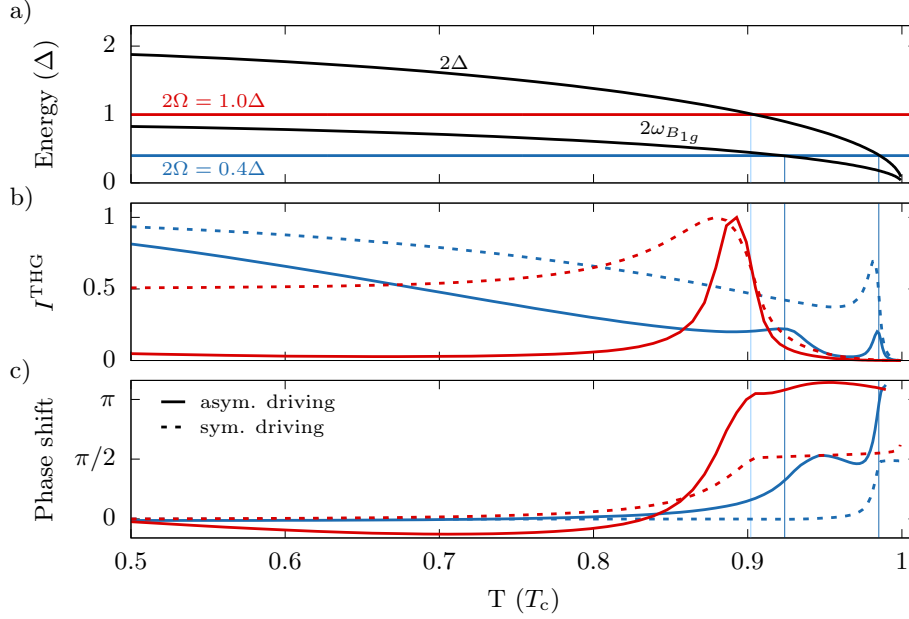


Figure 5.7 Temperature dependence of THG for d -wave for two different driving frequencies using the asymmetric driving scheme (5.58) with $g = 0.1$. a) Driving frequencies in relation to the energy gap and the second mode. b) THG intensity. c) Phase shift of THG signal. The result of the asymmetric driving (solid) is compared with the standard driving (dashed). For details about the parameters, see appendix A.5. Figure adapted from [8].

5.3 Linear Activation of Higgs Oscillations in Current-carrying States

In all chapters of this thesis, the coupling of light to the condensate was realized due to the nonlinear, quadratic coupling. The reason was the already mentioned property of the Higgs mode of being without charge. It has no dipole moment; thus, a linear activation is forbidden. The Hamiltonian is particle-hole symmetric and any linear coupling term vanishes due to parity.

However, a recent theoretical study investigated the excitation of the Higgs mode in superconductors carrying a supercurrent [80]. It was found that in the presence of the current, a linear activation is possible. With this mechanism, the Higgs mode can be probed in the linear regime. In contrast to the $2\Omega = 2\Delta$ resonance visible in the THG spectrum as discussed in the previous sections, now, a $\Omega = 2\Delta$ resonance occurs. The reason for this linear activation results from the fact that the current destroys particle-hole symmetry and provides additional momentum such that a linear coupling term is possible.

After this theoretical prediction, an experiment on the superconductor NbN was performed, which was driven by a dc supercurrent [109]. Indeed, a resonant behavior in the linear response could be observed. The question arises how this linear excitation can be understood on a microscopic level. The experiment claimed the excitation to be an infrared activation. Yet, one can ask whether the Higgs mode really changes its nature in the presence of the supercurrent and is excited by a single photon and thus, becomes infrared active.

This section investigates the linear excitation of the Higgs mode in the presence of a dc supercurrent to understand the process on a microscopic level. One finds that the activation can

be understood as a *current-assisted Raman* process, which can be described coherently within the usual two-photon excitation picture. It also fits within the description of the Higgs excitation due to a *difference-frequency generation* (DFG) or *sum-frequency generation* (SFG) process. This section is based on the publication [11], from which figures, text and calculations are partly taken.

5.3.1 Phenomenological Description

To describe the coupling of light to current-carrying superconductors, we start with a phenomenological description using the effective Lagrangian introduced in section 2.1.3

$$\mathcal{L} = (\partial_\mu H)(\partial^\mu H) + 2\alpha H^2 - \frac{1}{4}\mathcal{F}_{\mu\nu}\mathcal{F}^{\mu\nu} + e^2\psi_0^2 A_\mu A^\mu + 2e^2\psi_0 A_\mu A^\mu H, \quad (5.59)$$

where H are the amplitude (Higgs) oscillations and A_μ the gauge field. As discussed, there is only a quadratic coupling term $2e^2\psi_0 A_\mu A^\mu H$ between the gauge field and the Higgs mode. Now, we model both the coupling of the external driving with light and the dc supercurrent by the gauge field A^μ . The superconductor shall be driven by a periodic light field $\mathbf{A}(t) = \mathbf{A}_0 e^{i\Omega t}$ and simultaneously carry a constant dc supercurrent j . The gauge invariant expression for the current reads $\mathbf{j} = en_s \hbar/m(e\mathbf{A} - \nabla\theta) = en_s \hbar/m\mathbf{Q}$, with the superfluid density n_s and condensate momentum \mathbf{Q} . As discussed in 2.1.3, the phase (Goldstone) mode θ can be gauged out by a special gauge choice and redefinition of the gauge field A_μ . Thus, we include the condensate momentum in the gauge field as

$$A_\mu = \left(0, \mathbf{A}(t) + \mathbf{Q}/e\right). \quad (5.60)$$

Hereby, we choose the scalar potential $\phi = 0$. According to Eq. (2.20), the equation of motion for spatially constant Higgs field H reads

$$\begin{aligned} \partial_t^2 H &= 2\alpha H + e^2\psi_0 \left(\mathbf{A} + \frac{1}{e}\mathbf{Q}\right)^2 \\ &= 2\alpha H + e^2\psi_0 \mathbf{A}^2 + 2e\psi_0 \mathbf{Q}\mathbf{A} + \psi_0 \mathbf{Q}^2. \end{aligned} \quad (5.61)$$

One observes that for finite \mathbf{Q} , a linear coupling term $2e\psi_0 \mathbf{Q}\mathbf{A}$ arises. To solve the equation of motion, we choose a stationary solution ansatz $H = A + B e^{i\Omega t} + C e^{2i\Omega t}$. One obtains as solution

$$H = \frac{\psi_0 \mathbf{Q}^2}{\omega_H^2} - \frac{2e\psi_0 \mathbf{Q} A_0}{\Omega^2 - \omega_H^2} e^{i\Omega t} - \frac{e^2 \psi_0 A_0^2}{4\Omega^2 - \omega_H^2} e^{2i\Omega t} \quad (5.62)$$

with the energy of the Higgs mode $\omega_H^2 = -2\alpha$ as defined in Eq. (2.9a). For $\mathbf{Q} = 0$, only the nonlinear driven oscillations exists with $\omega = 2\Omega$ resonating at $2\Omega = 2\Delta$. This corresponds to the periodically driven Higgs oscillation at 2Ω discussed in the previous sections, leading to the resonant behavior in THG. For $\mathbf{Q} \neq 0$, a linear coupling is possible resulting in an oscillation with $\omega = \Omega$ resonating at $\Omega = 2\Delta$. This corresponds to a second-harmonic generation (SHG) in transmission with a modified resonance condition. Using similar arguments, this result of linear coupling was first derived in [80]. In general, one could have included an additional nonrelativistic Gross-Pitaevskii-like term $\propto \psi^* D_0 \psi$ in addition to the relativistic Klein-Gordon-like description of the dynamic. However, it is known that in the nonrelativistic case, there is no distinct Higgs

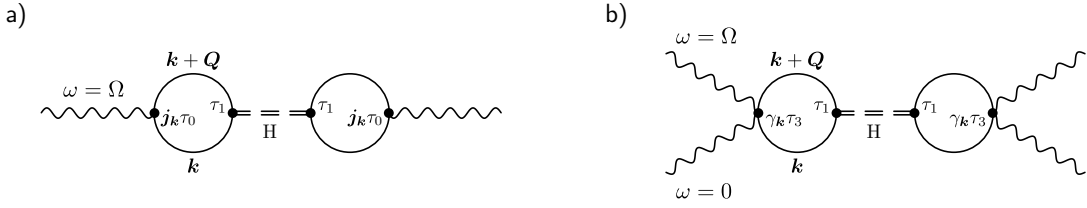


Figure 5.8 Feynman diagrams describing excitation of Higgs mode in current-carrying state with condensate momentum \mathbf{Q} and light frequency Ω . a) Single-photon infrared excitation with $j_{\mathbf{k}} \propto \partial_{\mathbf{k}} \epsilon_{\mathbf{k}}$. b) Effective Raman excitation with $\gamma_{\mathbf{k}} \propto \partial_{\mathbf{k}}^2 \epsilon_{\mathbf{k}}$. Wiggly, solid and double-dashed lines represent photon, electron and Higgs propagator. Figure adapted from [11].

mode as amplitude and phase channel are coupled [10]. Despite the fact that a current would support a particle-hole breaking term, its contribution cannot be large. Otherwise, a resonance at ω_H is not explainable.

Within this phenomenological description, we can describe the arising of a linear activation of the Higgs mode. Yet, it does not give insight how the linear coupling on a microscopic level is possible. At first glance, an infrared activation described by the diagram in Fig. 5.8a) seems reasonable, where light couples linearly to the electron bubble and the current provides additional momentum \mathbf{Q} within an effective vertex interaction. Yet, an evaluation of this diagram shows that for $\mathbf{Q} \rightarrow 0$, the response vanishes [11]. This is expected as for $\mathbf{Q} = 0$, there is no linear coupling. For small but finite \mathbf{Q} , the diagram is still negligible compared to the effective Raman process, which we will discuss next. Only for large \mathbf{Q} , the response of this diagram becomes significant; however, its response is no longer peaked at 2Δ but is shifted to higher energies. This can also be seen in the dispersion Eq. (2.9a) for the Higgs mode, which has a quadratic dependence on q . As such a shift is neither expected theoretically nor observed experimentally, the value of \mathbf{Q} must be small. Using parameters of the experiment in [109], one can estimate the value of the supercurrent induced momentum in units of the lattice constant $1/a_0 = 10^8 \text{ cm}^{-1}$

$$Qa_0 = \frac{m}{en_s \hbar} ja_0 \approx 3.7 \cdot 10^{-4} \quad (5.63)$$

with electron mass $m = m_e$ and charge e , superfluid density $n_s = 5.4 \cdot 10^{20} \text{ cm}^{-3}$ and current density $j = 3.7 \text{ MA/cm}^2$. The contribution of the diagram for this small value of Q is negligible. Thus, an infrared activation via such a process cannot explain a resonance at $\Omega = 2\Delta$ in the current-carrying state. To find a suitable description of the excitation process, one can be guided by a microscopic description, to which we will proceed in the next section.

5.3.2 Microscopic Description

To gain an understanding of the microscopic excitation process of the Higgs mode in the presence of a supercurrent, we extend the description of section 5.1 including the current in the pseudospin formulation. In addition to the light field $\mathbf{A}(t)$, we include the effect of the current by a shift of momentum \mathbf{Q} . Thus, the pseudomagnetic field reads

$$\mathbf{b}_{\mathbf{k}}^\top(t) = \left(-2\Delta_{\mathbf{k}}(t), \quad 0, \quad \epsilon_{\mathbf{k}-e\mathbf{A}(t)-\mathbf{Q}} + \epsilon_{\mathbf{k}+e\mathbf{A}(t)+\mathbf{Q}} \right). \quad (5.64)$$

Hereby, the imaginary part of the gap is neglected as it does not show a resonance behavior as shown in section 5.1 in Eq. (5.31). It is therefore unimportant for the following discussion. Now, we can expand again the z -component of the pseudomagnetic field in powers of A_0

$$b_{\mathbf{k}}^z \approx 2\epsilon_{\mathbf{k}} + \gamma_{\mathbf{k}}^{A^2}(t) + \gamma_{\mathbf{k}}^{AQ}(t) + \gamma_{\mathbf{k}}^{Q^2} + \mathcal{O}(A_0^3) \quad (5.65)$$

with $\gamma_{\mathbf{k}}^{A^2}(t)$ defined in Eq. (5.6) and

$$\gamma_{\mathbf{k}}^{AQ}(t) = 2e \sum_{ij} \partial_{ij}^2 \epsilon_{\mathbf{k}} A_i(t) Q_j = 2e A_0(t) D_{\epsilon_{\mathbf{k}}}^{AQ}(\chi), \quad (5.66a)$$

$$\gamma_{\mathbf{k}}^{Q^2} = \sum_{ij} \partial_{ij}^2 \epsilon_{\mathbf{k}} Q_i Q_j = D_{\epsilon_{\mathbf{k}}}^{Q^2}, \quad (5.66b)$$

where

$$D_{\epsilon_{\mathbf{k}}}^{AQ}(\chi) = \cos(\chi) Q_x \partial_{xx}^2 \epsilon_{\mathbf{k}} + \sin(\chi) Q_y \partial_{yy}^2 \epsilon_{\mathbf{k}} + (\cos(\chi) Q_y + \sin(\chi) Q_x) \partial_{xy}^2 \epsilon_{\mathbf{k}}, \quad (5.67a)$$

$$D_{\epsilon_{\mathbf{k}}}^{Q^2} = Q_x^2 \partial_{xx}^2 \epsilon_{\mathbf{k}} + Q_y^2 \partial_{yy}^2 \epsilon_{\mathbf{k}} + 2Q_x Q_y \partial_{xy}^2 \epsilon_{\mathbf{k}}. \quad (5.67b)$$

Compared with the $\mathbf{Q} = 0$ case, a linear coupling term $\gamma_{\mathbf{k}}^{AQ}(t)$ arises in analogy to the phenomenological description in the previous section. In the same way as in section 5.1 in Eq. (5.9), we can write down linearized Bloch equations in Laplace space

$$s x_{\mathbf{k}}(s) = -2\epsilon_{\mathbf{k}} y_{\mathbf{k}}(s), \quad (5.68a)$$

$$s y_{\mathbf{k}}(s) = 2\epsilon_{\mathbf{k}} x_{\mathbf{k}}(s) + 2f_{\mathbf{k}} \Delta z_{\mathbf{k}}(s) + \frac{f_{\mathbf{k}}}{E_{\mathbf{k}}} \left(\frac{\Delta}{2} \left(\gamma_{\mathbf{k}}^{A^2}(s) + \gamma_{\mathbf{k}}^{AQ}(s) + \gamma_{\mathbf{k}}^{Q^2}(s) \right) - \epsilon_{\mathbf{k}} \delta \Delta(s) \right), \quad (5.68b)$$

$$s z_{\mathbf{k}}(s) = -2\Delta f_{\mathbf{k}} y_{\mathbf{k}}(s), \quad (5.68c)$$

where the solution for $x_{\mathbf{k}}(s)$ reads

$$x_{\mathbf{k}}(s) = \frac{\epsilon_{\mathbf{k}} f_{\mathbf{k}} \left(2\epsilon_{\mathbf{k}} \delta \Delta(s) - \Delta \left(\gamma_{\mathbf{k}}^{A^2}(s) + \gamma_{\mathbf{k}}^{AQ}(s) + \gamma_{\mathbf{k}}^{Q^2}(s) \right) \right)}{E_{\mathbf{k}} (4E_{\mathbf{k}}^2 + s^2)}. \quad (5.69)$$

Hereby, the Laplace transform of the quadratic coupling term is given in Eq. (5.11) and for the new terms, it follows

$$\gamma_{\mathbf{k}}^{AQ}(s) = 2e A_0 \frac{\Omega}{\Omega^2 + s^2} D_{\epsilon_{\mathbf{k}}}^{AQ}(\chi), \quad (5.70a)$$

$$\gamma_{\mathbf{k}}^{Q^2}(s) = \frac{1}{s} D_{\epsilon_{\mathbf{k}}}^{Q^2}. \quad (5.70b)$$

Using the assumptions about isotropy of the dispersion and symmetry function of section 5.1, the interaction terms can be simplified under a summation over \mathbf{k} with an arbitrary factor $a_{\mathbf{k}}$

$$\sum_{\mathbf{k}} \gamma_{\mathbf{k}}^{AQ}(s) a_{\mathbf{k}} = 2e A_0(s) (\cos(\chi) Q_x + \sin(\chi) Q_y) \sum_{\mathbf{k}} (\alpha_0 + \alpha_1 \epsilon_{\mathbf{k}}) a_{\mathbf{k}}, \quad (5.71a)$$

$$\sum_{\mathbf{k}} \gamma_{\mathbf{k}}^{Q^2}(s) a_{\mathbf{k}} = \frac{1}{s} Q^2 \sum_{\mathbf{k}} (\alpha_0 + \alpha_1 \epsilon_{\mathbf{k}}) a_{\mathbf{k}}. \quad (5.71b)$$

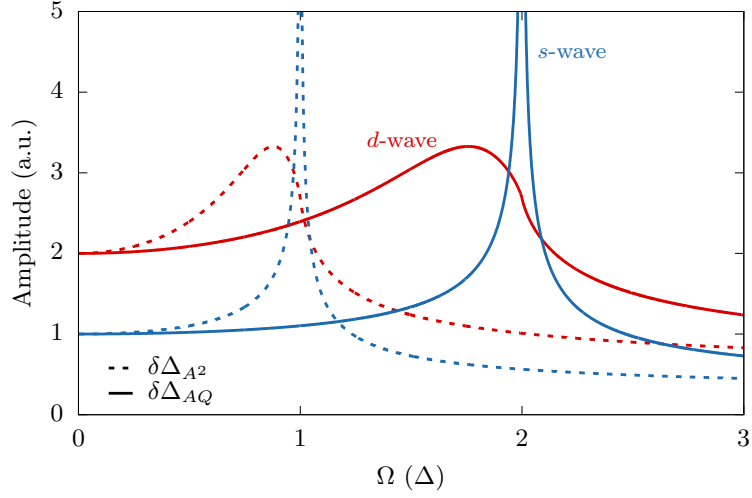


Figure 5.9 Amplitudes of the resonance terms of the induced gap oscillations of Eq. (5.77b) for s -wave superconductor (blue) in comparison to d -wave superconductor (red). Resonances of the driving light with the Higgs mode appear at $\Omega = 2\Delta$ with supercurrent in Eq. (5.77b) (solid lines) and at $2\Omega = 2\Delta$ without in Eq. (5.77a) (dotted lines). Figure adapted from [11].

Splitting the current momentum \mathbf{Q} into components parallel and perpendicular to the polarization

$$\mathbf{Q} = Q_{\parallel} \hat{e}_A^{\parallel} + Q_{\perp} \hat{e}_A^{\perp}, \quad (5.72)$$

we find

$$\sum_{\mathbf{k}} \gamma_{\mathbf{k}}^{AQ}(s) a_{\mathbf{k}} = 2eA_0(s)Q_{\parallel} \sum_{\mathbf{k}} (\alpha_0 + \alpha_1 \epsilon_{\mathbf{k}}) a_{\mathbf{k}}. \quad (5.73)$$

We can see that only the parallel component of the current momentum allows the linear coupling.

The next steps towards a solution for $\delta\Delta(t)$ are straight forward. We insert the solution for $x_{\mathbf{k}}(s)$ of Eq. (5.69) into the gap equation Eq. (5.16a) and we obtain in comparison with Eq. (5.17)

$$\delta\Delta(s) = \frac{1}{2} \alpha_1 \Delta \left(e^2 A_0^2 \frac{2\Omega^2}{s(4\Omega^2 + s^2)} + 2eA_0 Q_{\parallel} \frac{\Omega}{\Omega^2 + s^2} + Q^2 \frac{1}{s} \right) \left(1 - \frac{1}{\lambda F(s)} \right). \quad (5.74)$$

We split the expression into three parts

$$\delta\Delta(s) = \delta\Delta_{A^2}(s) + \delta\Delta_{AQ}(s) + \delta\Delta_{Q^2}(s), \quad (5.75)$$

where each term follows from the respective interaction. For the inverse Laplace transform, we use the same contour as shown in Fig. 5.1. The linear part $\delta\Delta_{AQ}(s)$ has poles at $s = \pm i\Omega$ and the constant part $\delta\Delta_{Q^2}(s)$ a pole at $s = 0$. In the following, we neglect the constant part as it only adds an irrelevant offset to the solution. The long-time solution is again given by the residues of the poles. For the linear term, it follows

$$\begin{aligned} \text{Ind}_{c_{2,7}}(\pm i\Omega) \text{Res}_{\pm i\Omega}(e^{st} \delta\Delta_{AQ}(s)) = \\ \frac{1}{2} \alpha_1 \Delta e A_0 Q_{\parallel} \left(\mp i e^{\pm i\Omega} \pm \frac{i\Omega e^{\pm i\Omega}}{\lambda \int d\varphi f^2 \sqrt{4\Delta^2 f^2 - \Omega^2} \sin^{-1}\left(\frac{\Omega}{2\Delta|f|}\right)} \right). \end{aligned} \quad (5.76)$$

Using the solution (5.25c) for the quadratic coupling, the final long-time solution of the oscillations reads

$$\delta\Delta_{A^2}(t) = \alpha_1 \Delta e^2 A_0^2 \left(\frac{1 - \cos(2\Omega t)}{4} - \frac{1}{4\lambda \int d\varphi f^2} + \frac{\Omega \cos(2\Omega t)}{4\lambda \int d\varphi f^2 \sqrt{\Delta^2 f^2 - \Omega^2} \sin^{-1}\left(\frac{\Omega}{\Delta|f|}\right)} \right), \quad (5.77a)$$

$$\delta\Delta_{AQ}(t) = \alpha_1 \Delta e A_0 Q_{\parallel} \left(\sin(\Omega t) - \frac{\Omega \sin(\Omega t)}{\lambda \int d\varphi f^2 \sqrt{4\Delta^2 f^2 - \Omega^2} \sin^{-1}\left(\frac{\Omega}{2\Delta|f|}\right)} \right). \quad (5.77b)$$

In addition to the already known 2Ω oscillation, a term oscillating with Ω exists, which was forbidden before. It has a resonance at $\Omega = 2\Delta$ in the s -wave case. The amplitudes of both resonance terms are shown in Fig. 5.9 evaluated for s - and d -wave. The same qualitative behavior compared to the phenomenological description is observed.

Yet, the microscopic description contains further details, which allows to understand the excitation process on a diagrammatic level. From the expansion in Eq. (5.65), we see that both the linear and quadratic couplings are proportional to the second derivative of the dispersion. In addition, the coupling occurs in the z -component of the pseudomagnetic field, i.e. the τ_3 channel, reflecting a Raman coupling [212, 213]. Thus, we might describe both processes, the quadratic and linear coupling, with an effective Raman vertex as shown in Fig. 5.8b). For the quadratic coupling, each incident photon line corresponds to one photon of frequency $\omega = \Omega$, resulting in the $2\Omega = 2\Delta$ resonance. For the linear coupling, one incident photon corresponds to the light photon with $\omega = \Omega$, whereas the second incident photon line is a virtual photon at $\omega = 0$, representing the dc supercurrent. An evaluation of the diagram shows that it is equivalent to the linearized solution in the pseudospin formalism [11]. Thus, such a current-assisted Raman diagram can explain the $\Omega = 2\Delta$ resonance in the current-carrying state.

5.3.3 Interpretation via Current-assisted Raman Process

With the knowledge from the previous section and the analysis of the pump-probe chapter 4, we can summarize and classify the possible excitation schemes of Higgs modes. The processes are shown schematically in Fig. 5.10.

The pump-probe excitation, in which the Mexican hat potential of the complex superconducting order is quenched, can be understood as an impulsive stimulated Raman process [213, 214] shown in Fig. 5.10a). Hereby, the Higgs mode is excited via the difference frequency of the photons Ω_1 and Ω_2 originating from the same pulse. The required frequencies are within the bandwidth of the ultrashort broadband THz pulse. This excitation scheme is used in the experiment on NbN, where the 2Δ Higgs response was observed [36].

In comparison, the periodic driving of the superconductor can be understood in a sum-frequency process, where Raman-active modes are excited [215]. This is shown in Fig. 5.10b). In this case, the two photons $\Omega_1 = \Omega_2 = \Omega$ have the same frequency and add up to an effective 2Ω drive. The 2Ω oscillations of the driven Higgs mode in NbN [39], Nb₃Sn [110, 111] and in cuprates [106, 108], as well as the driven Leggett mode in MgB₂ [216] can be understood in this way. In addition, in analogy to Fig. 5.10a), this process can also describe a quench of the system, where the two photons stem from the same pulse.

The possible infrared excitation of the Higgs mode in the presence of a supercurrent, discussed in the previous sections, would be a one photon absorption process shown in Fig. 5.10c). In this

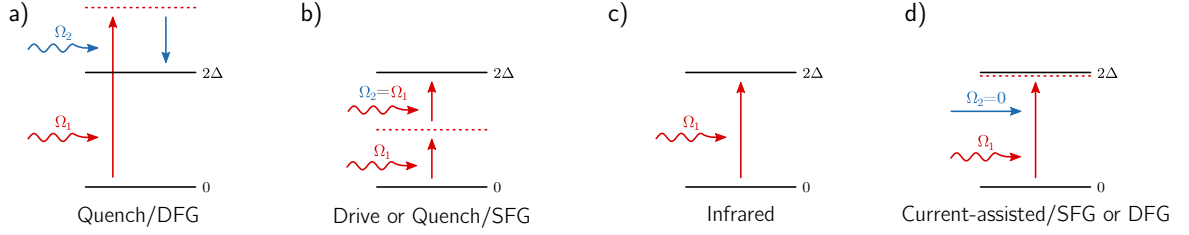


Figure 5.10 Different excitation schemes of Higgs mode. a) Excitation due to quench with two-photon Raman difference-frequency generation (DFG) process. The frequencies Ω_1 and Ω_2 are within the bandwidth of the quench pulse. b) Driving of Higgs mode with two-photon Raman sum-frequency generation (SFG) process. The frequencies of the photons are equal $\Omega_1 = \Omega_2 = \Omega$. Alternatively, a quench can be implemented as SFG process as well, where the two frequencies are within the bandwidth of the quench pulse. c) One-photon infrared process. d) Two-photon current-assisted Raman process with $\Omega_1 = \Omega$ and $\Omega_2 = 0$ reflecting a special case of a SFG or DFG process. Figure adapted from [11].

process, light would couple to the dipole moment of the mode. However, as the previous analysis has revealed, an infrared excitation is not possible. The linear excitation of the Higgs mode in the current-carrying state should rather be understood as a current-assisted Raman process. This process is still a two-photon process, in which one photon $\Omega_1 = \Omega$ corresponds to the light frequency, whereas the second photon $\Omega_2 = 0$ is a virtual photon representing the dc supercurrent. This excitation scheme is depicted in Fig. 5.10d). It can be understood as a difference-frequency generation (DFG) or sum-frequency generation (SFG) process with $\Omega_1 \pm \Omega_2 = \Omega$ in analogy to a) and b) leading to the new resonance condition $\Omega = 2\Delta$. Thus, this description fits coherently in the picture of the usual excitation mechanism. The Higgs mode does not change its nature in the presence of the current as the current-assisted Raman excitation is just a special case.

This mechanism also describes the observation of the Higgs mode in the linear THz spectrum of NbN in the presence of a dc current [109] correctly. Furthermore, it explains the additional Ω and higher uneven orders of Ω oscillations observed in the superconductor Nb₃Sn driven by THz light in recent experiments [110, 111]. Hereby, an effective dc current component is dynamically induced by driving the material with strong THz fields. As a result, the usually forbidden odd orders of Ω oscillations are allowed, describable through the current-assisted Raman process.

5.4 Discussion

Periodic driving of the superconductor with light enforces Higgs oscillations with twice the driving frequency. This happens both for *s*-wave and unconventional superconductors. The driving resonates with the energy of the intrinsic Higgs modes. Thus, for nontrivial gap symmetry, where multiple Higgs modes can occur, multiple resonances can be found in the spectrum. All resonances in the gap oscillation spectrum can also be found in the third-harmonic generation (THG) spectrum, which is the experimental measurable quantity. In addition, driving the superconductor in a symmetry channel different from its ground state can lead to additional resonances resulting from asymmetric Higgs modes. This allows to use THG experiments as an alternative probe for measuring Higgs modes in superconductors.

Here, in the analysis in the clean limit, the contribution of charge density fluctuations (CDF) to the total THG intensity is large and overlays the signal originating from the Higgs mode.

In real materials, impurity scattering can enhance the Higgs contribution significantly [65–70]. A calculation of the polarization dependence shows that under the assumption of isotropy for dispersion and gap symmetry, the Higgs contribution has no polarization dependence independent of the gap symmetry, whereas the CDF depends on the polarization of light. As long as impurity scattering has no preferred direction, the polarization dependence should be unaffected. This allows, in principle, to disentangle which contribution dominates in an experiment. Yet, it is important to note that dropping the assumptions about the isotropy of the dispersion and gap symmetry, the polarization dependence can change. For CDF, the polarization dependence can vary and the Higgs contribution can become polarization-dependent. This was also pointed out in a recent study [47]. Furthermore, even though impurity scattering might not change the overall shape of the polarization dependence of CDF, it can wash out the functional form leading to a reduction of the polarization dependence. This makes the distinction between the CDF and Higgs difficult. For a detailed analysis of the contributing terms measured in an experiment, special care has to be taken considering correct band structure data to interpret the data correctly.

Finally, in the presence of a dc supercurrent, a linear activation of the Higgs mode is possible. The additional momentum of the current gives rise to a new linear driving term. This leads to additional Ω oscillations of the order parameter resonating at a new resonance condition $\Omega = 2\Delta$ in comparison to the usual 2Ω oscillations resonating at $2\Omega = 2\Delta$. Consequently, there will also be a second-harmonic generation in emission, which was previously forbidden. The linear activation can be understood as a current-assisted two-photon effective Raman process, where one photon represents the external light and one photon is a virtual photon with zero frequency representing the dc supercurrent. This contrasts with a one photon infrared activation, which is negligible. Thus, the linear activation of the Higgs mode can be understood as a special case of a sum-frequency generation or difference-frequency generation process.

6 Discussion and Outlook

Summary and Discussion

In this thesis, the nonequilibrium response of unconventional superconductors was studied, which exhibits amplitude (Higgs) oscillations of the order parameter. It was found that the spectrum of these oscillations is more complex for unconventional superconductors compared to conventional superconductors as additional Higgs modes can occur. These oscillations were classified and characterized and it was shown that the extracted information can be used as a new spectroscopic tool to study ground state properties. Furthermore, predictions about new experimental schemes and observables suitable for Higgs spectroscopy were made within a quench or periodic driving setup.

In particular, quenches of the superconducting condensate were studied, which push the system out of equilibrium and trigger a nonequilibrium dynamic and collective Higgs oscillations. To describe the system and calculate the dynamic, the mean field BCS Hamiltonian in the Anderson pseudospin formalism was used. Within this formalism, analytic expressions for the occurring Higgs oscillations were derived and compared with the full numeric solution obtained by integrating the ensuing Bloch equations on a momentum grid.

Two types of quenches were considered, namely, first, an isotropic interaction quench, which is well-known in literature. It was already used to investigate Higgs oscillations in s -wave superconductors. If unconventional superconductors are excited with such a quench, the dynamic resembles the s -wave case, i.e. Higgs oscillations with a frequency of $2\Delta_\infty$ are induced, where Δ_∞ is the asymptotic gap after a long time. However, an important difference was found in the decay of the oscillations. While in the s -wave case, the oscillation decays with $1/\sqrt{t}$, the decay in the d -wave case is much stronger with approximately $1/t^2$. In both cases, the decay results from a dephasing of the underlying condensate oscillation at different momenta, where the frequency is given by the quasiparticle energy $\omega_p = 2E_k = 2\sqrt{\epsilon_k^2 + \Delta_\infty^2 f_k^2}$. Due to the variation of the gap from 0 to Δ in the d -wave case, there is a much wider frequency distribution and thus, a stronger decay.

Second, in order to find new effects resulting from nontrivial pairing symmetry, one has to go beyond the isotropic interaction quench. To this end, a new type of quench was introduced in this thesis. This state quench changes the superconducting condensate directly, which resembles more closely the effect of an experimental excitation with a light pulse, where the quasiparticle distribution is modified due to partly melting the condensate. Moreover, this quench allows a momentum-dependent excitation, which can change the induced Higgs dynamic for nontrivial pairing symmetry. If the superconductor is quenched in a symmetry channel different from its ground state, additional Higgs modes can arise, which result from an asymmetric oscillation of the condensate with respect to the ground state symmetry. These additional modes depend on the gap and quench symmetry and only occur if the change in the symmetry is significant, e.g. a change of nodal lines. Furthermore, for composite order parameters like $d+s$ -wave, an additional Higgs mode already arises in the symmetric excitation case, where each Higgs mode corresponds to the energy of a local gap maximum. Excited asymmetrically, up to three modes are visible. All occurring condensate oscillations can be classified according to the point group of the underlying lattice and a classification and characterization table is provided for all combinations of gap and quench symmetry for the D_{4h} point group.

A quench of a superconductor can be realized experimentally with an ultrafast THz laser pulse. The effect of the pulse is to melt a small portion of the condensate on a short timescale. This fast change in the Cooper pair or quasiparticle distribution acts as a quench and resembles the introduced state quench. To see these effects, pump-probe experiments were simulated by coupling the BCS Hamiltonian to a vector potential, which describes the light pulse. The ensuing equations of motion were solved numerically using a density matrix formalism. In the description of the coupling to light, the physical momentum of the light pulse was considered, which is small but turns out to be non-negligible. The effect of the provided momentum is two-fold. On the one hand, it allows a paramagnetic excitation, which would vanish otherwise, such that the coupling is enhanced. On the other hand, it introduces an asymmetry in the excitation due to a preferred direction resulting from the orientation of the light pulse.

The calculated gap oscillations show that with this description of the light-superconductor coupling, nonequilibrium Higgs oscillations can be excited. In addition, a change in the direction of the light pulse with respect to the pairing symmetry allows to control the asymmetry of the induced oscillation and to excite an additional Higgs mode. To connect the gap response with experimentally observable quantities, the time-resolved optical conductivity was calculated in a pump-probe setup. The Higgs oscillations can be observed as amplitude oscillations of the conductivity as a function of the time delay between pump and probe pulse. This demonstrates that with a carefully designed experimental setup, an excitation and observation of additional Higgs modes in unconventional superconductors is in principle possible. So far, an excitation and observation of Higgs oscillations in a pump-probe setup had only been realized in the *s*-wave system NbN [36]. There are also ongoing efforts to demonstrate Higgs oscillations for cuprates in a pump-probe geometry; yet, these kinds of experiments are difficult to conduct. Clean samples are required and experimental conditions like the usage of the required ultrashort THz laser pulses, heating and overdamping are still challenging problems.

To also study alternative setups, a time-resolved ARPES experiment was proposed and investigated. In comparison to an optical pump-probe experiment, a measurement of the ARPES intensity allows to study the condensate dynamic momentum-resolved. For that, the superconducting condensate was quenched and the time evolution of the experimentally observable spectral function was calculated. The simulation was performed by numerically integrating the equations of motions of the Bogoliubov quasiparticle operators in the Heisenberg picture with the help of the iterated equation of motion method. In contrast to previous theoretical studies on tr-ARPES [41, 42], two different dynamical quantities were considered. The first quantity is the time evolution of the maximum of the energy distribution curve, which is a direct measure of the gap. Confirming literature, oscillations of the position of the maximum in energy with respect to the Fermi level are observable, which correspond directly to the collective Higgs oscillations. Second, for the first time, amplitude oscillations of the spectral function were studied.

As the spectral function relates directly to the underlying condensate, any dynamic induced in the condensate is also observable in the ARPES intensity. This gives access to study the time evolution of the condensate and allows to understand the creation process of collective Higgs modes in detail. The collective Higgs modes result from a weighted summation process of the condensate oscillations over the whole Brillouin zone. Additional Higgs modes arise if the weight distribution of these oscillations is non-uniform, which can enhance different frequencies. Furthermore, by studying the phase of these oscillations, the collective condensate dynamic, e.g. an oscillating or rotating mode, is detectable. As a consequence, if superconductors are quenched in a defined symmetry channel, a distinction between superconducting symmetries with the

same absolute value but different phase, like *d*- or nodal *s*-wave, is possible as the induced condensate movement differs. This opens a new possibility for phase-sensitive measurements of the superconducting gap. So far, no THz quench tr-ARPES experiments have ever been performed. These kinds of experiments are still challenging; yet, first research in this direction has started.

Finally, periodically driven superconductors were studied. The periodic driving enforces the superconducting gap to oscillate with twice the driving frequency Ω due to the quadratic coupling of light to the condensate. It is already known that in the *s*-wave case, the periodic driving can resonate with the energy 2Δ of the Higgs mode, i.e. at $2\Omega = 2\Delta$, a massive enhancement of the Higgs oscillation amplitude occurs [40]. This resonant behavior is observable in the optical response as a resonance in the third-harmonic generation (THG) component and thus, allows a detection of the Higgs mode in such a setup. In this thesis, the periodic driving and THG response of superconductors with nontrivial pairing symmetry were studied. Analytic expressions of the driven gap oscillations and THG response were derived and the temperature and polarization dependence were studied. It was found that the driving also resonates with the 2Δ Higgs mode. Moreover, any other possible Higgs modes lead to additional resonances.

Furthermore, the additional contribution of charge density fluctuation to the THG intensity was analyzed. Unfortunately, as already known from literature [45], in the clean limit, these also lead to resonances at the same energy, which makes an observation of resonances in THG not unique if not special care is taken to disentangle all contributions. In this thesis, it was shown that polarization dependencies are one possibility to differentiate between the individual contributions. Under certain conditions, the polarization dependence for nontrivial symmetry is independent of the pairing symmetry and thus, the same for the already known *s*-wave case. The Higgs contribution is polarization-independent, whereas the CDF contribution is polarization-dependent. Nevertheless, THG experiments are in principle a suitable alternative to pump-probe experiments for the detection of Higgs modes in unconventional superconductors. Actually, until now, most experimental efforts for detecting nonequilibrium Higgs oscillations are in periodically driven or multi-cycle setups, where the transient response of the enforced oscillations is investigated [106, 107, 110, 111]. The resonances in THG were observed in NbN [39, 105] and recent experiments studying THG in different cuprates were performed [108].

If the nonequilibrium response of superconductors carrying a dc supercurrent is studied, a recent study found that a linear activation of the Higgs mode is possible [80], which is usually forbidden due to particle-hole symmetry of the Hamiltonian and the nonexistence of an electric dipole moment of the Higgs mode. In this thesis, the coupling of light to the superconductor in the presence of a dc supercurrent was studied, both on a phenomenological and microscopic level. The new resonance condition due to the linear coupling at $\Omega = 2\Delta$, found in the previous theoretical study and in an experiment [109], was recovered. Beyond that, the analysis reveals that this linear activation should not be understood as a single-photon infrared excitation, as some interpretations suggest [109], but still as an effective two-photon Raman process. Hereby, one photon represents the actual light photon, whereas the other one is a virtual photon with zero frequency representing the dc supercurrent. This interpretation is motivated by the microscopic analysis and in full agreement with the previous results. It also fits into the usual understanding of the Higgs excitation as an effective Raman process within a difference-frequency or sum-frequency generation scheme.

Future Directions of Higgs Spectroscopy

This thesis is only the beginning of further studies of nonequilibrium Higgs oscillations in unconventional superconductors. There are still many open questions and directions in this new field for future research. In this thesis, the classification and characterization of Higgs modes were mainly conducted for fundamental symmetries of the D_{4h} group. Additional important point groups should also be considered. Furthermore, multiband superconductors are also interesting to study with gap symmetries like s^{++} , s^{\pm} , $s + is$, $s + id$ or $d + id$. In these cases, an even richer spectrum is expected as each band will exhibit its own Higgs mode and in addition, Leggett modes, i.e. relative phase modes, can occur as well [33, 48–51, 64]. Moreover, triplet superconductors with e.g. p or chiral $p_x + ip_y$ symmetry are also worth to be considered. The vector character of the gap will probably enrich the spectrum as well.

In real materials, the physics is much more complex compared to the systems studied in this thesis, where mainly the influence of the pairing symmetry was investigated. In a material, competing or coexisting orders and phases can occur like charge density wave, spin density wave or the pseudogap phase. As an example, the charge density wave order in NbSe₂ couples to the Higgs mode and shifts its energy [16]. This coupling is possible despite the fact that the energy of this coexisting order is only close to the energy of the superconducting gap, but still above the gap. Thus, other collective modes, such as the magnetic-resonance mode in cuprates, whose energy is even below the gap, will certainly affect the Higgs spectrum. Moreover, strong coupling regimes are expected to influence collective modes. Furthermore, order parameters can be composite, like the $d+s$ -wave case also studied in this thesis, and there can be subleading pairing channels, which can give rise to collective Bardasis-Schrieffer modes. All of these additional features were not the main focus of this thesis and have been neglected for the most part. However, new effects are certainly expected for all of the mentioned extensions and it is crucial to understand the mechanisms if experimental data should be interpreted correctly for real materials. This will require to go beyond BCS theory including the explicit coupling to other modes or studying the effects in more general systems like the Hubbard model, where additional modes and phases arise naturally.

Another important point to study in more detail is the mentioned influence of the charge density fluctuations on the THG intensity. Even though the results of this thesis suggest that the polarization dependence might be usable to disentangle the contributions, the results are derived under certain conditions. Other studies have also shown [47] that the results are model-dependent and thus, can vary from system to system, which makes the polarization dependence criteria not easy to use. In this context, it is also worth to study the influence of impurity scattering in dirty superconductors. So far, most studies of quench, pump-probe or periodically driven excitation of Higgs modes were performed in the clean limit. Only few studies exist [65, 67, 68, 70], which include the effects of impurity scattering. New studies have to answer important questions like how and how much the Higgs contribution to THG is enhanced due to an additional paramagnetic coupling as the first studies suggest. Furthermore, how does the impurity scattering influence the polarization dependence? How is the damping of the oscillations changed? Is there an influence on the time-resolved optical conductivity? Does the response of multiband superconductors change? All of these questions are still unresolved and need further investigations.

The experimental excitation schemes also need further research. Unresolved questions include, how exactly the coupling to a light pulse happens experimentally. Does the phase of single-cycle pulses play a role and does it couple to the phase of the superconductor, which would allow

for additional phase-sensitive information to be extracted? What does actually determine the quench of the superconductor within a pump pulse? As the calculation has shown, even multi-cycle pulses longer than the intrinsic time scale of the Higgs oscillations can quench and induce Higgs oscillations for higher fluence. Does the subcycle dynamic play a role? Concerning the realization of the proposed state quenches in symmetry channels different from the ground state symmetry, there are also open questions to be answered. One possibility of an asymmetric quench was proposed in this thesis by an in-plane light wave momentum inducing a preferred direction. Yet, the question is, how this can be realized experimentally and whether the light momentum is large enough to have an effect. For example, the in-plane component could be enhanced and controlled with transient gradient or four-wave mixing setups. One can also ask if the polarization of light can be used as an additional knob for asymmetric excitations. So far, the results deny this, but maybe there are still unexplored effects. In addition to quenching with light, maybe there are also other possibilities of excitations, for example a tuning of pairing interactions with light or pressure to realize interaction quenches.

Finally, new experimental schemes can be considered for excitations and observations of Higgs modes. The first indirect observation of the Higgs mode was in NbSe₂, where the Higgs mode couples to the nearby CDW and thus, becomes Raman-active [16]. This experiment could be extended to nonequilibrium to perform a time-resolved Raman experiment. Hereby, the system is quenched prior to the Raman experiment and an oscillation of the peak in the spectrum associated with Higgs should oscillate in amplitude and position as the underlying order parameter oscillates. In general, the Higgs mode should also appear in the Raman spectrum of cuprates, where the Higgs mode is excited due to an effective Raman process depicted in the diagram in Fig. 5.8b). For example, the A_{1g} response of YBCO could never be fully described with the usual electron response [217]. There might be a contribution to the observed peak coming from Higgs, which should also be detectable in a tr-Raman experiment as an oscillation of the peak. Furthermore, Higgs modes could be observable in transport experiments as first studies on superconducting junctions suggest [87–89].

Measurements of Higgs oscillations have several possible applications. In future, this technique could be used to learn about the value of the gap, number of gaps, symmetry properties of the order parameter including nodal lines or phase and coupling to other modes. Compared to other methods like transport measurements, NMR, ARPES or Josephson interferometry, multiple properties can be, in principle, obtained simultaneously within one experiment, where a combination of multiple traditional experiments would be required to obtain the same information. This method can also be applied to other condensates where amplitude oscillations occur, like excitonic insulators, ultra cold atoms in optical lattices or magnetic systems. Yet, in contrast to superconductors, there is no Anderson-Higgs mechanism, which makes the amplitude (Higgs) mode unstable for a decay into lower Goldstone modes. In a more general sense, a measurement of Higgs modes may also serve as a new measure for defining superconductivity in nonequilibrium. Recent experiments and theoretical studies on light-induced superconductivity [218–227] raise the question on how one defines superconductivity in a short-lived nonequilibrium state. So far, the criterion only includes the vanishing resistivity property of superconductors measured by a divergent imaginary part of the optical conductivity for $\omega \rightarrow 0$. Yet, this criterion is not precise, as a measurement at $\omega = 0$ cannot be performed and thus, a divergence cannot be proven. In addition, the expelling of a magnetic field, i.e. the Meissner effect, as the second required criterion for superconductivity has not yet been considered. As the Meissner effect is induced by the Anderson-Higgs mechanism, a measurement of a stable Higgs mode should be

an equivalent fingerprint of superconductivity. While the repulsion of a magnetic field on an ultrashort timescale is difficult or even impossible to measure, a resonant behavior of the THG signal or even oscillations of the optical response in a pump-probe setup in the light-induced superconducting state could be realized potentially. This might also help to shine light on the questions if and how preformed pairs are induced or play a role in these experiments as possible amplitude oscillations should only be present in a coherent condensate state.

All in all, Higgs spectroscopy on superconductors in nonequilibrium has great potential as a new tool to investigate ground state properties of the order parameter.

A Numerical Implementation

A.1 Implementation of Bloch Equations

The Bloch equations (2.64) are solved numerically on a 2d grid in momentum space. For the integration, a Runge-Kutta Dormand-Prince algorithm¹ is used with adaptive stepsize. All differential equations on each point on the momentum grid are coupled through the gap and the self-consistency condition. Thus, it is important that in each time step, before evaluating the right hand side of the differential equation, the gap equation (2.60) is evaluated to fulfill the self-consistency condition.

To obtain a fine enough momentum grid resolution, only the region around the Fermi level within $\{\mathbf{k} \mid |\epsilon_{\mathbf{k}}| < \epsilon_c\}$ is considered. As all considered configurations for the quench problem separate in radial and angular parts, it is advantageous to discretize the momentum space in new coordinates (see Fig. A.1)

$$\epsilon = \epsilon(k_x, k_y), \quad \varphi = \arctan\left(\frac{k_y}{k_x}\right). \quad (\text{A.1})$$

In radial direction, we choose N_k points and in the angular direction N_φ . The discretization step widths are defined as

$$\Delta\epsilon = \frac{2\epsilon_c}{N_k - 1}, \quad \Delta\varphi = \frac{\phi_{\max}}{N_\varphi}, \quad (\text{A.2})$$

where ϕ_{\max} is either 2π or π depending on the symmetry as discussed below. The grid is then build via

$$\varphi_i = i\Delta\varphi \quad \text{for } i \in [0, N_\varphi - 1], \quad (\text{A.3a})$$

$$k_j(\varphi_i) = k' \quad \text{where } \epsilon(k', \varphi_i) = -\epsilon_c + j\Delta\epsilon \quad \text{for } j \in [0, N_k - 1]. \quad (\text{A.3b})$$

In the momentum sum of the gap equation, one has to consider the Jacobian element to account for the non-square integration elements. It follows

$$dA = dk_x dk_y = J d\epsilon d\varphi, \quad (\text{A.4})$$

$$J = \left| \begin{pmatrix} \partial_\epsilon k_x & \partial_\varphi k_x \\ \partial_\epsilon k_y & \partial_\varphi k_y \end{pmatrix} \right|. \quad (\text{A.5})$$

As in most cases, the dispersion cannot be inverted analytically, we consider the inverse relation

$$d\tilde{A} = d\epsilon d\varphi = \tilde{J} dk_x dk_y \quad (\text{A.6})$$

with $J = 1/\tilde{J}$ and

$$\tilde{J} = \left| \begin{pmatrix} \partial_{k_x} \epsilon & \partial_{k_y} \epsilon \\ \partial_{k_x} \varphi & \partial_{k_y} \varphi \end{pmatrix} \right|. \quad (\text{A.7})$$

¹https://www.boost.org/doc/libs/1_72_0/libs/numeric/odeint/doc/html/boost_numeric_odeint/runge_kutta_dopri5.html

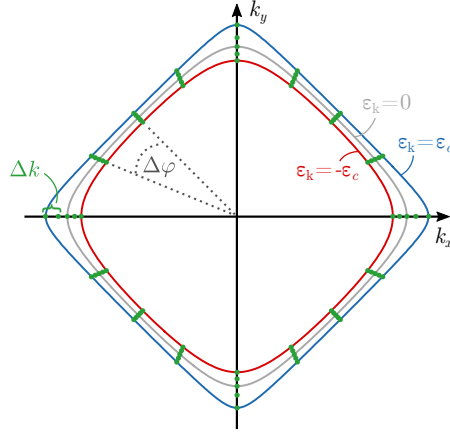


Figure A.1 Used discretization grid for evaluation of Bloch equations for quenched superconductor. The grey curve is the Fermi level $\epsilon_{\mathbf{k}} = 0$. The blue and red curves represent the upper and lower bound of the energy cutoff, i.e. $\epsilon_{\mathbf{k}} = \epsilon_c$ or $\epsilon_{\mathbf{k}} = -\epsilon_c$. The grid is chosen in polar coordinates with an equidistant spacing $\Delta\epsilon$ in radial and equidistant spacing $\Delta\varphi$ in azimuthal direction. Please note that the radial spacing Δk is not equidistant.

It follows

$$J = \frac{k_x^2 + k_y^2}{x\partial_{k_x}\epsilon + y\partial_{k_y}\epsilon}. \quad (\text{A.8})$$

One can make use of symmetry properties for the problem for certain parameters to restrict the momentum grid further. As an example, for s -wave symmetry with $\epsilon_{\mathbf{k}} = \epsilon(|\mathbf{k}|)$ and a symmetric quench, it is enough to use only a 1d grid as there is no angular dependence. If the values are periodic in the angular angle, e.g. for d -wave, one can restrict the momentum grid to one quarter. In appendix A.2, the influence of the number of discretization points on the result is explored to obtain an optimal value.

The following parameters are used in chapter 3 for the calculations of the quench dynamics

$$\begin{aligned} \Delta &= 1 \text{ meV}, & \epsilon_{\mathbf{k}} &= t_{\text{hop}}k^2 - \epsilon_{\text{F}}, \\ t_{\text{hop}} &= 50 \text{ meV}, & \epsilon_{\text{F}} &= 100 \text{ meV}, \\ \epsilon_c &= 10 \text{ meV}. \end{aligned} \quad (\text{A.9})$$

In the implementation, all energies are given in meV and the time in fs. All results shown in the thesis are rescaled. Energies are given in units of Δ or Δ_{∞} , times are given in \hbar/Δ or \hbar/Δ_{∞} . The chosen parameters do not correspond to a certain material but are chosen for convenience. All results do only depend quantitatively on the parameters but are qualitatively the same.

When calculating the Fourier transform of the gap oscillations $\Delta(\omega)$, the mean, i.e. Δ_{∞} , is subtracted first to remove an $\omega = 0$ peak due to the offset.

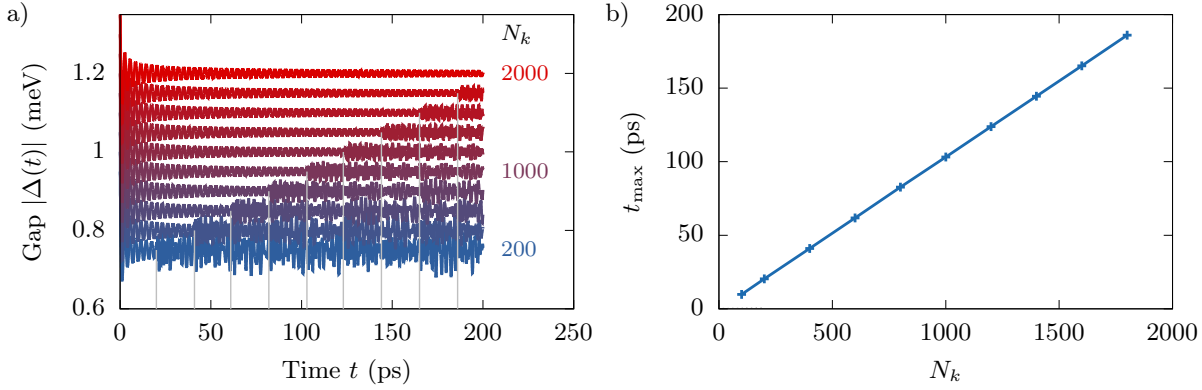


Figure A.2 Variation of the number of grid points N_k on a 1d grid for s -wave symmetry with A_{1g} quench and parameters from Eq. (A.9). a) Gap oscillations for varying number of grid points $N_k = 100\dots 2000$. As all curves lie on top of each other, they are shifted by 0.05 on the y -axis for each value of N_k for a better view. For each N_k , there is maximum time t_{\max} , beyond which the integration fails due to too low momentum resolution. b) Extracted time t_{\max} , which scales linearly with N_k .

A.2 Influence of Momentum Grid Resolution

Here, the influence of the momentum grid resolution on the result is explored. First, a calculation in 1d ($N_\varphi = 1$) of an s -wave superconductor quenched in the A_{1g} channel is performed with the parameters of Eq. (A.9) and a variation of the number of points N_k . The result can be found in Fig. A.2. The momentum grid resolution determines the maximum time t_{\max} , up to which a calculation is valid. For $t < t_{\max}$, the calculated result is independent of N_k and the curves lie exactly on top of each other. For larger t , the calculation breaks down and noisy oscillations occur. In Fig. A.2b), the time t_{\max} is shown as a function of N_k . It scales linearly with the number of points.

Next, the influence of N_k and N_φ in a 2d calculation is checked. For this, a d -wave order parameter is quenched in the A_{1g} channel with the parameters of Eq. (A.9). From the 1d case we know that $N_k = 2000$ points are required to calculate up to $t = 200$ ps, so N_k is fixed at this value and N_φ is varied. The result is shown in Fig. A.3. There is again a maximum time t_{\max} up to which a calculation is possible, which scales linearly with the number of points N_φ . An increase of N_k (not shown) does not improve the result (at least up to $t = 200$ ps), the time resolution here is restricted by N_φ . This qualitative behavior is independent of the parameters, but depends quantitatively on the calculation. For larger discretization range (depending on ϵ_k and ϵ_c) and more complex gap or quench symmetry, more points have to be chosen. The parameters of Eq. (A.9) require roughly $N_k = 2000$ and $N_\varphi = 1000$ points for $t_{\max} = 100$ ps.

There is another finite size effect resulting from the energy cutoff, namely, the resulting gap oscillations show a high-frequency oscillation at $2\epsilon_c$. Depending on the absolute value of the calculated gap oscillations, they are hardly visible if the gap oscillations are much larger. Yet, for smaller gap oscillations as in the d -wave case at longer times, these become prominently visible. Therefore, the cutoff should be chosen much higher than the gap, such that this frequency does not interfere with the actual dynamic.

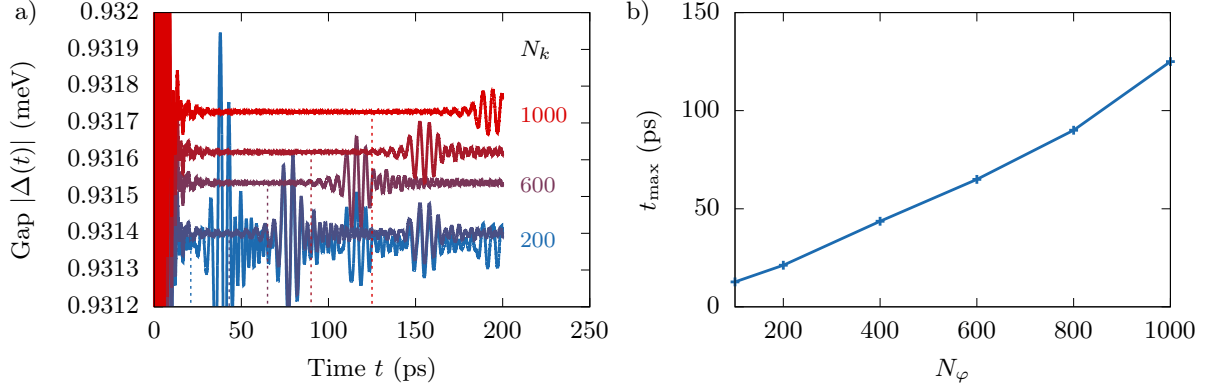


Figure A.3 Variation of the number of grid points N_φ on a 2d grid for d -wave symmetry with A_{1g} quench and parameters from Eq. (A.9). a) Gap oscillations for varying number of grid points $N_\varphi = 200, 400, 600, 800, 1000$. As all curves lie approximately on top of each other, they are shifted by 0.0001 on the y -axis for each value of N_φ for a better view. For each N_φ , there is maximum time t_{\max} , beyond which the integration fails due to too low momentum resolution. b) Extracted time t_{\max} , which scales linearly with N_φ .

A.3 Implementation of Density Matrix Formalism

The equations of motion in the density matrix formalism are implemented on a different grid in momentum space compared to the Bloch equations. As it can be seen e.g. in Eq. (4.10), off-diagonal expectation values at \mathbf{k} and \mathbf{k}' are coupled. This coupling is due to the finite momentum \mathbf{q}_0 originating from the light, i.e. there is a coupling of $(\mathbf{k}, \mathbf{k}' = \mathbf{k} \pm n\mathbf{q}_0)$ with $n \in \mathbb{N}$. As the coupling to more distant off-diagonal elements scales with A_0 , higher-order couplings can be neglected. One finds [28, 52] that it is sufficient for calculations of the pump pulse to include only couplings up to $n = 4$, whereas for the probe pulse, $n = 1$ is enough. To consider this coupling, we choose a 2d grid similar to [52], where the momentum space is discretized in x -direction (i.e. the direction of \mathbf{q}_0) with a step size of $|\mathbf{q}_0|$ and in y -direction, there are N_y points. By choosing such a grid, the resolution in x -direction is high enough to resolve the coupling due to the light, whereas the coupling in y -direction is only indirect via $\Delta(t)$ and can be chosen lower. Furthermore, the coupling between the off-diagonal elements $(\mathbf{k}, \mathbf{k}' = \mathbf{k} \pm n\mathbf{q}_0)$ can be captured directly. The grid is sketched in Fig. A.4a). If the incident direction of the light pulse is varied by varying the angle φ , the grid must be rotated accordingly to obtain the required grid resolution in the direction of the light pulse. Alternatively, the grid can be kept fixed and the gap symmetry is rotated in opposite direction. This is sketched in Fig. A.4b). For the calculation of the pump-probe experiment, the following parameters are chosen

$$\begin{aligned}
\Delta &= 1 \text{ meV}, & \epsilon_{\mathbf{k}} &= t_{\text{hop}}k^2 - \epsilon_{\text{F}}, & t_{\text{hop}} &= 2000 \text{ meV}, & \epsilon_{\text{F}} &= 10000 \text{ meV}, \\
A_0^{\text{pump}} &= 7 \cdot 10^{-8} \text{ Js}/(\text{Cm}), & \Omega^{\text{pump}} &= 2 \text{ meV}, & \tau^{\text{pump}} &= 400 \text{ fs}, \\
A_0^{\text{probe}} &= 5 \cdot 10^{-9} \text{ Js}/(\text{Cm}), & \Omega^{\text{probe}} &= 2 \text{ meV}, & \tau^{\text{probe}} &= 250 \text{ fs}, \\
T &= 0, & \epsilon_{\text{c}} &= 10 \text{ meV}, & N_y &= 200.
\end{aligned} \tag{A.10}$$

When implementing a second probe pulse, the equations of motion are first integrated for the pump pulse from $-t_c$ to t , where $t_c = \tau_p/2\sqrt{\log(1000)/\log(2)}$, i.e. the pulse is cut off at

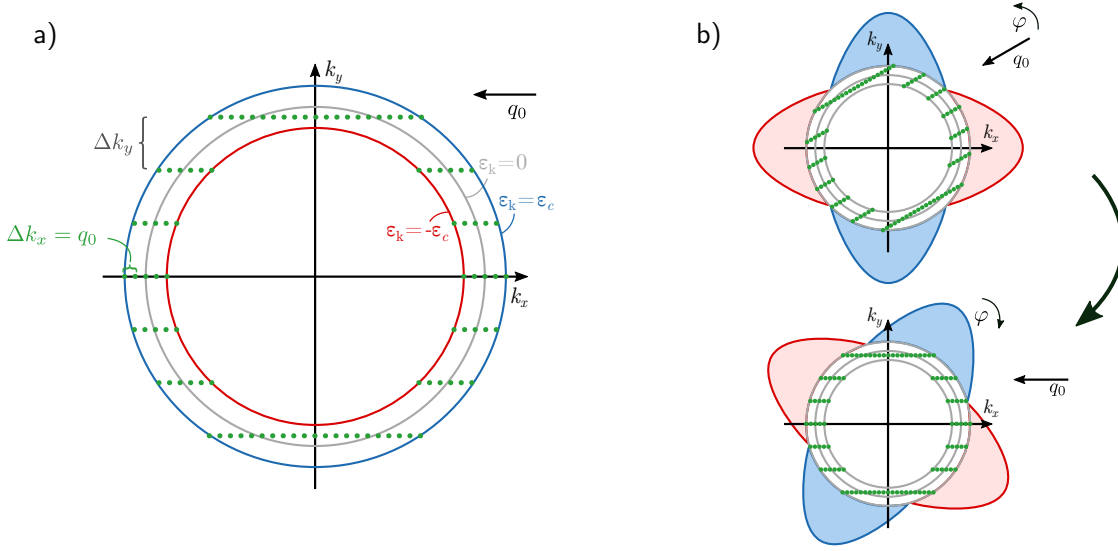


Figure A.4 Used discretization grid for calculating the time evolution in the density matrix formalism. a) The momentum space is discretized around the Fermi level in a region $\pm \epsilon_c$. The step width in direction of the light wave (x -direction) is chosen as the light momentum q_0 . In y -direction, the grid has N_y points. b) A rotation of the direction of the incident light by an angle φ is implemented as an opposite rotation of the gap symmetry to keep the same momentum grid.

1/1000 of its maximum value. Then, the equations of motion are integrated further using the nonequilibrium state induced by the pump pulse at variable time t as initial state while the probe pulse is applied. Hereby, it is ensured that pump and probe pulse do not overlap. The calculation of the optical conductivity contains certain numerical difficulties. To ensure that only the current induced by the probe pulse enters the calculation of the optical conductivity, the nonzero off-diagonal elements of the initial nonequilibrium state after the pump pulse are set to zero. This removes most of the pump current effects; nevertheless, a background is still visible in the current. This background, which would show up as a low frequency peak in the spectrum, is subtracted prior to the Fourier transform. Furthermore, as there are transient effects resulting from the two calculations of pump and probe pulse, the Fourier transform is started with a small time offset. These numerical issues lead to phase mixing between real and imaginary part of the optical conductivity, which has to be corrected to obtain the absorption and dispersion part. As a result of these issues, the $\omega \rightarrow 0$ behavior is not reliable. The spectra shown in section 4.1 are corrected by these methods as in some cases, the important features would otherwise be buried under the numerical background.

A.4 Implementation of Iterated Equation of Motion Approach

The iterated equation of motion approach is implemented on the same grid as the Bloch equations. The following parameters are used in chapter 4.2 for the calculations of the quench dynamics

$$\begin{aligned}
\Delta &= 1.35 \text{ meV}, & \epsilon_{\mathbf{k}} &= t_{\text{hop}}k^2 - \epsilon_{\text{F}}, & t_{\text{hop}} &= 2005.25 \text{ meV}, & \epsilon_{\text{F}} &= 9470 \text{ meV}, \\
g_{\text{s}} &= -0.4, & g_{\text{i}} &= 0.8, & T &= 0, \\
\epsilon_{\text{c}} &= 8.3 \text{ meV}, & N_{\mathbf{k}} &= 1000, & N_{\varphi} &= 1000.
\end{aligned} \tag{A.11}$$

The system parameters correspond to material parameters of lead, following [28]. All results depend only quantitatively on the parameters and can be rescaled to any other material values.

To evaluate the 2d time integral in Eq. (4.14) efficiently for the spectral function in frequency domain, the integral is rewritten with $\tau = t_1 - t_2$

$$\begin{aligned}
A(\mathbf{k}, \omega, t) &\propto \text{Im} \int dt_2 \int dt_1 p(t_1 - t)p(t_2 - t)e^{i\omega(t_1 - t_2)} G^<(\mathbf{k}, t_1, t_2) \\
&= \text{Im} \int dt_2 p(t_2 - t) \int d\tau p(t_2 + \tau - t)e^{i\omega\tau} G^<(\mathbf{k}, t_2 + \tau, t_2).
\end{aligned} \tag{A.12}$$

We define a new function \tilde{A} , which is A with an additional factor $e^{i\omega' t_2}$ in the integrand

$$\tilde{A}(\mathbf{k}, \omega, \omega', t) \propto \text{Im} \int dt_2 p(t_2 - t)e^{i\omega' t_2} \int d\tau p(t_2 + \tau - t)e^{i\omega\tau} G^<(\mathbf{k}, t_2 + \tau, t_2). \tag{A.13}$$

This can be interpreted as 2d Fourier transform in $(t_2, \tau) \rightarrow (\omega', \omega)$ of

$$p(t_2 - t)p(t_2 + \tau - t)G^<(\mathbf{k}, t_2 + \tau, t_2) \tag{A.14}$$

and implemented with a 2d FFT. After the 2d Fourier transform, we set $\omega' = 0$ to obtain the original result

$$A(\mathbf{k}, \omega, t) = \tilde{A}(\mathbf{k}, \omega, \omega' = 0, t). \tag{A.15}$$

A.5 Numerical Evaluation of THG Intensities

To calculate the temperature-dependent THG intensity, the interaction strength V is calculated for a chosen initial energy gap at $T = 0$. Then, the temperature dependence of the energy gap Δ_T is determined self-consistently for each temperature. To handle the divergences in the summations of the integrals and keep the required momentum grid resolution in a reasonable range, a residual broadening of $2i\Omega \rightarrow 2i\Omega + 0.01\Delta$ is introduced. This slightly broadens the resonance peaks and washes out the sharp phase jumps but does not change the overall result. The numerical calculation is implemented on the same grid as described in section A.1. For the calculation, the following parameters are used

$$\begin{aligned}
\Delta &= 20 \text{ meV}, & t &= 200 \text{ meV}, & \epsilon_{\text{F}} &= -400 \text{ meV}, & \epsilon_{\mathbf{k}} &= -2t(\cos(k_x) + \cos(k_y)) - \epsilon_{\text{F}}, \\
\epsilon_{\text{c}} &= 40 \text{ meV}, & N_{\mathbf{k}} &= 2000, & N_{\varphi} &= 2000.
\end{aligned} \tag{A.16}$$

B Derivation of Coupling to Light for Pump-Probe

Parts of the following derivation can be found e.g. in [228]. For free electrons, the Hamiltonian coupled to light with minimal substitution reads

$$\begin{aligned}
 H &= \frac{[\mathbf{p} + e\mathbf{A}(\mathbf{r}, t)]^2}{2m} \\
 &= -\frac{\hbar^2}{2m} \nabla^2 - i\frac{e\hbar}{2m} (\nabla\mathbf{A}(\mathbf{r}, t) + \mathbf{A}(\mathbf{r}, t)\nabla) + \frac{e^2}{2m} \mathbf{A}(\mathbf{r}, t)^2 \\
 &= -\frac{\hbar^2}{2m} \nabla^2 - i\frac{e\hbar}{2m} ((\nabla\mathbf{A}(\mathbf{r}, t)) + 2\mathbf{A}(\mathbf{r}, t)\nabla) + \frac{e^2}{2m} \mathbf{A}(\mathbf{r}, t)^2 \\
 &=: H_{\text{kin}} + H_{\text{em}}^{(1)} + H_{\text{em}}^{(2)},
 \end{aligned} \tag{B.1}$$

where we defined the linear $H_{\text{em}}^{(1)}$ and quadratic $H_{\text{em}}^{(2)}$ coupling term of the electromagnetic field. Now, we transform this Hamiltonian into second quantization

$$H = \sum_{\mathbf{k}, \mathbf{k}'} \langle \mathbf{k} | H | \mathbf{k}' \rangle c_{\mathbf{k}}^\dagger c_{\mathbf{k}'}. \tag{B.2}$$

Please note that for this derivation, the spin degree of freedom is neglected for shorter notation. It will be added again at the end. The momentum eigenstate is given by

$$|\mathbf{k}\rangle = \frac{1}{\sqrt{V}} \int d^3\mathbf{r} e^{i\mathbf{k}\mathbf{r}} |\mathbf{r}\rangle, \quad \langle \mathbf{k} | \mathbf{k}' \rangle = \delta_{\mathbf{k}, \mathbf{k}'} \tag{B.3}$$

with $\mathbf{k} = \frac{2\pi}{a}(n_x\hat{e}_x + n_y\hat{e}_y + n_z\hat{e}_z)$. The volume $V = a^3$ is the volume of a single unit cell with lattice constant a . The inverse relation is given by

$$|\mathbf{r}\rangle = \frac{1}{\sqrt{V}} \sum_{\mathbf{k}} e^{-i\mathbf{k}\mathbf{r}} |\mathbf{k}\rangle, \quad \langle \mathbf{r} | \mathbf{r}' \rangle = \delta(\mathbf{r} - \mathbf{r}') \tag{B.4}$$

and the second quantized wave function reads

$$\hat{\psi}(\mathbf{r}) = \frac{1}{\sqrt{V}} \sum_{\mathbf{k}} e^{i\mathbf{k}\mathbf{r}} c_{\mathbf{k}}. \tag{B.5}$$

The spatial Fourier transform of the vector potential reads

$$\mathbf{A}_{\mathbf{q}}(t) = \frac{1}{V} \int d^3\mathbf{r} \mathbf{A}(\mathbf{r}, t) e^{-i\mathbf{q}\mathbf{r}}, \quad \mathbf{A}(\mathbf{r}, t) = \sum_{\mathbf{q}} \mathbf{A}_{\mathbf{q}}(t) e^{i\mathbf{q}\mathbf{r}}. \tag{B.6}$$

The first term is the usual kinetic term

$$\begin{aligned}
 \left\langle \mathbf{k} \left| -\frac{\hbar^2}{2m} \nabla^2 \right| \mathbf{k}' \right\rangle &= -\frac{\hbar^2}{2m} \frac{1}{V} \int d^3\mathbf{r} e^{-i\mathbf{k}\mathbf{r}} \nabla^2 e^{i\mathbf{k}'\mathbf{r}} = \frac{\hbar^2 \mathbf{k}'^2}{2m} \frac{1}{V} \int d^3\mathbf{r} e^{-i(\mathbf{k}-\mathbf{k}')\mathbf{r}} \\
 &= \frac{\hbar^2 \mathbf{k}^2}{2m} \delta_{\mathbf{k}, \mathbf{k}'}
 \end{aligned} \tag{B.7}$$

and it follows

$$H_{\text{kin}} = \sum_{\mathbf{k}, \mathbf{k}'} \frac{\hbar^2 \mathbf{k}^2}{2m} \delta_{\mathbf{k}, \mathbf{k}'} c_{\mathbf{k}}^\dagger c_{\mathbf{k}'} = \sum_{\mathbf{k}} \frac{\hbar^2 \mathbf{k}^2}{2m} c_{\mathbf{k}}^\dagger c_{\mathbf{k}}. \quad (\text{B.8})$$

The second term describes the linear coupling to the electromagnetic field

$$\begin{aligned} & \left\langle \mathbf{k} \left| -i \frac{e\hbar}{2m} \left((\nabla \mathbf{A}(\mathbf{r}, t)) + 2\mathbf{A}(\mathbf{r}, t) \nabla \right) \right| \mathbf{k}' \right\rangle \\ &= -i \frac{e\hbar}{2m} \frac{1}{V} \int d^3 \mathbf{r} e^{-i(\mathbf{k}-\mathbf{k}')r} \left((\nabla \mathbf{A}(\mathbf{r}, t)) + 2i\mathbf{k}' \mathbf{A}(\mathbf{r}, t) \right) \\ &= \frac{e\hbar}{2m} \frac{1}{V} \int d^3 \mathbf{r} e^{-i(\mathbf{k}-\mathbf{k}')r} (\mathbf{k} - \mathbf{k}' + 2\mathbf{k}') \mathbf{A}(\mathbf{r}, t) \\ &= \frac{e\hbar}{2m} (\mathbf{k} + \mathbf{k}') A_{\mathbf{k}-\mathbf{k}'}(t), \end{aligned} \quad (\text{B.9})$$

where we used

$$\int d^3 \mathbf{r} e^{-i(\mathbf{k}-\mathbf{k}')r} (\nabla \mathbf{A}(\mathbf{r}, t)) = \underbrace{e^{-i(\mathbf{k}-\mathbf{k}')r} \mathbf{A}(\mathbf{r}, t)}_{=0} + \int d^3 \mathbf{r} i(\mathbf{k} - \mathbf{k}') e^{-i(\mathbf{k}-\mathbf{k}')r} \mathbf{A}(\mathbf{r}, t). \quad (\text{B.10})$$

It follows

$$\begin{aligned} H_{\text{em}}^{(1)} &= \sum_{\mathbf{k}, \mathbf{k}'} \frac{e\hbar}{2m} (\mathbf{k} + \mathbf{k}') A_{\mathbf{k}-\mathbf{k}'}(t) c_{\mathbf{k}}^\dagger c_{\mathbf{k}'} \\ &\stackrel{\substack{\mathbf{k} \rightarrow \mathbf{k} + \mathbf{q} \\ \mathbf{k}' \rightarrow \mathbf{k}}}{=} \frac{e\hbar}{2m} \sum_{\mathbf{k}, \mathbf{q}} (2\mathbf{k} + \mathbf{q}) A_{\mathbf{q}}(t) c_{\mathbf{k}+\mathbf{q}}^\dagger c_{\mathbf{k}}. \end{aligned} \quad (\text{B.11})$$

The third term describes the quadratic coupling to the electromagnetic field

$$\begin{aligned} & \left\langle \mathbf{k} \left| \frac{e^2}{2m} \mathbf{A}(\mathbf{r}, t)^2 \right| \mathbf{k}' \right\rangle \\ &= \frac{e^2}{2m} \frac{1}{V} \int d^3 \mathbf{r} e^{-i(\mathbf{k}-\mathbf{k}')r} \mathbf{A}(\mathbf{r}, t)^2 \\ &= \frac{e^2}{2m} \sum_{\mathbf{q}, \mathbf{q}'} \mathbf{A}_{\mathbf{q}}(t) \mathbf{A}_{\mathbf{q}'}(t) \frac{1}{V} \int d^3 \mathbf{r} e^{i(\mathbf{k}' - \mathbf{k} + \mathbf{q} + \mathbf{q}')r} \\ &= \frac{e^2}{2m} \sum_{\mathbf{q}'} \mathbf{A}_{\mathbf{q}'}(t) \mathbf{A}_{\mathbf{k}-\mathbf{k}'-\mathbf{q}'}(t). \end{aligned} \quad (\text{B.12})$$

It follows

$$\begin{aligned} H_{\text{em}}^{(2)} &= \sum_{\mathbf{k}, \mathbf{k}'} \frac{e^2}{2m} \left(\sum_{\mathbf{q}'} \mathbf{A}_{\mathbf{q}'}(t) \mathbf{A}_{\mathbf{k}-\mathbf{k}'-\mathbf{q}'}(t) \right) c_{\mathbf{k}}^\dagger c_{\mathbf{k}'} \\ &\stackrel{\substack{\mathbf{k} \rightarrow \mathbf{k} + \mathbf{q} \\ \mathbf{k}' \rightarrow \mathbf{k}}}{=} \frac{e^2}{2m} \sum_{\mathbf{k}, \mathbf{q}} \left(\sum_{\mathbf{q}'} \mathbf{A}_{\mathbf{q}'}(t) \mathbf{A}_{\mathbf{q}-\mathbf{q}'}(t) \right) c_{\mathbf{k}+\mathbf{q}}^\dagger c_{\mathbf{k}}. \end{aligned} \quad (\text{B.13})$$

Adding the spin degree of freedom, the interaction part of the Hamiltonian reads

$$H_{\text{em}}^{(1)} = \frac{e\hbar}{2m} \sum_{\mathbf{k}, \mathbf{q}, \sigma} (2\mathbf{k} + \mathbf{q}) \mathbf{A}_{\mathbf{q}}(t) c_{\mathbf{k}+\mathbf{q}, \sigma}^{\dagger} c_{\mathbf{k}, \sigma}, \quad (\text{B.14a})$$

$$H_{\text{em}}^{(2)} = \frac{e^2}{2m} \sum_{\mathbf{k}, \mathbf{q}, \sigma} \left[\sum_{\mathbf{q}'} \mathbf{A}_{\mathbf{q}-\mathbf{q}'}(t) \cdot \mathbf{A}_{\mathbf{q}'}(t) \right] c_{\mathbf{k}+\mathbf{q}, \sigma}^{\dagger} c_{\mathbf{k}, \sigma}. \quad (\text{B.14b})$$

Now, we apply the Bogoliubov transformation Eq. (2.39) to the interaction part. The first term $H_{\text{em}}^{(1)}$ is rewritten

$$\begin{aligned} H_{\text{em}}^{(1)} &= \frac{e\hbar}{2m} \sum_{\mathbf{k}, \mathbf{q}, \sigma} (2\mathbf{k} + \mathbf{q}) \mathbf{A}_{\mathbf{q}}(t) c_{\mathbf{k}+\mathbf{q}, \sigma}^{\dagger} c_{\mathbf{k}, \sigma} \\ &= \frac{e\hbar}{2m} \sum_{\mathbf{k}, \mathbf{q}} (2\mathbf{k} + \mathbf{q}) \mathbf{A}_{\mathbf{q}}(t) \left(c_{\mathbf{k}+\mathbf{q}\uparrow}^{\dagger} c_{\mathbf{k}\uparrow} + c_{\mathbf{k}+\mathbf{q}\downarrow}^{\dagger} c_{\mathbf{k}\downarrow} \right) \\ &= \frac{e\hbar}{2m} \sum_{\mathbf{k}, \mathbf{q}} (2\mathbf{k} + \mathbf{q}) \mathbf{A}_{\mathbf{q}}(t) \left(c_{\mathbf{k}+\mathbf{q}\uparrow}^{\dagger} c_{\mathbf{k}\uparrow} - c_{-\mathbf{k}\downarrow}^{\dagger} c_{-(\mathbf{k}+\mathbf{q})\downarrow} \right), \end{aligned} \quad (\text{B.15})$$

where $\mathbf{k} \rightarrow -(\mathbf{k} + \mathbf{q})$ was replaced in the second summand. We apply the Bogoliubov transformation and neglect terms $\propto \delta_{\mathbf{k}, \mathbf{k}+\mathbf{q}}$ as $\mathbf{q} \neq 0$

$$\begin{aligned} H_{\text{em}}^{(1)} &= \frac{e\hbar}{2m} \sum_{\mathbf{k}, \mathbf{q}} (2\mathbf{k} + \mathbf{q}) \mathbf{A}_{\mathbf{q}}(t) \left((u_{\mathbf{k}+\mathbf{q}} \alpha_{\mathbf{k}+\mathbf{q}}^{\dagger} + v_{\mathbf{k}+\mathbf{q}}^* \beta_{\mathbf{k}+\mathbf{q}}) (u_{\mathbf{k}}^* \alpha_{\mathbf{k}} + v_{\mathbf{k}} \beta_{\mathbf{k}}^{\dagger}) \right. \\ &\quad \left. - (-v_{\mathbf{k}}^* \alpha_{\mathbf{k}} + u_{\mathbf{k}} \beta_{\mathbf{k}}^{\dagger}) (-v_{\mathbf{k}+\mathbf{q}} \alpha_{\mathbf{k}+\mathbf{q}}^{\dagger} + u_{\mathbf{k}+\mathbf{q}}^* \beta_{\mathbf{k}+\mathbf{q}}) \right) \\ &= \frac{e\hbar}{2m} \sum_{\mathbf{k}, \mathbf{q}} (2\mathbf{k} + \mathbf{q}) \mathbf{A}_{\mathbf{q}}(t) \left(L_{\mathbf{k}, \mathbf{q}}^{(+)} \alpha_{\mathbf{k}+\mathbf{q}}^{\dagger} \alpha_{\mathbf{k}} - L_{\mathbf{k}, \mathbf{q}}^{(+)*} \beta_{\mathbf{k}}^{\dagger} \beta_{\mathbf{k}+\mathbf{q}} \right. \\ &\quad \left. + M_{\mathbf{k}, \mathbf{q}}^{(-)*} \alpha_{\mathbf{k}+\mathbf{q}}^{\dagger} \beta_{\mathbf{k}}^{\dagger} + M_{\mathbf{k}, \mathbf{q}}^{(-)} \alpha_{\mathbf{k}} \beta_{\mathbf{k}+\mathbf{q}} \right) \end{aligned} \quad (\text{B.16})$$

with the following abbreviations

$$L_{\mathbf{k}, \mathbf{q}}^{(\pm)} = u_{\mathbf{k}+\mathbf{q}} u_{\mathbf{k}}^* \pm v_{\mathbf{k}+\mathbf{q}} v_{\mathbf{k}}^*, \quad M_{\mathbf{k}, \mathbf{q}}^{(\pm)} = u_{\mathbf{k}+\mathbf{q}}^* v_{\mathbf{k}}^* \pm v_{\mathbf{k}+\mathbf{q}}^* u_{\mathbf{k}}^*. \quad (\text{B.17})$$

The transformation of $H_{\text{em}}^{(2)}$ is analogous except that the second summand in Eq. (B.15) does not have a negative sign. We find

$$\begin{aligned} H_{\text{em}}^{(2)} &= \frac{e^2}{2m} \sum_{\mathbf{k}, \mathbf{q}} \left[\sum_{\mathbf{q}'} \mathbf{A}_{\mathbf{q}-\mathbf{q}'}(t) \cdot \mathbf{A}_{\mathbf{q}'}(t) \right] \left(L_{\mathbf{k}, \mathbf{q}}^{(-)} \alpha_{\mathbf{k}+\mathbf{q}}^{\dagger} \alpha_{\mathbf{k}} + L_{\mathbf{k}, \mathbf{q}}^{(-)*} \beta_{\mathbf{k}}^{\dagger} \beta_{\mathbf{k}+\mathbf{q}} \right. \\ &\quad \left. + M_{\mathbf{k}, \mathbf{q}}^{(+)*} \alpha_{\mathbf{k}+\mathbf{q}}^{\dagger} \beta_{\mathbf{k}}^{\dagger} - M_{\mathbf{k}, \mathbf{q}}^{(+)} \alpha_{\mathbf{k}} \beta_{\mathbf{k}+\mathbf{q}} \right). \end{aligned} \quad (\text{B.18})$$

C Derivation of Equations of Motion for Pump-Probe

The full Hamiltonian reads

$$H = H_{\text{BCS}} + H_{\text{em}}^{(1)} + H_{\text{em}}^{(2)}, \quad (\text{C.1a})$$

$$H_{\text{BCS}} = \sum_{\mathbf{k}} R_{\mathbf{k}} (\alpha_{\mathbf{k}}^{\dagger} \alpha_{\mathbf{k}} + \beta_{\mathbf{k}}^{\dagger} \beta_{\mathbf{k}}) + \sum_{\mathbf{k}} C_{\mathbf{k}} \alpha_{\mathbf{k}}^{\dagger} \beta_{\mathbf{k}}^{\dagger} - C_{\mathbf{k}}^* \alpha_{\mathbf{k}} \beta_{\mathbf{k}}, \quad (\text{C.1b})$$

$$H_{\text{em}}^{(1)} = \frac{e\hbar}{2m} \sum_{\mathbf{k}, \mathbf{q}} (2\mathbf{k} + \mathbf{q}) \mathbf{A}_{\mathbf{q}}(t) \left(L_{\mathbf{k}, \mathbf{q}}^{(+)} \alpha_{\mathbf{k}+\mathbf{q}}^{\dagger} \alpha_{\mathbf{k}} - L_{\mathbf{k}, \mathbf{q}}^{(+)*} \beta_{\mathbf{k}}^{\dagger} \beta_{\mathbf{k}+\mathbf{q}} + M_{\mathbf{k}, \mathbf{q}}^{(-)*} \alpha_{\mathbf{k}+\mathbf{q}}^{\dagger} \beta_{\mathbf{k}}^{\dagger} + M_{\mathbf{k}, \mathbf{q}}^{(-)} \alpha_{\mathbf{k}} \beta_{\mathbf{k}+\mathbf{q}} \right), \quad (\text{C.1c})$$

$$H_{\text{em}}^{(2)} = \frac{e^2}{2m} \sum_{\mathbf{k}, \mathbf{q}} \left[\sum_{\mathbf{q}'} \mathbf{A}_{\mathbf{q}-\mathbf{q}'}(t) \cdot \mathbf{A}_{\mathbf{q}'}(t) \right] \left(L_{\mathbf{k}, \mathbf{q}}^{(-)} \alpha_{\mathbf{k}+\mathbf{q}}^{\dagger} \alpha_{\mathbf{k}} + L_{\mathbf{k}, \mathbf{q}}^{(-)*} \beta_{\mathbf{k}}^{\dagger} \beta_{\mathbf{k}+\mathbf{q}} + M_{\mathbf{k}, \mathbf{q}}^{(+)*} \alpha_{\mathbf{k}+\mathbf{q}}^{\dagger} \beta_{\mathbf{k}}^{\dagger} - M_{\mathbf{k}, \mathbf{q}}^{(+)} \alpha_{\mathbf{k}} \beta_{\mathbf{k}+\mathbf{q}} \right). \quad (\text{C.1d})$$

We want to evaluate Heisenberg's equation of motion

$$\begin{aligned} \partial_t \langle \alpha_{\mathbf{k}}^{\dagger} \beta_{\mathbf{k}'}^{\dagger} \rangle (t) &= \frac{i}{\hbar} \langle [H, \alpha_{\mathbf{k}}^{\dagger} \beta_{\mathbf{k}'}^{\dagger}] \rangle (t), & \partial_t \langle \alpha_{\mathbf{k}} \beta_{\mathbf{k}'} \rangle (t) &= \frac{i}{\hbar} \langle [H, \alpha_{\mathbf{k}} \beta_{\mathbf{k}'}] \rangle (t), \\ \partial_t \langle \alpha_{\mathbf{k}}^{\dagger} \alpha_{\mathbf{k}'} \rangle (t) &= \frac{i}{\hbar} \langle [H, \alpha_{\mathbf{k}}^{\dagger} \alpha_{\mathbf{k}'}] \rangle (t), & \partial_t \langle \beta_{\mathbf{k}}^{\dagger} \beta_{\mathbf{k}'} \rangle (t) &= \frac{i}{\hbar} \langle [H, \beta_{\mathbf{k}}^{\dagger} \beta_{\mathbf{k}'}] \rangle (t). \end{aligned} \quad (\text{C.2})$$

For the evaluation of the commutators, the following (anti)commutation relations are useful

$$\begin{aligned} [A, BC] &= [A, B]C + B[A, C], & [AB, C] &= A[B, C] + [A, C]B, \\ [A, BC] &= \{A, B\}C - B\{A, C\}, & [AB, C] &= A\{B, C\} - \{A, C\}B. \end{aligned} \quad (\text{C.3})$$

This allows to derive the relations

$$\begin{aligned} [AB, CD] &= [AB, C]D + C[AB, D] \\ &= A\{B, C\}D - \{A, C\}BD + CA\{B, D\} - C\{A, D\}B. \end{aligned} \quad (\text{C.4})$$

In addition, there are useful relations of the factors $L_{\mathbf{k}, \mathbf{q}}^{(\pm)}$ and $M_{\mathbf{k}, \mathbf{q}}^{(\pm)}$ defined in Eq. (B.17)

$$L_{\mathbf{k}-\mathbf{q}, \mathbf{q}}^{(\pm)} = u_{\mathbf{k}} u_{\mathbf{k}-\mathbf{q}}^* \pm v_{\mathbf{k}} v_{\mathbf{k}-\mathbf{q}}^* = L_{\mathbf{k}, -\mathbf{q}}^{(\pm)*}, \quad M_{\mathbf{k}-\mathbf{q}, \mathbf{q}}^{(\pm)} = u_{\mathbf{k}}^* v_{\mathbf{k}-\mathbf{q}}^* \pm v_{\mathbf{k}}^* u_{\mathbf{k}-\mathbf{q}}^* = \pm M_{\mathbf{k}, -\mathbf{q}}^{(\pm)}. \quad (\text{C.5})$$

We evaluate the three commutators for the first equation of motion

$$\begin{aligned} [H_{\text{BCS}}, \alpha_{\mathbf{k}}^{\dagger} \beta_{\mathbf{k}'}^{\dagger}] &= \left[\sum_{\tilde{\mathbf{k}}} \left(R_{\tilde{\mathbf{k}}} (\alpha_{\tilde{\mathbf{k}}}^{\dagger} \alpha_{\tilde{\mathbf{k}}} + \beta_{\tilde{\mathbf{k}}}^{\dagger} \beta_{\tilde{\mathbf{k}}}) + C_{\tilde{\mathbf{k}}} \alpha_{\tilde{\mathbf{k}}}^{\dagger} \beta_{\tilde{\mathbf{k}}}^{\dagger} - C_{\tilde{\mathbf{k}}}^* \alpha_{\tilde{\mathbf{k}}} \beta_{\tilde{\mathbf{k}}}) \right), \alpha_{\mathbf{k}}^{\dagger} \beta_{\mathbf{k}'}^{\dagger} \right] \\ &= \sum_{\tilde{\mathbf{k}}} R_{\tilde{\mathbf{k}}} \left(\alpha_{\tilde{\mathbf{k}}}^{\dagger} \delta_{\tilde{\mathbf{k}}, \mathbf{k}} \beta_{\mathbf{k}'}^{\dagger} + \alpha_{\mathbf{k}}^{\dagger} \beta_{\tilde{\mathbf{k}}}^{\dagger} \delta_{\tilde{\mathbf{k}}, \mathbf{k}'} \right) - C_{\tilde{\mathbf{k}}}^* \left(-\delta_{\tilde{\mathbf{k}}, \mathbf{k}} \underbrace{\beta_{\tilde{\mathbf{k}}}^{\dagger} \beta_{\mathbf{k}'}^{\dagger}}_{\delta_{\tilde{\mathbf{k}}, \mathbf{k}'} - \beta_{\mathbf{k}'}^{\dagger} \beta_{\tilde{\mathbf{k}}}^{\dagger}} + \alpha_{\tilde{\mathbf{k}}}^{\dagger} \alpha_{\tilde{\mathbf{k}}} \delta_{\tilde{\mathbf{k}}, \mathbf{k}'} \right) \\ &= (R_{\mathbf{k}} + R_{\mathbf{k}'}) \alpha_{\mathbf{k}}^{\dagger} \beta_{\mathbf{k}'}^{\dagger} - C_{\mathbf{k}}^* (\beta_{\mathbf{k}'}^{\dagger} \beta_{\mathbf{k}} - \delta_{\mathbf{k}, \mathbf{k}'}) - C_{\mathbf{k}'}^* \alpha_{\mathbf{k}}^{\dagger} \alpha_{\mathbf{k}'}, \end{aligned} \quad (\text{C.6})$$

$$\begin{aligned}
[H_{\text{em}}^{(1)}, \alpha_{\mathbf{k}}^\dagger \beta_{\mathbf{k}'}^\dagger] &= \left[\frac{e\hbar}{2m} \sum_{\tilde{\mathbf{k}}, \mathbf{q}} (2\tilde{\mathbf{k}} + \mathbf{q}) \mathbf{A}_{\mathbf{q}}(t) \left[L_{\tilde{\mathbf{k}}, \mathbf{q}}^{(+)} \alpha_{\tilde{\mathbf{k}}+\mathbf{q}}^\dagger \alpha_{\tilde{\mathbf{k}}} - L_{\tilde{\mathbf{k}}, \mathbf{q}}^{(+)*} \beta_{\tilde{\mathbf{k}}}^\dagger \beta_{\tilde{\mathbf{k}}+\mathbf{q}} \right. \right. \\
&\quad \left. \left. + M_{\tilde{\mathbf{k}}, \mathbf{q}}^{(-)*} \alpha_{\tilde{\mathbf{k}}+\mathbf{q}}^\dagger \beta_{\tilde{\mathbf{k}}}^\dagger + M_{\tilde{\mathbf{k}}, \mathbf{q}}^{(-)} \alpha_{\tilde{\mathbf{k}}} \beta_{\tilde{\mathbf{k}}+\mathbf{q}} \right], \alpha_{\mathbf{k}}^\dagger \beta_{\mathbf{k}'}^\dagger \right] \\
&= \frac{e\hbar}{2m} \sum_{\tilde{\mathbf{k}}, \mathbf{q}} (2\tilde{\mathbf{k}} + \mathbf{q}) \mathbf{A}_{\mathbf{q}}(t) \left[L_{\tilde{\mathbf{k}}, \mathbf{q}}^{(+)} \alpha_{\tilde{\mathbf{k}}+\mathbf{q}}^\dagger \delta_{\tilde{\mathbf{k}}, \mathbf{k}} \beta_{\mathbf{k}'}^\dagger - L_{\tilde{\mathbf{k}}, \mathbf{q}}^{(+)*} \alpha_{\mathbf{k}}^\dagger \beta_{\tilde{\mathbf{k}}}^\dagger \delta_{\tilde{\mathbf{k}}+\mathbf{q}, \mathbf{k}'} \right. \\
&\quad \left. + M_{\tilde{\mathbf{k}}, \mathbf{q}}^{(-)} \left(-\delta_{\tilde{\mathbf{k}}, \mathbf{k}} \underbrace{\beta_{\tilde{\mathbf{k}}+\mathbf{q}} \beta_{\mathbf{k}'}^\dagger}_{\delta_{\tilde{\mathbf{k}}+\mathbf{q}, \mathbf{k}'} - \beta_{\mathbf{k}'}^\dagger \beta_{\tilde{\mathbf{k}}+\mathbf{q}}} + \alpha_{\tilde{\mathbf{k}}}^\dagger \alpha_{\tilde{\mathbf{k}}} \delta_{\tilde{\mathbf{k}}+\mathbf{q}, \mathbf{k}'} \right) \right] \\
&= \frac{e\hbar}{2m} \sum_{\mathbf{q}} \mathbf{A}_{\mathbf{q}}(t) \left[(2\mathbf{k} + \mathbf{q}) \left(L_{\mathbf{k}, \mathbf{q}}^{(+)} \alpha_{\mathbf{k}+\mathbf{q}}^\dagger \beta_{\mathbf{k}'}^\dagger + M_{\mathbf{k}, \mathbf{q}}^{(-)} (\beta_{\mathbf{k}'}^\dagger \beta_{\mathbf{k}+\mathbf{q}} - \delta_{\mathbf{k}+\mathbf{q}, \mathbf{k}'}) \right) \right. \\
&\quad \left. - (2\mathbf{k}' - \mathbf{q}) \left(L_{\mathbf{k}'-\mathbf{q}, \mathbf{q}}^{(+)*} \alpha_{\mathbf{k}'}^\dagger \beta_{\mathbf{k}'-\mathbf{q}}^\dagger - M_{\mathbf{k}'-\mathbf{q}, \mathbf{q}}^{(-)} \alpha_{\mathbf{k}}^\dagger \alpha_{\mathbf{k}'-\mathbf{q}} \right) \right] \\
&= \frac{e\hbar}{2m} \sum_{\mathbf{q}} \mathbf{A}_{\mathbf{q}}(t) \left[(2\mathbf{k} + \mathbf{q}) \left(L_{\mathbf{k}, \mathbf{q}}^{(+)} \alpha_{\mathbf{k}+\mathbf{q}}^\dagger \beta_{\mathbf{k}'}^\dagger + M_{\mathbf{k}, \mathbf{q}}^{(-)} (\beta_{\mathbf{k}'}^\dagger \beta_{\mathbf{k}+\mathbf{q}} - \delta_{\mathbf{k}+\mathbf{q}, \mathbf{k}'}) \right) \right. \\
&\quad \left. - (2\mathbf{k}' - \mathbf{q}) \left(L_{\mathbf{k}'-\mathbf{q}, -\mathbf{q}}^{(+)} \alpha_{\mathbf{k}'}^\dagger \beta_{\mathbf{k}'-\mathbf{q}}^\dagger + M_{\mathbf{k}'-\mathbf{q}, -\mathbf{q}}^{(-)} \alpha_{\mathbf{k}}^\dagger \alpha_{\mathbf{k}'-\mathbf{q}} \right) \right], \tag{C.7}
\end{aligned}$$

$$\begin{aligned}
[H_{\text{em}}^{(2)}, \alpha_{\mathbf{k}}^\dagger \beta_{\mathbf{k}'}^\dagger] &= \left[\frac{e^2}{2m} \sum_{\tilde{\mathbf{k}}, \mathbf{q}} \left[\sum_{\mathbf{q}'} \mathbf{A}_{\mathbf{q}-\mathbf{q}'}(t) \cdot \mathbf{A}_{\mathbf{q}'}(t) \right] \left(L_{\tilde{\mathbf{k}}, \mathbf{q}}^{(-)} \alpha_{\tilde{\mathbf{k}}+\mathbf{q}}^\dagger \alpha_{\tilde{\mathbf{k}}} + L_{\tilde{\mathbf{k}}, \mathbf{q}}^{(-)*} \beta_{\tilde{\mathbf{k}}}^\dagger \beta_{\tilde{\mathbf{k}}+\mathbf{q}} \right. \right. \\
&\quad \left. \left. + M_{\tilde{\mathbf{k}}, \mathbf{q}}^{(+)*} \alpha_{\tilde{\mathbf{k}}+\mathbf{q}}^\dagger \beta_{\tilde{\mathbf{k}}}^\dagger - M_{\tilde{\mathbf{k}}, \mathbf{q}}^{(+)} \alpha_{\tilde{\mathbf{k}}} \beta_{\tilde{\mathbf{k}}+\mathbf{q}} \right), \alpha_{\mathbf{k}}^\dagger \beta_{\mathbf{k}'}^\dagger \right] \\
&= \frac{e^2}{2m} \sum_{\tilde{\mathbf{k}}, \mathbf{q}} \left[\sum_{\mathbf{q}'} \mathbf{A}_{\mathbf{q}-\mathbf{q}'}(t) \cdot \mathbf{A}_{\mathbf{q}'}(t) \right] \left(L_{\tilde{\mathbf{k}}, \mathbf{q}}^{(-)} \alpha_{\tilde{\mathbf{k}}+\mathbf{q}}^\dagger \delta_{\tilde{\mathbf{k}}, \mathbf{k}} \beta_{\mathbf{k}'}^\dagger + L_{\tilde{\mathbf{k}}, \mathbf{q}}^{(-)*} \alpha_{\mathbf{k}}^\dagger \beta_{\tilde{\mathbf{k}}}^\dagger \delta_{\tilde{\mathbf{k}}+\mathbf{q}, \mathbf{k}'} \right. \\
&\quad \left. - M_{\tilde{\mathbf{k}}, \mathbf{q}}^{(+)} \left(-\delta_{\tilde{\mathbf{k}}, \mathbf{k}} \underbrace{\beta_{\tilde{\mathbf{k}}+\mathbf{q}} \beta_{\mathbf{k}'}^\dagger}_{\delta_{\mathbf{k}', \tilde{\mathbf{k}}+\mathbf{q}} - \beta_{\mathbf{k}'}^\dagger \beta_{\tilde{\mathbf{k}}+\mathbf{q}}} + \alpha_{\tilde{\mathbf{k}}}^\dagger \alpha_{\tilde{\mathbf{k}}} \delta_{\tilde{\mathbf{k}}+\mathbf{q}, \mathbf{k}'} \right) \right] \\
&= \frac{e^2}{2m} \sum_{\mathbf{q}} \left[\sum_{\mathbf{q}'} \mathbf{A}_{\mathbf{q}-\mathbf{q}'}(t) \cdot \mathbf{A}_{\mathbf{q}'}(t) \right] \left(L_{\mathbf{k}, \mathbf{q}}^{(-)} \alpha_{\mathbf{k}+\mathbf{q}}^\dagger \beta_{\mathbf{k}'}^\dagger + L_{\mathbf{k}'-\mathbf{q}, \mathbf{q}}^{(-)*} \alpha_{\mathbf{k}'}^\dagger \beta_{\mathbf{k}'-\mathbf{q}}^\dagger \right. \\
&\quad \left. - M_{\mathbf{k}, \mathbf{q}}^{(+)} (\beta_{\mathbf{k}'}^\dagger \beta_{\mathbf{k}+\mathbf{q}} - \delta_{\mathbf{k}+\mathbf{q}, \mathbf{k}'}) - M_{\mathbf{k}'-\mathbf{q}, \mathbf{q}}^{(+)} \alpha_{\mathbf{k}}^\dagger \alpha_{\mathbf{k}'-\mathbf{q}} \right) \\
&= \frac{e^2}{2m} \sum_{\mathbf{q}} \left[\sum_{\mathbf{q}'} \mathbf{A}_{\mathbf{q}-\mathbf{q}'}(t) \cdot \mathbf{A}_{\mathbf{q}'}(t) \right] \left(L_{\mathbf{k}, \mathbf{q}}^{(-)} \alpha_{\mathbf{k}+\mathbf{q}}^\dagger \beta_{\mathbf{k}'}^\dagger + L_{\mathbf{k}'-\mathbf{q}, -\mathbf{q}}^{(-)} \alpha_{\mathbf{k}}^\dagger \beta_{\mathbf{k}'-\mathbf{q}}^\dagger \right. \\
&\quad \left. - M_{\mathbf{k}, \mathbf{q}}^{(+)} (\beta_{\mathbf{k}'}^\dagger \beta_{\mathbf{k}+\mathbf{q}} - \delta_{\mathbf{k}+\mathbf{q}, \mathbf{k}'}) - M_{\mathbf{k}'-\mathbf{q}, -\mathbf{q}}^{(+)} \alpha_{\mathbf{k}}^\dagger \alpha_{\mathbf{k}'-\mathbf{q}} \right). \tag{C.8}
\end{aligned}$$

All in all, we find for the first equation of motion

$$\begin{aligned}
 \partial_t \langle \alpha_{\mathbf{k}}^\dagger \beta_{\mathbf{k}'}^\dagger \rangle (t) = & \frac{i}{\hbar} \left\{ (R_{\mathbf{k}} + R_{\mathbf{k}'}) \langle \alpha_{\mathbf{k}}^\dagger \beta_{\mathbf{k}'}^\dagger \rangle - C_{\mathbf{k}}^* (\langle \beta_{\mathbf{k}'}^\dagger \beta_{\mathbf{k}} \rangle - \delta_{\mathbf{k},\mathbf{k}'}) - C_{\mathbf{k}'}^* \langle \alpha_{\mathbf{k}}^\dagger \alpha_{\mathbf{k}'} \rangle \right. \\
 & + \frac{e\hbar}{2m} \sum_{\mathbf{q}} \mathbf{A}_{\mathbf{q}}(t) \left[(2\mathbf{k} + \mathbf{q}) \left(L_{\mathbf{k},\mathbf{q}}^{(+)} \langle \alpha_{\mathbf{k}+\mathbf{q}}^\dagger \beta_{\mathbf{k}'}^\dagger \rangle + M_{\mathbf{k},\mathbf{q}}^{(-)} (\langle \beta_{\mathbf{k}'}^\dagger \beta_{\mathbf{k}+\mathbf{q}} \rangle - \delta_{\mathbf{k}+\mathbf{q},\mathbf{k}'}) \right) \right. \\
 & \quad \left. \left. - (2\mathbf{k}' - \mathbf{q}) \left(L_{\mathbf{k}',-\mathbf{q}}^{(+)} \langle \alpha_{\mathbf{k}}^\dagger \beta_{\mathbf{k}'-\mathbf{q}}^\dagger \rangle + M_{\mathbf{k}',-\mathbf{q}}^{(-)} \langle \alpha_{\mathbf{k}}^\dagger \alpha_{\mathbf{k}'-\mathbf{q}} \rangle \right) \right] \right. \\
 & + \frac{e^2}{2m} \sum_{\mathbf{q}} \left[\sum_{\mathbf{q}'} \mathbf{A}_{\mathbf{q}-\mathbf{q}'}(t) \cdot \mathbf{A}_{\mathbf{q}'}(t) \right] \left(L_{\mathbf{k},\mathbf{q}}^{(-)} \langle \alpha_{\mathbf{k}+\mathbf{q}}^\dagger \beta_{\mathbf{k}'}^\dagger \rangle + L_{\mathbf{k}',-\mathbf{q}}^{(-)} \langle \alpha_{\mathbf{k}}^\dagger \beta_{\mathbf{k}'-\mathbf{q}}^\dagger \rangle \right. \\
 & \quad \left. \left. - M_{\mathbf{k},\mathbf{q}}^{(+)} (\langle \beta_{\mathbf{k}'}^\dagger \beta_{\mathbf{k}+\mathbf{q}} \rangle - \delta_{\mathbf{k}+\mathbf{q},\mathbf{k}'}) - M_{\mathbf{k}',-\mathbf{q}}^{(+)} \langle \alpha_{\mathbf{k}}^\dagger \alpha_{\mathbf{k}'-\mathbf{q}} \rangle \right) \right\}. \quad (\text{C.9})
 \end{aligned}$$

If we assume a two-dimensional system and use the explicit form of the vector potential of Eq. (4.5) of the main text, the equations of motion can be simplified

$$\begin{aligned}
 \partial_t \langle \alpha_{\mathbf{k}}^\dagger \beta_{\mathbf{k}'}^\dagger \rangle (t) = & \frac{i}{\hbar} \left\{ (R_{\mathbf{k}} + R_{\mathbf{k}'}) \langle \alpha_{\mathbf{k}}^\dagger \beta_{\mathbf{k}'}^\dagger \rangle - C_{\mathbf{k}}^* (\langle \beta_{\mathbf{k}'}^\dagger \beta_{\mathbf{k}} \rangle - \delta_{\mathbf{k},\mathbf{k}'}) - C_{\mathbf{k}'}^* \langle \alpha_{\mathbf{k}}^\dagger \alpha_{\mathbf{k}'} \rangle \right. \\
 & + \frac{e\hbar}{2m} \sum_{\mathbf{q}=\pm\mathbf{q}_0} 2\mathbf{k} \mathbf{A}_{\mathbf{q}}(t) \left(L_{\mathbf{k},\mathbf{q}}^{(+)} \langle \alpha_{\mathbf{k}+\mathbf{q}}^\dagger \beta_{\mathbf{k}'}^\dagger \rangle + M_{\mathbf{k},\mathbf{q}}^{(-)} (\langle \beta_{\mathbf{k}'}^\dagger \beta_{\mathbf{k}+\mathbf{q}} \rangle - \delta_{\mathbf{k}+\mathbf{q},\mathbf{k}'}) \right. \\
 & \quad \left. - L_{\mathbf{k}',-\mathbf{q}}^{(+)} \langle \alpha_{\mathbf{k}}^\dagger \beta_{\mathbf{k}'-\mathbf{q}}^\dagger \rangle - M_{\mathbf{k}',-\mathbf{q}}^{(-)} \langle \alpha_{\mathbf{k}}^\dagger \alpha_{\mathbf{k}'-\mathbf{q}} \rangle \right) \\
 & + \frac{e^2}{2m} \sum_{\mathbf{q}=0,\pm 2\mathbf{q}_0} \left[\sum_{\mathbf{q}'=\pm\mathbf{q}_0} \mathbf{A}_{\mathbf{q}-\mathbf{q}'}(t) \cdot \mathbf{A}_{\mathbf{q}'}(t) \right] \left(L_{\mathbf{k},\mathbf{q}}^{(-)} \langle \alpha_{\mathbf{k}+\mathbf{q}}^\dagger \beta_{\mathbf{k}'}^\dagger \rangle + L_{\mathbf{k}',-\mathbf{q}}^{(-)} \langle \alpha_{\mathbf{k}}^\dagger \beta_{\mathbf{k}'-\mathbf{q}}^\dagger \rangle \right. \\
 & \quad \left. \left. - M_{\mathbf{k},\mathbf{q}}^{(+)} (\langle \beta_{\mathbf{k}'}^\dagger \beta_{\mathbf{k}+\mathbf{q}} \rangle - \delta_{\mathbf{k}+\mathbf{q},\mathbf{k}'}) - M_{\mathbf{k}',-\mathbf{q}}^{(+)} \langle \alpha_{\mathbf{k}}^\dagger \alpha_{\mathbf{k}'-\mathbf{q}} \rangle \right) \right\}. \quad (\text{C.10})
 \end{aligned}$$

As

$$\alpha_{\mathbf{k}} \beta_{\mathbf{k}'} = -(\alpha_{\mathbf{k}}^\dagger \beta_{\mathbf{k}'}^\dagger)^\dagger, \quad (\text{C.11})$$

the second equation of motion is the negative complex conjugated version of the first one, i.e.

$$\partial_t \langle \alpha_{\mathbf{k}} \beta_{\mathbf{k}'} \rangle (t) = - \left(\partial_t \langle \alpha_{\mathbf{k}}^\dagger \beta_{\mathbf{k}'}^\dagger \rangle (t) \right)^*. \quad (\text{C.12})$$

Now, we evaluate the three commutators for the third equation of motion

$$\begin{aligned}
 [H_{\text{BCS}}, \alpha_{\mathbf{k}}^\dagger \alpha_{\mathbf{k}'}] = & \left[\sum_{\tilde{\mathbf{k}}} \left(R_{\tilde{\mathbf{k}}} (\alpha_{\tilde{\mathbf{k}}}^\dagger \alpha_{\tilde{\mathbf{k}}} + \beta_{\tilde{\mathbf{k}}}^\dagger \beta_{\tilde{\mathbf{k}}}) + C_{\tilde{\mathbf{k}}} \alpha_{\tilde{\mathbf{k}}}^\dagger \beta_{\tilde{\mathbf{k}}}^\dagger - C_{\tilde{\mathbf{k}}}^* \alpha_{\tilde{\mathbf{k}}} \beta_{\tilde{\mathbf{k}}} \right), \alpha_{\mathbf{k}}^\dagger \alpha_{\mathbf{k}'} \right] \\
 = & \sum_{\tilde{\mathbf{k}}} R_{\tilde{\mathbf{k}}} \left(\alpha_{\tilde{\mathbf{k}}}^\dagger \delta_{\tilde{\mathbf{k}},\mathbf{k}} \alpha_{\mathbf{k}'} - \alpha_{\tilde{\mathbf{k}}}^\dagger \delta_{\tilde{\mathbf{k}},\mathbf{k}'} \alpha_{\tilde{\mathbf{k}}} \right) - C_{\tilde{\mathbf{k}}} \alpha_{\tilde{\mathbf{k}}}^\dagger \delta_{\tilde{\mathbf{k}},\mathbf{k}'} \beta_{\tilde{\mathbf{k}}}^\dagger + C_{\tilde{\mathbf{k}}}^* \delta_{\tilde{\mathbf{k}},\mathbf{k}} \beta_{\tilde{\mathbf{k}}} \alpha_{\mathbf{k}'} \\
 = & (R_{\mathbf{k}} - R_{\mathbf{k}'}) \alpha_{\mathbf{k}}^\dagger \alpha_{\mathbf{k}'} - C_{\mathbf{k}'} \alpha_{\mathbf{k}}^\dagger \beta_{\mathbf{k}'}^\dagger - C_{\mathbf{k}}^* \alpha_{\mathbf{k}'} \beta_{\mathbf{k}}, \quad (\text{C.13})
 \end{aligned}$$

$$\begin{aligned}
[H_{\text{em}}^{(1)}, \alpha_{\mathbf{k}}^\dagger \alpha_{\mathbf{k}'}] &= \left[\frac{e\hbar}{2m} \sum_{\tilde{\mathbf{k}}, \mathbf{q}} (2\tilde{\mathbf{k}} + \mathbf{q}) \mathbf{A}_{\mathbf{q}}(t) \left[L_{\tilde{\mathbf{k}}, \mathbf{q}}^{(+)} \alpha_{\tilde{\mathbf{k}}+\mathbf{q}}^\dagger \alpha_{\tilde{\mathbf{k}}} - L_{\tilde{\mathbf{k}}, \mathbf{q}}^{(+)*} \beta_{\tilde{\mathbf{k}}}^\dagger \beta_{\tilde{\mathbf{k}}+\mathbf{q}} \right. \right. \\
&\quad \left. \left. + M_{\tilde{\mathbf{k}}, \mathbf{q}}^{(-)*} \alpha_{\tilde{\mathbf{k}}+\mathbf{q}}^\dagger \beta_{\tilde{\mathbf{k}}}^\dagger + M_{\tilde{\mathbf{k}}, \mathbf{q}}^{(-)} \alpha_{\tilde{\mathbf{k}}} \beta_{\tilde{\mathbf{k}}+\mathbf{q}} \right], \alpha_{\mathbf{k}}^\dagger \alpha_{\mathbf{k}'} \right] \\
&= \frac{e\hbar}{2m} \sum_{\tilde{\mathbf{k}}, \mathbf{q}} (2\tilde{\mathbf{k}} + \mathbf{q}) \mathbf{A}_{\mathbf{q}}(t) \left[L_{\tilde{\mathbf{k}}, \mathbf{q}}^{(+)} \left(\alpha_{\tilde{\mathbf{k}}+\mathbf{q}}^\dagger \delta_{\tilde{\mathbf{k}}, \mathbf{k}} \alpha_{\mathbf{k}'} - \alpha_{\tilde{\mathbf{k}}}^\dagger \delta_{\tilde{\mathbf{k}}+\mathbf{q}, \mathbf{k}'} \alpha_{\tilde{\mathbf{k}}} \right) \right. \\
&\quad \left. - M_{\tilde{\mathbf{k}}, \mathbf{q}}^{(-)*} \alpha_{\tilde{\mathbf{k}}}^\dagger \delta_{\tilde{\mathbf{k}}+\mathbf{q}, \mathbf{k}'} \beta_{\tilde{\mathbf{k}}}^\dagger - M_{\tilde{\mathbf{k}}, \mathbf{q}}^{(-)} \delta_{\tilde{\mathbf{k}}, \mathbf{k}} \beta_{\tilde{\mathbf{k}}+\mathbf{q}} \alpha_{\mathbf{k}'} \right] \\
&= \frac{e\hbar}{2m} \sum_{\mathbf{q}} \mathbf{A}_{\mathbf{q}}(t) \left[(2\mathbf{k} + \mathbf{q}) \left(L_{\mathbf{k}, \mathbf{q}}^{(+)} \alpha_{\mathbf{k}+\mathbf{q}}^\dagger \alpha_{\mathbf{k}'} - M_{\mathbf{k}, \mathbf{q}}^{(-)} \beta_{\mathbf{k}+\mathbf{q}} \alpha_{\mathbf{k}'} \right) \right. \\
&\quad \left. - (2\mathbf{k}' - \mathbf{q}) \left(L_{\mathbf{k}', -\mathbf{q}}^{(+)} \alpha_{\mathbf{k}'}^\dagger \alpha_{\mathbf{k}'-\mathbf{q}} + M_{\mathbf{k}', -\mathbf{q}}^{(-)*} \alpha_{\mathbf{k}'}^\dagger \beta_{\mathbf{k}'-\mathbf{q}}^\dagger \right) \right] \\
&= \frac{e\hbar}{2m} \sum_{\mathbf{q}} \mathbf{A}_{\mathbf{q}}(t) \left[(2\mathbf{k} + \mathbf{q}) \left(L_{\mathbf{k}, \mathbf{q}}^{(+)} \alpha_{\mathbf{k}+\mathbf{q}}^\dagger \alpha_{\mathbf{k}'} + M_{\mathbf{k}, \mathbf{q}}^{(-)} \alpha_{\mathbf{k}'} \beta_{\mathbf{k}+\mathbf{q}} \right) \right. \\
&\quad \left. - (2\mathbf{k}' - \mathbf{q}) \left(L_{\mathbf{k}', -\mathbf{q}}^{(+)*} \alpha_{\mathbf{k}'}^\dagger \alpha_{\mathbf{k}'-\mathbf{q}} - M_{\mathbf{k}', -\mathbf{q}}^{(-)*} \alpha_{\mathbf{k}'}^\dagger \beta_{\mathbf{k}'-\mathbf{q}}^\dagger \right) \right], \quad (\text{C.14})
\end{aligned}$$

$$\begin{aligned}
[H_{\text{em}}^{(2)}, \alpha_{\mathbf{k}}^\dagger \alpha_{\mathbf{k}'}] &= \left[\frac{e^2}{2m} \sum_{\tilde{\mathbf{k}}, \mathbf{q}} \left[\sum_{\mathbf{q}'} \mathbf{A}_{\mathbf{q}-\mathbf{q}'}(t) \cdot \mathbf{A}_{\mathbf{q}'}(t) \right] \left(L_{\tilde{\mathbf{k}}, \mathbf{q}}^{(-)} \alpha_{\tilde{\mathbf{k}}+\mathbf{q}}^\dagger \alpha_{\tilde{\mathbf{k}}} + L_{\tilde{\mathbf{k}}, \mathbf{q}}^{(-)*} \beta_{\tilde{\mathbf{k}}}^\dagger \beta_{\tilde{\mathbf{k}}+\mathbf{q}} \right. \right. \\
&\quad \left. \left. + M_{\tilde{\mathbf{k}}, \mathbf{q}}^{(+)*} \alpha_{\tilde{\mathbf{k}}+\mathbf{q}}^\dagger \beta_{\tilde{\mathbf{k}}}^\dagger - M_{\tilde{\mathbf{k}}, \mathbf{q}}^{(+)} \alpha_{\tilde{\mathbf{k}}} \beta_{\tilde{\mathbf{k}}+\mathbf{q}} \right), \alpha_{\mathbf{k}}^\dagger \alpha_{\mathbf{k}'} \right] \\
&= \frac{e^2}{2m} \sum_{\tilde{\mathbf{k}}, \mathbf{q}} \left[\sum_{\mathbf{q}'} \mathbf{A}_{\mathbf{q}-\mathbf{q}'}(t) \cdot \mathbf{A}_{\mathbf{q}'}(t) \right] \left(L_{\tilde{\mathbf{k}}, \mathbf{q}}^{(-)} \left(\alpha_{\tilde{\mathbf{k}}+\mathbf{q}}^\dagger \delta_{\tilde{\mathbf{k}}, \mathbf{k}} \alpha_{\mathbf{k}'} - \alpha_{\tilde{\mathbf{k}}}^\dagger \delta_{\tilde{\mathbf{k}}+\mathbf{q}, \mathbf{k}'} \alpha_{\tilde{\mathbf{k}}} \right) \right. \\
&\quad \left. - M_{\tilde{\mathbf{k}}, \mathbf{q}}^{(+)*} \alpha_{\tilde{\mathbf{k}}}^\dagger \delta_{\tilde{\mathbf{k}}+\mathbf{q}, \mathbf{k}'} \beta_{\tilde{\mathbf{k}}}^\dagger + M_{\tilde{\mathbf{k}}, \mathbf{q}}^{(+)} \delta_{\tilde{\mathbf{k}}, \mathbf{k}} \beta_{\tilde{\mathbf{k}}+\mathbf{q}} \alpha_{\mathbf{k}'} \right) \\
&= \frac{e^2}{2m} \sum_{\mathbf{q}} \left[\sum_{\mathbf{q}'} \mathbf{A}_{\mathbf{q}-\mathbf{q}'}(t) \cdot \mathbf{A}_{\mathbf{q}'}(t) \right] \left(L_{\mathbf{k}, \mathbf{q}}^{(-)} \alpha_{\mathbf{k}+\mathbf{q}}^\dagger \alpha_{\mathbf{k}'} - L_{\mathbf{k}', -\mathbf{q}}^{(-)} \alpha_{\mathbf{k}'}^\dagger \alpha_{\mathbf{k}'-\mathbf{q}} \right. \\
&\quad \left. - M_{\mathbf{k}', -\mathbf{q}}^{(+)*} \alpha_{\mathbf{k}'}^\dagger \beta_{\mathbf{k}'-\mathbf{q}}^\dagger - M_{\mathbf{k}, \mathbf{q}}^{(+)} \alpha_{\mathbf{k}'} \beta_{\mathbf{k}+\mathbf{q}} \right) \\
&= \frac{e^2}{2m} \sum_{\mathbf{q}} \left[\sum_{\mathbf{q}'} \mathbf{A}_{\mathbf{q}-\mathbf{q}'}(t) \cdot \mathbf{A}_{\mathbf{q}'}(t) \right] \left(L_{\mathbf{k}, \mathbf{q}}^{(-)} \alpha_{\mathbf{k}+\mathbf{q}}^\dagger \alpha_{\mathbf{k}'} - L_{\mathbf{k}', -\mathbf{q}}^{(-)*} \alpha_{\mathbf{k}'}^\dagger \alpha_{\mathbf{k}'-\mathbf{q}} \right. \\
&\quad \left. - M_{\mathbf{k}', -\mathbf{q}}^{(+)*} \alpha_{\mathbf{k}'}^\dagger \beta_{\mathbf{k}'-\mathbf{q}}^\dagger - M_{\mathbf{k}, \mathbf{q}}^{(+)} \alpha_{\mathbf{k}'} \beta_{\mathbf{k}+\mathbf{q}} \right). \quad (\text{C.15})
\end{aligned}$$

All in all, we find for the third equation of motion

$$\begin{aligned}
 \partial_t \langle \alpha_{\mathbf{k}}^\dagger \alpha_{\mathbf{k}'} \rangle (t) = & \frac{i}{\hbar} \left\{ (R_{\mathbf{k}} - R_{\mathbf{k}'}) \langle \alpha_{\mathbf{k}}^\dagger \alpha_{\mathbf{k}'} \rangle - C_{\mathbf{k}'} \langle \alpha_{\mathbf{k}}^\dagger \beta_{\mathbf{k}'}^\dagger \rangle - C_{\mathbf{k}}^* \langle \alpha_{\mathbf{k}'} \beta_{\mathbf{k}} \rangle \right. \\
 & + \frac{e\hbar}{2m} \sum_{\mathbf{q}} \mathbf{A}_{\mathbf{q}}(t) \left[(2\mathbf{k} + \mathbf{q}) \left(L_{\mathbf{k},\mathbf{q}}^{(+)} \langle \alpha_{\mathbf{k}+\mathbf{q}}^\dagger \alpha_{\mathbf{k}'} \rangle + M_{\mathbf{k},\mathbf{q}}^{(-)} \langle \alpha_{\mathbf{k}'} \beta_{\mathbf{k}+\mathbf{q}} \rangle \right) \right. \\
 & \quad \left. - (2\mathbf{k}' - \mathbf{q}) \left(L_{\mathbf{k}',-\mathbf{q}}^{(+)*} \langle \alpha_{\mathbf{k}}^\dagger \alpha_{\mathbf{k}'-\mathbf{q}} \rangle - M_{\mathbf{k}',-\mathbf{q}}^{(-)*} \langle \alpha_{\mathbf{k}}^\dagger \beta_{\mathbf{k}'-\mathbf{q}}^\dagger \rangle \right) \right] \\
 & + \frac{e^2}{2m} \sum_{\mathbf{q}} \left[\sum_{\mathbf{q}'} \mathbf{A}_{\mathbf{q}-\mathbf{q}'}(t) \cdot \mathbf{A}_{\mathbf{q}'}(t) \right] \left(L_{\mathbf{k},\mathbf{q}}^{(-)} \langle \alpha_{\mathbf{k}+\mathbf{q}}^\dagger \alpha_{\mathbf{k}'} \rangle - L_{\mathbf{k}',-\mathbf{q}}^{(-)*} \langle \alpha_{\mathbf{k}}^\dagger \alpha_{\mathbf{k}'-\mathbf{q}} \rangle \right. \\
 & \quad \left. - M_{\mathbf{k}',-\mathbf{q}}^{(+)*} \langle \alpha_{\mathbf{k}}^\dagger \beta_{\mathbf{k}'-\mathbf{q}}^\dagger \rangle - M_{\mathbf{k},\mathbf{q}}^{(+)} \langle \alpha_{\mathbf{k}'} \beta_{\mathbf{k}+\mathbf{q}} \rangle \right) \left. \right\}. \tag{C.16}
 \end{aligned}$$

Finally, we evaluate the three commutators for the fourth equation of motion

$$\begin{aligned}
 [H_{\text{BCS}}, \beta_{\mathbf{k}}^\dagger \beta_{\mathbf{k}'}] = & \left[\sum_{\tilde{\mathbf{k}}} \left(R_{\tilde{\mathbf{k}}} (\alpha_{\tilde{\mathbf{k}}}^\dagger \alpha_{\tilde{\mathbf{k}}} + \beta_{\tilde{\mathbf{k}}}^\dagger \beta_{\tilde{\mathbf{k}}}) + C_{\tilde{\mathbf{k}}} \alpha_{\tilde{\mathbf{k}}}^\dagger \beta_{\tilde{\mathbf{k}}}^\dagger - C_{\tilde{\mathbf{k}}}^* \alpha_{\tilde{\mathbf{k}}} \beta_{\tilde{\mathbf{k}}} \right), \beta_{\mathbf{k}}^\dagger \beta_{\mathbf{k}'} \right] \\
 = & \sum_{\tilde{\mathbf{k}}} R_{\tilde{\mathbf{k}}} \left(\beta_{\tilde{\mathbf{k}}}^\dagger \delta_{\tilde{\mathbf{k}},\mathbf{k}} \beta_{\mathbf{k}'} - \beta_{\tilde{\mathbf{k}}}^\dagger \delta_{\tilde{\mathbf{k}},\mathbf{k}'} \beta_{\tilde{\mathbf{k}}} \right) + C_{\tilde{\mathbf{k}}} \beta_{\tilde{\mathbf{k}}}^\dagger \alpha_{\tilde{\mathbf{k}}}^\dagger \delta_{\tilde{\mathbf{k}},\mathbf{k}'} - C_{\tilde{\mathbf{k}}}^* \alpha_{\tilde{\mathbf{k}}} \delta_{\tilde{\mathbf{k}},\mathbf{k}} \beta_{\mathbf{k}'} \\
 = & (R_{\mathbf{k}} - R_{\mathbf{k}'}) \beta_{\mathbf{k}}^\dagger \beta_{\mathbf{k}'} - C_{\mathbf{k}'} \alpha_{\mathbf{k}'}^\dagger \beta_{\mathbf{k}}^\dagger - C_{\mathbf{k}}^* \alpha_{\mathbf{k}} \beta_{\mathbf{k}'}, \tag{C.17}
 \end{aligned}$$

$$\begin{aligned}
 [H_{\text{em}}^{(1)}, \beta_{\mathbf{k}}^\dagger \beta_{\mathbf{k}'}] = & \left[\frac{e\hbar}{2m} \sum_{\tilde{\mathbf{k}},\mathbf{q}} (2\tilde{\mathbf{k}} + \mathbf{q}) \mathbf{A}_{\mathbf{q}}(t) \left[L_{\tilde{\mathbf{k}},\mathbf{q}}^{(+)} \alpha_{\tilde{\mathbf{k}}+\mathbf{q}}^\dagger \alpha_{\tilde{\mathbf{k}}} - L_{\tilde{\mathbf{k}},\mathbf{q}}^{(+)*} \beta_{\tilde{\mathbf{k}}}^\dagger \beta_{\tilde{\mathbf{k}}+\mathbf{q}} \right. \right. \\
 & \quad \left. \left. + M_{\tilde{\mathbf{k}},\mathbf{q}}^{(-)*} \alpha_{\tilde{\mathbf{k}}+\mathbf{q}}^\dagger \beta_{\tilde{\mathbf{k}}}^\dagger + M_{\tilde{\mathbf{k}},\mathbf{q}}^{(-)} \alpha_{\tilde{\mathbf{k}}} \beta_{\tilde{\mathbf{k}}+\mathbf{q}} \right], \beta_{\mathbf{k}}^\dagger \beta_{\mathbf{k}'} \right] \\
 = & \frac{e\hbar}{2m} \sum_{\tilde{\mathbf{k}},\mathbf{q}} (2\tilde{\mathbf{k}} + \mathbf{q}) \mathbf{A}_{\mathbf{q}}(t) \left[-L_{\tilde{\mathbf{k}},\mathbf{q}}^{(+)*} \left(\beta_{\tilde{\mathbf{k}}}^\dagger \delta_{\tilde{\mathbf{k}}+\mathbf{q},\mathbf{k}} \beta_{\mathbf{k}'} - \beta_{\tilde{\mathbf{k}}}^\dagger \delta_{\tilde{\mathbf{k}},\mathbf{k}'} \beta_{\tilde{\mathbf{k}}+\mathbf{q}} \right) \right. \\
 & \quad \left. + M_{\tilde{\mathbf{k}},\mathbf{q}}^{(-)*} \beta_{\tilde{\mathbf{k}}}^\dagger \alpha_{\tilde{\mathbf{k}}+\mathbf{q}}^\dagger \delta_{\tilde{\mathbf{k}},\mathbf{k}'} + M_{\tilde{\mathbf{k}},\mathbf{q}}^{(-)} \alpha_{\tilde{\mathbf{k}}} \delta_{\tilde{\mathbf{k}}+\mathbf{q},\mathbf{k}} \beta_{\mathbf{k}'} \right] \\
 = & \frac{e\hbar}{2m} \sum_{\mathbf{q}} \mathbf{A}_{\mathbf{q}}(t) \left[(2\mathbf{k}' + \mathbf{q}) \left(L_{\mathbf{k}',\mathbf{q}}^{(+)*} \beta_{\mathbf{k}}^\dagger \beta_{\mathbf{k}'+\mathbf{q}} + M_{\mathbf{k}',\mathbf{q}}^{(-)*} \beta_{\mathbf{k}}^\dagger \alpha_{\mathbf{k}'+\mathbf{q}}^\dagger \right) \right. \\
 & \quad \left. + (2\mathbf{k} - \mathbf{q}) \left(-L_{\mathbf{k}-\mathbf{q},\mathbf{q}}^{(+)*} \beta_{\mathbf{k}-\mathbf{q}}^\dagger \beta_{\mathbf{k}'} + M_{\mathbf{k}-\mathbf{q},\mathbf{q}}^{(-)} \alpha_{\mathbf{k}-\mathbf{q}} \beta_{\mathbf{k}'} \right) \right] \\
 = & \frac{e\hbar}{2m} \sum_{\mathbf{q}} \mathbf{A}_{\mathbf{q}}(t) \left[(2\mathbf{k}' + \mathbf{q}) \left(L_{\mathbf{k}',\mathbf{q}}^{(+)*} \beta_{\mathbf{k}}^\dagger \beta_{\mathbf{k}'+\mathbf{q}} - M_{\mathbf{k}',\mathbf{q}}^{(-)*} \alpha_{\mathbf{k}'+\mathbf{q}}^\dagger \beta_{\mathbf{k}}^\dagger \right) \right. \\
 & \quad \left. + (2\mathbf{k} - \mathbf{q}) \left(-L_{\mathbf{k},-\mathbf{q}}^{(+)} \beta_{\mathbf{k}-\mathbf{q}}^\dagger \beta_{\mathbf{k}'} - M_{\mathbf{k},-\mathbf{q}}^{(-)} \alpha_{\mathbf{k}-\mathbf{q}} \beta_{\mathbf{k}'} \right) \right], \tag{C.18}
 \end{aligned}$$

$$\begin{aligned}
[H_{\text{em}}^{(2)}, \beta_{\mathbf{k}}^\dagger \beta_{\mathbf{k}'}] &= \left[\frac{e^2}{2m} \sum_{\tilde{\mathbf{k}}, \mathbf{q}} \left[\sum_{\mathbf{q}'} \mathbf{A}_{\mathbf{q}-\mathbf{q}'}(t) \cdot \mathbf{A}_{\mathbf{q}'}(t) \right] \left(L_{\tilde{\mathbf{k}}, \mathbf{q}}^{(-)} \alpha_{\tilde{\mathbf{k}}+\mathbf{q}}^\dagger \alpha_{\tilde{\mathbf{k}}} + L_{\tilde{\mathbf{k}}, \mathbf{q}}^{(-)*} \beta_{\tilde{\mathbf{k}}}^\dagger \beta_{\tilde{\mathbf{k}}+\mathbf{q}} \right. \right. \\
&\quad \left. \left. + M_{\tilde{\mathbf{k}}, \mathbf{q}}^{(+)*} \alpha_{\tilde{\mathbf{k}}+\mathbf{q}}^\dagger \beta_{\tilde{\mathbf{k}}}^\dagger - M_{\tilde{\mathbf{k}}, \mathbf{q}}^{(+)} \alpha_{\tilde{\mathbf{k}}} \beta_{\tilde{\mathbf{k}}+\mathbf{q}} \right), \beta_{\mathbf{k}}^\dagger \beta_{\mathbf{k}'} \right] \\
&= \frac{e^2}{2m} \sum_{\tilde{\mathbf{k}}, \mathbf{q}} \left[\sum_{\mathbf{q}'} \mathbf{A}_{\mathbf{q}-\mathbf{q}'}(t) \cdot \mathbf{A}_{\mathbf{q}'}(t) \right] \left(L_{\tilde{\mathbf{k}}, \mathbf{q}}^{(-)*} \left(\beta_{\tilde{\mathbf{k}}}^\dagger \delta_{\tilde{\mathbf{k}}+\mathbf{q}, \mathbf{k}} \beta_{\mathbf{k}'} - \beta_{\tilde{\mathbf{k}}}^\dagger \delta_{\tilde{\mathbf{k}}, \mathbf{k}'} \beta_{\tilde{\mathbf{k}}+\mathbf{q}} \right) \right. \\
&\quad \left. + M_{\tilde{\mathbf{k}}, \mathbf{q}}^{(+)*} \beta_{\tilde{\mathbf{k}}}^\dagger \alpha_{\tilde{\mathbf{k}}+\mathbf{q}}^\dagger \delta_{\tilde{\mathbf{k}}, \mathbf{k}'} - M_{\tilde{\mathbf{k}}, \mathbf{q}}^{(+)} \alpha_{\tilde{\mathbf{k}}} \delta_{\tilde{\mathbf{k}}+\mathbf{q}, \mathbf{k}} \beta_{\mathbf{k}'} \right) \\
&= \frac{e^2}{2m} \sum_{\mathbf{q}} \left[\sum_{\mathbf{q}'} \mathbf{A}_{\mathbf{q}-\mathbf{q}'}(t) \cdot \mathbf{A}_{\mathbf{q}'}(t) \right] \left(L_{\mathbf{k}-\mathbf{q}, \mathbf{q}}^{(-)*} \beta_{\mathbf{k}-\mathbf{q}}^\dagger \beta_{\mathbf{k}'} - L_{\mathbf{k}', \mathbf{q}}^{(-)*} \beta_{\mathbf{k}}^\dagger \beta_{\mathbf{k}'+\mathbf{q}} \right. \\
&\quad \left. + M_{\mathbf{k}', \mathbf{q}}^{(+)*} \beta_{\mathbf{k}}^\dagger \alpha_{\mathbf{k}'+\mathbf{q}}^\dagger - M_{\mathbf{k}-\mathbf{q}, \mathbf{q}}^{(+)} \alpha_{\mathbf{k}-\mathbf{q}} \beta_{\mathbf{k}'} \right) \\
&= \frac{e^2}{2m} \sum_{\mathbf{q}} \left[\sum_{\mathbf{q}'} \mathbf{A}_{\mathbf{q}-\mathbf{q}'}(t) \cdot \mathbf{A}_{\mathbf{q}'}(t) \right] \left(L_{\mathbf{k}, -\mathbf{q}}^{(-)} \beta_{\mathbf{k}-\mathbf{q}}^\dagger \beta_{\mathbf{k}'} - L_{\mathbf{k}', \mathbf{q}}^{(-)*} \beta_{\mathbf{k}}^\dagger \beta_{\mathbf{k}'+\mathbf{q}} \right. \\
&\quad \left. - M_{\mathbf{k}', \mathbf{q}}^{(+)*} \alpha_{\mathbf{k}'+\mathbf{q}}^\dagger \beta_{\mathbf{k}}^\dagger - M_{\mathbf{k}, -\mathbf{q}}^{(+)} \alpha_{\mathbf{k}-\mathbf{q}} \beta_{\mathbf{k}'} \right). \tag{C.19}
\end{aligned}$$

All in all, we find for the fourth equation of motion

$$\begin{aligned}
\partial_t \langle \beta_{\mathbf{k}}^\dagger \beta_{\mathbf{k}'} \rangle (t) &= \frac{i}{\hbar} \left\{ (R_{\mathbf{k}} - R_{\mathbf{k}'}) \langle \beta_{\mathbf{k}}^\dagger \beta_{\mathbf{k}'} \rangle - C_{\mathbf{k}'} \langle \alpha_{\mathbf{k}'}^\dagger \beta_{\mathbf{k}}^\dagger \rangle - C_{\mathbf{k}}^* \langle \alpha_{\mathbf{k}} \beta_{\mathbf{k}'} \rangle \right. \\
&\quad + \frac{e\hbar}{2m} \sum_{\mathbf{q}} \mathbf{A}_{\mathbf{q}}(t) \left[(2\mathbf{k}' + \mathbf{q}) \left(L_{\mathbf{k}', \mathbf{q}}^{(+)*} \langle \beta_{\mathbf{k}}^\dagger \beta_{\mathbf{k}'+\mathbf{q}} \rangle - M_{\mathbf{k}', \mathbf{q}}^{(-)*} \langle \alpha_{\mathbf{k}'+\mathbf{q}}^\dagger \beta_{\mathbf{k}}^\dagger \rangle \right) \right. \\
&\quad \left. + (2\mathbf{k} - \mathbf{q}) \left(-L_{\mathbf{k}, -\mathbf{q}}^{(+)} \langle \beta_{\mathbf{k}-\mathbf{q}}^\dagger \beta_{\mathbf{k}'} \rangle - M_{\mathbf{k}, -\mathbf{q}}^{(-)} \langle \alpha_{\mathbf{k}-\mathbf{q}} \beta_{\mathbf{k}'} \rangle \right) \right] \\
&\quad + \frac{e^2}{2m} \sum_{\mathbf{q}} \left[\sum_{\mathbf{q}'} \mathbf{A}_{\mathbf{q}-\mathbf{q}'}(t) \cdot \mathbf{A}_{\mathbf{q}'}(t) \right] \left(L_{\mathbf{k}, -\mathbf{q}}^{(-)} \langle \beta_{\mathbf{k}-\mathbf{q}}^\dagger \beta_{\mathbf{k}'} \rangle - L_{\mathbf{k}', \mathbf{q}}^{(-)*} \langle \beta_{\mathbf{k}}^\dagger \beta_{\mathbf{k}'+\mathbf{q}} \rangle \right. \\
&\quad \left. - M_{\mathbf{k}', \mathbf{q}}^{(+)*} \langle \alpha_{\mathbf{k}'+\mathbf{q}}^\dagger \beta_{\mathbf{k}}^\dagger \rangle - M_{\mathbf{k}, -\mathbf{q}}^{(+)} \langle \alpha_{\mathbf{k}-\mathbf{q}} \beta_{\mathbf{k}'} \rangle \right) \left. \right\}. \tag{C.20}
\end{aligned}$$

D Derivation of Probe Pulse Current

This derivation of the expressions for the current follows [228, p. 221ff.]. During the derivation, we neglect the spin degree of freedom. It is added again at the end.

The quantum mechanical electrical current density in the presence of a transverse electromagnetic field is given by

$$\mathbf{j}(\mathbf{r}, t) = -\frac{e\hbar}{2mi} \left(\psi^*(\mathbf{r}) \nabla \psi(\mathbf{r}) - (\nabla \psi^*(\mathbf{r})) \psi(\mathbf{r}) \right) - \frac{e^2}{m} \mathbf{A}(\mathbf{r}, t) |\psi(\mathbf{r})|^2. \quad (\text{D.1})$$

We transform the expression into second quantization with the help of Eq. (B.5) and find

$$\begin{aligned} \mathbf{j}(\mathbf{r}, t) &= -\frac{e\hbar}{2miV} \sum_{\mathbf{k}\mathbf{k}'} \left(e^{-i\mathbf{k}r} \nabla e^{i\mathbf{k}'r} c_{\mathbf{k}}^\dagger c_{\mathbf{k}'} - e^{i\mathbf{k}r} \nabla e^{-i\mathbf{k}'r} c_{\mathbf{k}'}^\dagger c_{\mathbf{k}} \right) \\ &\quad - \frac{e^2}{mV} \mathbf{A}(\mathbf{r}, t) \sum_{\mathbf{k}\mathbf{k}'} e^{-i(\mathbf{k}-\mathbf{k}')r} c_{\mathbf{k}}^\dagger c_{\mathbf{k}'} \\ &= -\frac{e\hbar}{2mV} \sum_{\mathbf{k}\mathbf{k}'} \mathbf{k}' \left(e^{-i(\mathbf{k}-\mathbf{k}')r} c_{\mathbf{k}}^\dagger c_{\mathbf{k}'} + e^{i(\mathbf{k}-\mathbf{k}')r} c_{\mathbf{k}'}^\dagger c_{\mathbf{k}} \right) \\ &\quad - \frac{e^2}{mV} \mathbf{A}(\mathbf{r}, t) \sum_{\mathbf{k}\mathbf{k}'} e^{-i(\mathbf{k}-\mathbf{k}')r} c_{\mathbf{k}}^\dagger c_{\mathbf{k}'} . \end{aligned} \quad (\text{D.2})$$

Exchanging $\mathbf{k} \leftrightarrow \mathbf{k}'$ in the second term in Eq. (D.2), we find

$$\mathbf{j}(\mathbf{r}, t) = -\frac{e\hbar}{2mV} \sum_{\mathbf{k}\mathbf{k}'} (\mathbf{k}' + \mathbf{k}) e^{-i(\mathbf{k}-\mathbf{k}')r} c_{\mathbf{k}}^\dagger c_{\mathbf{k}'} - \frac{e^2}{mV} \mathbf{A}(\mathbf{r}, t) \sum_{\mathbf{k}\mathbf{k}'} e^{-i(\mathbf{k}-\mathbf{k}')r} c_{\mathbf{k}}^\dagger c_{\mathbf{k}'} . \quad (\text{D.3})$$

We perform a Fourier transformation

$$\begin{aligned} \mathbf{j}_q(t) &= \frac{1}{V} \int d^3\mathbf{r} \mathbf{j}(\mathbf{r}, t) e^{-i\mathbf{q}r} \\ &= -\frac{e\hbar}{2mV} \sum_{\mathbf{k}\mathbf{k}'} (\mathbf{k}' + \mathbf{k}) c_{\mathbf{k}}^\dagger c_{\mathbf{k}'} \frac{1}{V} \int d^3\mathbf{r} e^{-i(\mathbf{k}-\mathbf{k}'+\mathbf{q})r} \\ &\quad - \frac{e^2}{mV} \sum_{\mathbf{k}\mathbf{k}'} c_{\mathbf{k}}^\dagger c_{\mathbf{k}'} \frac{1}{V} \int d^3\mathbf{r} \mathbf{A}(\mathbf{r}, t) e^{-i(\mathbf{k}-\mathbf{k}'+\mathbf{q})r} \\ &= -\frac{e\hbar}{2mV} \sum_{\mathbf{k}\mathbf{k}'} (\mathbf{k}' + \mathbf{k}) c_{\mathbf{k}}^\dagger c_{\mathbf{k}'} \delta_{\mathbf{k}', \mathbf{k}+\mathbf{q}} - \frac{e^2}{mV} \sum_{\mathbf{k}\mathbf{k}'} c_{\mathbf{k}}^\dagger c_{\mathbf{k}'} \mathbf{A}_{\mathbf{k}-\mathbf{k}'+\mathbf{q}}(t) \\ &= -\frac{e\hbar}{2mV} \sum_{\mathbf{k}} (2\mathbf{k} + \mathbf{q}) c_{\mathbf{k}}^\dagger c_{\mathbf{k}+\mathbf{q}} - \frac{e^2}{mV} \sum_{\mathbf{k}\mathbf{q}'} \mathbf{A}_{\mathbf{q}-\mathbf{q}'}(t) c_{\mathbf{k}}^\dagger c_{\mathbf{k}+\mathbf{q}'}. \end{aligned} \quad (\text{D.4})$$

Adding the spin degree of freedom again, we end up with

$$\mathbf{j}_q(t) = \mathbf{j}_q^{(1)} + \mathbf{j}_q^{(2)}(t), \quad (\text{D.5a})$$

$$\mathbf{j}_q^{(1)} = -\frac{e\hbar}{2mV} \sum_{\mathbf{k}\sigma} (2\mathbf{k} + \mathbf{q}) c_{\mathbf{k}\sigma}^\dagger c_{\mathbf{k}+\mathbf{q}\sigma}, \quad (\text{D.5b})$$

$$\mathbf{j}_q^{(2)}(t) = -\frac{e^2}{mV} \sum_{\mathbf{k}\mathbf{q}'\sigma} \mathbf{A}_{\mathbf{q}-\mathbf{q}'}(t) c_{\mathbf{k}\sigma}^\dagger c_{\mathbf{k}+\mathbf{q}'\sigma}. \quad (\text{D.5c})$$

We apply the Bogoliubov transformation and find

$$\begin{aligned}
j_{\mathbf{q}}^{(1)} &= -\frac{e\hbar}{2mV} \sum_{\mathbf{k}} (2\mathbf{k} + \mathbf{q}) (c_{\mathbf{k}\uparrow}^\dagger c_{\mathbf{k}+\mathbf{q}\uparrow} - c_{-(\mathbf{k}+\mathbf{q})\downarrow}^\dagger c_{-\mathbf{k}\downarrow}) \\
&= -\frac{e\hbar}{2mV} \sum_{\mathbf{k}} (2\mathbf{k} + \mathbf{q}) \left(L^{(+)*} \alpha_{\mathbf{k}}^\dagger \alpha_{\mathbf{k}+\mathbf{q}} - L^{(+)} \beta_{\mathbf{k}+\mathbf{q}}^\dagger \beta_{\mathbf{k}} \right. \\
&\quad \left. - M^{(-)*} \alpha_{\mathbf{k}}^\dagger \beta_{\mathbf{k}+\mathbf{q}}^\dagger - M^{(-)} \alpha_{\mathbf{k}+\mathbf{q}} \beta_{\mathbf{k}} \right) .
\end{aligned} \tag{D.6}$$

E Derivation of Equations of Motion for tr-ARPES

Using the iterated equation of motion ansatz Eq. (2.69), the BCS Hamiltonian in the Bogoliubov quasiparticle basis Eq. (2.41) in the Heisenberg picture reads

$$\begin{aligned}
\tilde{H}(t) &= U^\dagger(t) \left(\sum_{\mathbf{k}} R_{\mathbf{k}}(t) (\alpha_{\mathbf{k}}^\dagger \alpha_{\mathbf{k}} + \beta_{\mathbf{k}}^\dagger \beta_{\mathbf{k}}) + \sum_{\mathbf{k}} C_{\mathbf{k}}(t) \alpha_{\mathbf{k}}^\dagger \beta_{\mathbf{k}}^\dagger - C_{\mathbf{k}}^*(t) \alpha_{\mathbf{k}} \beta_{\mathbf{k}} \right) U(t) \\
&= \sum_{\mathbf{k}} R_{\mathbf{k}}(t) \left[(a_{0\mathbf{k}}(t) \alpha_{\mathbf{k}}^\dagger + a_{1\mathbf{k}}(t) \beta_{\mathbf{k}}) (a_{0\mathbf{k}}^*(t) \alpha_{\mathbf{k}} + a_{1\mathbf{k}}^*(t) \beta_{\mathbf{k}}^\dagger) \right. \\
&\quad \left. + (b_{0\mathbf{k}}(t) \beta_{\mathbf{k}}^\dagger + b_{1\mathbf{k}}(t) \alpha_{\mathbf{k}}) (b_{0\mathbf{k}}^*(t) \beta_{\mathbf{k}} + b_{1\mathbf{k}}^*(t) \alpha_{\mathbf{k}}^\dagger) \right] \\
&\quad + C_{\mathbf{k}}(t) (a_{0\mathbf{k}}(t) \alpha_{\mathbf{k}}^\dagger + a_{1\mathbf{k}}(t) \beta_{\mathbf{k}}) (b_{0\mathbf{k}}(t) \beta_{\mathbf{k}}^\dagger + b_{1\mathbf{k}}(t) \alpha_{\mathbf{k}}) \\
&\quad - C_{\mathbf{k}}^*(t) (a_{0\mathbf{k}}^*(t) \alpha_{\mathbf{k}} + a_{1\mathbf{k}}^*(t) \beta_{\mathbf{k}}^\dagger) (b_{0\mathbf{k}}^*(t) \beta_{\mathbf{k}} + b_{1\mathbf{k}}^*(t) \alpha_{\mathbf{k}}^\dagger) \\
&= \sum_{\mathbf{k}} \alpha_{\mathbf{k}}^\dagger \alpha_{\mathbf{k}} \left[R_{\mathbf{k}}(t) (|a_{0\mathbf{k}}(t)|^2 - |b_{1\mathbf{k}}(t)|^2) + C_{\mathbf{k}}(t) a_{0\mathbf{k}}(t) b_{1\mathbf{k}}(t) + C_{\mathbf{k}}^*(t) a_{0\mathbf{k}}^*(t) b_{1\mathbf{k}}^*(t) \right] \\
&\quad + \beta_{\mathbf{k}}^\dagger \beta_{\mathbf{k}} \left[R_{\mathbf{k}}(t) (|b_{0\mathbf{k}}(t)|^2 - |a_{1\mathbf{k}}(t)|^2) - C_{\mathbf{k}}(t) a_{1\mathbf{k}}(t) b_{0\mathbf{k}}(t) - C_{\mathbf{k}}^*(t) a_{1\mathbf{k}}^*(t) b_{0\mathbf{k}}^*(t) \right] \\
&\quad + \alpha_{\mathbf{k}}^\dagger \beta_{\mathbf{k}}^\dagger \left[R_{\mathbf{k}}(t) (a_{0\mathbf{k}}(t) a_{1\mathbf{k}}^*(t) - b_{0\mathbf{k}}(t) b_{1\mathbf{k}}^*(t)) + C_{\mathbf{k}}(t) a_{0\mathbf{k}}(t) b_{0\mathbf{k}}(t) + C_{\mathbf{k}}^*(t) a_{1\mathbf{k}}^*(t) b_{1\mathbf{k}}^*(t) \right] \\
&\quad + \alpha_{\mathbf{k}} \beta_{\mathbf{k}} \left[R_{\mathbf{k}}(t) (b_{0\mathbf{k}}^*(t) b_{1\mathbf{k}}(t) - a_{0\mathbf{k}}^*(t) a_{1\mathbf{k}}(t)) - C_{\mathbf{k}}(t) a_{1\mathbf{k}}(t) b_{1\mathbf{k}}(t) - C_{\mathbf{k}}^*(t) a_{0\mathbf{k}}^*(t) b_{0\mathbf{k}}^*(t) \right] \\
&\quad + \text{const.} \tag{E.1}
\end{aligned}$$

For the evaluation of the commutators in Eq. (2.67), the (anti)-commutation rule $[AB, C] = A\{B, C\} - \{A, C\}B$ is useful, which allows to derive the following expressions

$$\begin{aligned}
[\alpha_{\mathbf{k}}^\dagger \alpha_{\mathbf{k}}, \alpha_{\mathbf{k}}^\dagger] &= \alpha_{\mathbf{k}}^\dagger, & [\beta_{\mathbf{k}}^\dagger \beta_{\mathbf{k}}, \alpha_{\mathbf{k}}^\dagger] &= 0, & [\alpha_{\mathbf{k}}^\dagger \beta_{\mathbf{k}}^\dagger, \alpha_{\mathbf{k}}^\dagger] &= 0, & [\alpha_{\mathbf{k}} \beta_{\mathbf{k}}, \alpha_{\mathbf{k}}^\dagger] &= -\beta_{\mathbf{k}}, \\
[\alpha_{\mathbf{k}}^\dagger \alpha_{\mathbf{k}}, \alpha_{\mathbf{k}}] &= -\alpha_{\mathbf{k}}, & [\beta_{\mathbf{k}}^\dagger \beta_{\mathbf{k}}, \alpha_{\mathbf{k}}] &= 0, & [\alpha_{\mathbf{k}}^\dagger \beta_{\mathbf{k}}^\dagger, \alpha_{\mathbf{k}}] &= -\beta_{\mathbf{k}}^\dagger, & [\alpha_{\mathbf{k}} \beta_{\mathbf{k}}, \alpha_{\mathbf{k}}] &= 0, \\
[\alpha_{\mathbf{k}}^\dagger \alpha_{\mathbf{k}}, \beta_{\mathbf{k}}^\dagger] &= 0, & [\beta_{\mathbf{k}}^\dagger \beta_{\mathbf{k}}, \beta_{\mathbf{k}}^\dagger] &= \beta_{\mathbf{k}}^\dagger, & [\alpha_{\mathbf{k}}^\dagger \beta_{\mathbf{k}}^\dagger, \beta_{\mathbf{k}}^\dagger] &= 0, & [\alpha_{\mathbf{k}} \beta_{\mathbf{k}}, \beta_{\mathbf{k}}^\dagger] &= \alpha_{\mathbf{k}}, \\
[\alpha_{\mathbf{k}}^\dagger \alpha_{\mathbf{k}}, \beta_{\mathbf{k}}] &= 0, & [\beta_{\mathbf{k}}^\dagger \beta_{\mathbf{k}}, \beta_{\mathbf{k}}] &= -\beta_{\mathbf{k}}, & [\alpha_{\mathbf{k}}^\dagger \beta_{\mathbf{k}}^\dagger, \beta_{\mathbf{k}}] &= \alpha_{\mathbf{k}}^\dagger, & [\alpha_{\mathbf{k}} \beta_{\mathbf{k}}, \beta_{\mathbf{k}}] &= 0. \tag{E.2}
\end{aligned}$$

With the help of the derived (anti)-commutation rules, Heisenberg's equation of motion

$$\partial_t \alpha_{\mathbf{k}}^\dagger(t) = \frac{i}{\hbar} [\tilde{H}(t), \alpha_{\mathbf{k}}^\dagger(t)] \qquad \partial_t \beta_{\mathbf{k}}^\dagger(t) = \frac{i}{\hbar} [\tilde{H}(t), \beta_{\mathbf{k}}^\dagger(t)] \tag{E.3}$$

can be evaluated.

It follows

$$\begin{aligned}
& \partial_t a_{0\mathbf{k}}(t) \alpha_{\mathbf{k}}^\dagger + \partial_t a_{1\mathbf{k}}(t) \beta_{\mathbf{k}} \\
&= \frac{i}{\hbar} [\tilde{H}(t), a_{0\mathbf{k}}(t) \alpha_{\mathbf{k}}^\dagger + a_{1\mathbf{k}}(t) \beta_{\mathbf{k}}] \\
&= \frac{i}{\hbar} \left[a_{0\mathbf{k}}(t) \alpha_{\mathbf{k}}^\dagger \left[R_{\mathbf{k}}(t) \left(|a_{0\mathbf{k}}(t)|^2 - |b_{1\mathbf{k}}(t)|^2 \right) + C_{\mathbf{k}}(t) a_{0\mathbf{k}}(t) b_{1\mathbf{k}}(t) + C_{\mathbf{k}}^*(t) a_{0\mathbf{k}}^*(t) b_{1\mathbf{k}}^*(t) \right] \right. \\
&\quad - a_{1\mathbf{k}}(t) \beta_{\mathbf{k}} \left[R_{\mathbf{k}}(t) \left(|b_{0\mathbf{k}}(t)|^2 - |a_{1\mathbf{k}}(t)|^2 \right) - C_{\mathbf{k}}(t) a_{1\mathbf{k}}(t) b_{0\mathbf{k}}(t) - C_{\mathbf{k}}^*(t) a_{1\mathbf{k}}^*(t) b_{0\mathbf{k}}^*(t) \right] \\
&\quad + a_{1\mathbf{k}}(t) \alpha_{\mathbf{k}}^\dagger \left[R_{\mathbf{k}}(t) \left(a_{0\mathbf{k}}(t) a_{1\mathbf{k}}^*(t) - b_{0\mathbf{k}}(t) b_{1\mathbf{k}}^*(t) \right) + C_{\mathbf{k}}(t) a_{0\mathbf{k}}(t) b_{0\mathbf{k}}(t) + C_{\mathbf{k}}^*(t) a_{1\mathbf{k}}^*(t) b_{1\mathbf{k}}^*(t) \right] \\
&\quad \left. - a_{0\mathbf{k}}(t) \beta_{\mathbf{k}} \left[R_{\mathbf{k}}(t) \left(b_{0\mathbf{k}}^*(t) b_{1\mathbf{k}}(t) - a_{0\mathbf{k}}^*(t) a_{1\mathbf{k}}(t) \right) - C_{\mathbf{k}}(t) a_{1\mathbf{k}}(t) b_{1\mathbf{k}}(t) - C_{\mathbf{k}}^*(t) a_{0\mathbf{k}}^*(t) b_{0\mathbf{k}}^*(t) \right] \right] \\
&= \frac{i}{\hbar} \left[\alpha_{\mathbf{k}}^\dagger \left\{ R_{\mathbf{k}}(t) \left[a_{0\mathbf{k}}(t) \left(|a_{0\mathbf{k}}(t)|^2 + |a_{1\mathbf{k}}(t)|^2 - |b_{1\mathbf{k}}(t)|^2 \right) - a_{1\mathbf{k}}(t) b_{0\mathbf{k}}(t) b_{1\mathbf{k}}^*(t) \right] \right. \right. \\
&\quad \left. \left. + C_{\mathbf{k}}(t) \left[a_{0\mathbf{k}}(t) \left(a_{0\mathbf{k}}(t) b_{1\mathbf{k}}(t) + a_{1\mathbf{k}}(t) b_{0\mathbf{k}}(t) \right) \right] + C_{\mathbf{k}}^*(t) \left[b_{1\mathbf{k}}^*(t) \left(|a_{0\mathbf{k}}(t)|^2 + |a_{1\mathbf{k}}(t)|^2 \right) \right] \right\} \right. \\
&\quad \left. - \beta_{\mathbf{k}} \left\{ R_{\mathbf{k}} \left[a_{1\mathbf{k}}(t) \left(|b_{0\mathbf{k}}(t)|^2 - |a_{1\mathbf{k}}(t)|^2 - |a_{0\mathbf{k}}(t)|^2 \right) + a_{0\mathbf{k}}(t) b_{0\mathbf{k}}^*(t) b_{1\mathbf{k}}(t) \right] \right. \right. \\
&\quad \left. \left. - C_{\mathbf{k}}(t) \left[a_{0\mathbf{k}}(t) a_{1\mathbf{k}}(t) b_{1\mathbf{k}}(t) + a_{1\mathbf{k}}(t)^2 b_{0\mathbf{k}}(t) \right] - C_{\mathbf{k}}^*(t) \left[b_{0\mathbf{k}}^*(t) \left(|a_{0\mathbf{k}}(t)|^2 + |a_{1\mathbf{k}}(t)|^2 \right) \right] \right\} \right], \tag{E.4}
\end{aligned}$$

$$\begin{aligned}
& \partial_t b_{0\mathbf{k}}(t) \beta_{\mathbf{k}}^\dagger + \partial_t b_{1\mathbf{k}}(t) \alpha_{\mathbf{k}} \\
&= \frac{i}{\hbar} [\tilde{H}(t), b_{0\mathbf{k}}(t) \beta_{\mathbf{k}}^\dagger + b_{1\mathbf{k}}(t) \alpha_{\mathbf{k}}] \\
&= \frac{i}{\hbar} \left[-b_{1\mathbf{k}}(t) \alpha_{\mathbf{k}} \left[R_{\mathbf{k}}(t) \left(|a_{0\mathbf{k}}(t)|^2 - |b_{1\mathbf{k}}(t)|^2 \right) + C_{\mathbf{k}}(t) a_{0\mathbf{k}}(t) b_{1\mathbf{k}}(t) + C_{\mathbf{k}}^*(t) a_{0\mathbf{k}}^*(t) b_{1\mathbf{k}}^*(t) \right] \right. \\
&\quad + b_{0\mathbf{k}}(t) \beta_{\mathbf{k}}^\dagger \left[R_{\mathbf{k}}(t) \left(|b_{0\mathbf{k}}(t)|^2 - |a_{1\mathbf{k}}(t)|^2 \right) - C_{\mathbf{k}}(t) a_{1\mathbf{k}}(t) b_{0\mathbf{k}}(t) - C_{\mathbf{k}}^*(t) a_{1\mathbf{k}}^*(t) b_{0\mathbf{k}}^*(t) \right] \\
&\quad - b_{1\mathbf{k}}(t) \beta_{\mathbf{k}}^\dagger \left[R_{\mathbf{k}}(t) \left(a_{0\mathbf{k}}(t) a_{1\mathbf{k}}^*(t) - b_{0\mathbf{k}}(t) b_{1\mathbf{k}}^*(t) \right) + C_{\mathbf{k}}(t) a_{0\mathbf{k}}(t) b_{0\mathbf{k}}(t) + C_{\mathbf{k}}^*(t) a_{1\mathbf{k}}^*(t) b_{1\mathbf{k}}^*(t) \right] \\
&\quad \left. + b_{0\mathbf{k}}(t) \alpha_{\mathbf{k}} \left[R_{\mathbf{k}}(t) \left(b_{0\mathbf{k}}^*(t) b_{1\mathbf{k}}(t) - a_{0\mathbf{k}}^*(t) a_{1\mathbf{k}}(t) \right) - C_{\mathbf{k}}(t) a_{1\mathbf{k}}(t) b_{1\mathbf{k}}(t) - C_{\mathbf{k}}^*(t) a_{0\mathbf{k}}^*(t) b_{0\mathbf{k}}^*(t) \right] \right] \\
&= \frac{i}{\hbar} \left[\beta_{\mathbf{k}}^\dagger \left\{ R_{\mathbf{k}}(t) \left[b_{0\mathbf{k}}(t) \left(|b_{0\mathbf{k}}(t)|^2 + |b_{1\mathbf{k}}(t)|^2 - |a_{1\mathbf{k}}(t)|^2 \right) - a_{0\mathbf{k}}(t) a_{1\mathbf{k}}^*(t) b_{1\mathbf{k}}(t) \right] \right. \right. \\
&\quad \left. \left. - C_{\mathbf{k}} \left[a_{1\mathbf{k}}(t) b_{0\mathbf{k}}(t)^2 + a_{0\mathbf{k}}(t) b_{0\mathbf{k}}(t) b_{1\mathbf{k}}(t) \right] - C_{\mathbf{k}}^* \left[a_{1\mathbf{k}}^*(t) \left(|b_{0\mathbf{k}}(t)|^2 + |b_{1\mathbf{k}}(t)|^2 \right) \right] \right\} \right. \\
&\quad \left. + \alpha_{\mathbf{k}} \left\{ -R_{\mathbf{k}}(t) \left[b_{1\mathbf{k}}(t) \left(|a_{0\mathbf{k}}(t)|^2 - |b_{0\mathbf{k}}(t)|^2 - |b_{1\mathbf{k}}(t)|^2 \right) + a_{0\mathbf{k}}^*(t) a_{1\mathbf{k}}(t) b_{0\mathbf{k}}(t) \right] \right. \right. \\
&\quad \left. \left. - C_{\mathbf{k}} \left[a_{1\mathbf{k}}(t) b_{0\mathbf{k}}(t) b_{1\mathbf{k}}(t) + a_{0\mathbf{k}}(t) b_{1\mathbf{k}}(t)^2 \right] - C_{\mathbf{k}}^*(t) \left[a_{0\mathbf{k}}^*(t) \left(|b_{0\mathbf{k}}(t)|^2 + |b_{1\mathbf{k}}(t)|^2 \right) \right] \right\} \right]. \tag{E.5}
\end{aligned}$$

Comparing the coefficients, one obtains the differential equations for the prefactors Eq. (4.19) in the main text.

To express the gap equation and the lesser Green's function and to obtain initial values for the coefficients, we need the expectation values of the quasiparticle operators expressed in the iterated equation of motion ansatz. We obtain

$$\begin{aligned} \langle \alpha_{\mathbf{k}}^\dagger(t) \alpha_{\mathbf{k}}(t') \rangle &= \langle \psi_0 \left| \left(a_{0\mathbf{k}}(t) \alpha_{\mathbf{k}}^\dagger + a_{1\mathbf{k}}(t) \beta_{\mathbf{k}} \right) \left(a_{0\mathbf{k}}^*(t') \alpha_{\mathbf{k}} + a_{1\mathbf{k}}^*(t') \beta_{\mathbf{k}}^\dagger \right) \right| \psi_0 \rangle \\ &= a_{0\mathbf{k}}(t) a_{0\mathbf{k}}^*(t') \langle \alpha_{\mathbf{k}}^\dagger \alpha_{\mathbf{k}} \rangle + a_{1\mathbf{k}}(t) a_{1\mathbf{k}}^*(t') \left(1 - \langle \beta_{\mathbf{k}}^\dagger \beta_{\mathbf{k}} \rangle \right) \\ &\quad + a_{0\mathbf{k}}(t) a_{1\mathbf{k}}^*(t') \langle \alpha_{\mathbf{k}}^\dagger \beta_{\mathbf{k}}^\dagger \rangle - a_{1\mathbf{k}}(t) a_{0\mathbf{k}}^*(t') \langle \alpha_{\mathbf{k}} \beta_{\mathbf{k}} \rangle, \end{aligned} \quad (\text{E.6a})$$

$$\begin{aligned} \langle \beta_{\mathbf{k}}^\dagger(t) \beta_{\mathbf{k}}(t') \rangle &= b_{0\mathbf{k}}(t) b_{0\mathbf{k}}^*(t') \langle \beta_{\mathbf{k}}^\dagger \beta_{\mathbf{k}} \rangle + b_{1\mathbf{k}}(t) b_{1\mathbf{k}}^*(t') \left(1 - \langle \alpha_{\mathbf{k}}^\dagger \alpha_{\mathbf{k}} \rangle \right) \\ &\quad - b_{0\mathbf{k}}(t) b_{1\mathbf{k}}^*(t') \langle \alpha_{\mathbf{k}}^\dagger \beta_{\mathbf{k}}^\dagger \rangle + b_{1\mathbf{k}}(t) b_{0\mathbf{k}}^*(t') \langle \alpha_{\mathbf{k}} \beta_{\mathbf{k}} \rangle, \end{aligned} \quad (\text{E.6b})$$

$$\begin{aligned} \langle \alpha_{\mathbf{k}}(t) \beta_{\mathbf{k}}(t') \rangle &= a_{0\mathbf{k}}^*(t) b_{0\mathbf{k}}^*(t') \langle \alpha_{\mathbf{k}} \beta_{\mathbf{k}} \rangle + a_{0\mathbf{k}}^*(t) b_{1\mathbf{k}}^*(t') \left(1 - \langle \alpha_{\mathbf{k}}^\dagger \alpha_{\mathbf{k}} \rangle \right) \\ &\quad + a_{1\mathbf{k}}^*(t) b_{0\mathbf{k}}^*(t') \langle \beta_{\mathbf{k}}^\dagger \beta_{\mathbf{k}} \rangle - a_{1\mathbf{k}}^*(t) b_{1\mathbf{k}}^*(t') \langle \alpha_{\mathbf{k}}^\dagger \beta_{\mathbf{k}}^\dagger \rangle, \end{aligned} \quad (\text{E.6c})$$

$$\begin{aligned} \langle \alpha_{\mathbf{k}}^\dagger(t) \beta_{\mathbf{k}}^\dagger(t') \rangle &= a_{0\mathbf{k}}(t) b_{0\mathbf{k}}(t') \langle \alpha_{\mathbf{k}}^\dagger \beta_{\mathbf{k}}^\dagger \rangle + a_{0\mathbf{k}}(t) b_{1\mathbf{k}}(t') \langle \alpha_{\mathbf{k}}^\dagger \alpha_{\mathbf{k}} \rangle \\ &\quad + a_{1\mathbf{k}}(t) b_{0\mathbf{k}}(t') \left(1 - \langle \beta_{\mathbf{k}}^\dagger \beta_{\mathbf{k}} \rangle \right) - a_{1\mathbf{k}}(t) b_{1\mathbf{k}}(t') \langle \alpha_{\mathbf{k}} \beta_{\mathbf{k}} \rangle. \end{aligned} \quad (\text{E.6d})$$

The expectation values on the right-hand side are the equilibrium quasiparticle distributions for temperature T , such that according to section 2.2.4, $\langle \alpha_{\mathbf{k}} \beta_{\mathbf{k}} \rangle = \langle \alpha_{\mathbf{k}}^\dagger \beta_{\mathbf{k}}^\dagger \rangle = 0$ and $\langle \alpha_{\mathbf{k}}^\dagger \alpha_{\mathbf{k}} \rangle = \langle \beta_{\mathbf{k}}^\dagger \beta_{\mathbf{k}} \rangle$ are given by the Fermi distribution Eq. (2.54). The equations then simplify to

$$\langle \alpha_{\mathbf{k}}^\dagger(t) \alpha_{\mathbf{k}}(t') \rangle = a_{0\mathbf{k}}(t) a_{0\mathbf{k}}^*(t') \langle \alpha_{\mathbf{k}}^\dagger \alpha_{\mathbf{k}} \rangle_T + a_{1\mathbf{k}}(t) a_{1\mathbf{k}}^*(t') \left(1 - \langle \beta_{\mathbf{k}}^\dagger \beta_{\mathbf{k}} \rangle_T \right), \quad (\text{E.7a})$$

$$\langle \beta_{\mathbf{k}}^\dagger(t) \beta_{\mathbf{k}}(t') \rangle = b_{0\mathbf{k}}(t) b_{0\mathbf{k}}^*(t') \langle \beta_{\mathbf{k}}^\dagger \beta_{\mathbf{k}} \rangle_T + b_{1\mathbf{k}}(t) b_{1\mathbf{k}}^*(t') \left(1 - \langle \alpha_{\mathbf{k}}^\dagger \alpha_{\mathbf{k}} \rangle_T \right), \quad (\text{E.7b})$$

$$\langle \alpha_{\mathbf{k}}(t) \beta_{\mathbf{k}}(t') \rangle = a_{0\mathbf{k}}^*(t) b_{1\mathbf{k}}^*(t') \left(1 - \langle \alpha_{\mathbf{k}}^\dagger \alpha_{\mathbf{k}} \rangle_T \right) + a_{1\mathbf{k}}^*(t) b_{0\mathbf{k}}^*(t') \langle \beta_{\mathbf{k}}^\dagger \beta_{\mathbf{k}} \rangle_T, \quad (\text{E.7c})$$

$$\langle \alpha_{\mathbf{k}}^\dagger(t) \beta_{\mathbf{k}}^\dagger(t') \rangle = a_{0\mathbf{k}}(t) b_{1\mathbf{k}}(t') \langle \alpha_{\mathbf{k}}^\dagger \alpha_{\mathbf{k}} \rangle_T + a_{1\mathbf{k}}(t) b_{0\mathbf{k}}(t') \left(1 - \langle \beta_{\mathbf{k}}^\dagger \beta_{\mathbf{k}} \rangle_T \right). \quad (\text{E.7d})$$

To obtain the initial values at $t = t' = 0$ for the factors $a_{0\mathbf{k}}$, $a_{1\mathbf{k}}$, $b_{0\mathbf{k}}$ and $b_{1\mathbf{k}}$, we set the expectation values on the left-hand side to the quasiparticle distribution for $t = 0$ and solve for the factors. If the system is initially in equilibrium, we have $\langle \alpha_{\mathbf{k}}^\dagger(0) \alpha_{\mathbf{k}}(0) \rangle = \langle \alpha_{\mathbf{k}}^\dagger \alpha_{\mathbf{k}} \rangle_T$ etc., i.e. at $t = 0$, the quasiparticle distributions are just the temperature expectation values and we find

$$a_{0\mathbf{k}}(0) = 1, \quad b_{0\mathbf{k}}(0) = 1, \quad a_{1\mathbf{k}}(0) = 0, \quad b_{1\mathbf{k}}(0) = 0. \quad (\text{E.8})$$

For a nonequilibrium distribution at $t = 0$, the solution for $T = 0$ reads

$$\begin{aligned} a_0(0) &= \frac{\langle \alpha_{\mathbf{k}} \beta_{\mathbf{k}} \rangle(0)}{\sqrt{\langle \beta_{\mathbf{k}}^\dagger \beta_{\mathbf{k}} \rangle(0)}}, & b_0(0) &= \frac{\langle \alpha_{\mathbf{k}}^\dagger \beta_{\mathbf{k}}^\dagger \rangle(0)}{\sqrt{\langle \alpha_{\mathbf{k}}^\dagger \alpha_{\mathbf{k}} \rangle(0)}}, \\ a_1(0) &= \sqrt{\langle \alpha_{\mathbf{k}}^\dagger \alpha_{\mathbf{k}} \rangle(0)}, & b_1(0) &= \sqrt{\langle \beta_{\mathbf{k}}^\dagger \beta_{\mathbf{k}} \rangle(0)}. \end{aligned} \quad (\text{E.9})$$

For finite temperature, the expressions are rather lengthy, such that we do not explicitly list them here.

Depending on the choice of the initial expectation values, using Eq. (E.9) causes numerical problems if $\langle \beta_{\mathbf{k}}^\dagger \beta_{\mathbf{k}} \rangle(0)$ or $\langle \alpha_{\mathbf{k}}^\dagger \alpha_{\mathbf{k}} \rangle(0)$ are zero for certain \mathbf{k} values. It is therefore advantageous to rewrite these expressions. To this end, we first derive the (anti-)commutation rules for the time-dependent operators

$$\{\alpha_{\mathbf{k}}(t), \alpha_{\mathbf{k}'}^\dagger(t')\} = \delta_{\mathbf{k}\mathbf{k}'} \left(a_{0\mathbf{k}}^*(t) a_{0\mathbf{k}'}(t') + a_{1\mathbf{k}}^*(t) a_{1\mathbf{k}'}(t') \right), \quad (\text{E.10a})$$

$$\{\beta_{\mathbf{k}}(t), \beta_{\mathbf{k}'}^\dagger(t')\} = \delta_{\mathbf{k}\mathbf{k}'} \left(b_{0\mathbf{k}}^*(t) b_{0\mathbf{k}'}(t') + b_{1\mathbf{k}}^*(t) b_{1\mathbf{k}'}(t') \right), \quad (\text{E.10b})$$

$$\{\alpha_{\mathbf{k}}(t), \beta_{\mathbf{k}'}(t')\} = \delta_{\mathbf{k}\mathbf{k}'} \left(a_{0\mathbf{k}}^*(t) b_{1\mathbf{k}'}^*(t') + a_{1\mathbf{k}}^*(t) b_{0\mathbf{k}'}^*(t') \right), \quad (\text{E.10c})$$

$$\{\alpha_{\mathbf{k}}^\dagger(t), \beta_{\mathbf{k}'}^\dagger(t')\} = \delta_{\mathbf{k}\mathbf{k}'} \left(a_{0\mathbf{k}}(t) b_{1\mathbf{k}'}(t') + a_{1\mathbf{k}}(t) b_{0\mathbf{k}'}(t') \right). \quad (\text{E.10d})$$

At equal times $t = t'$, the commutation rules must be equal to Eq. (2.40). It follows therefore for the coefficients

$$a_{0\mathbf{k}}^*(t) a_{0\mathbf{k}'}(t) + a_{1\mathbf{k}}^*(t) a_{1\mathbf{k}'}(t) = 1, \quad (\text{E.11a})$$

$$b_{0\mathbf{k}}^*(t) b_{0\mathbf{k}'}(t) + b_{1\mathbf{k}}^*(t) b_{1\mathbf{k}'}(t) = 1, \quad (\text{E.11b})$$

$$a_{0\mathbf{k}}(t) b_{1\mathbf{k}'}(t) + a_{1\mathbf{k}}(t) b_{0\mathbf{k}'}(t) = 0. \quad (\text{E.11c})$$

For $T = 0$, we can rewrite Eq. (E.7) at $t = t' = 0$ using the conditions Eq. (E.11). It follows

$$\langle \alpha_{\mathbf{k}}^\dagger \alpha_{\mathbf{k}} \rangle(0) = 1 - |a_{0\mathbf{k}}(0)|^2, \quad (\text{E.12a})$$

$$\langle \beta_{\mathbf{k}}^\dagger \beta_{\mathbf{k}} \rangle(0) = 1 - |b_{0\mathbf{k}}(0)|^2, \quad (\text{E.12b})$$

$$\langle \alpha_{\mathbf{k}} \beta_{\mathbf{k}} \rangle(0) = a_{0\mathbf{k}}^*(0) b_{1\mathbf{k}}^*(0), \quad (\text{E.12c})$$

$$\langle \alpha_{\mathbf{k}}^\dagger \beta_{\mathbf{k}}^\dagger \rangle(0) = a_{1\mathbf{k}}(0) b_{0\mathbf{k}}(0). \quad (\text{E.12d})$$

A solution for the prefactors yields the expression Eq. (4.20) in the main text. In these expressions, a division by zero for vanishing expectation values is prevented.

To calculate the Green's function, we need to express the electron expectation values for unequal times. One cannot use the expression of Eq. (2.48) as the modified commutation rules Eq. (E.10) have to be considered. Taking these into account, one obtains

$$\begin{aligned} \langle c_{-\mathbf{k}\downarrow}(t) c_{\mathbf{k}\uparrow}(t') \rangle &= \left\langle \left(-v_{\mathbf{k}} \alpha_{\mathbf{k}}^\dagger(t) + u_{\mathbf{k}}^* \beta_{\mathbf{k}}(t) \right) \left(u_{\mathbf{k}}^* \alpha_{\mathbf{k}}(t') + v_{\mathbf{k}} \beta_{\mathbf{k}}^\dagger(t') \right) \right\rangle \\ &= -v_{\mathbf{k}} u_{\mathbf{k}}^* \langle \alpha_{\mathbf{k}}^\dagger(t) \alpha_{\mathbf{k}}(t') \rangle + u_{\mathbf{k}}^* v_{\mathbf{k}} \langle \beta_{\mathbf{k}}(t) \beta_{\mathbf{k}}^\dagger(t') \rangle \\ &\quad + u_{\mathbf{k}}^* u_{\mathbf{k}}^* \langle \beta_{\mathbf{k}}(t) \alpha_{\mathbf{k}}(t') \rangle - v_{\mathbf{k}} v_{\mathbf{k}} \langle \alpha_{\mathbf{k}}^\dagger(t) \beta_{\mathbf{k}}^\dagger(t') \rangle \\ &= -v_{\mathbf{k}} u_{\mathbf{k}}^* \langle \alpha_{\mathbf{k}}^\dagger(t) \alpha_{\mathbf{k}}(t') \rangle \\ &\quad + u_{\mathbf{k}}^* v_{\mathbf{k}} \left(b_{0\mathbf{k}}^*(t) b_{0\mathbf{k}}(t') + b_{1\mathbf{k}}^*(t) b_{1\mathbf{k}}(t') - \langle \beta_{\mathbf{k}}^\dagger(t') \beta_{\mathbf{k}}(t) \rangle \right) \\ &\quad + u_{\mathbf{k}}^* u_{\mathbf{k}}^* \left(a_{0\mathbf{k}}^*(t') b_{1\mathbf{k}}^*(t) + a_{1\mathbf{k}}^*(t') b_{0\mathbf{k}}^*(t) - \langle \alpha_{\mathbf{k}}(t') \beta_{\mathbf{k}}(t) \rangle \right) \\ &\quad - v_{\mathbf{k}} v_{\mathbf{k}} \langle \alpha_{\mathbf{k}}^\dagger(t) \beta_{\mathbf{k}}^\dagger(t') \rangle, \end{aligned} \quad (\text{E.13a})$$

$$\begin{aligned}
 \langle c_{\mathbf{k}\uparrow}^\dagger(t)c_{-\mathbf{k}\downarrow}^\dagger(t') \rangle &= \left\langle \left(u_{\mathbf{k}}\alpha_{\mathbf{k}}^\dagger(t) + v_{\mathbf{k}}^*\beta_{\mathbf{k}}(t) \right) \left(-v_{\mathbf{k}}^*\alpha_{\mathbf{k}}(t') + u_{\mathbf{k}}\beta_{\mathbf{k}}^\dagger(t') \right) \right\rangle \\
 &= -u_{\mathbf{k}}v_{\mathbf{k}}^* \langle \alpha_{\mathbf{k}}^\dagger(t)\alpha_{\mathbf{k}}(t') \rangle + v_{\mathbf{k}}^*u_{\mathbf{k}} \langle \beta_{\mathbf{k}}(t)\beta_{\mathbf{k}}^\dagger(t') \rangle \\
 &\quad - v_{\mathbf{k}}^*v_{\mathbf{k}}^* \langle \beta_{\mathbf{k}}(t)\alpha_{\mathbf{k}}(t') \rangle + u_{\mathbf{k}}u_{\mathbf{k}} \langle \alpha_{\mathbf{k}}^\dagger(t)\beta_{\mathbf{k}}^\dagger(t') \rangle \\
 &= -u_{\mathbf{k}}v_{\mathbf{k}}^* \langle \alpha_{\mathbf{k}}^\dagger(t)\alpha_{\mathbf{k}}(t') \rangle \\
 &\quad + v_{\mathbf{k}}^*u_{\mathbf{k}} \left(b_{0\mathbf{k}}^*(t)b_{0\mathbf{k}}(t') + b_{1\mathbf{k}}^*(t)b_{1\mathbf{k}}(t') - \langle \beta_{\mathbf{k}}^\dagger(t')\beta_{\mathbf{k}}(t) \rangle \right) \\
 &\quad - v_{\mathbf{k}}^*v_{\mathbf{k}}^* \left(a_{0\mathbf{k}}^*(t')b_{1\mathbf{k}}^*(t) + a_{1\mathbf{k}}^*(t')b_{0\mathbf{k}}^*(t) - \langle \alpha_{\mathbf{k}}(t')\beta_{\mathbf{k}}(t) \rangle \right) \\
 &\quad + u_{\mathbf{k}}u_{\mathbf{k}} \langle \alpha_{\mathbf{k}}^\dagger(t)\beta_{\mathbf{k}}^\dagger(t') \rangle , \tag{E.13b}
 \end{aligned}$$

$$\begin{aligned}
 \langle c_{\mathbf{k}\uparrow}^\dagger(t)c_{\mathbf{k}\uparrow}^\dagger(t') \rangle &= \left\langle \left(u_{\mathbf{k}}\alpha_{\mathbf{k}}^\dagger(t) + v_{\mathbf{k}}^*\beta_{\mathbf{k}}(t) \right) \left(u_{\mathbf{k}}\alpha_{\mathbf{k}}(t') + v_{\mathbf{k}}\beta_{\mathbf{k}}^\dagger(t') \right) \right\rangle \\
 &= u_{\mathbf{k}}u_{\mathbf{k}}^* \langle \alpha_{\mathbf{k}}^\dagger(t)\alpha_{\mathbf{k}}(t') \rangle + v_{\mathbf{k}}^*v_{\mathbf{k}} \langle \beta_{\mathbf{k}}(t)\beta_{\mathbf{k}}^\dagger(t') \rangle \\
 &\quad + v_{\mathbf{k}}^*u_{\mathbf{k}}^* \langle \beta_{\mathbf{k}}(t)\alpha_{\mathbf{k}}(t') \rangle + u_{\mathbf{k}}v_{\mathbf{k}} \langle \alpha_{\mathbf{k}}^\dagger(t)\beta_{\mathbf{k}}^\dagger(t') \rangle \\
 &= u_{\mathbf{k}}u_{\mathbf{k}}^* \langle \alpha_{\mathbf{k}}^\dagger(t)\alpha_{\mathbf{k}}(t') \rangle \\
 &\quad + v_{\mathbf{k}}^*v_{\mathbf{k}} \left(b_{0\mathbf{k}}^*(t)b_{0\mathbf{k}}(t') + b_{1\mathbf{k}}^*(t)b_{1\mathbf{k}}(t') - \langle \beta_{\mathbf{k}}^\dagger(t')\beta_{\mathbf{k}}(t) \rangle \right) \\
 &\quad + v_{\mathbf{k}}^*u_{\mathbf{k}}^* \left(a_{0\mathbf{k}}^*(t')b_{1\mathbf{k}}^*(t) + a_{1\mathbf{k}}^*(t')b_{0\mathbf{k}}^*(t) - \langle \alpha_{\mathbf{k}}(t')\beta_{\mathbf{k}}(t) \rangle \right) \\
 &\quad + u_{\mathbf{k}}v_{\mathbf{k}} \langle \alpha_{\mathbf{k}}^\dagger(t)\beta_{\mathbf{k}}^\dagger(t') \rangle , \tag{E.13c}
 \end{aligned}$$

$$\begin{aligned}
 \langle c_{-\mathbf{k}\downarrow}(t)c_{-\mathbf{k}\downarrow}^\dagger(t') \rangle &= \left\langle \left(-v_{\mathbf{k}}\alpha_{\mathbf{k}}^\dagger(t) + u_{\mathbf{k}}^*\beta_{\mathbf{k}}(t) \right) \left(-v_{\mathbf{k}}^*\alpha_{\mathbf{k}}(t') + u_{\mathbf{k}}\beta_{\mathbf{k}}^\dagger(t') \right) \right\rangle \\
 &= v_{\mathbf{k}}v_{\mathbf{k}}^* \langle \alpha_{\mathbf{k}}^\dagger(t)\alpha_{\mathbf{k}}(t') \rangle + u_{\mathbf{k}}^*u_{\mathbf{k}} \langle \beta_{\mathbf{k}}(t)\beta_{\mathbf{k}}^\dagger(t') \rangle \\
 &\quad - u_{\mathbf{k}}^*v_{\mathbf{k}}^* \langle \beta_{\mathbf{k}}(t)\alpha_{\mathbf{k}}(t') \rangle - v_{\mathbf{k}}u_{\mathbf{k}} \langle \alpha_{\mathbf{k}}^\dagger(t)\beta_{\mathbf{k}}^\dagger(t') \rangle \\
 &= v_{\mathbf{k}}v_{\mathbf{k}}^* \langle \alpha_{\mathbf{k}}^\dagger(t)\alpha_{\mathbf{k}}(t') \rangle \\
 &\quad + u_{\mathbf{k}}^*u_{\mathbf{k}} \left(b_{0\mathbf{k}}^*(t)b_{0\mathbf{k}}(t') + b_{1\mathbf{k}}^*(t)b_{1\mathbf{k}}(t') - \langle \beta_{\mathbf{k}}^\dagger(t')\beta_{\mathbf{k}}(t) \rangle \right) \\
 &\quad - u_{\mathbf{k}}^*v_{\mathbf{k}}^* \left(a_{0\mathbf{k}}^*(t')b_{1\mathbf{k}}^*(t) + a_{1\mathbf{k}}^*(t')b_{0\mathbf{k}}^*(t) - \langle \alpha_{\mathbf{k}}(t')\beta_{\mathbf{k}}(t) \rangle \right) \\
 &\quad - v_{\mathbf{k}}u_{\mathbf{k}} \langle \alpha_{\mathbf{k}}^\dagger(t)\beta_{\mathbf{k}}^\dagger(t') \rangle . \tag{E.13d}
 \end{aligned}$$

F Effective Interaction Quench due to Periodic Driving

The term $\delta\Delta_{\text{H}}(s)$ arising in the solution Eq. (5.24) is induced by an effective interaction quench due to the periodic driving, as it was also concluded in [40]. One can understand this by considering the high-frequency limit. We compare the solution Eq. (5.17) for the driven case

$$\delta\Delta^{\text{drive}}(s) = \frac{1}{2}\alpha_1\Delta e^2 A_0^2 \frac{2\Omega^2}{s(s^2 + 4\Omega^2)} \left(1 - \frac{1}{\lambda F(s)}\right) \quad (\text{F.1})$$

with the solution Eq. (3.20) for the interaction quench case

$$\delta\Delta^{\text{quench}}(s) = \frac{\Delta - \Delta_{\text{q}}}{s} \left(1 - \frac{1}{\lambda F(s)}\right). \quad (\text{F.2})$$

In the limit $\Omega \rightarrow \infty$, one obtains

$$\delta\Delta^{\text{drive}}(s) = \frac{1}{4} \frac{1}{s} \alpha_1 \Delta e^2 A_0^2 \left(1 - \frac{1}{\lambda F(s)}\right), \quad (\text{F.3})$$

which has the same form as the solution for the interaction quench. Using $\Delta_{\text{q}} = g\Delta$, a comparison of the expression yields a value for the effective interaction quench strength

$$g = 1 - \frac{1}{4} \alpha_1 e^2 A_0^2. \quad (\text{F.4})$$

Bibliography

- [1] C. Beenakker, “Search for Majorana Fermions in Superconductors”, *Annu. Rev. Condens. Matter Phys.* **4**, 113 (2013).
- [2] N. P. Armitage, E. J. Mele, and A. Vishwanath, “Weyl and Dirac semimetals in three-dimensional solids”, *Rev. Mod. Phys.* **90**, 015001 (2018).
- [3] P. W. Anderson, “Plasmons, Gauge Invariance, and Mass”, *Phys. Rev.* **130**, 439 (1963).
- [4] F. Englert and R. Brout, “Broken Symmetry and the Mass of Gauge Vector Mesons”, *Phys. Rev. Lett.* **13**, 321 (1964).
- [5] P. W. Higgs, “Broken Symmetries and the Masses of Gauge Bosons”, *Phys. Rev. Lett.* **13**, 508 (1964).
- [6] G. S. Guralnik, C. R. Hagen, and T. W. B. Kibble, “Global Conservation Laws and Massless Particles”, *Phys. Rev. Lett.* **13**, 585 (1964).
- [7] L. Schwarz, B. Fauseweh, N. Tsuji, N. Cheng, N. Bittner, H. Krull, M. Berciu, G. S. Uhrig, A. P. Schnyder, S. Kaiser, and D. Manske, “Classification and characterization of nonequilibrium Higgs modes in unconventional superconductors”, *Nat. Commun.* **11**, 287 (2020).
- [8] L. Schwarz and D. Manske, “Theory of driven Higgs oscillations and third-harmonic generation in unconventional superconductors”, *Phys. Rev. B* **101**, 184519 (2020).
- [9] C. M. Varma, “Higgs Boson in Superconductors”, *J. Low Temp. Phys.* **126**, 901 (2002).
- [10] D. Pekker and C. Varma, “Amplitude/Higgs Modes in Condensed Matter Physics”, *Annu. Rev. Condens. Matter Phys.* **6**, 269 (2015).
- [11] M. Puviani, L. Schwarz, X.-X. Zhang, S. Kaiser, and D. Manske, “Current-assisted Raman activation of the Higgs mode in superconductors”, *Phys. Rev. B* **101**, 220507 (2020).
- [12] R. Sooryakumar and M. V. Klein, “Raman Scattering by Superconducting-Gap Excitations and Their Coupling to Charge-Density Waves”, *Phys. Rev. Lett.* **45**, 660 (1980).
- [13] R. Sooryakumar and M. V. Klein, “Raman scattering from superconducting gap excitations in the presence of a magnetic field”, *Phys. Rev. B* **23**, 3213 (1981).
- [14] P. B. Littlewood and C. M. Varma, “Gauge-Invariant Theory of the Dynamical Interaction of Charge Density Waves and Superconductivity”, *Phys. Rev. Lett.* **47**, 811 (1981).
- [15] P. B. Littlewood and C. M. Varma, “Amplitude collective modes in superconductors and their coupling to charge-density waves”, *Phys. Rev. B* **26**, 4883 (1982).
- [16] M.-A. Méasson, Y. Gallais, M. Cazayous, B. Clair, P. Rodière, L. Cario, and A. Sacuto, “Amplitude Higgs mode in the $2H - \text{NbSe}_2$ superconductor”, *Phys. Rev. B* **89**, 060503 (2014).
- [17] T. Cea and L. Benfatto, “Nature and Raman signatures of the Higgs amplitude mode in the coexisting superconducting and charge-density-wave state”, *Phys. Rev. B* **90**, 224515 (2014).

- [18] R. Grasset, T. Cea, Y. Gallais, M. Cazayous, A. Sacuto, L. Cario, L. Benfatto, and M.-A. Méasson, “Higgs-mode radiance and charge-density-wave order in $2H - \text{NbSe}_2$ ”, *Phys. Rev. B* **97**, 094502 (2018).
- [19] R. Grasset, Y. Gallais, A. Sacuto, M. Cazayous, S. Mañas Valero, E. Coronado, and M.-A. Méasson, “Pressure-Induced Collapse of the Charge Density Wave and Higgs Mode Visibility in $2H - \text{TaS}_2$ ”, *Phys. Rev. Lett.* **122**, 127001 (2019).
- [20] A. F. Volkov and S. M. Kogan, “Collisionless relaxation of the energy gap in superconductors”, *Sov. Phys. JETP* **38**, 1018 (1974).
- [21] E. A. Yuzbashyan, O. Tsyplyatyev, and B. L. Altshuler, “Relaxation and Persistent Oscillations of the Order Parameter in Fermionic Condensates”, *Phys. Rev. Lett.* **96**, 097005 (2006).
- [22] R. A. Barankov and L. S. Levitov, “Synchronization in the BCS Pairing Dynamics as a Critical Phenomenon”, *Phys. Rev. Lett.* **96**, 230403 (2006).
- [23] E. A. Yuzbashyan and M. Dzero, “Dynamical Vanishing of the Order Parameter in a Fermionic Condensate”, *Phys. Rev. Lett.* **96**, 230404 (2006).
- [24] R. A. Barankov, L. S. Levitov, and B. Z. Spivak, “Collective Rabi Oscillations and Solitons in a Time-Dependent BCS Pairing Problem”, *Phys. Rev. Lett.* **93**, 160401 (2004).
- [25] E. A. Yuzbashyan, B. L. Altshuler, V. B. Kuznetsov, and V. Z. Enolskii, “Solution for the dynamics of the BCS and central spin problems”, *J. Phys. A: Math. Gen.* **38**, 7831 (2005).
- [26] E. A. Yuzbashyan, V. B. Kuznetsov, and B. L. Altshuler, “Integrable dynamics of coupled Fermi-Bose condensates”, *Phys. Rev. B* **72**, 144524 (2005).
- [27] E. A. Yuzbashyan, B. L. Altshuler, V. B. Kuznetsov, and V. Z. Enolskii, “Nonequilibrium cooper pairing in the nonadiabatic regime”, *Phys. Rev. B* **72**, 220503 (2005).
- [28] T. Papenkort, V. M. Axt, and T. Kuhn, “Coherent dynamics and pump-probe spectra of BCS superconductors”, *Phys. Rev. B* **76**, 224522 (2007).
- [29] J. Unterhinninghofen, D. Manske, and A. Knorr, “Theory of ultrafast nonequilibrium dynamics in d -wave superconductors”, *Phys. Rev. B* **77**, 180509 (2008).
- [30] T. Papenkort, T. Kuhn, and V. M. Axt, “Coherent control of the gap dynamics of BCS superconductors in the nonadiabatic regime”, *Phys. Rev. B* **78**, 132505 (2008).
- [31] A. P. Schnyder, D. Manske, and A. Avella, “Resonant generation of coherent phonons in a superconductor by ultrafast optical pump pulses”, *Phys. Rev. B* **84**, 214513 (2011).
- [32] M. Zachmann, M. D. Croitoru, A. Vagov, V. M. Axt, T. Papenkort, and T. Kuhn, “Ultrafast terahertz-field-induced dynamics of superconducting bulk and quasi-1D samples”, *New J. Phys.* **15**, 055016 (2013).
- [33] A. Akbari, A. P. Schnyder, D. Manske, and I. Eremin, “Theory of nonequilibrium dynamics of multiband superconductors”, *Europhys. Lett.* **101**, 17002 (2013).
- [34] M. Greiter, “Is electromagnetic gauge invariance spontaneously violated in superconductors?”, *Ann. Phys.* **319**, 217 (2005).
- [35] D. Podolsky, A. Auerbach, and D. P. Arovas, “Visibility of the amplitude (Higgs) mode in condensed matter”, *Phys. Rev. B* **84**, 174522 (2011).

-
- [36] R. Matsunaga, Y. I. Hamada, K. Makise, Y. Uzawa, H. Terai, Z. Wang, and R. Shimano, “Higgs Amplitude Mode in the BCS Superconductors $\text{Nb}_{1-x}\text{Ti}_x\text{N}$ Induced by Terahertz Pulse Excitation”, *Phys. Rev. Lett.* **111**, 057002 (2013).
- [37] G. Aad et al., “Observation of a new particle in the search for the Standard Model Higgs boson with the ATLAS detector at the LHC”, *Phys. Lett. B* **716**, 1 (2012).
- [38] S. Chatrchyan et al., “Observation of a new boson at a mass of 125 GeV with the CMS experiment at the LHC”, *Phys. Lett. B* **716**, 30 (2012).
- [39] R. Matsunaga, N. Tsuji, H. Fujita, A. Sugioka, K. Makise, Y. Uzawa, H. Terai, Z. Wang, H. Aoki, and R. Shimano, “Light-induced collective pseudospin precession resonating with Higgs mode in a superconductor”, *Science* **345**, 1145 (2014).
- [40] N. Tsuji and H. Aoki, “Theory of Anderson pseudospin resonance with Higgs mode in superconductors”, *Phys. Rev. B* **92**, 064508 (2015).
- [41] A. F. Kemper, M. A. Sentef, B. Moritz, J. K. Freericks, and T. P. Devereaux, “Direct observation of Higgs mode oscillations in the pump-probe photoemission spectra of electron-phonon mediated superconductors”, *Phys. Rev. B* **92**, 224517 (2015).
- [42] B. Nosarzewski, B. Moritz, J. K. Freericks, A. F. Kemper, and T. P. Devereaux, “Amplitude mode oscillations in pump-probe photoemission spectra from a d -wave superconductor”, *Phys. Rev. B* **96**, 184518 (2017).
- [43] H. P. Ojeda Collado, G. Usaj, J. Lorenzana, and C. A. Balseiro, “Nonlinear dynamics of driven superconductors with dissipation”, *Phys. Rev. B* **101**, 054502 (2020).
- [44] T. Xu, T. Morimoto, A. Lanzara, and J. E. Moore, “Efficient prediction of time- and angle-resolved photoemission spectroscopy measurements on a nonequilibrium BCS superconductor”, *Phys. Rev. B* **99**, 035117 (2019).
- [45] T. Cea, C. Castellani, and L. Benfatto, “Nonlinear optical effects and third-harmonic generation in superconductors: Cooper pairs versus Higgs mode contribution”, *Phys. Rev. B* **93**, 180507 (2016).
- [46] N. Tsuji, Y. Murakami, and H. Aoki, “Nonlinear light–Higgs coupling in superconductors beyond BCS: Effects of the retarded phonon-mediated interaction”, *Phys. Rev. B* **94**, 224519 (2016).
- [47] T. Cea, P. Barone, C. Castellani, and L. Benfatto, “Polarization dependence of the third-harmonic generation in multiband superconductors”, *Phys. Rev. B* **97**, 094516 (2018).
- [48] Y. Murotani, N. Tsuji, and H. Aoki, “Theory of light-induced resonances with collective Higgs and Leggett modes in multiband superconductors”, *Phys. Rev. B* **95**, 104503 (2017).
- [49] M. A. Müller, P. Shen, M. Dzero, and I. Eremin, “Short-time dynamics in $s + is$ -wave superconductor with incipient bands”, *Phys. Rev. B* **98**, 024522 (2018).
- [50] H. Krull, N. Bittner, G. S. Uhrig, D. Manske, and A. P. Schnyder, “Coupling of Higgs and Leggett modes in non-equilibrium superconductors”, *Nat. Commun.* **7**, 11921 (2016).
- [51] T. Cui, M. Schütt, P. P. Orth, and R. M. Fernandes, “Postquench gap dynamics of two-band superconductors”, *Phys. Rev. B* **100**, 144513 (2019).
- [52] H. Krull, D. Manske, G. S. Uhrig, and A. P. Schnyder, “Signatures of nonadiabatic BCS state dynamics in pump-probe conductivity”, *Phys. Rev. B* **90**, 014515 (2014).

- [53] F. Peronaci, M. Schiró, and M. Capone, “Transient Dynamics of d -Wave Superconductors after a Sudden Excitation”, *Phys. Rev. Lett.* **115**, 257001 (2015).
- [54] Y.-Z. Chou, Y. Liao, and M. S. Foster, “Twisting Anderson pseudospins with light: Quench dynamics in terahertz-pumped BCS superconductors”, *Phys. Rev. B* **95**, 104507 (2017).
- [55] A. Avella, “BCS superconductors: The out-of-equilibrium response to a laser pulse”, *Physica B* **536**, 713 (2018).
- [56] J. P. Revelle, A. Kumar, and A. F. Kemper, “Theory of Time-Resolved Optical Conductivity of Superconductors: Comparing Two Methods for Its Evaluation”, *Condens. Matter* **4**, 79 (2019).
- [57] A. Kumar and A. F. Kemper, “Higgs oscillations in time-resolved optical conductivity”, *Phys. Rev. B* **100**, 174515 (2019).
- [58] M. Udina, T. Cea, and L. Benfatto, “Theory of coherent-oscillations generation in terahertz pump-probe spectroscopy: From phonons to electronic collective modes”, *Phys. Rev. B* **100**, 165131 (2019).
- [59] S. Maiti and P. J. Hirschfeld, “Collective modes in superconductors with competing s - and d -wave interactions”, *Phys. Rev. B* **92**, 094506 (2015).
- [60] M. A. Müller, P. A. Volkov, I. Paul, and I. M. Eremin, “Collective modes in pumped unconventional superconductors with competing ground states”, *Phys. Rev. B* **100**, 140501 (2019).
- [61] Z. Sun, M. M. Fogler, D. N. Basov, and M. A. J., “Collective modes and THz near field response of superconductors”, *arXiv* **2001.03704** (2020).
- [62] Z. M. Raines, V. G. Stanev, and V. M. Galitski, “Hybridization of Higgs modes in a bond-density-wave state in cuprates”, *Phys. Rev. B* **92**, 184511 (2015).
- [63] A. Moor, P. A. Volkov, A. F. Volkov, and K. B. Efetov, “Dynamics of order parameters near stationary states in superconductors with a charge-density wave”, *Phys. Rev. B* **90**, 024511 (2014).
- [64] M. Dzero, M. Khodas, and A. Levchenko, “Amplitude modes and dynamic coexistence of competing orders in multicomponent superconductors”, *Phys. Rev. B* **91**, 214505 (2015).
- [65] T. Jujo, “Two-Photon Absorption by Impurity Scattering and Amplitude Mode in Conventional Superconductors”, *J. Phys. Soc. Jpn.* **84**, 114711 (2015).
- [66] T. Jujo, “Quasiclassical Theory on Third-Harmonic Generation in Conventional Superconductors with Paramagnetic Impurities”, *J. Phys. Soc. Jpn.* **87**, 024704 (2018).
- [67] Y. Murotani and R. Shimano, “Nonlinear optical response of collective modes in multiband superconductors assisted by nonmagnetic impurities”, *Phys. Rev. B* **99**, 224510 (2019).
- [68] M. Silaev, “Nonlinear electromagnetic response and Higgs-mode excitation in BCS superconductors with impurities”, *Phys. Rev. B* **99**, 224511 (2019).
- [69] F. Yang and M. wu, “Influence of scattering on optical response of superconductivity”, *arXiv* **1907.01548** (2019).
- [70] N. Tsuji and Y. Nomura, “Higgs-mode resonance in third harmonic generation in NbN superconductors: multiband electron-phonon coupling, impurity scattering, and polarization-angle dependence”, *arXiv* **2004.00286** (2020).

-
- [71] T. Cui, X. Yang, C. Vaswani, J. Wang, R. M. Fernandes, and P. P. Orth, “Impact of damping on the superconducting gap dynamics induced by intense terahertz pulses”, *Phys. Rev. B* **100**, 054504 (2019).
- [72] Y. Murakami, P. Werner, N. Tsuji, and H. Aoki, “Damping of the collective amplitude mode in superconductors with strong electron-phonon coupling”, *Phys. Rev. B* **94**, 115126 (2016).
- [73] H. P. Ojeda Collado, G. Usaj, J. Lorenzana, and C. A. Balseiro, “Fate of dynamical phases of a BCS superconductor beyond the dissipationless regime”, *Phys. Rev. B* **99**, 174509 (2019).
- [74] T. Yu and M. W. Wu, “Gauge-invariant theory of quasiparticle and condensate dynamics in response to terahertz optical pulses in superconducting semiconductor quantum wells. I. s -wave superconductivity in the weak spin-orbit coupling limit”, *Phys. Rev. B* **96**, 155311 (2017).
- [75] T. Yu and M. W. Wu, “Gauge-invariant theory of quasiparticle and condensate dynamics in response to terahertz optical pulses in superconducting semiconductor quantum wells. II. $(s + p)$ -wave superconductivity in the strong spin-orbit coupling limit”, *Phys. Rev. B* **96**, 155312 (2017).
- [76] F. Yang and M. W. Wu, “Gauge-invariant microscopic kinetic theory of superconductivity in response to electromagnetic fields”, *Phys. Rev. B* **98**, 094507 (2018).
- [77] F. Yang and M. W. Wu, “Gauge-invariant microscopic kinetic theory of superconductivity: Application to the optical response of Nambu-Goldstone and Higgs modes”, *Phys. Rev. B* **100**, 104513 (2019).
- [78] F. Yang and M. Wu, “Theory of Higgs Modes in d -Wave Superconductors”, *arXiv* **2001.06183** (2020).
- [79] Y. Murakami, P. Werner, N. Tsuji, and H. Aoki, “Multiple amplitude modes in strongly coupled phonon-mediated superconductors”, *Phys. Rev. B* **93**, 094509 (2016).
- [80] A. Moor, A. F. Volkov, and K. B. Efetov, “Amplitude Higgs Mode and Admittance in Superconductors with a Moving Condensate”, *Phys. Rev. Lett.* **118**, 047001 (2017).
- [81] S. Nakamura, K. Katsumi, H. Terai, and R. Shimano, “Nonreciprocal Terahertz Second Harmonic Generation in Superconducting NbN under Supercurrent Injection”, *arXiv* **2003.00417** (2020).
- [82] H. Uematsu, T. Mizushima, A. Tsuruta, S. Fujimoto, and J. A. Sauls, “Chiral Higgs Mode in Nematic Superconductors”, *Phys. Rev. Lett.* **123**, 237001 (2019).
- [83] R. Soto-Garrido, Y. Wang, E. Fradkin, and S. L. Cooper, “Higgs modes in the pair density wave superconducting state”, *Phys. Rev. B* **95**, 214502 (2017).
- [84] S.-K. Jian, M. M. Scherer, and H. Yao, “Mass hierarchy in collective modes of pair-density-wave superconductors”, *Phys. Rev. Research* **2**, 013034 (2020).
- [85] E. A. Yuzbashyan, M. Dzero, V. Gurarie, and M. S. Foster, “Quantum quench phase diagrams of an s -wave BCS-BEC condensate”, *Phys. Rev. A* **91**, 033628 (2015).
- [86] B. Rosenstein, B. Y. Shapiro, and I. Shapiro, “Collective modes, ac response, and magnetic properties of the three-dimensional Dirac semimetal in the triplet superconducting state”, *Phys. Rev. B* **92**, 054503 (2015).

- [87] V. L. Vadimov, I. M. Khaymovich, and A. S. Mel'nikov, "Higgs modes in proximized superconducting systems", *Phys. Rev. B* **100**, 104515 (2019).
- [88] M. A. Silaev, R. Ojajärvi, and H. T. T., "Spin currents driven by the Higgs mode in magnetic superconductors", arXiv **1907.00539** (2019).
- [89] G. Tang, W. Belzig, U. Zülicke, and C. Bruder, "Signatures of the Higgs mode in transport through a normal-metal–superconductor junction", arXiv **2003.00204** (2020).
- [90] H. P. O. Collado, J. Lorenzana, G. Usaj, and C. A. Balseiro, "Population inversion and dynamical phase transitions in a driven superconductor", *Phys. Rev. B* **98**, 214519 (2018).
- [91] P. Kettmann, S. Hannibal, M. Croitoru, A. Vagov, V. Axt, and T. Kuhn, "Spectral characteristics of the coherent dynamics of the order parameter in superconducting nanorods", *Physica C* **533**, 133 (2017).
- [92] B. Huang, X. Yang, N. Xu, J. Zhou, and M. Gong, "Dynamical instability with respect to finite-momentum pairing in quenched BCS superconducting phases", *Phys. Rev. B* **99**, 014517 (2019).
- [93] M. Lu, H. Liu, P. Wang, and X. C. Xie, "Higgs amplitude mode in massless Dirac fermion systems", *Phys. Rev. B* **93**, 064516 (2016).
- [94] Y. Barlas and C. M. Varma, "Amplitude or Higgs modes in *d*-wave superconductors", *Phys. Rev. B* **87**, 054503 (2013).
- [95] S. Tsuchiya, D. Yamamoto, R. Yoshii, and M. Nitta, "Hidden charge-conjugation, parity, and time-reversal symmetries and massive Goldstone (Higgs) modes in superconductors", *Phys. Rev. B* **98**, 094503 (2018).
- [96] A. Pashkin and A. Leitenstorfer, "Particle physics in a superconductor", *Science* **345**, 1121 (2014).
- [97] P. W. Anderson, "Higgs, Anderson and all that", *Nat. Phys.* **11**, 93 (2015).
- [98] T. Cea, C. Castellani, G. Seibold, and L. Benfatto, "Nonrelativistic Dynamics of the Amplitude (Higgs) Mode in Superconductors", *Phys. Rev. Lett.* **115**, 157002 (2015).
- [99] D. Fraser and A. Koberinski, "The Higgs mechanism and superconductivity: A case study of formal analogies", *Stud. Hist. Philos. Sci. B* **55**, 72 (2016).
- [100] S. Fischer, M. Hecker, M. Hoyer, and J. Schmalian, "Short-distance breakdown of the Higgs mechanism and the robustness of the BCS theory for charged superconductors", *Phys. Rev. B* **97**, 054510 (2018).
- [101] M. Faccioli and L. Salasnich, "Spontaneous Symmetry Breaking and Higgs Mode: Comparing Gross-Pitaevskii and Nonlinear Klein-Gordon Equations", *Symmetry* **10**, 80 (2018).
- [102] N. R. Poniatowski, "Superconductivity, broken gauge symmetry, and the Higgs mechanism", *Am. J. Phys.* **87**, 436 (2019).
- [103] B. Mansart, J. Lorenzana, A. Mann, A. Odeh, M. Scarongella, M. Chergui, and F. Carbone, "Coupling of a high-energy excitation to superconducting quasiparticles in a cuprate from coherent charge fluctuation spectroscopy", *Proc. Natl. Acad. Sci. USA* **110**, 4539 (2013).
- [104] D. Sherman et al., "The Higgs mode in disordered superconductors close to a quantum phase transition", *Nat. Phys.* **11**, 188 (2015).

-
- [105] R. Matsunaga, N. Tsuji, K. Makise, H. Terai, H. Aoki, and R. Shimano, “Polarization-resolved terahertz third-harmonic generation in a single-crystal superconductor NbN: Dominance of the Higgs mode beyond the BCS approximation”, *Phys. Rev. B* **96**, 020505 (2017).
- [106] K. Katsumi, N. Tsuji, Y. I. Hamada, R. Matsunaga, J. Schneeloch, R. D. Zhong, G. D. Gu, H. Aoki, Y. Gallais, and R. Shimano, “Higgs Mode in the d -Wave Superconductor $\text{Bi}_2\text{Sr}_2\text{CaCu}_2\text{O}_{8+x}$ Driven by an Intense Terahertz Pulse”, *Phys. Rev. Lett.* **120**, 117001 (2018).
- [107] K. Katsumi, Z. Z. Li, H. Raffy, Y. Gallais, and R. Shimano, “Superconducting fluctuation probed by the Higgs mode in $\text{Bi}_2\text{Sr}_2\text{CaCu}_2\text{O}_{8+x}$ thin films”, *arXiv* **1910.07695** (2019).
- [108] H. Chu et al., “Phase-resolved Higgs response in superconducting cuprates”, *Nat. Commun.* **11**, 1793 (2020).
- [109] S. Nakamura, Y. Iida, Y. Murotani, R. Matsunaga, H. Terai, and R. Shimano, “Infrared Activation of the Higgs Mode by Supercurrent Injection in Superconducting NbN”, *Phys. Rev. Lett.* **122**, 257001 (2019).
- [110] C. Vaswani et al., “Discovery of Terahertz Second Harmonic Generation from Lightwave Acceleration of Symmetry-Breaking Nonlinear Supercurrents”, *arXiv* **1912.01676** (2019).
- [111] X. Yang, C. Vaswani, C. Sundahl, M. Mootz, L. Luo, J. H. Kang, I. E. Perakis, C. B. Eom, and J. Wang, “Lightwave-driven gapless superconductivity and forbidden quantum beats by terahertz symmetry breaking”, *Nat. Photonics* **13**, 707 (2019).
- [112] A. A. Kirmani and M. Dzero, “Non-adiabatic Dynamics in $d + id$ -Wave Fermionic Superfluids”, *J. Supercond. Nov. Magn.* **32**, 3473 (2019).
- [113] A. J. Beekman, L. Rademaker, and J. van Wezel, “An Introduction to Spontaneous Symmetry Breaking”, *SciPost Phys. Lect. Notes*, 11 (2019).
- [114] M. Tinkham, *Introduction to Superconductivity*, 2nd ed. (Dover Publications, 1996).
- [115] M. Cyrot, “Ginzburg-Landau theory for superconductors”, *Rep. Prog. Phys.* **36**, 103 (1973).
- [116] P. C. J. and H. Smith, *Bose–Einstein Condensation in Dilute Gases*, 2nd ed. (Cambridge University Press, 2008).
- [117] S. D. Huber, B. Theiler, E. Altman, and G. Blatter, “Amplitude Mode in the Quantum Phase Model”, *Phys. Rev. Lett.* **100**, 050404 (2008).
- [118] L. Pollet and N. Prokof’ev, “Higgs Mode in a Two-Dimensional Superfluid”, *Phys. Rev. Lett.* **109**, 010401 (2012).
- [119] D. Jaksch and P. Zoller, “The cold atom Hubbard toolbox”, *Ann. Phys.* **315**, Special Issue, 52 (2005).
- [120] C. Chin, R. Grimm, P. Julienne, and E. Tiesinga, “Feshbach resonances in ultracold gases”, *Rev. Mod. Phys.* **82**, 1225 (2010).
- [121] S. D. Huber, E. Altman, H. P. Büchler, and G. Blatter, “Dynamical properties of ultracold bosons in an optical lattice”, *Phys. Rev. B* **75**, 085106 (2007).

- [122] U. Bissbort, S. Götze, Y. Li, J. Heinze, J. S. Krauser, M. Weinberg, C. Becker, K. Sengstock, and W. Hofstetter, “Detecting the Amplitude Mode of Strongly Interacting Lattice Bosons by Bragg Scattering”, *Phys. Rev. Lett.* **106**, 205303 (2011).
- [123] M. Endres, T. Fukuhara, D. Pekker, M. Cheneau, P. Schauß, C. Gross, E. Demler, S. Kuhr, and I. Bloch, “The ‘Higgs’ amplitude mode at the two-dimensional superfluid/Mott insulator transition”, *Nature* **487**, 454 (2012).
- [124] P. Nozières and S. Schmitt-Rink, “Bose condensation in an attractive fermion gas: From weak to strong coupling superconductivity”, *J. Low Temp. Phys.* **59**, 195 (1985).
- [125] C. A. Regal, M. Greiner, and D. S. Jin, “Observation of Resonance Condensation of Fermionic Atom Pairs”, *Phys. Rev. Lett.* **92**, 040403 (2004).
- [126] M. W. Zwierlein, C. A. Stan, C. H. Schunck, S. M. F. Raupach, A. J. Kerman, and W. Ketterle, “Condensation of Pairs of Fermionic Atoms near a Feshbach Resonance”, *Phys. Rev. Lett.* **92**, 120403 (2004).
- [127] S. Tsuchiya, R. Ganesh, and T. Nikuni, “Higgs mode in a superfluid of Dirac fermions”, *Phys. Rev. B* **88**, 014527 (2013).
- [128] R. G. Scott, F. Dalfovo, L. P. Pitaevskii, and S. Stringari, “Rapid ramps across the BEC-BCS crossover: A route to measuring the superfluid gap”, *Phys. Rev. A* **86**, 053604 (2012).
- [129] X. Han, B. Liu, and J. Hu, “Observability of Higgs mode in a system without Lorentz invariance”, *Phys. Rev. A* **94**, 033608 (2016).
- [130] G. M. Bruun, “Long-lived Higgs mode in a two-dimensional confined Fermi system”, *Phys. Rev. A* **90**, 023621 (2014).
- [131] S. Hannibal, P. Kettmann, M. D. Croitoru, V. M. Axt, and T. Kuhn, “Dynamical vanishing of the order parameter in a confined Bardeen-Cooper-Schrieffer Fermi gas after an interaction quench”, *Phys. Rev. A* **97**, 013619 (2018).
- [132] S. Hannibal, P. Kettmann, M. D. Croitoru, V. M. Axt, and T. Kuhn, “Persistent oscillations of the order parameter and interaction quench phase diagram for a confined Bardeen-Cooper-Schrieffer Fermi gas”, *Phys. Rev. A* **98**, 053605 (2018).
- [133] A. Behrle, T. Harrison, J. Kombe, K. Gao, M. Link, J.-S. Bernier, C. Kollath, and M. Köhl, “Higgs mode in a strongly interacting fermionic superfluid”, *Nat. Phys.* **14**, 781 (2018).
- [134] D. M. Lee, “The extraordinary phases of liquid ^3He ”, *Rev. Mod. Phys.* **69**, 645 (1997).
- [135] P. Wölfle, “Collisionless collective modes in superfluid ^3He ”, *Physica B+C* **90**, 96 (1977).
- [136] G. Shchedrin and D. M. Lee, “Nambu identity and collective modes in superconductors and superfluid ^3He ”, *Phys. Scr.* **91**, 013006 (2015).
- [137] J. A. Sauls and T. Mizushima, “On the Nambu fermion-boson relations for superfluid ^3He ”, *Phys. Rev. B* **95**, 094515 (2017).
- [138] M. D. Nguyen, A. M. Zimmerman, and W. P. Halperin, “Corrections to Higgs mode masses in superfluid ^3He from acoustic spectroscopy”, *Phys. Rev. B* **99**, 054510 (2019).
- [139] G. E. Volovik and M. A. Zubkov, “Higgs Bosons in Particle Physics and in Condensed Matter”, *J. Low Temp. Phys.* **175**, 486 (2014).

-
- [140] D. B. Mast, B. K. Sarma, J. R. Owers-Bradley, I. D. Calder, J. B. Ketterson, and W. P. Halperin, “Measurements of High-Frequency Sound Propagation in $^3\text{He-B}$ ”, *Phys. Rev. Lett.* **45**, 266 (1980).
- [141] R. W. Giannetta, A. Ahonen, E. Polturak, J. Saunders, E. K. Zeise, R. C. Richardson, and D. M. Lee, “Observation of a New Sound-Attenuation Peak in Superfluid $^3\text{He-B}$ ”, *Phys. Rev. Lett.* **45**, 262 (1980).
- [142] P. N. Fraenkel, R. Keolian, and J. D. Reppy, “Pressure dependence of the zero temperature real squashing mode in ^3B ”, *Phys. Rev. Lett.* **62**, 1126 (1989).
- [143] J. P. Davis, H. Choi, J. Pollanen, and W. P. Halperin, “Collective Modes and f -Wave Pairing Interactions in Superfluid ^3He ”, *Phys. Rev. Lett.* **97**, 115301 (2006).
- [144] V. V. Zavjalov, S. Autti, V. B. Eltsov, P. J. Heikkinen, and G. E. Volovik, “Light Higgs channel of the resonant decay of magnon condensate in superfluid $^3\text{He-B}$ ”, *Nat. Commun.* **7**, 10294 (2016).
- [145] D. Jérôme, T. M. Rice, and W. Kohn, “Excitonic Insulator”, *Phys. Rev.* **158**, 462 (1967).
- [146] Y. Wakisaka, T. Sudayama, K. Takubo, T. Mizokawa, M. Arita, H. Namatame, M. Taniguchi, N. Katayama, M. Nohara, and H. Takagi, “Excitonic Insulator State in Ta_2NiSe_5 Probed by Photoemission Spectroscopy”, *Phys. Rev. Lett.* **103**, 026402 (2009).
- [147] G. Mazza, M. Rösner, L. Windgätter, S. Latini, H. Hübener, A. J. Millis, A. Rubio, and G. Antoine, “Nature of symmetry breaking at the excitonic insulator transition: Ta_2NiSe_5 ”, *arXiv* **1911.11835** (2019).
- [148] D. Werdehausen et al., “Ultrafast dynamics and coherent order parameter oscillations under photo-excitation in the excitonic insulator Ta_2NiSe_5 ”, in *Ultrafast Bandgap Photonics III*, Vol. 10638 (2018), pp. 1–6.
- [149] D. Werdehausen, T. Takayama, M. Höppner, G. Albrecht, A. W. Rost, Y. Lu, D. Manske, H. Takagi, and S. Kaiser, “Coherent order parameter oscillations in the ground state of the excitonic insulator Ta_2NiSe_5 ”, *Sci. Adv.* **4**, eaap8652 (2018).
- [150] G. Grüner, “The dynamics of charge-density waves”, *Rev. Mod. Phys.* **60**, 1129 (1988).
- [151] J. Demsar, K. Biljaković, and D. Mihailovic, “Single Particle and Collective Excitations in the One-Dimensional Charge Density Wave Solid $\text{K}_{0.3}\text{MoO}_3$ Probed in Real Time by Femtosecond Spectroscopy”, *Phys. Rev. Lett.* **83**, 800 (1999).
- [152] H. Y. Liu et al., “Possible observation of parametrically amplified coherent phasons in $\text{K}_{0.3}\text{MoO}_3$ using time-resolved extreme-ultraviolet angle-resolved photoemission spectroscopy”, *Phys. Rev. B* **88**, 045104 (2013).
- [153] H. Schaefer, V. V. Kabanov, and J. Demsar, “Collective modes in quasi-one-dimensional charge-density wave systems probed by femtosecond time-resolved optical studies”, *Phys. Rev. B* **89**, 045106 (2014).
- [154] R. Mankowsky, B. Liu, S. Rajasekaran, H. Y. Liu, D. Mou, X. J. Zhou, R. Merlin, M. Först, and A. Cavalleri, “Dynamical Stability Limit for the Charge Density Wave in $\text{K}_{0.3}\text{MoO}_3$ ”, *Phys. Rev. Lett.* **118**, 116402 (2017).
- [155] R. Yuzupov, T. Mertelj, V. V. Kabanov, S. Brazovskii, P. Kusar, J.-H. Chu, I. R. Fisher, and D. Mihailovic, “Coherent dynamics of macroscopic electronic order through a symmetry breaking transition”, *Nat. Phys.* **6**, 681 (2010).

- [156] R. Y. Chen, S. J. Zhang, M. Y. Zhang, T. Dong, and N. L. Wang, “Revealing Extremely Low Energy Amplitude Modes in the Charge-Density-Wave Compound LaAgSb_2 ”, *Phys. Rev. Lett.* **118**, 107402 (2017).
- [157] J. P. Hinton, J. D. Koralek, Y. M. Lu, A. Vishwanath, J. Orenstein, D. A. Bonn, W. N. Hardy, and R. Liang, “New collective mode in $\text{YBa}_2\text{Cu}_3\text{O}_{6+x}$ observed by time-domain reflectometry”, *Phys. Rev. B* **88**, 060508 (2013).
- [158] D. Geffroy, J. Kaufmann, A. Hariki, P. Gunacker, A. Hausoel, and J. Kuneš, “Collective Modes in Excitonic Magnets: Dynamical Mean-Field Study”, *Phys. Rev. Lett.* **122**, 127601 (2019).
- [159] C. Rüegg, B. Normand, M. Matsumoto, A. Furrer, D. F. McMorrow, K. W. Krämer, H. U. Güdel, S. N. Gvasaliya, H. Mutka, and M. Boehm, “Quantum Magnets under Pressure: Controlling Elementary Excitations in TlCuCl_3 ”, *Phys. Rev. Lett.* **100**, 205701 (2008).
- [160] P. Merchant, B. Normand, K. W. Krämer, M. Boehm, D. F. McMorrow, and C. Rüegg, “Quantum and classical criticality in a dimerized quantum antiferromagnet”, *Nat. Phys.* **10**, 373 (2014).
- [161] A. Jain, M. Krautloher, J. Porras, G. H. Ryu, D. P. Chen, D. L. Abernathy, J. T. Park, A. Ivanov, J. Chaloupka, G. Khaliullin, B. Keimer, and B. J. Kim, “Higgs mode and its decay in a two-dimensional antiferromagnet”, *Nat. Phys.* **13**, 633 (2017).
- [162] S.-M. Souliou, J. c. ř. Chaloupka, G. Khaliullin, G. Ryu, A. Jain, B. J. Kim, M. Le Tacon, and B. Keimer, “Raman Scattering from Higgs Mode Oscillations in the Two-Dimensional Antiferromagnet Ca_2RuO_4 ”, *Phys. Rev. Lett.* **119**, 067201 (2017).
- [163] T. Hong et al., “Higgs amplitude mode in a two-dimensional quantum antiferromagnet near the quantum critical point”, *Nat. Phys.* **13**, 638 (2017).
- [164] T. Ying, K. P. Schmidt, and S. Wessel, “Higgs Mode of Planar Coupled Spin Ladders and its Observation in $\text{C}_9\text{H}_{18}\text{N}_2\text{CuBr}_4$ ”, *Phys. Rev. Lett.* **122**, 127201 (2019).
- [165] A. Marthinsen, S. M. Griffin, M. Moreau, T. Grande, T. Tybell, and S. M. Selbach, “Goldstone-like phonon modes in a (111)-strained perovskite”, *Phys. Rev. Materials* **2**, 014404 (2018).
- [166] D. M. Juraschek, Q. N. Meier, and P. Narang, “Parametric Excitation of an Optically Silent Goldstone-Like Phonon Mode”, *Phys. Rev. Lett.* **124**, 117401 (2020).
- [167] Q. N. Meier, A. Stucky, J. Teyssier, S. M. Griffin, D. v. d. Marel, and S. N. A., “Manifestation of crystallographic Higgs and Goldstone modes in the hexagonal manganites”, *arXiv* **1912.04942** (2019).
- [168] M. Vallone, “Higgs and Goldstone Modes in Crystalline Solids”, *Phys. Status Solidi B* **2019**, 1900443 (2019).
- [169] Y. Yi-Xiang, J. Ye, and W.-M. Liu, “Goldstone and Higgs modes of photons inside a cavity”, *Sci. Rep.* **3**, 3476 (2013).
- [170] Z. M. Raines, A. A. Allocca, M. Hafezi, and V. M. Galitski, “Cavity Higgs polaritons”, *Phys. Rev. Research* **2**, 013143 (2020).

-
- [171] M. Steger, R. Hanai, A. O. Edelman, P. B. Littlewood, D. W. Snoke, J. Beaumariage, B. Fluegel, K. West, L. N. Pfeiffer, and A. Mascarenhas, “Direct observation of the quantum-fluctuation driven amplitude mode in a microcavity polariton condensate”, arXiv **1912.06687** (2019).
- [172] J. Léonard, A. Morales, P. Zupancic, T. Donner, and T. Esslinger, “Monitoring and manipulating Higgs and Goldstone modes in a supersolid quantum gas”, *Science* **358**, 1415 (2017).
- [173] J. Hertkorn, F. Böttcher, M. Guo, J. N. Schmidt, T. Langen, H. P. Büchler, and T. Pfau, “Fate of the Amplitude Mode in a Trapped Dipolar Supersolid”, *Phys. Rev. Lett.* **123**, 193002 (2019).
- [174] D. Inotani, S. Yasui, and M. Nitta, “Strong-coupling effects of pairing fluctuations and Anderson-Bogoliubov and Higgs modes in neutron $^1\text{S}_0$ superfluids in neutron stars”, arXiv **1912.12420** (2019).
- [175] W. Wen, Y. Wang, and J. Wang, “Collective oscillation modes of a superfluid Bose–Fermi mixture”, *New J. Phys.* **21**, 093011 (2019).
- [176] J. Bardeen, L. N. Cooper, and J. R. Schrieffer, “Microscopic Theory of Superconductivity”, *Phys. Rev.* **106**, 162 (1957).
- [177] J. Bardeen, L. N. Cooper, and J. R. Schrieffer, “Theory of Superconductivity”, *Phys. Rev.* **108**, 1175 (1957).
- [178] J. F. Annett, *Superconductivity, Superfluids and Condensates*, Oxford Master Series in Condensed Matter Physics (Oxford University Press, 2004).
- [179] P. W. Anderson, “Random-Phase Approximation in the Theory of Superconductivity”, *Phys. Rev.* **112**, 1900 (1958).
- [180] M. Kalthoff, F. Keim, H. Krull, and G. S. Uhrig, “Comparison of the iterated equation of motion approach and the density matrix formalism for the quantum Rabi model”, *Eur. Phys. J. B* **90**, 97 (2017).
- [181] H. Krull, “Conductivity of strongly pumped superconductors: An electron-phonon system far from equilibrium”, PhD thesis (TU Dortmund, 2014).
- [182] N. Bittner, “Novel Non-Equilibrium Dynamics in Superconductors: Induced Superconductivity and Higgs Modes”, PhD thesis (FU Berlin, 2016).
- [183] F. Peronaci, “Transient dynamics of unconventional superconductors: d-wave symmetry and strong correlations”, PhD thesis (Oct. 2016).
- [184] J. Kombe, J.-S. Bernier, M. Köhl, and C. Kollath, “Finite-duration interaction quench in dilute attractively interacting Fermi gases: Emergence of preformed pairs”, *Phys. Rev. A* **100**, 013604 (2019).
- [185] I. Bronstein, K. Semendjajew, G. Musiol, and H. Mühlig, *Taschenbuch der Mathematik*, 7th ed. (Verlag Harri Deutsch, 2008).
- [186] A. P. Schnyder, C. Mudry, and D. Manske, “Screening in $(d + s)$ -wave superconductors: Application to Raman scattering”, *Phys. Rev. B* **75**, 174525 (2007).

- [187] M. Bakr, A. P. Schnyder, L. Klam, D. Manske, C. T. Lin, B. Keimer, M. Cardona, and C. Ulrich, “Electronic and phononic Raman scattering in detwinned $\text{YBa}_2\text{Cu}_3\text{O}_{6.95}$ and $\text{Y}_{0.85}\text{Ca}_{0.15}\text{Ba}_2\text{Cu}_3\text{O}_{6.95}$: s -wave admixture to the $d_{x^2-y^2}$ -wave order parameter”, *Phys. Rev. B* **80**, 064505 (2009).
- [188] J. R. Kirtley, C. C. Tsuei, Ariando, C. J. M. Verwijs, S. Harkema, and H. Hilgenkamp, “Angle-resolved phase-sensitive determination of the in-plane gap symmetry in $\text{YBa}_2\text{Cu}_3\text{O}_{7-\delta}$ ”, *Nat. Phys.* **2**, 190 (2006).
- [189] J. Wosnitza, “Superconductivity of Organic Charge-Transfer Salts”, *J. Low Temp. Phys.* **197**, 250 (2019).
- [190] V. Gurarie, “Nonequilibrium Dynamics of Weakly and Strongly Paired Superconductors”, *Phys. Rev. Lett.* **103**, 075301 (2009).
- [191] T. Cui, “Disorder effects and non-equilibrium dynamics on the electronic orders of strongly correlated materials”, PhD thesis (University of Minnesota, 2019).
- [192] A. R. Strnad, C. F. Hempstead, and Y. B. Kim, “Dissipative Mechanism in Type-II Superconductors”, *Phys. Rev. Lett.* **13**, 794 (1964).
- [193] Y. B. Kim, C. F. Hempstead, and A. R. Strnad, “Resistive States of Hard Superconductors”, *Rev. Mod. Phys.* **36**, 43 (1964).
- [194] C. Caroli and K. Maki, “Fluctuations of the Order Parameter in Type-II Superconductors. I. Dirty Limit”, *Phys. Rev.* **159**, 306 (1967).
- [195] C. Caroli and K. Maki, “Fluctuations of the Order Parameter in Type-II Superconductors. II. Pure Limit”, *Phys. Rev.* **159**, 316 (1967).
- [196] M. Tinkham, “Viscous Flow of Flux in Type-II Superconductors”, *Phys. Rev. Lett.* **13**, 804 (1964).
- [197] J. Bardeen and M. J. Stephen, “Theory of the Motion of Vortices in Superconductors”, *Phys. Rev.* **140**, A1197 (1965).
- [198] A. Schmid, “A time dependent Ginzburg-Landau equation and its application to the problem of resistivity in the mixed state”, *Phys. Kondens. Mater.* **5**, 302 (1966).
- [199] C. Caroli and K. Maki, “Motion of the Vortex Structure in Type-II Superconductors in High Magnetic Field”, *Phys. Rev.* **164**, 591 (1967).
- [200] K. Maki, “Resistive States in High-Field Type-II Superconductors”, *Phys. Rev.* **169**, 381 (1968).
- [201] C.-R. Hu and R. S. Thompson, “Dynamic Structure of Vortices in Superconductors. II. $H \ll H_{c2}$ ”, *Phys. Rev. B* **6**, 110 (1972).
- [202] M. Sigrist and K. Ueda, “Phenomenological theory of unconventional superconductivity”, *Rev. Mod. Phys.* **63**, 239 (1991).
- [203] R. Comin and A. Damascelli, “ARPES: A Probe of Electronic Correlations”, in *Strongly Correlated Systems: Experimental Techniques*, Vol. 180, Springer Series in Solid-State Sciences (Springer, 2015) Chap. 2, p. 31.
- [204] S. Hüfner, *Photoelectron Spectroscopy: Principles and Applications*, 3rd ed. (Springer, 2003).

-
- [205] A. Damascelli, Z. Hussain, and Z.-X. Shen, “Angle-resolved photoemission studies of the cuprate superconductors”, *Rev. Mod. Phys.* **75**, 473 (2003).
- [206] A. Damascelli, “Probing the Electronic Structure of Complex Systems by ARPES”, *Phys. Scr.* **T109**, 61 (2004).
- [207] L. Schwarz, B. Fauseweh, and D. Manske, “Momentum-resolved analysis of condensate dynamic and Higgs oscillations in quenched superconductors with time-resolved ARPES”, *Phys. Rev. B* **101**, 224510 (2020).
- [208] J. K. Freericks, H. R. Krishnamurthy, and T. Pruschke, “Theoretical Description of Time-Resolved Photoemission Spectroscopy: Application to Pump-Probe Experiments”, *Phys. Rev. Lett.* **102**, 136401 (2009).
- [209] H. R. K. James K. Freericks, “Constant Matrix Element Approximation to Time-Resolved Angle-Resolved Photoemission Spectroscopy”, *Photonics* **3**, 58 (2016).
- [210] J. K. Freericks, H. R. Krishnamurthy, M. A. Sentef, and T. P. Devereaux, “Gauge invariance in the theoretical description of time-resolved angle-resolved pump/probe photoemission spectroscopy”, *Phys. Scr.* **T165**, 014012 (2015).
- [211] M. Sentef, A. F. Kemper, B. Moritz, J. K. Freericks, Z.-X. Shen, and T. P. Devereaux, “Examining Electron-Boson Coupling Using Time-Resolved Spectroscopy”, *Phys. Rev. X* **3**, 041033 (2013).
- [212] T. P. Devereaux and R. Hackl, “Inelastic light scattering from correlated electrons”, *Rev. Mod. Phys.* **79**, 175 (2007).
- [213] T. E. Stevens, J. Kuhl, and R. Merlin, “Coherent phonon generation and the two stimulated Raman tensors”, *Phys. Rev. B* **65**, 144304 (2002).
- [214] Y. Yan, E. B. Gamble, and K. A. Nelson, “Impulsive stimulated scattering: General importance in femtosecond laser pulse interactions with matter, and spectroscopic applications”, *J. Chem. Phys.* **83**, 5391 (1985).
- [215] S. Maehrlein, A. Paarmann, M. Wolf, and T. Kampfrath, “Terahertz Sum-Frequency Excitation of a Raman-Active Phonon”, *Phys. Rev. Lett.* **119**, 127402 (2017).
- [216] F. Giorgianni, T. Cea, C. Vicario, C. P. Hauri, W. K. Withanage, X. Xi, and L. Benfatto, “Leggett mode controlled by light pulses”, *Nat. Phys.* **15**, 341 (2019).
- [217] T. P. Devereaux and D. Einzel, “Electronic Raman scattering in superconductors as a probe of anisotropic electron pairing”, *Phys. Rev. B* **51**, 16336 (1995).
- [218] D. Fausti, R. I. Tobey, N. Dean, S. Kaiser, A. Dienst, M. C. Hoffmann, S. Pyon, T. Takayama, H. Takagi, and A. Cavalleri, “Light-Induced Superconductivity in a Stripe-Ordered Cuprate”, *Science* **331**, 189 (2011).
- [219] W. Hu, S. Kaiser, D. Nicoletti, C. R. Hunt, I. Gierz, M. C. Hoffmann, M. Le Tacon, T. Loew, B. Keimer, and A. Cavalleri, “Optically enhanced coherent transport in YBa₂Cu₃O_{6.5} by ultrafast redistribution of interlayer coupling”, *Nature* **13**, 705 (2014).
- [220] R. Mankowsky et al., “Nonlinear lattice dynamics as a basis for enhanced superconductivity in YBa₂Cu₃O_{6.5}”, *Nature* **516**, 71 (2014).

- [221] S. Kaiser, C. R. Hunt, D. Nicoletti, W. Hu, I. Gierz, H. Y. Liu, M. Le Tacon, T. Loew, D. Haug, B. Keimer, and A. Cavalleri, “Optically induced coherent transport far above T_c in underdoped $\text{YBa}_2\text{Cu}_3\text{O}_{6+\delta}$ ”, *Phys. Rev. B* **89**, 184516 (2014).
- [222] R. Mankowsky, M. Först, T. Loew, J. Porras, B. Keimer, and A. Cavalleri, “Coherent modulation of the $\text{YBa}_2\text{Cu}_3\text{O}_{6+x}$ atomic structure by dispersive stimulated ionic Raman scattering”, *Phys. Rev. B* **91**, 094308 (2015).
- [223] E. Casandruc, D. Nicoletti, S. Rajasekaran, Y. Laplace, V. Khanna, G. D. Gu, J. P. Hill, and A. Cavalleri, “Wavelength-dependent optical enhancement of superconducting interlayer coupling in $\text{La}_{1.885}\text{Ba}_{0.115}\text{CuO}_4$ ”, *Phys. Rev. B* **91**, 174502 (2015).
- [224] M. Mitrano, A. Cantaluppi, D. Nicoletti, S. Kaiser, A. Perucchi, S. Lupi, P. Di Pietro, D. Pontiroli, M. Riccò, S. R. Clark, D. Jaksch, and A. Cavalleri, “Possible light-induced superconductivity in K_3C_60 at high temperature”, *Nature* **530**, 461 (2016).
- [225] M. Buzzi, G. Jotzu, A. Cavalleri, J. I. Cirac, E. A. Demler, B. I. Halperin, M. D. Lukin, T. Shi, Y. Wang, and D. Podolsky, “Higgs-mediated optical amplification in a non-equilibrium superconductor”, arXiv **1908.10879** (2019).
- [226] S. Paeckel, B. Fauseweh, A. Osterkorn, T. Köhler, D. Manske, and S. R. Manmana, “Detecting superconductivity out-of-equilibrium”, arXiv **1905.08638** (2019).
- [227] N. Bittner, T. Tohyama, S. Kaiser, and D. Manske, “Possible Light-Induced Superconductivity in a Strongly Correlated Electron System”, *J. Phys. Soc. Jpn.* **88**, 044704 (2019).
- [228] G. Rickayzen, *Theory of superconductivity*, Monographs and Texts in Physics and Astronomy (Interscience, 1965).

Statement of Authorship

I hereby declare that I am the sole author of this thesis and that I have not used any sources other than those listed in the bibliography and identified as references. I further declare that I have not submitted this thesis at any other institution in order to obtain a degree.

Lukas Schwarz

Stuttgart, April 15th, 2020

Acknowledgements

I want to thank several people who supported me during my time as a PhD student and contributed to the success of this work. First of all, I want to thank Prof. Dr. Walter Metzner for the opportunity to work in his group at the Max Planck Institute for Solid State Research in Stuttgart. I highly appreciated the large number of possibilities I had during the time in his group including the attendance at several workshops, conferences and schools and I am also thankful for the freedom to select and work on different research projects. I am very grateful to my supervisor Prof. Dr. Dirk Manske, who always encouraged me to follow my research interests. I am thankful for the interesting research topics he introduced to me and I appreciate the countless interesting discussions I enjoyed having with him. I also highly appreciate all the help and support I received from him during my time at the MPI Stuttgart as well as his experience and advice inside and outside of science he shared with me. It was a great pleasure to have him as a supervisor. I also want to thank Prof. Dr. Piet Brouwer for co-referring this thesis and for the possibility of giving a seminar talk in his group at the FU Berlin and to have helpful discussions afterwards.

I want to thank Dr. Nikolaj Bittner, who took the time during the first months of my PhD to introduce the Higgs physics and the numerical implementation of the density matrix formalism to me. Knowing all the little tricks and possible obstacles was a great help. I also appreciate and enjoyed the discussions with him after he left the institute. I am also thankful to Dr. Benedikt Fauseweh for all the helpful discussions about physics and numerics we had during his time at the institute and afterwards. I am also grateful to Dr. Matteo Puviani for all the discussions and projects we did together. I am also thankful to Dr. Andreas Schnyder for various discussions about my research. It was a great pleasure to work with all of them.

Furthermore, I want to thank Prof. Dr. Stefan Kaiser from the experimental ultrafast spectroscopy research group at the MPI Stuttgart and his group members Dr. Hao Chu and Min-Jae Kim. The discussions with them about the experimental implementation and realization of my theoretical calculations were extremely helpful in understanding the related physics in more detail, which helped to develop the required theories. Connected with this, I am very thankful to have had the opportunity to work at the MPI Stuttgart with all its possibilities, ranging from the close connection to experimental groups, the excellent equipment and computational resources, the great number of interesting seminars and the travel opportunities to several conferences, schools and workshops.

I would like to thank Hirsh Kamakari and Paul Fröse from the UBC, for who I had the pleasure in helping to supervise their eight-month stay in Stuttgart during their co-op program. I enjoyed the many discussion I had with them. I also want to thank Nathan Cheng for the exchange of experience he had in various numerical implementations. I want to thank Dr. Hans Boschker for being my external adviser in the PhD committee and for his helpful comments. I want to thank Dr. Hans-Georg Libuda and the IMPRS for the opportunity to be part of this research school and the interesting workshops and experiences. I also want to thank the IT department of the Max Planck Institute for their excellent work in providing a stable and functional environment to work with. I always received competent and fast response and help for any kind of problems which occurred. I am also grateful for having enjoyed the possibilities within the Max-Planck-UBC-UTokyo Center for Quantum Materials and the collaborations within. I had several possibilities to participate in schools and workshops in Stuttgart, Tokyo and Vancouver.

I also want to thank Dr. Eslam Khalaf, Paul Fröse and Simon Klein for being my office

Acknowledgements

colleagues. It was always a nice work atmosphere. I also want to thank Jeanette Schüller-Knapp, who was a great help in any administrative tasks. I further want to thank all colleagues of the Metzner department. It was always a nice environment to work in and I enjoyed the common lunch and coffee breaks. Special thanks also goes to Sarah Möhrle, Kira Neubehler, Simon Klein and Dr. Matteo Puviani for proof reading my thesis. Finally, I want to thank my parents Gisela and Rüdiger Schwarz for supporting me all the time during my study and the time as a PhD student.

Publications

Parts of this thesis were published in the following articles:

- L. Schwarz, B. Fauseweh, N. Tsuji, N. Cheng, N. Bittner, H. Krull, M. Berciu, G. S. Uhrig, A. P. Schnyder, S. Kaiser, and D. Manske, “Classification and characterization of nonequilibrium Higgs modes in unconventional superconductors”, *Nat. Commun.* **11**, 287 (2020).
- L. Schwarz and D. Manske, “Theory of driven Higgs oscillations and third-harmonic generation in unconventional superconductors”, *Phys. Rev. B* **101**, 184519 (2020).
- L. Schwarz, B. Fauseweh, and D. Manske, “Momentum-resolved analysis of condensate dynamic and Higgs oscillations in quenched superconductors with time-resolved ARPES”, *Phys. Rev. B* **101**, 224510 (2020).
- M. Puviani, L. Schwarz, X.-X. Zhang, S. Kaiser, and D. Manske, “Current-assisted Raman activation of the Higgs mode in superconductors”, *Phys. Rev. B* **101**, 220507 (2020).
- H. Chu et al., “Phase-resolved Higgs response in superconducting cuprates”, *Nat. Commun.* **11**, 1793 (2020).

Additional publications

- M. Geiger, L. Schwarz, U. Zschieschang, D. Manske, J. Pflaum, J. Weis, H. Klauk, and R. T. Weitz, “Quantitative Analysis of the Density of Trap States in Semiconductors by Electrical Transport Measurements on Low-Voltage Field-Effect Transistors”, *Phys. Rev. Applied* **10**, 044023 (2018).
- H. Cartarius, Z. H. Musslimani, L. Schwarz, and G. Wunner, “Computing eigenfunctions and eigenvalues of boundary-value problems with the orthogonal spectral renormalization method”, *Phys. Rev. A* **97**, 032134 (2018).
- L. Schwarz, H. Cartarius, Z. H. Musslimani, J. Main, and G. Wunner, “Vortices in Bose-Einstein condensates with \mathcal{PT} -symmetric gain and loss”, *Phys. Rev. A* **95**, 053613 (2017).
- L. Schwarz, H. Cartarius, G. Wunner, W. D. Heiss, and J. Main, “Fano resonances in scattering: an alternative perspective”, *The European Physical Journal D* **69**, 196 (2015).

